New Concepts of Metallic Bonding

Thesis by

Mark Herbert McAdon

In partial fulfillment of the requirements
for the degree of Doctor of Philosophy

California Institute of Technology

Pasadena, California

1988

(Submitted September 29, 1987)

To Eva

Acknowledgements

I thank Bill Goddard, my research advisor, for having faith in me. My performance at Caltech has been far from uniform. Thank you, Bill, for your patience and expert advice.

I thank Eva, Derek, and Sean, for inspiration, for giving life perspective, and for love. I thank my parents for their support. I thank Chuen Jin Goh, Ron Grosz, Jeff Simmen, and Thien Soon Tan, whose friendships made life bearable during my "early years" at Caltech.

I thank all members of the Goddard research group, especially Mark Brusich, Emily Carter, Bob Donnelly, Marv Goodgame, Chih-Mai Kao, John Low, Adel Naylor, and Art Voter, for friendship, for scientific interaction, and for pitching in to help in times of need.

Finally, I thank the ARCS foundation for financial support for 1985-86.

Abstract

This thesis presents results derived from ab initio wavefunctions, leading to new concepts of metallic bonding — real-space concepts that do not require "thinking in reciprical (k) space." As the first step in this study of metallic bonding, Hartree-Fock and generalized valence bond wavefunctions are presented for ring clusters composed of monovalent atoms (Cu, Ag, Au, Li, and Na). These results show that one-dimensional metals need not exhibit Peierls instabilities, charge density waves, or spin density waves. In addition, magnon spectra calculated using various wavefunctions are compared with each other and with magnon spectra obtained with simple nearest-neighbor Ising and Heisenberg hamiltonians.

Generalized valence bond wavefunctions for small metal clusters lead to the conclusion that, for metallic systems, the valence electrons occupy interstitial regions — bond midpoints for one-dimensional systems, triangular hollows for two-dimensional systems, and tetrahedral hollows for three-dimensional systems. The new concepts of metallic bonding are summarized by a set of rules for the valence sp electrons of metallic systems. These rules are used to derive the low-lying isomers of small metal clusters, and are expected to prove useful in predicting the chemistry and catalytic properties of such systems. Applying these rules to bulk metals leads to a new explanation of the solubility limits governing alloys of monovalent, divalent, trivalent, and tetravalent atoms. These rules are expected to prove valuable in describing the localized states in metals and alloys such as defects or interfaces.

Contents

Thesis Introduction

Valence bond theory[1] provides a powerful framework for understanding and predicting structures and properties of *nonmetallic* systems, where the electrons can be described as being localized into hybridized atomic orbitals, spin-paired to form bonds and nonbonding lone pairs. This framework is quite useful in describing molecules, bulk structures, surface structures, and the localized states at defects and interfaces.[2,3,4]

However, for *metallic* systems, simple valence bond theory has been ambiguous and of little use. For example, each atom in a face-centered cubic monovalent metal has twelve nearest neighbors but only one valence electron. How does one form a valence bond description for systems having far too few valence electrons to form two-center two-electron bonds between all the nearest neighbors?

As a first step in addressing the issue of a valence bond description of metals, Chapters 1-4 present restricted Hartree-Fock (HF), unrestricted Hartree-Fock (UHF), and generalized valence bond (GVB) wavefunctions for ring clusters composed of copper, silver, gold, lithium, and sodium. These systems provide a sensitive test of the HF, UHF, and GVB wavefunctions because of the importance of electron correlation effects. For these "one-dimensional" metals, strong cohesion results from two-center one-electron (localized) bonding.

Chapter 5 presents HF, UHF, and GVB wavefunctions for 2D and 3D clusters of lithium atoms. Chapter 5 leads to a *generalized* valence bond model of metallic bonding, based on electrons localized into interstitial regions such as bond midpoints (1D), triangular hollows (2D), and tetrahedral hollows (3D). Hence, for the n-dimensional metallic system, the "characteristic" localized orbital is composed of sp hybrid orbitals from $n+1$ adjacent atoms. Applying this model to bulk metals leads to a new explanation of solid solubility limits governing the alloys of monovalent, divalent, trivalent, and tetravalent metals.

References

[1] L. Pauling, *The Nature of the Chemical Bond, 3rd Ed* (Cornell University Press, Ithaca, New York, 1960).

[2] W. A. Goddard III, T. H. Dunning, Jr, W. J. Hunt, and P. J. Hay, *Accts. Chem. Res.* **6**, 368 (1973); W. A. Goddard III and L. B. Harding, *Ann. Rev. Phys. Chem.* **29**, 363 (1978).

[3] P. A. Schultz and R. P. Messmer, Phys. Rev. B **34**, 2532 (1986); G. T. Surratt and W. A. Goddard III, Phys. Rev. B **18**, 2831 (1978) and Solid State Commun. **22**, 413 (1977).

[4] C. A. Swarts, T. C. McGill and W. A. Goddard III, Surf. Sci. **110**, 400 (1981); A. Redondo and W. A. Goddard III, J. Vac. Sci. Technol. **21**, 344 (1982); A. Redondo, W. A. Goddard III and T. C. McGill, Surf. Sci. **132**, 49 (1983).

Chapter 1

Charge Density Waves, Spin Density Waves, and Peierls Distortions in One-Dimensional Metals: Hartree-Fock Studies of Cu, Ag, Au, Li, and Na

Chapter 1 consists of an article coauthored with William A. Goddard III that has been accepted for publication in the Journal of Chemical Physics.

Charge Density Waves, Spin Density Waves, and Peierls Distortions in One-Dimensional Metals: I. Hartree-Fock Studies of Cu, Ag, Au, Li, and Na

Mark H. McAdon and William A. Goddard III

Contribution No. 6986 from the Arthur Amos Noyes Laboratory of Chemical Physics, California Institute of Technology, Pasadena, California 91125

(Received June 25, 1987; revised manuscript received August 22, 1987)

Abstract: Ab initio calculations indicate that each of the one-dimensional elemental metals composed of Cu, Ag, Au, Li and Na is *stable* with respect to the Peierls distortion if spin polarization is allowed [unrestricted Hartree-Fock (UHF)], leading to a spin density wave. Disallowing spin polarization [restricted Hartree-Fock (HF)] leads to a half-filled energy band, Peierls instability and a charge density wave. For each case, the UHF wavefunction leads to an antiferromagnetic (non-metallic) ground state, with a spin density wave resulting from electron correlation effects, consistent with the Mott-Hubbard low-density antiferromagnetic insulator. The UHF antiferromagnetic (non-metallic) ground states have large cohesive energies resulting from *two-center one-electron bonds* (similar to the one-electron bonds of the diatomic molecular cations).

I. Introduction

The electronic structure of a crystalline solid is usually described in terms of energy bands involving Bloch functions delocalized over the infinite lattice.[1,2,3] These energy bands for crystalline solids [analogous to the molecular orbital (MO) energy levels of molecules] determine the electronic properties. Metals result when one or more energy bands are only partially occupied. Insulators (or semiconductors) result when the valence band and conduction bands are separated by a finite energy gap, so that the valence band is completely occupied (each orbital occupied with two electrons, one of each spin), and the conduction bands are completely unoccupied.

Peierls[1] has shown that one-dimensional metals having partially filled energy bands are susceptible to a distortion leading to an energy band gap at the Fermi level and hence a metal-to-insulator transition. Consequently, linear metallic chains with equidistant adjacent atoms ("symmetical" chains) are predicted to distort such that the distances between adjacent atoms are not all equal.[1] For a homonuclear linear chain composed of monovalent atoms, the energy band description leads to a half-filled band (in the absence of strong electron-electron interactions) and a Peierls distortion pairing up adjacent atoms to form a diatomic lattice.[1] The *Peierls instability* is often associated with a *charge density wave* having maxima and minima at alternating bond midpoints (the absence of such a charge density wave does not preclude a Peierls distortion).

Crystalline solids of the alkali or noble metals are metals whereas the monatomic gases (infinite interatomic distance) are insulators. Mott[2] has suggested that a crystalline lattice of monovalent atoms should exhibit a sharp metal-to-insulator transition as the distance a between the atoms is increased. However, the normal energy

band theory (restricted Hartree-Fock theory) predicts that such a system is a metal for all a.[2] This contradiction has been referred to as the *Mott paradox*.

The problem with normal energy band theory is that it does not include the electron correlation effects required to obtain nonmetallic behavior for metallic systems at large a.[2,4] However, the necessary electron correlation effects are included in both unrestricted Hartree-Fock and generalized valence bond theory.[4,5]

In order to modify normal energy band theory to account for the metal-to-insulator transition, Hubbard[6] introduced a hamiltonian for monovalent atoms including the normal one-electron terms and in addition, the intra-atomic coulomb energy

$$\mathcal{U} = \langle \omega_1(1)\omega_1(2)|r_{12}^{-1}|\omega_1(1)\omega_1(2)\rangle$$

that tends to prevent two electrons from occupying the *same* localized Wannier[3] orbital ω_1, where r_{ij}^{-1} is the electrostatic interaction between electrons i and j (in atomic units where $e = 1$). Hubbard showed that this hamiltonian splits the usual half-filled valence band (doubly-occupied orbitals) into two sets of energy bands; for each spin there is a lower-energy band consisting of singly-occupied orbitals and a higher-energy band consisting of unoccupied orbitals. These two bands presumably overlap[2,6] when a is sufficiently small that

$$\mathcal{B}/\mathcal{U} \geq \sqrt{4/3} \approx 1.15$$

[where $\mathcal{B}$ is the band width for $\mathcal{U} = 0$], leading to a transition from an antiferromagnetic insulator[2,7] — with a *spin density wave* — at large a ("low-density") to a metal at small a ("high-density"). However, the critical ratio $\mathcal{B}/\mathcal{U} = 1.15$ is based on an approximate solution of the Hubbard hamiltonian,[2,6] and the exact solution[8] of the Hubbard hamiltonian for a *one-dimensional* lattice of monovalent atoms with

a single band leads to a transition from antiferromagnetic insulator to metal only in the limit as B/U approaches infinity.

These ideas of Peierls instability, charge density waves, antiferromagnetic insulators, and spin density waves have proved useful in characterizing pseudo-one-dimensional inorganic and organic compounds[9,10] such as (*i*) NbI_4, consisting of dimerized chains of edge-sharing octahedral complexes (presumably due to Peierls instability),[11] (*ii*) $CuCl_2$ and $(CH_3)_4NMnCl_3$ antiferromagnetic insulators,[12] consisting of symmetric chains, (*iii*) organic polymers such as polyacetylene,[13] and (*iv*) organic charge transfer salts such as those based on the tetracyanoquinodimethane (TCNQ) anion.[9,10] Such pseudo-one-dimensional solids are believed to be likely candidates for high-temperature superconductivity.[10]

Testing these concepts of Peierls instability, charge density waves, antiferromagnetic insulators, and spin density waves with high quality ab initio[14] total energy calculations for one-dimensional metallic systems should prove valuable in understanding the properties of such pseudo-one-dimensional solids.

Here we present results of extensive ab initio total energy calculations for various one-dimensional ring clusters composed of copper, silver, gold, lithium and sodium. We discuss the electronic structure of the one-dimensional metal from the energy band point of view, using results of the ab initio calculations to illustrate the concepts. Section II presents results calculated with single-determinant self-consistent field wavefunctions [restricted Hartree-Fock (HF, non-spin-polarized) and Unrestricted Hartree-Fock (UHF, spin-polarized)]. Details of these many-electron wavefunctions are given in Appendix A.

After submission of this article, a paper appeared in this journal presenting *ab initio* HF results for the Li_6, Li_{10}, and Li_{14} ring clusters and coupled-cluster results

for Li_8.[15] This study also showed that at the HF level, Li_8, Li_{10}, and Li_{14} are each unstable with respect to dissociation into Li_2 molecules, and that HF leads to Peierls instability for Li_{10} and Li_{14}.[15]

Here we show that the Peierls instability and lack of cohesion of the one-dimensional ring clusters composed of Cu, Ag, Au, Li, and Na are artifacts of the HF wavefunction. Hence, UHF leads to stable one-dimensional structures (no Peierls instability) for Cu, Ag, Au, Li, and Na. The stabilities of these one-dimensional systems are confirmed by the results of generalized valence bond calculations (presented elsewhere).[16]

II. Results

In the process of exploring the bonding in metal clusters,[17] we performed extensive *ab initio* calculations on various one-dimensional ring and chain clusters of lithium atoms up to $N = 14$, where N is the number of atoms in the cluster, and extrapolated the various results to infinite N.[16] These studies show that the cohesive properties of the ring clusters converge rather quickly, and that the eight and ten atom ring clusters are qualitatively correct and fairly accurate as models for the infinite chain (each are periodic in one dimension). Herein we examine M_N ring clusters composed of copper, silver, gold, lithium, and sodium, where the lattice constants (a) for the undistorted (symmetric) clusters are taken equal to the nearest-neighbor distances for the bulk metals.[18] We model the Peierls dimerized chains with ring clusters containing alternating long and short internuclear separations $a \pm \delta a$, as shown in Figure 1, where the *average* nearest-neighbor distance is equal to that for the symmetric cluster.

We find that the cohesive properties of the one-dimensional alkali and noble metals are dominated by the valence *sp* electrons. The standard Mulliken[19] orbital

population analysis for the M_{10} ring clusters leads to the average atomic configurations (UHF, see Appendix A.2) $3d^{9.972}4s^{0.624}4p^{0.404}$ (Cu), $4d^{9.971}5s^{0.608}5p^{0.421}$ (Ag), $5d^{9.959}6s^{0.862}6p^{0.179}$ (Au), $2s^{0.494}2p^{0.506}$ (Li), and $3s^{0.649}3p^{0.351}$ (Na). For the ground and low-lying excited electronic states of the noble metal clusters, there is minimal hybridization of the d core orbitals with the sp valence orbitals, and hence the closed-shell d^{10} configurations are maintained (see Appendix A.2). For both the noble and alkali metals, sp hybridization is crucial in describing the valence electronic structures. However, the $p\pi$ conduction bands are significantly higher in energy than the valence band for both the alkali metals and the noble metals and hence for the ground electronic states the $p\pi$ conduction bands are unoccupied (see Appendix A.2).

A. Energy Band Theory — Non-Interacting Electrons

The normal energy band theory of metals is based on one-electron Bloch functions (ψ_m) which for a M_N symmetric ring cluster can be written as

$$\begin{aligned} \psi_m^{(\omega)} &= N^{-1/2}\sum_{j=1}^{N}\omega_j \exp(ikR_j) \\ k &= \frac{2\pi m}{aN} \\ R_j &= ja \end{aligned}$$

where m is an integer ($|m| \leq N/2$), $\{\omega_j\}$ is the optimal set of N equivalent real orthogonal localized (Wannier)[3] orbitals, k is the wave vector, and R_j denotes the position of ω_j (going around the circumference). The one-electron energies are given as

$$\epsilon_k = \langle\psi_m|\hat{h}^{EFF}|\psi_m\rangle \tag{1}$$

where $\hat{h}^{EFF}$ is an effective one-electron hamiltonian including the electronic kinetic energy and the potential energy [due to both the ion cores and the remaining $(n-1)$

valence electrons]. A given set of Bloch functions can always be combined to give an equivalent set of real functions (see Appendix A.6), and we use the real representations of the Bloch functions except where noted otherwise. The real representations of the Bloch functions are equivalent to molecular orbitals, and the non-interacting electrons approximation for bulk solids is somewhat analogous to the Hückel approximation for molecules.[20]

The Bloch functions for the valence band of each M_N ring cluster (M = Cu, Ag, Au, Li and Na) can be written in terms of localized orbitals $\{\omega_j\}$ *centered symmetrically at the bond midpoints*, as shown in Figure 2 for the Ag_8 ring cluster. It is important to note that the valence Bloch functions for these M_N ring clusters *cannot* be written in terms of localized orbitals that are centered symmetrically *at the atoms*. This is because the valence band $k = \pi/a$ orbital ($m = N/2$, even N) has nodes passing through the atomic centers whereas (in each case) the $k = \pi/a$ orbital with nodes passing through the bond midpoints is much higher in energy (hence part of a conduction band).

The one-electron energies for the Ag_8 ring cluster are given in Figure 3, where the data points representing the discrete levels are joined by a solid curve approximating the continuous band that would be obtained in the limit as N approaches infinity. The orbitals and energy levels[21] presented in Figures 2-4 are obtained from the HF valence *high-spin* state where each Bloch function is occupied with a single electron (total spin $S = 4$, see Appendix A).[22]

In the energy band model (with the usual non-interacting electrons approximation), the ϵ_k are independent of occupation because two-electron terms are not explicitly included in the effective hamiltonian (1). Thus, the ground state for the one-dimensional metal composed of monovalent atoms consists of a half-filled band

of doubly-occupied Bloch functions.

In the HF description, the two-electron terms are explicitly included in the hamiltonian, and as a result the ϵ_k are *not* independent of occupation.[23]

1. The Peierls Instability

Peierls[1] showed that the application of band theory to symmetric one-dimensional metals with partially occupied valence bands leads to instability with respect to geometric distortions. Thus, for a one-dimensional metal with a partially occupied valence band, Peierls showed that it is always possible to find a distortion lowering the energies of the one-electron states below the Fermi level (and raising the energies of the one-electron states above the Fermi level).

The Peierls instability[1] for one-dimensional metals is analogous to the Jahn-Teller[24] and pseudo-Jahn-Teller instabilities for open-shell molecules with high symmetry.

For a monovalent one-dimensional metal, the Peierls instability leads to a dimerized chain,[1] as shown in Figure 1b. The valence energy band for the dimerized Ag_8 ring cluster is shown in Figure 4. The effect of the dimerization is to produce a band gap at $k_F = \pm\pi/2a$ (0.011 eV at $\delta a = 0.10$ Å). In the usual non-interacting electrons approximation, this results in a metal-to-insulator transition since the one-electron states below the band gap are all doubly-occupied and the one-electron states above the band gap are all unoccupied. The origin of the band gap can be explained in a qualitative fashion by examining the degenerate $|m| = 2$ orbitals of the Ag_8 symmetric ring (Figure 2). Each $m = 2$ orbital has nodes bisecting alternate bond midpoints. Upon dimerization, the orbital with nodes bisecting the expanded bond midpoints is stabilized while the orbital with nodes bisecting the compressed bond midpoints

is destabilized.

We chose the eight-atom cluster as opposed to six- or ten-atom clusters for modeling the anticipated Peierls instability, since only clusters where N is divisible by four have one-electron states at $k_F = \pm\pi/2a$ ($m = 5/2$ is not an allowed state for M_{10}). Hence, with respect to the Peierls instability, $N = 4i$ ring clusters are expected to be better models of the one-dimensional metal than $N = 4i + 2$ ring clusters, although the distinction between $N = 4i$ and $N = 4i + 2$ is expected to vanish in the limit as N approaches infinity.[25]

B. Hartree-Fock

1. Cohesive Energies

Using HF wavefunctions we calculated cohesive energies of the Cu_{10}, Ag_6, Ag_8, Ag_{10}, Au_{10}, Li_6, Li_{10}, Li_{14}, and Na_{10} symmetric ring clusters (low-spin) with respect to atomization

$$M_N \rightarrow N\,M \tag{2}$$

and dimerization

$$M_N \rightarrow N/2\,M_2 \tag{3}$$

(dissociation into diatomic molecules). These are reported in Table 1, where the total cohesive energies have been divided by N. These cohesive energies are calculated using (i) the total energies of low-spin ring clusters at fixed values of the lattice constant (a), (ii) the total energies of diatomic molecules at their calculated equilibrium internuclear separations (R_e), and (iii) the total energies of the isolated atoms. In all cases the HF wavefunctions are optimized with *no orbital symmetry restrictions.* [For HF, the orbitals are each occupied with two electrons (except for

the isolated atoms where the core orbitals are doubly-occupied and the valence s orbital is singly-occupied).][23] Further details are given in Appendices A-B.

At the HF level, Na_{10} is unstable with respect to atomization, and Li_{10} and Li_{14} are just barely stable with respect to atomization. However, Cu_{10}, Ag_6, Ag_8, Ag_{10}, and Au_{10} each have large cohesive energies with respect to atomizaton (see Table 1). A second criterion for stability is cohesion with respect to dissociation into diatomic molecules.(3) Here, Ag_8, Li_6, Li_{10}, Li_{14}, and Na_{10} are unstable while Cu_{10}, Ag_{10}, and Au_{10} are just barely stable.

As expected, the series Ag_6, Ag_8, Ag_{10} indicates that, at the HF level, the $N = 4i$ clusters are significantly less stable than the $N = 4i + 2$ clusters. This is consistent with the Hückel model of $4i + 2$ aromaticity where the $N = 4i + 2$ rings have fully occupied bonding Fermi levels whereas the $N = 4i$ rings have partially occupied nonbonding Fermi levels.[20] However, the UHF results (see Table 1 and Section C) exhibit no distinction between $N = 4i$ and $N = 4i + 2$.

Results for the series Li_6, Li_{10}, Li_{14}, and the series Ag_6, Ag_8, Ag_{10} indicate that the HF cohesive energies *decrease* with increasing N. Hence, we expect that at the HF level, the Ag_{14} and Au_{14} ring clusters would each have a negative cohesive energy with respect to dissociation into diatomic molecules.

In each case the HF atomization and dimerization energies are substantially smaller than the respective UHF values (see Table 1). Both the HF and UHF cohesive energies for the one-dimensional metal clusters (Table 1) are much smaller than the respective experimental values for the three-dimensional bulk metals (Table 2).[26,27,28]

Despite the poor cohesive energies, HF often yields accurate geometries. Thus, for Na_2 HF yields a potential well with a reasonably accurate bond length (too long by 3.8%) and force constant (too small by 4.2%; see Appendix B and Table 10),

while the cohesive energy for Na_2 is *negative* at the HF level (the HF energy of Na_2 at the minimum of the well is higher than twice the HF energy of the isolated Na atom)!

For Li_6, Li_{10}, and Li_{14}, the HF cohesive energies reported here differ somewhat from those reported by Förner and Seel (FS).[15] There are several factors that lead to these differences (see Table 3): (*i*) The HF results reported by FS are for optimized lattice constants (a_e = 3.076 ± .004 Å) whereas our results are reported at fixed lattice constants (a = 3.014 Å). However, the force constants (symmetric stretch) for these systems are small enough that a displacement from the equilibrium lattice constant by 0.06 Å increases the total energy by only 1.5 meV/atom.[15] (*ii*) FS used a basis set that has more *s* flexibility but less *p* flexibility in comparison to our basis set (see Appendix A). (*iii*) By calculating two sets of HF results with the same basis set — (a) HF with full D_{Nh} orbital symmetry restrictions and (b) HF with no orbital symmetry restrictions — it is clear that the results reported by FS are for the fully symmetric states (see Table 3). Thus, for Li_6, Li_{10}, and Li_{14}, our D_{Nh} HF total energies are higher than those reported by FS by 11.973, 11.701, and 11.429 meV/atom, respectively (note that the increment is exactly 0.272 meV/atom). Hence, for both Li_{10} and Li_{14}, FS did not obtain the lowest energy low spin HF solution (which has a charge density wave) — although their conclusion that both Li_{10} and Li_{14} exhibit Peierls instability at the HF level is undoubtedly correct.

2. Charge Density Waves

First, we present results for the M_N, $N = 4i + 2$ low-spin symmetric ring clusters, and then we present results for $N = 4i$ (Ag_8).

For Cu_{10}, Ag_6, Ag_{10}, Au_{10}, and Li_6, the HF wavefunction leads to a fully symmet-

rical electronic charge density (having periodicity a) even if the orbitals are optimized without symmetry restrictions.

However, for Li_{10}, Li_{14}, and Na_{10}, HF (optimized without symmetry restrictions) leads to an electronic charge density having periodicity $2a$ (twice that of the lattice). Since the electronic charge density does not have the same periodicity as the lattice, each of these systems is said to have a charge density wave (defined by the difference between the net charge density and the symmetric component of the net charge density). For these systems, the charge density wave has maxima and minima centered about alternate atoms, as shown for Li_{14} in Figure 5, where the seven doubly-occupied valence orbitals lead to a charge density wave with maxima centered about atoms 1, 3, 5, 7, 9, 11, and 13, and minima centered about atoms 2, 4, 6, 8, 10, 12, and 14.

Charge density waves can be avoided for the low-spin HF states of the M_N ring clusters by optimizing the wavefunctions with full D_{Nh} orbital symmetry restrictions; i.e., restricting the orbitals to be Bloch functions. Hence, for M_{10} and M_{14}, the states described by the valence configurations

$$M_{10}: \quad \psi_0(\uparrow\downarrow)\psi_{-1}(\uparrow\downarrow)\psi_1(\uparrow\downarrow)\psi_{-2}(\uparrow\downarrow)\psi_2(\uparrow\downarrow)$$

$$M_{14}: \quad \psi_0(\uparrow\downarrow)\psi_{-1}(\uparrow\downarrow)\psi_1(\uparrow\downarrow)\psi_{-2}(\uparrow\downarrow)\psi_2(\uparrow\downarrow)\psi_{-3}(\uparrow\downarrow)\psi_3(\uparrow\downarrow)$$

each lead to a fully symmetrical charge density. Orbitals optimized in this fashion are shown for Li_{14} in Figure 6.

However, the optimum HF symmetric state is higher in energy than the optimum HF charge density wave state by 5.99 meV/atom, 23.22 meV/atom, and 0.70 meV/atom for Li_{10}, Li_{14}, and Na_{10}, respectively (see Table 3). For each of these cases, allowing the HF wavefunction to break symmetry — leading to a charge den-

sity wave — reduces the total electron-electron repulsion energy (two-electron energy; see Table 3). However, this is countered by one electron terms (such as the electronic kinetic energy) favoring the fully delocalized (smooth) orbitals (see Table 3).

The charge density wave states of these ring clusters can each be characterized by the D_{Nh} symmetry-projection of their canonical orbitals (having in each case D_{nh} symmetry where $n = N/2$). In each case, the D_{nh} real canonical orbitals can be combined to give complex D_{nh} functions $\{\psi'_m,\ 0 \leq |m| \leq N/4\}$ that can be decomposed into D_{Nh} Bloch functions $\{\psi_m,\ 0 \leq |m| \leq N/2\}$ as

$$\psi'_m = c_m\psi_m + c_{n-m}\psi_{n-m}.$$

Summing up the squares of the coefficients c_m gives populations p_m of the Bloch (D_{Nh}) energy levels above and below the Fermi level ($|m_F| = N/4$). These populations are given in Table 4, and, for Li_{10} and Li_{14}, are plotted as a function of wave vector in Figure 7. The magnitude of the charge density wave increases as the populations of energy levels above m_F increases. Note that in each case the sum $p_m + p_{n-m}$ is an integer and is independent of the magnitude of the charge density wave.

At the HF level, charge density waves are enhanced by (*i*) a narrow, partially occupied energy band (low overlap, low density) and (*ii*) a large density of states immediately above and below the Fermi level.[22] These properties enhance the orbital mixings required in order for the orbitals to break symmetry (and form the charge density wave) by minimizing the concomitant one-electron energy penalty. For M_{10}, the valence band widths follow the trend Cu > Au > Ag $\gg$ Na > Li (see Appendix C). Hence, (*i*) the charge density wave for Li_{10} is greater than that for Na_{10} (see Tables 3-4), and (*ii*) Cu_{10}, Ag_{10}, and Au_{10} do not have charge density waves because

their valence bands are too wide.

This is also consistent with the increase in charge density wave magnitude with increasing N for the series Li_6, Li_{10}, Li_{14} (HF does not lead to a charge density wave for Li_6). The full band width, defined as

$$\mathcal{B} = |4h_{12}^{\omega}|$$

where h_{12}^{ω} is the one-electron nearest-neighbor hopping integral (see Appendix C; h_{12}^{ω} is closely related to the Hückel β parameter),[20] actually decreases substantially with increasing N ($\mathcal{B}$ = 3.999, 2.838, and 2.334 eV for Li_6, Li_{10}, and Li_{14}, respectively; see Appendix C). Also, the number of one-electron states in the valence band is N, and hence, the energy gap between the occupied and empty one-electron states at the Fermi level

$$\delta\epsilon_F \approx \mathcal{B} \sin \pi/N \text{ for } N = 4i + 2$$

decreases dramatically with increasing N ($\delta\epsilon_F$ = 1.397, 0.792, and 0.544 eV for Li_6, Li_{10}, and Li_{14}, respectively).[22] Based on these results for the series Li_6, Li_{10}, and Li_{14}, we cannot rule out charge density waves for the HF low-spin states of the $N = 4i+2$ Cu_N, Ag_N, and Au_N clusters for $N > 10$.

The effects that control the charge density waves for the $N = 4i + 2$ ring clusters are also important for the $N = 4i$ rings. However, unlike the $N = 4i + 2$ rings, for $N = 4i$ the Fermi level is partially occupied; hence, for $N = 4i$, charge density wave states can always be obtained from the symmetry-restricted HF state by mixing the orbitals at the Fermi level (this does *not* raise the total one-electron energy). The orbitals below the Fermi level respond to this perturbation by breaking symmetry, further enhancing the charge density wave. Therefore, at the HF level, a $N = 4i$ cluster can have a charge density wave even if the neighboring $N = 4i \pm 2$ clusters

do not have charge density waves (this is true for the series Ag_6, Ag_8, and Ag_{10}).

As an example, for the M_8 symmetrical ring, the two D_{8h} HF states

$$\psi_0(\uparrow\downarrow)\psi_{-1}(\uparrow\downarrow)\psi_1(\uparrow\downarrow)\psi_{-2}(\uparrow\downarrow)$$

$$\psi_0(\uparrow\downarrow)\psi_{-1}(\uparrow\downarrow)\psi_1(\uparrow\downarrow)\psi_{2}(\uparrow\downarrow)$$

are degenerate and both lead to a fully symmetrical charge density (see Appendix A.6). However, combining the complex orbitals ψ_{-2} and ψ_2 to form the real orbitals $\overline{\psi}_{-2}$ and $\overline{\psi}_2$, and forming the analogous configurations in terms of these real orbitals leads to states having charge density waves.

For low-spin Ag_8, the HF fully symmetrical state (optimized with D_{8h} orbital symmetry restrictions) has a total energy higher than that of the lowest energy HF state by 27.8 meV/atom (see Tables 3-4 and Figure 8a). For low-spin Ag_8, the lowest energy HF wavefunction leads to a charge density wave having maxima and minima centered about alternate atoms (see Figure 8a). The orbital population analysis for this state (Table 4) indicates that the three HF valence orbitals below the Fermi level break symmetry, whereas the fourth orbital at the Fermi level has the same symmetry as $\overline{\psi}_{\pm 2}$.

For low-spin Ag_8, we also solved for a higher energy HF wavefunction leading to a charge density wave having maxima and minima centered about alternate *bond midpoints* (see Figure 8b); hence, the charge density wave of this excited state is "phase-shifted" from that of the lowest energy state (Figure 8a) by $a/2$. This excited charge density wave HF state (Figure 8b) was optimized self-consistently by imposing D_{4h} orbital symmetry restrictions, leading to four orbitals that are D_{4h} symmetry combinations of four two-center, two-electron bonds (similar to the bond of Ag_2).

Neither of these low-spin Ag_8 HF states leads to cohesion with respect to disso-

ciation into Ag_2 molecules (see Table 3). The energy splitting of these two *distinct* low-lying charge density wave states is 14.9 meV/atom for the Ag_8 symmetric ring cluster. If the lack of cohesion (with respect to diatomic molecules), and the charge density waves were directly related, one would expect that the charge density wave state having maxima and minima centered about alternate bond midpoints (Figure 8b) — consistent with the superposition of two-center two-electron bonds — would be the lowest in energy. However, for Ag_8, the lowest energy charge density wave state is the one having maxima and minima centered about alternate atoms (Figure 8a).

For Ag_8, the HF *triplet state* described by the valence configuration

$$\psi_0(\uparrow\downarrow)\psi_{-1}(\uparrow\downarrow)\psi_1(\uparrow\downarrow)\psi_{-2}(\uparrow)\psi_2(\uparrow)$$

leads to a fully symmetrical charge density and an energy lower than that of the low-spin charge density wave state (Figure 8a) by 33.6 meV/atom. However, the *lowest energy* Ag_8 HF triplet state leads to both charge and spin density waves and a total energy lower than that of the singlet charge density wave state (Figure 8a) by 38.7 meV/atom. Nevertheless, even the lowest energy Ag_8 HF triplet state is unstable with respect to the limit of four low-spin Ag_2 molecules by 4.5 meV/atom. Further details of the Ag_8 HF triplet states are given in Appendix E.

3. Peierls Instability

We chose Ag_8 for modeling the anticipated Peierls instability. The two charge density wave states (Figures 8a-b) for the low-spin Ag_8 symmetric ring cluster are each doubly degenerate. In each case, "translating" the valence orbitals by a (or rotating by $2\pi/8$) results in an equivalent but different charge density wave state. All four

charge density wave states are invariant to translations by integral multiples of $2a$.

The HF energy of low-spin Ag_8 as a function of the Peierls distortion (δa) is shown in Figure 9. As predicted by Peierls[1] the optimum geometry is a distorted (D_{4h}) structure. The HF wavefunctions optimized without orbital symmetry restrictions lead to an adiabatic potential energy curve having the correct symmetry [$E(\delta a) = E(-\delta a)$; the solid curve in Figure 9]. The HF wavefunctions optimized with D_{4h} orbital symmetry restrictions lead to a set of diabatic potential energy curves crossing at $\delta a = 0$ (the dashed curves in Figure 9). The D_{4h} orbital symmetry restrictions ensure that the valence charge density has maxima centered on a particular set of four alternating bond midpoints, as in Figure 8b.

The Peierls distortion breaks the degeneracy of the two states having charge density wave maxima centered at alternate bond midpoints (as in Figure 8b). Numbering the bond midpoints 1 through 8, the Peierls distortion compressing bonds 2, 4, 6, and 8 (and expanding bonds 1, 3, 5, and 7) lowers the energy of the state having charge density wave maxima centered at bond midpoints 2, 4, 6, and 8, and raises the energy of the state having charge density wave maxima centered at bond midpoints 1, 3, 5, and 7 (for small distortions δa). Hence, Peierls instability results for the low-spin states having charge density wave maxima centered at bond midpoints.

For small δa, the energy splitting is approximately equal to twice the band gap at $k = \pi/2a$ (as defined by the valence high-spin state; see Appendix A). Thus, the band gap and total energy splitting are 0.121 eV and 0.257 eV, respectively, for $\delta a = 0.04$ Å, and 0.301 eV and 0.641 eV, respectively, for $\delta a = 0.10$ Å [the ratio of band gap to total energy splitting is 0.4705 and 0.4698 for $\delta a = 0.04$ Å and $\delta a = 0.10$ Å, respectively].

Although small Peierls distortions do not break the degeneracy of the two states

having charge density wave maxima centered at alternate atoms (as in Figure 8a), these states also lead to Peierls instability. For the small distortion of $\delta a = 0.04$ Å, the Peierls distortion causes the charge density wave maxima to slide towards the compressed bond midpoints and the charge density wave minima to slide towards the expanded bond midpoints, resulting in a net stabilization of the total energy. For $\delta a \geq 0.10$ Å, the charge density wave maxima and minima are located at the exact centers of alternate bond midpoints (as in Figure 8b).

The optimum value of the Peierls distortion $\delta a_{opt} = 0.189$ Å, leads to alternating internuclear separations of 2.700 and 3.078 Å. The optimum value of the compressed bond length is somewhat smaller than the 2.724 Å equilibrium bond length calculated for Ag_2 at the HF level (see Appendix B and Table 10), indicating that the interaction between dimers in the distorted ring cluster is repulsive. This is consistent with the observation that the Ag_8 ring cluster with $\delta a_{opt} = 0.189$ Å is higher in total energy than four Ag_2 molecules ($R_e = 2.72$ Å) by 0.143 eV (17.9 meV/atom).

C. Unrestricted Hartree-Fock

1. Cohesive Energies

Using UHF wavefunctions we calculated cohesive energies of the Cu_{10}, Ag_6, Ag_8, Ag_{10}, Au_{10}, Li_6, Li_{10}, Li_{14}, and Na_{10} symmetric ring clusters (low-spin) with respect to atomization (2) and dimerization (3). These are reported in Table 1, where the total cohesive energies have been divided by N. These cohesive energies are calculated using (*i*) the total energies of low-spin ring clusters at fixed values of the lattice constant (a), (*ii*) the total energies of diatomic molecules at their calculated equilibrium internuclear separations (R_e), and (*iii*) the total energies of the isolated

atoms. In all cases the UHF wavefunctions are optimized with *no orbital symmetry restrictions.* The UHF total energies are lower than the HF total energies in all cases except for Au_2 and the isolated atoms, where the UHF and HF total energies are equal. Further details are given in Appendices A-B.

The results given in Table 1 indicate that at the UHF level the symmetric ring clusters are all quite stable with respect to dissociation into both atoms and diatomic molecules. In contrast with HF, for UHF the cohesive energy per atom increases with increasing N.

Comparison of the UHF cohesive energies calculated for the M_{10} ring clusters with the experimental cohesive energies for the three-dimensional bulk metals (given in Table 2) indicates that the trend in the cohesive energy with respect to dimerization differs dramatically for the one-dimensional (Ag > Cu > Au) and three-dimensional (Au > Cu > Ag) noble metals. However, the experimental and calculated atomization energies for the diatomic molecules both follow the trend Au > Cu > Ag (see Appendix B). This could indicate a fundamental difference in the bonding for the one-dimensional and three-dimensional systems.

2. Spin Density Waves

The UHF wavefunction contains a separate orbital for each valence electron, where the orbitals occupied with up-spin electrons ($\uparrow$ or α) are allowed to overlap the orbitals occupied with down-spin electrons ($\downarrow$ or β). For each of the Cu_{10}, Ag_6, Ag_8, Ag_{10}, Au_{10}, Li_6, Li_{10}, Li_{14}, and Na_{10} symmetric ring clusters, the UHF ground state optimized without orbital symmetry restrictions is low spin and leads to valence orbitals having maximum absolute amplitudes centered at the *bond midpoints*, as shown in Figure 10 for Ag_8.

By imposing orbital symmetry restrictions, we solved self-consistently for low-spin "excited" states having valence orbitals with maximum absolute amplitudes centered at the atoms (as shown in Figure 11 for Ag_8), leading to significantly higher total energies [for Ag_8, the UHF energy for the atom-centered state is higher than that of the ground state (bond-centered) by 109.6 meV/atom; further details of these atom-centered (excited) UHF states are given in Appendix D].

In each case, the α-spin orbitals and β-spin orbitals optimized without symmetry restrictions for the low-spin ground state break symmetry in such a manner that (*i*) the total valence α-spin density has maxima and minima on alternating sets of bond midpoints (periodicity $2a$), (*ii*) the total valence β-spin density is phase-shifted from the total total valence α-spin density by a such that the maxima (and minima) of the valence α-spin and β-spin densities are staggered, leading to a spin density (defined by the difference between the α-spin density and the β-spin density) with periodicity $2a$, and (*iii*) the total valence electronic charge density (disregarding spin) is *fully* symmetric (with periodicity a). Hence, for each of the low-spin Cu_{10}, Ag_6, Ag_8, Ag_{10}, Au_{10}, Li_6, Li_{10}, Li_{14}, and Na_{10} symmetric ring clusters, UHF leads to an antiferromagnetic description having a charge density with periodicity a and spin density with periodicity $2a$. The local description of the ground state valence electronic structure in each case involves electrons centered at the bond midpoints with alternating spins, e.g., $\alpha\ \beta\ \alpha\ \beta\ \alpha\ \beta$, etc.[16]

3. Peierls Instability

In contrast with HF, the UHF description of the low-spin Ag_8 ring cluster leads to *stability* with respect to the Peierls distortion (δa). The UHF total energy calculated without orbital symmetry restrictions increases quadratically as a function of δa as

shown in Figure 12.

At sufficiently large values of δa, we anticipated the possibility that the valence orbitals could slide away from the bond midpoints (as shown in Figure 10) towards the atoms (as shown in Figure 11). However, this does not occur for $\delta a \leq 0.30$ Å even though these UHF wavefunctions are optimized without orbital symmetry restrictions, allowing complete freedom for the positions of maximum absolute orbital amplitudes. As a further test for sliding valence orbitals, we constructed a set of skewed "starting guess" orbitals for $\delta a = 0.30$ Å having maximum absolute amplitudes centered at alternate positions midway between the atoms and the bond midpoints. The UHF iterative self-consistent optimization of these skewed orbitals resulted in orbitals having maximum absolute amplitudes centered exactly at bond midpoints.

The UHF orbitals shown in Figure 10 imply that the cohesion of the symmetric ring cluster is due to two-center one-electron bonds, similar to the one-electron bonds of the diatomic molecular cations.[16,17] Hence, the Peierls-distorted diatomic lattice is unfavorable because alternate one-electron bonds are stretched and compressed.

D. UHF Energy Bands

In order to further characterize the UHF antiferromagnetic ground state, we examine the effect of spin polarization on the one-electron energy bands. In general, the UHF wavefunction results in separate energy bands for the α-spin and the β-spin energy levels.

1. The Symmetric Cluster

For the symmetric cluster, the α-spin and the β-spin levels coincide. The discrete α-spin levels for the Ag_8 cluster are shown by the data points in Figure 13, where the solid curve approximates the continuous band of energy levels obtained in the limit as N approaches infinity. Since the periodicity of the α-spin orbitals is $2a$, the α-spin Brillouin zone [the unit cell in reciprocal (k) space] extends from $-\pi/2a$ to $\pi/2a$ (half that of the lattice). This is consistent with the energy bands obtained with the Hubbard hamiltonian.[6] Hence, when spin polarization effects are included (UHF) the energy band description of the chain of monovalent metal atoms consists of completely filled energy bands. The Peierls instability is predicted only for one-dimensional metals with partially filled energy bands, and hence the M_N clusters composed of Cu, Ag, Au, Li and Na are expected to be stable with respect to the Peierls distortion.

The second band shown in Figure 13 (α-spin conduction band, unoccupied states, plotted in the extended zone, $\pi/2a \leq |k| \leq \pi/a$) is obtained with the improved virtual orbital method[29] and corresponds to σ orbitals (symmetric with respect to bond axes) having large amplitudes in the bond midpoints occupied by the β-spin valence electrons. This leads to large electron-electron repulsions resulting in the large energy gap (2.89 eV) between these two bands. The net result is that at the UHF level the Ag_8 symmetric ring cluster is an antiferromagnetic insulator.

The UHF band structure of Figure 13 is in qualitative agreement with that obtained from the Hubbard hamiltonian;[6] a quantitative analysis of the UHF energy bands and comparison with those obtained with the Hubbard hamiltonian is given in Appendix C. Values of the Hubbard parameters $\mathcal{B}$ and $\mathcal{U}$ obtained directly from

the ab initio calculations indicate that the $\mathcal{B}/\mathcal{U}$ ratio follows the trend Li < Na $\ll$ Ag < Cu < Au (Appendix C, Table 11).

2. The Peierls-Distorted Cluster

The Peierls distortion does not alter the $2a$ periodicities of the α-spin and β-spin orbitals. Figure 14 shows the effect of a small Peierls distortion ($\delta a = 0.10$ Å) on the one-electron energy bands, where we merged together (*i*) the α-spin valence half-band ($-\pi/2a \geq k \geq 0$), (*ii*) the β-spin valence half-band ($0 \geq k \geq \pi/2a$), (*iii*) the α-spin conduction half-band ($-\pi/a \geq k \geq -\pi/2a$), and (*iii*) the β-spin conduction half-band ($\pi/2a \geq k \geq \pi/a$). The energy bands for the symmetric ring are shown by the thin dashed lines. The Peierls distortion stabilizes the α-spin valence orbitals since they have nodes bisecting the expanded bond midpoints but destabilizes the β-spin valence orbitals since they have nodes bisecting the compressed bond midpoints. The net result is that the one-dimensional metal composed of monovalent atoms does *not* lead to a Peierls instability (if spin polarization effects are allowed).

III. Discussion

The ab initio calculations indicate that the one-dimensional elemental metals composed of Cu, Ag, Au, Li and Na are *stable* with respect to the Peierls distortion, and have large cohesive energies with respect to both atomization and dissociation into diatomic molecules, as long as spin polarization effects of the UHF wavefunctions are allowed (see Table 1). The UHF wavefunction for each of these systems leads to an antiferromagnetic (nonmetallic) ground state having a spin density wave, although in each case the *net* electronic charge density of the ground state (obtained by adding

the up-spin and down-spin densities) is fully symmetrical. This is consistent with the low-density (or large a) solution of the Hubbard hamiltonian.[2,6,7,8] In each case, the local description of the valence electronic structure consists of electrons centered at the bond midpoints with alternating spins.

The HF wavefunctions (which do not allow spin polarization effects) give spurious results, such as charge density waves for the Ag_8 ring cluster and negative cohesive energies with respect to atomization for both the Na_{10} ring cluster (see Table 1) and the Na_2 molecule (see Appendix B). The HF wavefunctions for these one-dimensional metallic clusters lead to Peierls instabilities, and very small or negative cohesive energies with respect to dissociation into diatomic molecules.[15]

Thus, the HF and UHF results calculated for the one-dimensional metals composed of Cu, Ag, Au, Li and Na *are in absolute disagreement with one another.* Since the UHF total energies are all lower than the HF total energies, (as shown in Figure 15 for Ag_8), the variational principle suggests that the UHF results are more likely to be correct. However, unlike HF, the low-spin UHF wavefunctions are "spin-contaminated," i.e., they are not eigenfunctions of the many-electron spin operator $\hat{S}^2$ (see Appendices A.4 and A.5) and hence contain contributions from both the many-electron singlet ($S = 0$) and higher spin states such as triplet ($S = 1$), quintet ($S = 2$), etc., up to high-spin ($S = N/2$, where N is the number of atoms in the cluster). It is likely that errors due to spin contamination do not affect the diatomic molecules (M_2) and the ring clusters (M_N) in a consistent manner. For example, the Ag_8 symmetric cluster has a UHF total energy 1.801 eV (225.1 meV/atom) lower than the HF total energy, whereas the Ag_2 molecule has a UHF total energy only 0.020 eV (10.1 meV/atom) lower than the HF total energy (see Figure 15). Hence, the results of the ab initio calculations based on single-determinant wavefunctions

(HF and UHF) are somewhat inconclusive.

In order to resolve the disagreement between the HF and UHF results, we performed ab initio total energy calculations for each of these systems with the multideterminant generalized valence bond (GVB) wavefunction,[30] which is a multideterminant generalization of UHF that is a proper eigenfunction of $\hat{S}^2$ (no spin contamination); details of these results are reported elsewhere.[16] The GVB total energies are all lower than the UHF and HF total energies, as shown in Figure 15 for the Ag_8 ring cluster. For Ag_8, the GVB total energy calculations confirm the UHF result of stability with respect to the Peierls distortion (see Figure 15). In general, for the ground electronic states of the one-dimensional M_N ring clusters composed of Cu, Ag, Au, Li, and Na, the GVB results confirm that the HF-Peierls description is fundamentally *incorrect* and that the UHF-Hubbard description is basically *correct* except that (unlike UHF) the GVB description of the antiferromagnetic ground state leads to fully symmetrical spin and charge densities (no spin-contamination or spin density wave).[16]

Thus, spin polarization is crucial for a proper *single-determinant* description of the valence electronic structures of these one-dimensional metals, especially for the antiferromagnetic ground states. However, both the spin contamination and the spin density waves resulting from UHF wavefunctions for these systems are due to an incomplete treatment of the electron correlation forced by the use of a single determinant wavefunction.[16]

The UHF calculations indicate that the trend in the cohesive energy with respect to dissociation into diatomic molecules differs dramatically for the one-dimensional (Ag > Cu > Au) and three-dimensional (Au > Cu > Ag) noble metals (see Tables 1-2). The experimental atomization energies for the diatomic molecules and bulk

metals both follow the trend Au > Cu > Ag (see Appendix B). However, the trend for the one-dimensional metals *is* consistent with both the atomic *s*-to-*p* excitation energies [Ag (3.740 eV) < Cu (3.806 eV) < Au (4.947 eV)],[31] and with the extent of *p* hybridization for the M_{10} ring clusters as revealed by the standard Mulliken[19] orbital population analysis [Ag (42 %) > Cu (40 %) > Au (18 %); see Appendix A].

The cohesive energies (Li > Na; see Tables 1-2), the atomic *s*-to-*p* excitation energies (Li, 1.848 eV; Na, 2.104 eV),[31] and the extent of *p* hybridization (Li, 51 %; Na, 35 %) are all consistent for Li and Na. Hence, it is clear that *sp* hybridization plays a crucial role in the cohesion of these one-dimensional metals.

The participation of the low-lying *p* orbitals in the valence electronic structures of these one-dimensional metal clusters leads to singly-occupied UHF valence orbitals having maximum absolute amplitudes centered at bond midpoints (see Figure 10). The UHF up-spin and down-spin orbitals are staggered, leading to a localized description where electrons are centered at the bond midpoints with alternating spins (antiferromagnetism). This implies that the cohesion in these one-dimensional metals is due to two-center one-electron bonds, similar to the one-electron bonds of the diatomic molecular cations.[16,17] Hence, the Peierls-distorted diatomic lattice is unfavorable because alternate one-electron bonds are stretched and compressed.

In terms of energy band theory, spin polarization effects resulting from the UHF wavefunction lead to a reduction of the Brillouin zone by a factor of two, resulting in a ground state having completely filled energy bands, explaining the lack of Peierls instability (which is predicted only for one-dimensional metals with partially filled energy bands).

The UHF calculations indicate that the usual half-filled band model for these systems is fundamentally incorrect due to spin polarization effects; hence, the Peierls

instability occurs for HF but not for UHF. A generalization of the one-dimensional Peierls instability[1,32] has been used to explain the Hume-Rothery rules[33] [these rules correlate particular alloy structures with particular valence-electron to atom ratios, e.g., the γ-brass structure occurs frequently for alloys with electron/atom ratios of approximately 21/13 (1.54 - 1.70)[33,34] such as Ag_5Zn_8, Cu_9Al_4, etc]. The present results raise doubts concerning this energy band explanation of the stability of the Hume-Rothery phases, since spin polarization effects are neglected.

IV. Summary

The results for the one-dimensional metals composed of Cu, Ag, Au, Li and Na are summarized as follows.

(*i*) In each case, the UHF wavefunction leads to an antiferromagnetic (non-metallic) low-spin ground state having a spin density wave, consistent with the low-density (or large a) solution of the Hubbard hamiltonian.[2,6,7,8] The local description of the valence electronic structure consists of electrons centered at the bond midpoints with alternating spins. In each case the net electronic charge density of the ground state (obtained by adding the up-spin and down-spin densities) is fully symmetrical.

(*ii*) When electron correlation effects are included (spin polarization, UHF-Hubbard description), the undistorted linear structures are stable in one dimension. Therefore, the HF-Peierls description of the electronic structure (half-filled valence band) is fundamentally incorrect because of the neglect of electron correlation effects. The HF wavefunctions (which do not allow spin polarization effects) give spurious results, such as charge density waves for the Ag_8 ring cluster and negative cohesive energies with respect to atomization for both the Na_{10} ring cluster and the Na_2 molecule.

(*iii*) The cohesive energies with respect to dissociation into diatomic molecules are large when spin polarization effects are included (UHF). The Peierls instability does *not* occur for these one-dimensional metals because of the strong cohesion resulting from two-center one-electron bonds, similar to the one-electron bonds of the diatomic molecular cations.[16,17] Hence, the Peierls-distorted diatomic lattice is unfavorable because alternate one-electron bonds are stretched and compressed.

Acknowledgement

This work was supported by the National Science Foundation – Materials Research Groups – Grant DMR-8421119 and by a grant (DMR-8215650) from the Division of Materials Research of the National Science Foundation. We also thank the referee for raising several interesting points, including the relationships of several HF anomalies to topological ($N = 4i$ / $N = 4i + 2$) alternations.

Appendix A. Details of the Calculations

1. Basis Sets and Effective Potentials

We solved for both the unrestricted Hartree-Fock (UHF, spin polarized) and the restricted Hartree-Fock (HF, non spin polarized) many-electron wavefunctions for the low-spin states ($S = 0$) of the various M_N ring clusters (M = Cu, Ag, Au, Li, and Na) where the one-electron orbitals $\{\varphi_i\}$ are expanded in terms of contracted gaussian type basis functions (f_ν)

$$\varphi_i = \sum_\nu f_\nu c_{\nu i}$$

and where the orbital expansion coefficients ($c_{\nu i}$) are optimized by the usual iterative self-consistent field method[35] to give the lowest possible total energy. The basis sets $\{f_\nu\}$ used for the various cases[36,37,38] are summarized in Table 5. For Li and Na, these wavefunctions treated both the valence and core electrons explicitly. For the noble metals, eleven electrons per atom ($d^{10}s^1$) were included in the wavefunction, and ab initio effective potentials were utilized to include the effects of all remaining core electrons.[36] These effective potentials include relativistic effects for Ag and Au but not for Cu (relativistic effects are much less important for Cu in comparison to Ag and Au).

The basis set for Li includes nine s primitive gaussian functions and four sets of p primitive gaussian functions that are contracted to give a total of three s functions and two sets of p functions [hence, the notation (9s,4p)/(3s,2p)]. The $1s^2$ core electrons of Li are described predominantly by the first contracted s function, leaving two s functions and two sets of p functions (two functions each for p_x, p_y and p_z) to describe the valence electron. The basis sets chosen for Na, Cu, Ag and Au are of similar quality to that for Li; in each case the core electrons are described by the smallest possible number of functions and the valence electrons are described by twice the minimum number of valence and polarization functions. Hence, the basis sets have sufficient flexibility to describe the valence polarization and hybridization effects crucial for describing the metallic cohesion.

2. Energy Bands and Atomic Orbital Populations

All results reported in this section are for HF or UHF wavefunctions where in each case we optimized all orbitals (both valence and core) self-consistently. In this section, the HF wavefunctions are optimized under full orbital symmetry restrictions

(Bloch orbitals, ψ_m) whereas the UHF wavefunctions are optimized without any orbital symmetry restrictions whatsoever.

We find that the HF wavefunction for the low-spin state of M_{10} with valence electron configuration

$$\psi_0^{(v)}(\uparrow\downarrow)\psi_{-1}^{(v)}(\uparrow\downarrow)\psi_1^{(v)}(\uparrow\downarrow)\psi_{-2}^{(v)}(\uparrow\downarrow)\psi_2^{(v)}(\uparrow\downarrow) \tag{A1}$$

leads to core energy levels that are well separated from the valence energy levels for each case (M = Cu, Ag, Au, Li, and Na).

For the noble metal ring clusters, the d bands are well separated from the valence sp bands. The energy gaps between the highest-energy d-band orbital and the lowest-energy valence-band orbital (as defined by the Koopmans' theorem[21] ionization potentials) are 4.91 eV, 5.88 eV and 2.85 eV for Cu_{10}, Ag_{10} and Au_{10}, respectively, and the widths of the d-bands are 1.64 eV, 1.99 eV and 3.00 eV for Cu_{10}, Ag_{10} and Au_{10}, respectively. In addition, hybridization between the atomic d and sp orbitals is minimal, as shown by atomic orbital populations[19] calculated separately for the d bands [$\psi_m^{(d)}$, core] and the valence sp band [$\psi_m^{(v)}$, valence] given in Table 6.

This is in agreement with previous HF calculations for two- and three-dimensional Cu_N clusters up to $N = 8$,[39,40] e.g., $^1A_{1g}$ Cu_6 octahedron, 1.89 eV d-band width and 2.97 eV d-valence gap;[40] $^1A_{1g}$ Cu_8 cube, 2.31 eV d-band width and 1.85 eV d-valence gap.[39] For Cu_{13} clusters containing one bulk atom and twelve surface atoms (cubo-octahedron and icosahedron), the d-band and valence band overlap at the HF-Koopmans' theorem level of theory.[39] However, allowing relaxation effects for the positive ion states (localized d holes) results in a description where the d band is embedded in the valence band for the smaller copper clusters.[41]

For Ag_8 and Au_{10}, we also optimized the UHF wavefunction for the low-spin

(antiferromagnetic) ground states. For Ag_8, the energy gap between the *d* band and the valence band is 5.55 eV (UHF; the HF band gap is 5.90 eV), and the width of the *d* band is 1.842 eV (UHF; the HF band width is 1.851 eV). For Au_{10}, the energy gap between the *d* band and the valence band is 2.71 eV (UHF; the HF band gap is 2.85 eV), and the width of the *d* band is 3.005 eV (UHF; the HF band width is 2.996 eV). In each case, hybridization between the atomic *d* and *sp* orbitals is minimal, as shown by atomic orbital populations[19] calculated separately for the *d* bands and the valence *sp* band as given in Table 7 (UHF).

We also find that the core levels are well separated from the valence levels for the many-electron "high-spin" states (one unpaired electron per atom) of the various ring clusters. The lowest energy high-spin state for each of the M_{10} ring clusters is described by the valence electron configuration

$$\psi_0^{(v)}(\uparrow)\psi_{-1}^{(v)}(\uparrow)\psi_1^{(v)}(\uparrow)\psi_{-2}^{(v)}(\uparrow)\psi_2^{(v)}(\uparrow)\psi_{-3}^{(v)}(\uparrow)\psi_3^{(v)}(\uparrow)\psi_{-4}^{(v)}(\uparrow)\psi_4^{(v)}(\uparrow)\psi_5^{(v)}(\uparrow) \qquad \text{(A2)}$$

where each valence band orbital $[\psi_m^{(v)}]$ is occupied by a single up-spin electron. Again, hybridization between the atomic *d* and *sp* orbitals is minimal, as shown by the atomic orbital populations[19] given in Table 6.

Valence-excited high-spin states such as that described by the valence electron configuration

$$\psi_0^{(v)}(\uparrow)\psi_{-1}^{(v)}(\uparrow)\psi_1^{(v)}(\uparrow)\psi_{-2}^{(v)}(\uparrow)\psi_2^{(v)}(\uparrow)\psi_{-3}^{(v)}(\uparrow)\psi_3^{(v)}(\uparrow)\psi_{-4}^{(v)}(\uparrow)\psi_4^{(v)}(\uparrow)\psi_0^{(\pi)}(\uparrow) \qquad \text{(A3)}$$

where $\psi_5^{(v)}$ is the highest energy valence orbital and $\psi_0^{(\pi)}$ is the lowest energy π-conduction orbital are significantly higher in energy than the lowest energy high-spin state (A2), e.g., the total energy splitting between (A2) and (A3) is 0.468 eV for Cu_{10} and 2.168 eV for Li_{10}.

3. The Frozen Core Approximation

We find that the optimum core orbitals obtained from the lowest energy high-spin state (A2) are very similar to those obtained from the lowest energy low-spin state (A1). Hence, for the M_N ring clusters we freeze the core orbitals at the high-spin HF level, allowing an enormous reduction in the computational effort. This is especially important since in our study of the M_{10} ring clusters we optimized more than 150 many-electron wavefunctions [six different magnetizations for each of the five M_{10} clusters, with five different types of wavefunctions (HF with D_{10h} and C_{2h} orbital symmetry restrictions, HF without orbital symmetry restrictions, UHF, and generalized valence bond)].[16]

The high-spin state was chosen for defining the core orbitals because of the absence of various peculiarities associated with the low-spin states at both the HF level (e.g., charge density waves and fluctuations in the Fermi level as a function of N) and at the UHF level (e.g., spin density waves). The savings in computational effort afforded by the frozen core approximation described above is obtained by performing integral transformations;[42] hence, for M_{10} clusters where M is a noble metal this results in a reduction from 110 electrons and 140 basis functions (our integrals codes use "cartesian" sets of d functions) to 10 electrons and 60 basis functions (we eliminate the π virtual orbitals).

We do not use the frozen core approximation for the M_2 diatomic molecules because it is substantially less accurate for the M_2 diatomic molecules than it is for the M_N ring clusters (see Table 8).[43] Hence, for all diatomic molecules we optimized both the core orbitals and the valence orbitals simultaneously. Hence, for the M_N ring clusters, cohesive energies with respect to both atomization and dimerization calcu-

lated with the frozen core approximation are always smaller than those calculated by optimizing all orbitals self-consistently.

In order to test this frozen core approximation, we calculated total energies for the symmetry-restricted low-spin states (A1) of the various M_N clusters by the method described above and also by the usual method of optimizing all orbitals self-consistently. We also tested the HF low-spin charge density wave state of the Ag_8 symmetric and Peierls distorted clusters. In addition, we tested this frozen core approximation for the HF low-spin spin density wave state for both the Ag_8 and Au_{10} symmetric clusters.

The results given in Tables 7-8 indicate that the frozen core approximation described above is reasonably accurate for the M_N ring clusters composed of Cu, Ag, Au, Li, and Na. For the Li_{10} and Na_{10} ring clusters, total energies calculated with the frozen core approximation are less than 0.4 meV/atom higher than total energies calculated by optimizing all orbitals self-consistently. The HF atomization energies for the Cu_{10}, Ag_{10}, and Au_{10} symmetric ring clusters calculated with the frozen core approximation are 2-3% smaller values calculated by optimizing all orbitals self-consistently. The UHF atomization energies calculated with the frozen core approximation are smaller than values calculated by optimizing all orbitals self-consistently by 8.7% and 11.4% for Ag_8 and Au_{10}, respectively. The UHF dimerization energies calculated with the frozen core approximation are smaller than values calculated by optimizing all orbitals self-consistently by 17.0% and 32.3% for Ag_8 and Au_{10}, respectively.

4. Details of the Valence Electron Wavefunctions

The UHF and HF many-electron valence wavefunctions for the various M_N ring clusters can all be written in the general form

$$\Psi_{N,A} = \hat{\mathcal{A}}[\Phi_{N,A}\,\chi_{N,A}]$$
$$\Phi_{N,A} = \varphi_1(1)\varphi_2(2)\varphi_3(3)\cdots\varphi_N(N)$$

where $\hat{\mathcal{A}}$ is the antisymmetrizer or determinantal operator, $\Phi_{N,A}$ is the many-electron spatial product function, $\{\varphi_i\}$ are the canonical valence one-electron orbitals optimized self-consistently for each state A, and $\chi_{N,A}$ is the many-electron spin function, e.g.,

$$\chi_{N,A}^{HF} = \chi_{N,A}^{UHF} = \alpha(1)\alpha(2)\cdots\alpha(A)\beta(A+1)\beta(A+2)\cdots\beta(N),$$

where α and β are the one-electron spin functions for the up-spin ($\uparrow$ or $m_s = +\frac{1}{2}$) and down-spin ($\downarrow$ or $m_s = -\frac{1}{2}$) projections, respectively (m_s is the quantum number describing the projection of the electron's spin angular momentum on an arbitrary axis, z), and where A and B are the number of valence electrons with spins α and β, respectively ($A + B = N$).

For wavefunctions such as HF or UHF where both Φ and χ are products of one-electron functions, $\hat{\mathcal{A}}$ forms a single Slater determinant. For brevity, the electron coordinates are often omitted; by standard convention the orbital product is ordered such that the electron coordinates are sequential (the electron coordinates and the orbital subscripts are independent), e.g.,

$$\varphi_3\varphi_1\varphi_4\ldots \equiv \varphi_3(1)\varphi_1(2)\varphi_4(3)\ldots$$

$$\chi_{N,A}^{HF} = \chi_{N,A}^{UHF} = \alpha^A\beta^B.$$

We solved self-consistently for the [unrestricted Hartree-Fock (UHF, spin-polarized) and restricted Hartree-Fock (HF, non-spin-polarized)] valence wavefunctions using the hamiltonian

$$\begin{aligned}
\widehat{\mathcal{H}} &= E_N^{CORE} + \sum_{i=1}^{N} \hat{h}(i) + \sum_{i>j}^{N} \frac{1}{r_{ij}} \\
\hat{h}(i) &= -\frac{1}{2}\widehat{\nabla}_i^2 + \hat{V}(\vec{r}_i) + \hat{V}^{CORE} \\
\hat{V}^{CORE} &= \sum_c (2\hat{J}_c - \hat{K}_c)
\end{aligned}$$

where (i) E_N^{CORE} includes the nuclear repulsion energy and all one-electron and two-electron energy terms involving only the core electrons {the [Ar]$3d^{10}$, [Kr]$4d^{10}$, [Xe]$4f^{14}5d^{10}$, $1s^2$, and $1s^22s^22p^6$ shells for Cu, Ag, Au, Li, and Na,[36] respectively (see Section A.3)}, (ii) the "one-electron" operator $\hat{h}(i)$ includes the electronic kinetic energy $(-\frac{1}{2}\widehat{\nabla}^2)$, the electron-nuclear attraction $[\hat{V}(\vec{r})]$, and all two-electron interactions [coulomb $(\hat{J})$ and exchange $(\hat{K})$] between core electrons and valence electrons $(\hat{V}^{CORE})$[42], and (iii) r_{ij}^{-1} is the electrostatic interaction between electrons i and j (r_{ij} is the distance between electrons i and j).

The HF and UHF wavefunctions differ in the restrictions applied to the valence orbitals prior to the self-consistent field optimization (energy minimization), as discussed below.

HF: Orbitals of opposite spin are forced to be equal, e.g.,

$$\varphi_{A+i} = \varphi_i,\ i = 1, 2, \ldots, B$$

(thus for low-spin the orbitals are all doubly-occupied). In addition, the $\{\varphi_i\}$ are restricted to be orthonormal, e.g.,

$$S_{ij} = \langle \varphi_i | \varphi_j \rangle = \delta_{ij},\ i, j \leq A.$$

These restrictions ensure that $\Psi_{N,A}^{HF}$ is an eigenfunction of $\widehat{S}^2$

$$\begin{aligned} \widehat{S}^2\Psi_{N,A}^{HF} &= S(S+1)\hbar^2\Psi_{N,A}^{HF} \\ S &= \frac{|A-B|}{2} \end{aligned} \tag{A4}$$

where $\widehat{S}^2$ and S are the total (many-electron) spin angular momentum operator and quantum number, respectively. The HF orbitals are optimized either with full symmetry restrictions (complex Bloch functions, average field calculation; see section A.6), insuring a fully symmetrical charge distribution, or with selected or no symmetry restrictions, often resulting in charge density waves.

UHF: No orbital restrictions are made, generally leading to wavefunctions that are *not* eigenfunctions of $\widehat{S}^2$ (A4). In addition, UHF wavefunctions do not always have the correct spatial symmetry, e.g., a spin density wave sometimes occurs. However, both $\Psi_{N,A}^{UHF}$ and $\Psi_{N,A}^{HF}$ are eigenfunctions of $\widehat{S}_z$

$$\begin{aligned} \widehat{S}^2 &= \widehat{S}_x^2 + \widehat{S}_y^2 + \widehat{S}_z^2 \\ \widehat{S}_z\Psi_{N,A} &= M_S\hbar\Psi_{N,A} \\ M_S &= \frac{A-B}{2} \end{aligned} \tag{A5}$$

where $\widehat{S}_z$ and M_S are the total (many-electron) spin angular momentum projection operator and quantum number, respectively.

The operators $\widehat{\mathcal{H}}$, $\widehat{S}^2$, and $\widehat{S}_z$ all commute with one another, and hence, the *exact* wavefunctions can be taken as simultaneous eigenfunctions of all three operators. For the high-spin state ($A = N$), the HF and UHF wavefunctions are equivalent. However, for other spin states, the HF and UHF descriptions can differ quite remarkably.

5. UHF Spin Contamination

The UHF wavefunction for a two-electron "singlet"

$$\begin{aligned}\Psi_{2,1}^{UHF} &= \hat{\mathcal{A}}[(\varphi_1\varphi_2)(\alpha\beta)] = (\varphi_1\varphi_2)(\alpha\beta) - (\varphi_2\varphi_1)(\beta\alpha) \\ &= \frac{1}{2}(\varphi_1\varphi_2 + \varphi_2\varphi_1)(\alpha\beta - \beta\alpha) + \frac{1}{2}(\varphi_1\varphi_2 - \varphi_2\varphi_1)(\alpha\beta + \beta\alpha)\end{aligned}$$

consists of a combination of singlet and triplet wavefunctions (if $\varphi_1 \neq \varphi_2$). Pure spin states for a two-electron system are given by the valence bond wavefunctions

$$\begin{aligned}\Psi_{2,S=1}^{VB} &= \hat{\mathcal{A}}[(\varphi_1\varphi_2)(\alpha\beta + \beta\alpha)] = (\varphi_1\varphi_2 - \varphi_2\varphi_1)(\alpha\beta + \beta\alpha)/\sqrt{(2 - 2\mathcal{S}_{12}^2)} \\ \Psi_{2,S=0}^{VB} &= \hat{\mathcal{A}}[(\varphi_1\varphi_2)(\alpha\beta - \beta\alpha)] = (\varphi_1\varphi_2 + \varphi_2\varphi_1)(\alpha\beta - \beta\alpha)/\sqrt{(2 + 2\mathcal{S}_{12}^2)}\end{aligned}$$

where

$$\mathcal{S}_{ij} = \langle\varphi_i|\varphi_j\rangle$$

is the overlap between normalized orbitals φ_i and φ_j ($\mathcal{S}_{ii} = 1.0$). The UHF low-spin wavefunction can be expanded in terms of these VB wavefunctions as

$$\Psi_{2,1}^{UHF} = \left[\sqrt{1 - \mathcal{S}_{12}^2}\,\Psi_{2,S=1}^{VB} + \sqrt{1 + \mathcal{S}_{12}^2}\,\Psi_{2,S=0}^{VB}\right]/\sqrt{2}.$$

Thus, the low-spin UHF wavefunction is a pure singlet state only when $\varphi_1 = \varphi_2$ (where it reduces to the HF wavefunction).

In general,

$$\Psi_{N,A}^{UHF} = \hat{\mathcal{A}}\left[(\varphi_1\varphi_2\cdots\varphi_A\varphi_{A+1}\varphi_{A+2}\cdots\varphi_N)\alpha^A\beta^B\right] \qquad \text{(A6)}$$

contains a mixture of spins $|M_S| \leq S \leq N/2$.

We evaluated the spin contaminations of the UHF wavefunctions for the various M_N ring clusters and M_2 diatomic molecules, by calculating the "average" spin

quantum numbers ($\bar{S}$) from the expectation values of $\hat{S}^2$

$$\begin{aligned} \langle \hat{S}^2 \rangle &= \langle \Phi_{N,A} \chi_{N,A} | \hat{S}^2 | \Psi_{N,A} \rangle \\ \bar{S} &= -1/2 + \sqrt{\langle \hat{S}^2 \rangle + 1/4} \end{aligned}$$

(the results are given in Table 9). Of the diatomic molecules, Na_2 has the greatest spin contamination. This is consistent with the *negative* atomization energy of Na_2 at the HF level (see Appendix B), since any improvement in the total energy afforded by UHF is at the expense of mixing in higher-spin states. For Au_2, Ψ^{UHF} collapses into Ψ^{HF} at $R \leq 2.70$ Å, so there is no spin contamination for $R_e = 2.678$ Å. For Cu_2, Ag_2, Li_2, and Na_2, Ψ^{UHF} collapses into Ψ^{HF} at bond lengths of 2.34, 2.55, 2.51, and 2.41 Å, respectively (these bond lengths are smaller than the respective calculated R_e values).

Values of $\langle \hat{S}^2 \rangle$ are calculated by expanding $\hat{S}^2$ as

$$\begin{aligned} \hat{S}^2 &= \hat{S}_z^2 + \hat{S}_z + \hat{S}^- \hat{S}^+ \\ \hat{S}^- &= \sum_{i=1}^{N} \hat{s}^-(i) \\ \hat{S}^+ &= \sum_{i=1}^{N} \hat{s}^+(i) \end{aligned}$$

where $\hat{S}_z$ is defined in Equation (A5), and $\hat{s}^+$ and $\hat{s}^-$ are the one-electron raising and lowering spin operators

$$\hat{s}^+\alpha = 0 \qquad \hat{s}^+\beta = \alpha$$

$$\hat{s}^-\alpha = \beta \qquad \hat{s}^-\beta = 0.$$

Hence, for the two-electron singlet ($\Psi_{2,1}^{UHF}$)

$$\langle \hat{S}^2 \rangle = \langle (\phi_1\phi_2)(\alpha\beta) | \hat{S}^- \hat{\mathcal{A}} [(\phi_1\phi_2)(\alpha\alpha)] \rangle$$

$$= \langle(\phi_1\phi_2)(\alpha\beta)|\hat{\mathcal{A}}[(\phi_1\phi_2)(\alpha\beta+\beta\alpha)]\rangle$$

$$= \langle(\phi_1\phi_2)(\alpha\beta)|(\phi_1\phi_2-\phi_2\phi_1)(\alpha\beta)]\rangle$$

$$= 1-\mathcal{S}_{12}^2.$$

For $N > 2$, we divide the canonical orbitals into two sets according to their spins

$$\mathrm{A}: \ \{\varphi_i,\ 1 \le i \le A\}$$

$$\mathrm{B}: \ \{\varphi_j,\ A+1 \le j \le N\}$$

($A \ge B$) and diagonalize the overlap matrix between the two sets

$$\mathcal{S}_{ij} = \langle\varphi_i|\varphi_j\rangle,\ 1 \le i \le A,\ A+1 \le j \le N$$

to obtain two sets of orbitals

$$\bar{\mathrm{A}}: \ \{\bar{\varphi}_i,\ 1 \le i \le A\}$$

$$\bar{\mathrm{B}}: \ \{\bar{\varphi}_j,\ A+1 \le j \le N\}$$

such that each orbital of set $\bar{\mathrm{A}}$ has at most one nonzero overlap with an orbital of set $\bar{\mathrm{B}}$

$$\langle\bar{\varphi}_i|\bar{\varphi}_j\rangle = \begin{cases} \bar{\mathcal{S}}_{ij} & \text{if } j = i+A \\ 0 & \text{otherwise} \end{cases}$$

(hence, sets $\bar{\mathrm{A}}$ and $\bar{\mathrm{B}}$ are biorthogonal).[44] The wavefunction

$$\bar{\Psi}_{N,A}^{UHF} = \hat{\mathcal{A}}\left[(\bar{\varphi}_1\bar{\varphi}_2\cdots\bar{\varphi}_A\bar{\varphi}_{A+1}\bar{\varphi}_{A+2}\cdots\bar{\varphi}_N)\alpha^A\beta^B\right]$$

is equivalent to $\Psi_{N,A}^{UHF}$ (A6) since orbital sets A and $\bar{\mathrm{A}}$, and orbital sets B and $\bar{\mathrm{B}}$ are both related by orthogonal transformations and single determinant wavefunctions are invariant to such orthogonal orbital transformations. This simplifies the evaluation of $\langle\hat{S}^2\rangle$. Hence,

$$\langle\hat{S}^2\rangle = M_S^2 + M_S + \sum_{i=1}^{B}\bar{\mathcal{S}}_{i\,i+A}. \qquad \text{(A7)}$$

6. The Energy Expression for Complex Bloch Orbitals

The energy band theory of metals is based on one-electron Bloch functions (ψ_m) which for a M_N symmetric ring cluster can be written as

$$\begin{aligned} \psi_m^{(\omega)} &= N^{-1/2} \sum_{j=1}^{N} \omega_j \exp(ikR_j) \\ k &= \frac{2\pi m}{aN} \\ R_j &= ja \end{aligned}$$

where m is an integer ($|m| \leq 0.5N$), $\{\omega_j\}$ is an optimal set of N equivalent real nonorthogonal localized (Wannier)[3] orbitals, k is the wave vector, and R_j denotes the position of ω_j (going around the circumference).

A given set of complex Bloch functions can always be combined to give an equivalent set of real functions

$$\begin{aligned} \overline{\psi}_{|m|} &= \frac{\psi_{|m|} + \psi_{-|m|}}{\sqrt{2}} = (N/2)^{-1/2} \sum_{j=1}^{N} \omega_j \cos(kR_j) \\ \overline{\psi}_{-|m|} &= \frac{\psi_{|m|} - \psi_{-|m|}}{i\sqrt{2}} = (N/2)^{-1/2} \sum_{j=1}^{N} \omega_j \sin(kR_j) \end{aligned}$$

since energy levels resulting from complex Bloch functions are doubly degenerate ($\epsilon_{-|k|} = \epsilon_{|k|}$) and non-degenerate energy levels ($k = 0,\ \pi/a$) are always described by real Bloch functions.

Single-determinant wavefunctions written in terms of the $\{\psi_m\}$ always lead to fully symmetrical charge distributions, e.g.,

$$\psi_m^*(1)\psi_m(1) = N^{-1} \sum_{j=1}^{N} \omega_j(1)\omega_j(1) + 2N^{-1} \sum_{j>j'}^{N} \omega_j(1)\omega_{j'}(1) \cos[k(R_j - R_{j'})]$$

($\omega_j = \omega_j^*$). This is not always true for single-determinant wavefunctions written in terms of the $\{\overline{\psi}_m\}$.

The energy expression for the configuration

$$\psi_m(1)\psi_{m'}(2)\ \alpha(1)\beta(2)$$

can be written in terms of the $\{\overline{\psi}_m\}$ as

$$\begin{aligned} E \;=\; & \frac{1}{2}\left[\langle\overline{\psi}_m|\hat{h}|\overline{\psi}_m\rangle + \langle\overline{\psi}_{-m}|\hat{h}|\overline{\psi}_{-m}\rangle + \langle\overline{\psi}_{m'}|\hat{h}|\overline{\psi}_{m'}\rangle + \langle\overline{\psi}_{-m'}|\hat{h}|\overline{\psi}_{-m'}\rangle\right] \\ & + \frac{1}{4}\left[\langle\overline{\psi}_m\overline{\psi}_m|r_{12}^{-1}|\overline{\psi}_{m'}\overline{\psi}_{m'}\rangle + \langle\overline{\psi}_{-m}\overline{\psi}_{-m}|r_{12}^{-1}|\overline{\psi}_{m'}\overline{\psi}_{m'}\rangle\right. \\ & \left. + \langle\overline{\psi}_m\overline{\psi}_m|r_{12}^{-1}|\overline{\psi}_{-m'}\overline{\psi}_{-m'}\rangle + \langle\overline{\psi}_{-m}\overline{\psi}_{-m}|r_{12}^{-1}|\overline{\psi}_{-m'}\overline{\psi}_{-m'}\rangle\right]. \end{aligned}$$

This energy expression is simply the average of the energy expressions for each of the configurations

$$\begin{array}{cccc} \overline{\psi}_m(1) & \overline{\psi}_{m'}(2) & \alpha(1) & \beta(2) \\ \overline{\psi}_{-m}(1) & \overline{\psi}_{m'}(2) & \alpha(1) & \beta(2) \\ \overline{\psi}_m(1) & \overline{\psi}_{-m'}(2) & \alpha(1) & \beta(2) \\ \overline{\psi}_{-m}(1) & \overline{\psi}_{-m'}(2) & \alpha(1) & \beta(2). \end{array}$$

Energy expressions for single-determinant wavefunctions written in terms of the $\{\psi_m\}$ can always be expressed in terms of the $\{\overline{\psi}_m\}$, leading to an "average field" description in terms of the $\{\overline{\psi}_m\}$.

Appendix B. Results for the Diatomic Molecules

We calculated the optimum internuclear separations (R_e), dissociation energies (D_e), and force constants (k_e) for homonuclear diatomic molecules composed of Cu, Ag, Au, Li, and Na at the HF and UHF levels. The frozen core approximation of Appendix A.3, which is fairly accurate for the M_N ring cluster calculations, is substantially less accurate for diatomic molecules (see Table 8);[43] hence, we optimized both the core orbitals and the valence orbitals for all diatomic molecules.

These HF and UHF results are compared with results obtained both from experiment and from calculations[45,46] including treatments of the electron correlation effects that are more complete than that of HF or UHF (see Table 10). The errors in the HF values of R_e, k_e and D_e for the various metal dimers in comparison with experiment are as follows. R_e too large by 8-10 % (Cu,Ag,Au), 4-5 % (Li,Na); k_e too small by 42-45 % (Cu,Ag), 23 % (Au), 5-8 % (Li,Na); D_e too small by 77 % (Cu,Ag), 68 % (Au), 87 % (Li), 104 % (Na).

Note that although the HF value of D_e for Na_2 is negative (for our basis set, the energy of Na_2 is higher than twice the energy of the isolated Na atom), the HF values of R_e and k_e for Na_2 are rather accurate. Due to ionic terms in the HF wavefunction (which are present in the HF description of the dimer but absent in the HF description of the isolated atom), HF rarely gives accurate bond energies, and occasionally gives negative bond energies. The HF D_e value for Na_2 in the limit of a complete basis set (e.g., numerical HF) is approximately 0.014 eV (too small by 98 %).[47]

For Cu_2, our HF results (R_e = 2.44 Å, D_e = 0.463 eV, k_e = 4.44 eV/Å^2) calculated with an effective potential (22-electron wavefunction) and an inflexible d-basis are in very good agreement with "all-electron" HF results (R_e = 2.42 Å, D_e = 0.54 eV, k_e = 4.05 eV/Å^2) calculated with all 58 electrons included in the wavefunction and a flexible (triple-ζ) d-basis.[45] Similar agreement has been reported for Ag_2 between the effective potential and all-electron HF results.[48]

These results indicate that our basis sets are sufficiently flexible for the HF description, and that the effective potentials are fairly accurate. Hence, the errors in the various HF results (in comparison to experiment) are mainly due to the neglect of electron correlation effects (inherent to the single-determinant form of the HF

wavefunction).

The UHF wavefunctions lead to somewhat more accurate D_e values in comparison to HF. However, UHF leads to values of R_e and k_e that are less accurate than the corresponding HF values (especially for Na_2). The reason for the decreased accuracy for the R_e and k_e values is that any improvement in D_e afforded by UHF is at the expense of mixing in triplet character (see Appendix A.5). The lone exception of these trends is Au_2, where the HF and UHF results are identical.

A reasonably accurate description of the potential energy well (R_e, k_e and D_e) for each of these metal dimers requires an accurate description of valence electron correlation effects.[45,46,48] The noble metal dimers also require correlation effects involving the subvalence d^{10} electrons as well as relativistic effects (especially for Ag and Au).[45,48] The effective potentials used in this study include relativistic effects for Ag and Au but not for Cu.

Appendix C. Details of the UHF Energy Bands

For the UHF description of the Ag_8 symmetric ring cluster, the valence energy band of the high-spin state (Figure 3, band width $\mathcal{B}$) splits into upper and lower energy bands for the low-spin state (Figure 13, band widths $\mathcal{B}_1$ and $\mathcal{B}_2$, respectively) when spin polarization effects are allowed. This results in an antiferromagnetic insulator since the energy gap (ΔW) between the upper and lower energy bands is at the Fermi level. This is in qualitative agreement with the Hubbard hamiltonian[2,6]

$$H^{HUB} = \mathcal{B}\sum_{i=1}^{N}[c_{i,\uparrow}^{\dagger}c_{i+1,\uparrow} + c_{i+1,\downarrow}^{\dagger}c_{i,\downarrow}] + \mathcal{U}\sum_{i=1}^{N} n_{i,\uparrow}n_{i,\downarrow}$$

$$\mathcal{B} = -2zh_{12}^{\omega} \qquad \text{(C1)}$$

$$
\begin{aligned}
h_{ij}^{\omega} &= \langle \omega_i | \hat{h} | \omega_j \rangle \\
\mathcal{U} &= J_{11}^{\omega} \qquad \text{(C2)} \\
J_{ij}^{\omega} &= \langle \omega_i \omega_j | r_{12}^{-1} | \omega_i \omega_j \rangle \\
n_{i,\uparrow} &= c_{i,\uparrow}^{\dagger} c_{i,\uparrow} \\
n_{i,\downarrow} &= c_{i,\downarrow}^{\dagger} c_{i,\downarrow}
\end{aligned}
$$

where $\mathcal{B}$ is the band width without correlation (the band width for $\mathcal{U} = 0$), z is the coordination number ($z = 2$ for one-dimensional metals), $c_{i,\sigma}$ ($c_{i,\sigma}^{\dagger}$) are operators for creating (annihilating) an electron with spin σ in the localized Wannier[3] orbital ω_i, and $\mathcal{U}$ is the intra-atomic coulomb energy. $\mathcal{U} > 0$ tends to prevent two electrons from occupying the *same* localized orbital ω_i.

In this appendix we assess for Ag_8 the quantitative agreement of the UHF energy bands with those obtained with the Hubbard model. To do this we obtained Hubbard parameters ($\mathcal{B}$ and $\mathcal{U}$) directly from the ab initio calculations by two methods.

(*i*) Equations (C1) and (C2) [using the high-spin $\{\omega_i\}$] result in the values $\mathcal{U} =$ 8.001 eV, $\mathcal{B} = 5.433$ eV, and $\mathcal{B}/\mathcal{U} = 0.679$ for Ag_8. The value $\mathcal{B} = 5.433$ eV obtained from the nearest-neighbor one-electron integral $h_{12}^{\omega} = -1.358$ eV is in very good agreement with the high-spin valence band width $\mathcal{B} = 5.524$ eV obtained from the orbital energies [hence including all one-electron interactions and two-electron interactions with $(N-1)$ valence electrons;[21] see Figure 3]. Values of $\mathcal{B}$ and $\mathcal{U}$ for Cu_{10}, Ag_6, Ag_8, Ag_{10}, Au_{10}, Li_8, Li_{10}, Li_{14}, and Na_{10} obtained by this method are given in Table 11.

(*ii*) "Effective" values of $\mathcal{B}$ and $\mathcal{U}$ are obtained by satisfying the relations[2,8]

$$\Delta W = \mathcal{U} - 0.5(\mathcal{B}_1 + \mathcal{B}_2)$$

$$\Delta W = \mathcal{U} - \mathcal{B} + 2\mathcal{B}\int_0^\infty \frac{J_1(u)du}{u(1+\exp[(2\mathcal{U}/\mathcal{B})u]} \qquad \text{(C3)}$$

$$= \mathcal{U} - \mathcal{B} - 2\mathcal{B}\sum_{j=1}^{\infty}(-1)^j\left[\sqrt{1+j^2(2\mathcal{U}/\mathcal{B})^2} - j(2\mathcal{U}/\mathcal{B})\right]$$

[$J_1(u)$ is the Bessel function][8] where ΔW, $\mathcal{B}_1$ and $\mathcal{B}_2$ are taken directly from the UHF energy bands (see Figure 13). For Ag_8, the UHF values $\Delta W = 2.893$ eV, $\mathcal{B}_1 = 2.626$ eV, and $\mathcal{B}_2 = 1.187$ eV lead to $\mathcal{U}^{EFF} = 4.800$ eV, $\mathcal{B}^{EFF} = 2.273$ eV, and $\mathcal{B}^{EFF}/\mathcal{U}^{EFF} = 0.474$).

The values $\mathcal{U}$ and $\mathcal{B}$ are much larger than $\mathcal{U}^{EFF}$ and $\mathcal{B}^{EFF}$, respectively. The values $\mathcal{U} = 8.001$ eV and $\mathcal{B} = 5.433$ eV lead to a Hubbard band gap $\Delta W = 3.802$ eV (C3) 31% larger than the UHF band gap $\Delta W = 2.893$ eV for Ag_8.

The value $\mathcal{B}^{EFF} = 2.273$ eV is much closer to the average of the widths of the upper ($\mathcal{B}_1$) and lower ($\mathcal{B}_2$) energy bands[2] ($\mathcal{B}^{AVE} = 1.907$ eV) than it is to $\mathcal{B} = 5.433$ eV. Indeed, $\mathcal{B}_1$ and $\mathcal{B}_2$

$$\mathcal{B}_1 \approx -2z \ \langle\phi_1^{UPPER}|\hat{h}|\phi_3^{UPPER}\rangle$$

$$\mathcal{B}_2 \approx -2z \ \langle\phi_1^{LOWER}|\hat{h}|\phi_3^{LOWER}\rangle$$

are based on *next-nearest neighbor* hopping integrals where $\{\phi_i^{UPPER}\}$ and $\{\phi_i^{LOWER}\}$ are sets of localized nonorthogonal orbitals obtained from separate localizations (Fourier transformations) of the up-spin and down-spin canonical orbitals for the upper and lower energy bands, respectively (see Figure 10).[16]

For M_8, the two-electron coulomb energy for the covalent configuration

$$\omega_1(\uparrow)\omega_2(\downarrow)\omega_3(\uparrow)\omega_4(\downarrow)\omega_5(\uparrow)\omega_6(\downarrow)\omega_7(\uparrow)\omega_8(\downarrow)$$

can be simplified as

$$E^{COUL} = 8J_{12}^{\omega} + 8J_{13}^{\omega} + 8J_{14}^{\omega} + 4J_{15}^{\omega}$$

due to the cyclical nature of the $\{\omega_i\}$. For M_8 there are two different types of localized ionic configurations occuring with equal weights:

$$\omega_1(\uparrow)\omega_1(\downarrow)\omega_3(\uparrow)\omega_4(\downarrow)\omega_5(\uparrow)\omega_6(\downarrow)\omega_7(\uparrow)\omega_8(\downarrow)$$

$$E^{COUL} = J^{\omega}_{11} + 7J^{\omega}_{12} + 8J^{\omega}_{13} + 8J^{\omega}_{14} + 4J^{\omega}_{15}$$

where the doubly-occupied orbital and hole are adjacent (ω_1 and ω_2), and

$$\omega_1(\uparrow)\omega_2(\downarrow)\omega_3(\uparrow)\omega_1(\downarrow)\omega_5(\uparrow)\omega_6(\downarrow)\omega_7(\uparrow)\omega_8(\downarrow)$$

$$E^{COUL} = J^{\omega}_{11} + 8J^{\omega}_{12} + 8J^{\omega}_{13} + 7J^{\omega}_{14} + 4J^{\omega}_{15}$$

where the doubly-occupied orbital and hole are third-nearest neighbors (ω_1 and ω_4). Hence, for M_8 a more accurate definition of $\mathcal{U}$ is

$$\mathcal{U}_8 = J^{\omega}_{11} - 0.5(J^{\omega}_{12} + J^{\omega}_{14}).$$

For Ag_8, the values $J^{\omega}_{11} = 8.001$ eV, $J^{\omega}_{12} = 4.536$ eV, and $J^{\omega}_{14} = 2.028$ eV lead to the value $\mathcal{U}_8 = 4.719$ eV, in very good agreement with $\mathcal{U}^{EFF} = 4.800$ eV.

The $\mathcal{U}_N$ values for M_N symmetric ring clusters (even N)

$$\begin{aligned} \mathcal{U}_N &= J^{\omega}_{11} - 2N^{-1}\sum_{i=1}^{N/2} J^{\omega}_{1\,2i} \\ \lim_{N\to\infty} \mathcal{U}_N &= J^{\omega}_{11} \end{aligned}$$

are hence expected to converge as N^{-1}. Hence, Equation (C2) does not accurately define $\mathcal{U}$ for a finite cluster. Since $\mathcal{B}^{EFF}$ is expected to decrease with increasing N for M_N clusters composed of Cu, Ag, Au, Li, and Na[16] (the $\{\omega_i\}$, $\{\phi_i^{UPPER}\}$, and $\{\phi_i^{LOWER}\}$ are all centered at the bond midpoints and the distances between adjacent bond midpoints and next-nearest neighbor bond midpoints increases with increasing N), the net result is that $\mathcal{B}^{EFF}/\mathcal{U}^{EFF}$ is expected to decrease with increasing N and ΔW is expected to increase with increasing N.

Appendix D. Further Details of UHF Spin Density Wave States

1. Symmetric Ring Clusters

For each of the Cu_{10}, Ag_6, Ag_8, Ag_{10}, Au_{10}, Li_6, Li_{10}, Li_{14}, and Na_{10} symmetric ring clusters, optimizing the UHF wavefunction without orbital symmetry restrictions for the low-spin ground state leads to valence orbitals having maximum absolute amplitudes centered at the bond midpoints, resulting in a spin density wave with periodicity $2a$ (with maxima and minima centered at alternate bond midpoints) but a fully symmetric charge density. This is shown for Ag_8 in Figure 10. We refer to these states of the M_N ring clusters as the bond-centered states.

For each of these systems, we were able to optimize a low-spin UHF wavefunction with orbitals having maximum absolute amplitudes centered at the atoms by imposing D_{nh} orbital symmetry restrictions ($n = N/2$), also leading to a spin density wave with periodicity $2a$ (with maxima and minima centered at alternate atoms), but a fully symmetric charge density. This is shown for Ag_8 in Figure 11. We refer to these states of the M_N ring clusters as the atom-centered states. Thus, the atom-centered state spin density wave and the bond-centered state spin density wave are phase-shifted by $a/2$.

There are two distinct choices for D_{nh} orbital symmetry restrictions for the M_N symmetric ring cluster. Each orbital can be required to be either symmetric or antisymmetric with respect to one of two types of C_2 symmetry axes (perpendicular to the principle C_N symmetry axis). (i) Choosing a C_2 symmetry axis bisecting a particular set of opposite bond midpoints leads to the bond-centered state (Figure

10). (*ii*) Choosing a C_2 symmetry axis bisecting a particular set of opposite atoms leads to the atom-centered state (Figure 11).

Details of the low-spin UHF wavefunctions for both states are given in Table 12. In each case, the atom-centered state leads to a significantly higher total energy than the bond-centered state, although both states have positive cohesive energies with respect to dissociation into diatomic molecules. The atom-centered state has less spin contamination than the bond-centered state, and the atom-centered state has less *p* hybridization than the bond-centered state.

2. Peierls-Distorted Ring Clusters

We already showed that the antiferromagnetic ground state of the Ag_8 ring cluster (bond-centered, Figure 10) is stable with respect to the Peierls distortion (see Figures 12 and 15).

In addition, for Ag_8 we solved for the atom-centered UHF antiferromagnetic state as a function of the Peierls distortion (δa) by optimizing the valence orbitals under the symmetry restriction that each α-spin orbital must be related to one of the β-spin orbitals by a particular symmetry plane bisecting two opposite bond midpoints.

This leads to total energies (Figure 16, dashed curve) much higher than those calculated without the orbital symmetry restriction (Figure 16, solid curve), e.g., the energy difference between these two states is 109.6, meV/atom for $\delta a = 0$ and 69.0 meV/atom for $\delta a = 0.30$ Å.

In summary, for Ag_8 the spin density wave shows a very strong preference for centering about the bond midpoints for Peierls distortions up to $\delta a \leq 0.30$ Å. Neither the bond-centered state (Figure 10) nor the atom-centered state (Figure 11) leads to Peierls instability at the UHF level (see Figure 16).

3. Comparison with GVB–PP

Total energies of Ag_8 as a function of the Peierls distortion (δa) for both the bond-centered state and the atom-centered state calculated with perfect-pairing generalized valence bond wavefunctions (GVB–PP)[49] are also given in Figure 16. The GVB–PP wavefunction is a restricted form of the full GVB wavefunction. Hence, GVB–PP leads to higher total energies than full GVB (compare Figures 15 and 16; further details of these GVB–PP results are presented elsewhere).[16] For both Ag_8 and Ag_2, the GVB–PP total energies are lower than the UHF total energies. In addition, the GVB–PP wavefunction is an eigenfunction of $\hat{S}^2$ while the UHF wavefunction is not (see Appendix A and Tables 9 and 12).

For the bond-centered (ground) state of Ag_8, GVB–PP and UHF both lead to a positive cohesive energy with respect to dissociation into Ag_2 molecules, and stability with respect to the Peierls distortion.

However, for the atom-centered (excited) state of Ag_8, GVB–PP leads a negative cohesive energy with respect to dissociation into Ag_2 molecules, and a Peierls instability (in disagreement with UHF).

Further details of the GVB–PP results for the Cu_{10}, Ag_6, Ag_8, Ag_{10}, Au_{10}, Li_6, Li_{10}, Li_{14}, and Na_{10} ring clusters are presented elsewhere.[16]

Appendix E. HF Results for the Ag_8 Triplet State

The triplet state of Ag_8 described by the valence configuration

$$\psi_0(\uparrow\downarrow)\psi_{-1}(\uparrow\downarrow)\psi_1(\uparrow\downarrow)\psi_{-2}(\uparrow)\psi_2(\uparrow) \qquad \text{(E1)}$$

leads to fully symmetrical electronic spin and charge densities; however, optimizing the orbitals at the HF level without orbital symmetry restrictions

$$\varphi_1(\uparrow\downarrow)\varphi_2(\uparrow\downarrow)\varphi_3(\uparrow\downarrow)\varphi_4(\uparrow)\varphi_5(\uparrow)$$

leads to a triplet state having both a spin density wave and a charge density wave with a total energy lower than that of (E1) by 0.041 eV for the symmetric ring cluster.

The HF total energies for these two states as a function of the Peierls distortion (δa) are shown in Figure 17, where the dashed curve shows the results obtained with D_{4h} orbital symmetry restrictions. Figure 17 also includes the HF total energy for the lowest-energy low-spin state (singlet, dotted curve). Neither triplet state leads to a Peierls instability, although they both are unstable with respect to the limit of four low-spin diatomic molecules. Both of these triplet states are lower in energy than the singlet state for the symmetric ring cluster ($\delta a = 0$), but for $|\delta a| > 0.13$ Å the energy of the singlet drops below that of the triplet due to the Peierls instability for the singlet.

The HF orbitals optimized without symmetry restrictions for the triplet state are shown in Figure 18 for $\delta a = 0.00$, 0.10, 0.20, and 0.30 Å. Although the triplet spin state having spin and charge density waves is stable with respect to the Peierls distortion, the spin and charge density waves slide as a function of δa in such a manner that the two singly-occupied orbitals localize about a pair of adjacent atoms forming a compressed bond for $\delta a = 0.30$ Å.

Appendix F. Detailed Energy Data for Ag_8

In this appendix we use the energy expression

$$\begin{aligned} E^{TOTAL} &= E_N^{CORE} + E^{ONE} + E^{TWO} \\ E^{ONE} &= \sum_{i=1}^{N} h_{ii} \\ h_{ij} &= \langle \varphi_i(1) | \hat{h}(1) | \varphi_j(1) \rangle \\ E^{TWO} &= \sum_{i>j}^{N} J_{ij} - \sum_{i>j}^{A} K_{ij} - \sum_{i>j>A}^{N} K_{ij} \\ J_{ij} &= \langle \varphi_i(1)\varphi_j(2) | \frac{1}{r_{12}} | \varphi_i(1)\varphi_j(2) \rangle \\ K_{ij} &= \langle \varphi_i(1)\varphi_j(2) | \frac{1}{r_{12}} | \varphi_j(1)\varphi_i(2) \rangle \end{aligned}$$

based on the valence electron hamiltonian of Appendix A.4 where (*i*) E^{CORE} includes the nuclear repulsion energy and all one-electron and two-electron energy terms involving only the core electrons {the [Ar]$3d^{10}$, [Kr]$4d^{10}$, [Xe]$4f^{14}5d^{10}$, $1s^2$, and $1s^22s^22p^6$ shells for Cu, Ag, Au, Li, and Na,[36] respectively (see Section A.3)}, (*ii*) E^{ONE} is the total "one-electron" (valence) contribution to the total energy including the electron-nuclear attraction and kinetic energy of the valence electrons, and all two-electron interactions between core electrons and valence electrons, and (*iii*) E^{TWO} is the total two-electron (valence) contribution to the total energy where J_{ij} and K_{ij} are the valence two-electron integrals (coulomb and exchange, respectively).

Calculated values of E^{CORE}, E^{ONE}, E^{TWO}, and E^{TOTAL} are given in Table 13 as a function of the Peierls distortion (δa) for selected states of the Ag_8 ring cluster where the average nearest-neighbor internuclear separation is $a = 2.889$ Å. Table 13 also includes similar data for low-spin Ag_8 calculated with the GVB wavefunction. The total energy of low-spin Ag_8 as a function of δa is also presented in Figure 15 for HF, UHF and GVB. The total energies for these wavefunctions were all optimized

using the same basis sets and frozen core hamiltonian (see Appendix A); further details of the GVB calculations are given elsewhere.[16]

In all cases, E^{CORE} increases quadratically as a function of δa. For the low-spin HF wavefunction optimized with D_{4h} orbital symmetry restrictions, the variation of E^{ONE} with δa is approximately linear, leading to the Peierls instability (the variation of E^{TWO} with δa is negligible for this case). Likewise, the Peierls instability for the low-spin HF wavefunction optimized with C_s orbital symmetry restrictions is driven by E^{ONE}. For the high-spin HF wavefunction and the low-spin UHF and GVB wavefunctions the variations of E^{ONE} and E^{TWO} with δa are quadratic but the variations cancel one another, i.e., in each case the variation of $E^{ONE} + E^{TWO}$ with δa is negligible. Hence, the symmetric ring is stable for these cases due to E^{CORE}.

Appendix G. Results for Hydrogen Ring Clusters

Since the stable form of hydrogen is the diatomic molecule, we tested our model calculations by performing analogous calculations for ring clusters composed of hydrogen. Extensive total energy calculations for one-dimensional arrays of hydrogen atoms are presented elsewhere.[50]

In order to model the anticipated Peierls instability, we chose the H_8 ring cluster with an average internuclear separation ($a = 1.483$ Å) equal to twice the experimental bond length of the H_2 molecule[51] [the Huzinaga[52] (5s/3s) unscaled basis set was used]. The results of these calculations are given in Table 14. The low-spin HF wavefunction leads to a charge density wave for the symmetric cluster. The low-spin UHF wavefunction leads to a spin density wave (but no charge density wave). The low-spin GVB wavefunction leads to fully symmetrical spin and charge densities. All

[10] *Low-Dimensional Cooperative Phenomena. The Possibility of High-Temperature Superconductivity*, edited by H. J. Keller (Plenum, New York, 1974); *Chemistry and Physics of One-Dimensional Metals*, edited by H. J. Keller (Plenum, New York, 1977); *One-Dimensional Conductors*, edited by H. G. Schuster (Springer-Verlag, New York, 1975); *Extended Linear Chain Compounds*, edited by J. S. Miller (Plenum, New York, 1982, 1982, 1983), Vols. 1-3.

[11] L. F. Dahl and D. L. Wampler, *Acta Crystall.* **15**, 903 (1962). Also see M.-H. Whangbo and M. J. Foshee, *Inorg. Chem.* **20**, 113 (1981).

[12] Z. G. Soos, in *Low-Dimensional Cooperative Phenomena. The Possibility of High-Temperature Superconductivity*, edited by H. J. Keller (Plenum, New York, 1974).

[13] C. Castiglioni, G. Zerbi, and M. Gussoni, *Solid State Commun.* **56**, 863 (1985); K. A. Chao and S. Stafstroem, *Mol. Cryst. Liq. Cryst.* **118**, 45 (1985); I. Bozovic, *Phys. Rev.* **B 32**, 8136 (1985); M. Kertesz and R. Hoffmann, *Solid State Commun.* **47**, 97 (1983).

[14] The calculations for Li and Na are "ab initio" in the traditional definition in that the total energy expressions $\langle\Psi|\mathcal{H}|\Psi\rangle/\langle\Psi|\Psi\rangle$ include *all terms resulting from the true Hamiltonian* ($\widehat{\mathcal{H}}$) [within the usual Born-Oppenheimer approximation (frozen nuclei)] and no additional terms. The only approximations utilized in ab initio calculations are in the many-electron wavefunction (Ψ). "Exact" calculations would require Ψ to include essentially an infinite number of configurations within an infinite basis set and are generally unattainable; the configuration and basis set expansions are truncated in actual applications. Both the HF and

UHF wavefunctions include only a single configuration. Local density functional calculations (such as $X\alpha$) are not ab initio in this traditional definition since the exchange integrals are replaced by a local "exchange-correlation" potential obtained from calculations on the free electron gas. The calculations for Cu, Ag and Au are ab initio for eleven electrons per atom ($d^{10}s^1$), where "ab initio" effective potentials model all effects of the remaining core electrons. See Appendix A and Reference [36] for further details.

[15] W. Förner and M. Seel, *J. Chem. Phys.* **87**, 443 (1987).

[16] M. H. McAdon and W. A. Goddard III, *J. Phys. Chem.*, accepted for publication; M. H. McAdon and W. A. Goddard III, unpublished.

[17] M. H. McAdon and W. A. Goddard III, *J. Phys. Chem.* **91**, 2607 (1987); M. H. McAdon and W. A. Goddard III, *J. Non-Cryst. Solids* **75**, 149 (1985); M. H. McAdon and W. A. Goddard III, *Phys. Rev. Lett.* **55**, 2563 (1985).

[18] J. Donohue, *The Structure of the Elements* (Wiley, New York, 1974).

[19] R. S. Mulliken, *J. Chem. Phys.* **23**, 1833 (1955).

[20] C. A. Coulson, B. O'Leary, and R. B. Mallion, *Hückel Theory for Organic Chemists* (Academic, New York, 1978); L. Salem, *The Molecular Orbital Theory of Conjugated Systems* (Benjamin, New York, 1966).

[21] T. Koopmans, *Physica* **1**, 104 (1933).

[22] Orbital energies from the valence electron high-spin state provide energy levels that are consistent for the entire valence energy band — see Reference [29].

These energy levels are used in the qualitative description of other valence many-electron spin states.

[23] Actually, the lowest energy HF states for the Cu_{10}, Ag_6, Ag_{10}, and Au_{10} rings are low-spin, but the lowest energy HF states for the Ag_8, Na_{10}, Li_6, Li_{10}, and Li_{14} rings contain 0.25, 0.6, 1.0, 1.0, and 1.0 unpaired electrons per atom, respectively. The lowest energy UHF state for each of these nine clusters is low-spin (M. H. McAdon and W. A. Goddard III, unpublished results).

[24] H. A. Jahn and E. Teller, *Proc. Roy. Soc. London* A **161**, 220 (1937). Also see R. Englman, *The Jahn-Teller Effect in Molecules and Crystals* (Wiley, New York, 1972).

[25] This is consistent with the HF results of Reference [15] leading to Peierls instability for Li_{10} and Li_{14} but apparently not for Li_6.

[26] R. Hultgren, P. D. Desai, D. T. Hawkins, M. Gleiser, K. K. Kelley and D. D. Wagman, *Selected Values of the Thermodynamic Properties of the Elements* (American Society for Metals, Metals Park, Ohio, 1973).

[27] M. D. Morse, *Chem. Rev.* **86**, 1049 (1986).

[28] M. M. Kappes, M. Schär and E. Schumacher, *J. Phys. Chem.* **89**, 1499 (1985).

[29] W. J. Hunt and W. A. Goddard III, *Chem. Phys. Lett.* **3**, 414 (1969).

[30] W. A. Goddard III, T. H. Dunning, Jr, W. J. Hunt, and P. J. Hay, *Accts. Chem. Res.* **6**, 368 (1973); W. A. Goddard III and L. B. Harding, *Ann. Rev. Phys. Chem.* **29**, 363 (1978).

[31] C. E. Moore, *Atomic Energy Levels* (Nat. Stand. Rev. Data Ser., Nat. Bur. Stand. (U.S.), 1971). Values of atomic excitation energies are obtained weighting the various J values for each configuration by the $2J+1$ degeneracy, e.g., for the noble metal atoms the s-to-p excitation energy involves the $d^{10}s^1$ ($J = 0$) and $d^{10}p^1$ ($J = 3/2$ and $J = 1/2$) atomic states.

[32] H. Jones, *Proc. Phys. Soc. London*, **A 49**, 250 (1937); N. F. Mott and H. Jones, *Properties of Metals and Alloys* (Oxford Univ. Press, London, 1936); H. Jones, *The Theory of Brillouin Zones and Electronic States in Crystals* (North-Holland, Amsterdam, 1960).

[33] W. Hume-Rothery and G. V. Raynor, *The Structure of Metals and Alloys, 4th Ed.* (Institute of Metals, London, 1962).

[34] C. Barrett and T. B. Massalski, *Structure of Metals, Crystallographic Methods, Principles and Data, 3rd (revised) Ed.* (Pergamon Press, New York, 1980).

[35] T. H. Upton and W. A. Goddard III, UHF program, unpublished; R. A. Bair, W. A. Goddard III, A. F. Voter, A. K. Rappé, L. G. Yaffe, F. W. Bobrowicz, W. R. Wadt, P. J. Hay and W. J. Hunt, GVB2P5 program, unpublished; see R. A. Bair, Ph. D. Thesis, California Institute of Technology, 1980; also see F. W. Bobrowicz and W. A. Goddard III, in: *Modern Theoretical Chemistry: Methods of Electronic Structure Theory*, edited by H. F. Schaefer III (Plenum, New York, 1977) Vol. III, Chap. 4. The UHF and HF calculations were performed using the UHF and GVB2P5 programs, respectively.

[36] P. J. Hay and W. R. Wadt, *J. Chem. Phys.* **82**, 270, 1985.

[37] T. H. Dunning, Jr., and P. J. Hay, in: *Modern Theoretical Chemistry: Methods of Electronic Structure Theory*, edited by H. F. Schaefer III (Plenum, New York, 1977), Vol. III, Chap. 1.

[38] S. Huzinaga, J. Andzelm, M. Kłobukowski, E. Radzio-Andzelm, Y. Sakai, and H. Tatewaki, *Gaussian Basis Sets for Molecular Calculations* (Elsevier, New York, 1984).

[39] J. Demuynck, M.-M. Rohmer, A. Strich and A. Veillard, *J. Chem. Phys.* **75**, 3443 (1981); C. Bachmann, J. Demuynck, and A. Veillard, *Faraday Symp. Chem. Soc.* **14**, 170 (1980).

[40] H. Tatewaki, E. Miyoshi and T. Nakamura, *J. Chem. Phys.* **76**, 5073 (1982).

[41] E. Miyoshi, H. Tatewaki, and T. Nakamura, *J. Chem. Phys.* **78**, 815 (1983).

[42] L. G. Yaffe, LTRAN program, unpublished; see L. G. Yaffe and W. A. Goddard III, *Phys. Rev. A.* **13**, 1682 (1976). Also see W. J. Hunt, T. H. Dunning, Jr., and W. A. Goddard III, *Chem. Phys. Lett.* **3**, 606 (1969).

[43] The electronic structure of the M_2 molecule differs markedly from that of the M_N ring cluster for M = Cu, Ag, Au, Li, and Na; hence, it is not surprising that the frozen core approximation — using core orbitals optimized for the high-spin valence state to describe other valence states — does not treat M_2 and M_N consistently. For example, at a = 2.889 Å, high-spin Ag_{10} is unbound with respect to the separated atom limit by 86.3 meV/atom, whereas high-spin Ag_2 is unbound with respect to the separated atom limit by 157.7 meV/atom.

[44] A. T. Amos and G. G. Hall, *Proc. Roy. Soc. London* A **263**, 483 (1961).

[45] S. R. Langhoff, C. W. Bauschlicher, Jr., S. P. Walch, and B. C. Laskowski, *J. Chem. Phys.* **85**, 7211 (1986); S. P. Walch, C. W. Bauschlicher, Jr. and S. R. Langhoff, *J. Chem. Phys.* **85**, 5900 (1986).

[46] D. D. Konowalow and M. L. Olson, *J. Chem. Phys.* **71**, 450 (1979); D. D. Konowalow, M. E. Rosenkrantz and M. L. Olson, *J. Chem. Phys.* **72**, 2612 (1980).

[47] R. L. Martin and E. R. Davidson, *Mol. Phys.* **35**, 1713 (1978).

[48] P. J. Hay and R. L. Martin, *J. Chem. Phys.* **83**, 5174 (1985); R. L. Martin, *J. Chem. Phys.* **86**, 5027 (1987).

[49] W. J. Hunt, P. J. Hay, and W. A. Goddard III, *J. Chem. Phys.* **57**, 738 (1972).

[50] R. D. Poshusta and D. J. Klein, *Phys. Rev. Lett.* **48**, 1555 (1982); M. Seel, P. S. Bagus and J. Ladik, *J. Chem. Phys.* **77**, 3123 (1982); A. Karpfen, *Chem. Phys. Lett.* **61**, 363 (1979); M. Kertesz, J. Koller, and A. Azman, *Phys. Rev.* **B 14**, 76 (1976); S. P. Ionov, I. I. Amelin, V. S. Lyubimov, G. V. Ionova, and E. F. Makarov, *Physica Status Solidi* **B 77**, 441 (1976).

[51] K. P. Huber and G. Herzberg, *Molecular Spectra and Molecular Structure: IV. Constants of Diatomic Molecules* (Van Nostrand Reinhold, New York, 1979).

[52] S. Huzinaga, *J. Chem. Phys.* **42**, 1293 (1965).

Table 1. Cohesive energies for low-spin ring clusters. [a)]

system	a (Å)	atomization [b)] energy (meV/atom) HF	UHF	dimerization [c)] energy (meV/atom) HF	UHF
Ag_6	2.889	246.4	352.8	57.6	153.8
Ag_8	2.889	145.7	370.8	−43.1	171.8
Ag_{10}	2.889	191.3	379.8	2.4	180.8
Li_6	3.014	60.4	361.7	−10.3	269.1
Li_{10}	3.014	15.0	398.2	−55.8	305.6
Li_{14}	3.014	9.6	408.9	−61.1	316.3
Cu_{10}	2.556	239.7	388.7	8.1	152.6
Ag_{10}	2.889	191.3	379.8	2.4	180.8
Au_{10}	2.884	374.0	511.5	1.1	138.6
Li_{10}	3.014	15.0	398.2	−55.8	305.6
Na_{10}	3.659	−72.9	177.6	−56.3	136.5

a) Results for the lowest energy low-spin states (HF, $S = 0$; UHF, $M_S = 0$) calculated without orbital symmetry restrictions. A frozen core approximation was in effect. See Appendix A for further details.

b) The total atomization energy $M_N \rightarrow N\,M$ divided by N atoms.

c) The total dimerization energy $M_N \rightarrow N/2\,M_2$ divided by N atoms. In calculating the dimerization energies, the bond length of the diatomic molecule is optimized (see Table 10).

Table 2. Experimental cohesive energies for bulk three-dimensional metals.

system	atomization energy [a] (eV/atom)	dimerization energy [b] (eV/atom)
Cu	3.49	2.47
Ag	2.94	2.11
Au	3.82	2.66
Li	1.64	1.11
Na	1.11	0.74

a) Reference [26].
b) Cohesion with respect to diatomic molecules, e.g., $M_{(s)} \rightarrow 1/2\ M_2$, References [26,27,28].

Table 3. Details of selected HF low-spin wavefunctions.

system	a (Å)	E^{TOTAL}/N (Hartree/atom)	cohesive energy atomization (meV/atom)	cohesive energy dimerization (meV/atom)	energy relative to HF, D_{Nh} [a] $\Delta E^{TOTAL}/N$ (meV/atom)	$\Delta E^{ONE}/N$ (meV/atom)	$\Delta E^{TWO}/N$ (meV/atom)
—— HF, D_{Nh} orbital symmetry restrictions ——							
Li_6 [b]	3.072	−7.43440	52.2	−5.4			
Li_{10} [b]	3.075	−7.43250	0.5	−57.1			
Li_{14} [b]	3.080	−7.43166	−22.3	−80.0			
Li_6	3.014	−7.43396	60.4	−10.3			
Li_{10}	3.014	−7.43207	9.0	−61.8			
Li_{14}	3.014	−7.43124	−13.6	−84.3			
Na_{10}	3.659	−161.79260	−73.6	−57.0			
Ag_8	2.889	−37.41101	117.9	−70.9			
—— HF, no orbital symmetry restrictions [c] ——							
Li_6	3.014	−7.43396	60.4	−10.3	(no charge density wave)		
Li_{10}	3.014	−7.43229	15.0	−55.8	−5.99	20.87	−26.87
Li_{14}	3.014	−7.43209	9.6	−61.1	−23.22	23.79	−47.01
Na_{10}	3.659	−161.79262	−72.9	−56.3	−0.70	10.02	−10.72
Ag_8	2.889	−37.41203	145.7	−43.1	−27.79	−0.39	−27.40
Ag_8 [d]	2.889	−37.41148	130.7	−58.1	−12.85	10.45	−23.30

a) ΔE^{TOTAL} is the total energy stabilization of the HF charge density wave state relative to the HF D_{Nh} symmetry-restricted state. ΔE^{ONE} and ΔE^{TWO} are the one-electron and two-electron components of ΔE^{TOTAL}.
b) Results from Reference [15] — calculated with a (13s,1p/4s,1p) basis set. The basis set we use — (9s,4p/3s,2p); see Appendix A — leads to a total energy for the Li atom higher by 20.27 meV/atom, and a total energy for the Li_2 molecule higher by 7.21 meV/atom. For Li_6, Li_{10}, and Li_{14}, the D_{Nh} HF (9s,4p/3s,2p) total energy (at $a = 3.014$ Å) is higher than the D_{Nh} HF (13s,1p/4s,1p) total energy (at optimum a) by 11.97, 11.70, and 11.43 meV/atom, respectively.
c) Results are for the lowest energy HF state (having charge density wave maxima and minima centered at alternate atoms) except where noted otherwise.
d) Results for the HF state having charge density wave maxima and minima centered at alternate bond midpoints.

Table 4. Details of the HF charge density wave states. [a)]

system	a (Å)	orbital population analysis [b] p_0	p_1	p_2	p_3	p_4	p_5	p_6	p_7
Na_{10}	3.659	1.99954	3.99105	3.85246	0.14754	0.00895	0.00046		
Li_{10}	3.014	1.99882	3.97227	3.62391	0.37609	0.02773	0.00118		
Li_{14}	3.014	1.99820	3.97928	3.87492	3.19105	0.80895	0.12508	0.02072	0.00180
Ag_8	2.889	1.99908	3.95559	2.00000	0.04441	0.00092			
Ag_8 [c)]	2.889	1.99946	3.97195	2.00000	0.02805	0.00054			

b) Results are for the lowest energy HF state (having charge density wave maxima and minima centered at alternate atoms) except where noted otherwise.

b) The p_m are populations of fully symmetrical (D_{Nh}) Bloch orbitals obtained by symmetry-projecting the canonical orbitals of the HF charge density wave state.

c) Results for the HF state having charge density wave maxima and minima centered at alternate bond midpoints.

Table 5. Basis set summary.

element	basis set [a]	ground state configuration	energy [b] (hartrees)
Cu	(3s,2p,5d)/(2s,2p,1d)	$[Ar]3d^{10}4s^1$	−50.43769
Ag	(3s,3p,4d)/(2s,2p,1d)	$[Kr]4d^{10}5s^1$	−37.40668
Au	(3s,3p,3d)/(2s,2p,1d)	$[Xe]4f^{14}5d^{10}6s^1$	−33.38745
Li	(9s,4p)/(3s,2p)	$1s^22s^1$	−7.43174
Na	(11s,7p)/(4s,3p)	$1s^22s^22p^63s^1$	−161.79530

a) The basis sets are composed of contracted gaussian-type functions and contain the smallest possible number of functions to describe the core orbitals and twice the minimum number of functions to describe the valence s and low-lying p orbitals. Calculations for Cu, Ag and Au utilize basis sets and ab initio effective potentials from Reference [36]. Calculations for Li and Na are all-electron ab initio, with basis sets from Reference [37] and Reference [38], respectively.
b) For each case the energy of the isolated atom is the same for HF and UHF.

Table 6. Atomic orbital populations for the M_{10} ring clusters, HF [a)]

system	a (Å)	S	atomic orbital populations: core orbitals d	core orbitals s	core orbitals p	valence orbitals d	valence orbitals s	valence orbitals p	all orbitals d	all orbitals s	all orbitals p
Cu_{10}	2.556	0	9.965	0.018	0.017	0.008	0.704	0.288	9.973	0.722	0.305
Cu_{10}	2.556	5	9.970	0.013	0.017	0.001	0.450	0.549	9.971	0.463	0.566
Ag_{10}	2.889	0	9.966	0.018	0.016	0.008	0.643	0.350	9.974	0.661	0.365
Ag_{10}	2.889	5	9.970	0.014	0.017	0.001	0.495	0.504	9.971	0.508	0.521
Au_{10}	2.884	0	9.934	0.048	0.019	0.027	0.871	0.102	9.961	0.918	0.121
Au_{10}	2.884	5	9.952	0.027	0.021	0.005	0.673	0.322	9.958	0.699	0.343
Li_{10}	3.014	0		1.999	0.001		0.609	0.391			
Li_{10}	3.014	5		1.999	0.001		0.385	0.615			
Na_{10}	3.659	0		4.001	5.999		0.902	0.098			
Na_{10}	3.659	5		4.001	5.999		0.482	0.518			

a) Results are given for the lowest energy $S = 0$ and $S = 5$ HF states where both the core and valence orbitals are optimized with D_{10h} symmetry restrictions (Bloch functions, no frozen core approximation). The atomic orbital populations are calculated in the Mulliken approximation [19].

Table 7. Atomic orbital populations for selected M_N ring clusters; $M_S = 0$, UHF (low-spin).

system	a (Å)	d	atomic orbital populations [a] core orbitals s	p	valence orbitals d	s	p	all orbitals d	s	p
—— all orbitals optimized [b] ——										
Ag_8	2.889	9.956	0.021	0.023	0.012	0.627	0.362	9.968	0.647	0.385
Au_{10}	2.884	9.913	0.056	0.031	0.035	0.811	0.154	9.948	0.867	0.185
—— frozen core approximation [c] ——										
Ag_6	2.889	9.971	0.014	0.015	0.002	0.684	0.314	9.973	0.698	0.329
Ag_8	2.889	9.970	0.014	0.016	0.001	0.629	0.370	9.971	0.643	0.386
Ag_{10}	2.889	9.970	0.014	0.017	0.001	0.594	0.404	9.971	0.608	0.421
Li_6	3.014		2.000	0.000		0.595	0.405			
Li_{10}	3.014		1.999	0.001		0.494	0.506			
Li_{14}	3.014		1.999	0.001		0.433	0.567			
Cu_{10}	2.556	9.970	0.013	0.017	0.002	0.611	0.386	9.972	0.624	0.404
Ag_{10}	2.889	9.970	0.014	0.017	0.001	0.594	0.404	9.971	0.608	0.421
Au_{10}	2.884	9.952	0.027	0.021	0.007	0.835	0.158	9.959	0.862	0.179
Li_{10}	3.014		1.999	0.001		0.494	0.506			
Na_{10}	3.659		4.001	5.999		0.649	0.351			

a) Atomic Mulliken populations.
b) UHF results where all orbitals (both valence and core) are optimized without symmetry restrictions.
c) UHF results where the valence orbitals are optimized without symmetry restrictions.

Table 8. Errors (ΔE) of the frozen core approximation. [a)]

system	a (Å)	δa (Å)	valence configuration [b)]	HF total energy — optimized core (hartree)	HF total energy — frozen core (hartree)	$\Delta E/N$ (meV/atom)
Cu_2	2.443		$D_{\infty h}$ $(\sigma_g)^2$	−100.89240	−100.89028	28.9
Ag_2	2.589		$D_{\infty h}$ $(\sigma_g)^2$	−74.82554	−74.82288	36.1
Ag_2	2.889		$D_{\infty h}$ $(\sigma_g)^2$	−74.82549	−74.82285	36.0
Au_2	2.672		$D_{\infty h}$ $(\sigma_g)^2$	−66.80230	−66.79773	62.2
Ag_6	2.889	0.00	D_{6h}: $(a_{1g})^2\,(e_{1u})^4$	−224.49669	−224.49440	10.4
Ag_8	2.889	0.00	D_{8h}: $(a_{1g})^2\,(e_{1u})^4\,(e_{2g})^2$	−299.29045	−299.28808	8.1
Ag_{10}	2.889	0.00	D_{10h}: $(a_{1g})^2\,(e_{1u})^4\,(e_{2g})^4$	−374.13900	−374.13707	5.3
Ag_8	2.889	0.00	C_s: $(a')^2\,(a')^2\,(a')^2\,(a')^2$	−299.29960	−299.29625	11.4
Ag_8	2.889	0.00	D_{4h}: $(a_{1g})^2\,(e_{1u})^4\,(b_{1g})^2$	−299.29750	−299.29186	19.2
Ag_8	2.889	0.04	D_{4h}: $(a_{1g})^2\,(e_{1u})^4\,(b_{1g})^2$	−299.30180	−299.29616	19.2
Ag_8	2.889	0.10	D_{4h}: $(a_{1g})^2\,(e_{1u})^4\,(b_{1g})^2$	−299.30654	−299.30088	19.3
Ag_8	2.889	0.20	D_{4h}: $(a_{1g})^2\,(e_{1u})^4\,(b_{1g})^2$	−299.30938	−299.30363	19.6
Ag_8	2.889	0.30	D_{4h}: $(a_{1g})^2\,(e_{1u})^4\,(b_{1g})^2$	−299.30441	−299.29853	20.0
Cu_{10}	2.556	0.00	D_{10h}: $(a_{1g})^2\,(e_{1u})^4\,(e_{2g})^4$	−504.46706	−504.46500	5.6
Ag_{10}	2.889	0.00	D_{10h}: $(a_{1g})^2\,(e_{1u})^4\,(e_{2g})^4$	−374.13900	−374.13707	5.3
Au_{10}	2.884	0.00	D_{10h}: $(a_{1g})^2\,(e_{1u})^4\,(e_{2g})^4$	−334.01543	−334.01193	9.5
Li_{10}	3.014	0.00	D_{10h}: $(a_{1g})^2\,(e_{1u})^4\,(e_{2g})^4$	−74.32068	−74.32066	0.0
Na_{10}	3.659	0.00	D_{10h}: $(a_{1g})^2\,(e_{1u})^4\,(e_{2g})^4$	−1617.92612	−1617.92596	0.4
				UHF total energy		
Ag_8	2.889	0.00	C_s: (UHF)	−299.37282	−299.36244	35.3
Au_{10}	2.884	0.00	C_s: (UHF)	−334.08671	−334.06245	66.0

a) Since the frozen core approximation is less accurate for the M_2 molecules than for the M_N ring clusters by factors of 1.8-6.8, we do not use the frozen core approximation for the M_2 molecules [43].

b) Orbital symmetry restriction followed by the orbital symmetries and occupations, e.g., D_{10h}: $(a_{1g})^2\,(e_{1u})^4\,(e_{2g})^4$ is equivalent to $\psi_0(\uparrow\downarrow)\,\psi_{-1}(\uparrow\downarrow)\,\psi_1(\uparrow\downarrow)\,\psi_{-2}(\uparrow\downarrow)\,\psi_2(\uparrow\downarrow)$. All states are low spin.

Table 9. Spin contaminations for low-spin UHF wavefunctions

system	a (Å)	$\langle \hat{S}^2 \rangle$	$\bar{S}$
—— M_2 molecules [a] ——			
Cu_2	2.476	0.168	0.147
Ag_2	2.778	0.261	0.215
Au_2	2.672	0.000	0.000
Li_2	2.994	0.367	0.285
Na_2	3.620	0.644	0.446
—— M_N ring clusters ——			
Ag_6	2.889	1.515	0.828
Ag_8	2.889	2.219	1.071
Ag_{10}	2.889	2.789	1.243
Li_6	3.014	2.306	1.099
Li_{10}	3.014	3.973	1.555
Li_{14}	3.014	5.618	1.922
Cu_{10}	2.556	2.417	1.133
Ag_{10}	2.889	2.789	1.243
Au_{10}	2.884	2.343	1.110
Li_{10}	3.014	3.973	1.555
Na_{10}	3.659	3.541	1.447

a) Results for the diatomic molecules (M_2) are given for the equilibrium bond lengths (R_e) calculated at the UHF level.

Table 10. Comparison of calculated and experimental results for M_2 clusters. [a)]

	HF			UHF			better theory [b)]			experiment [c)]		
system	R_e (Å)	D_e (eV)	k_e (eV/Å^2)	R_e (Å)	D_e (eV)	k_e (eV/Å^2)	R_e (Å)	D_e (eV)	k_e (eV/Å^2)	R_e (Å)	D_e (eV)	k_e (eV/Å^2)
Cu_2	2.44	0.463	4.44	2.48	0.472	3.03	2.25	1.97	7.64	2.220	2.04	8.10
Ag_2	2.72	0.378	4.24	2.78	0.398	2.56	2.59	1.48	6.29	2.47	1.67	7.34
Au_2	2.67	0.746	10.23	2.67	0.746 [d)]	10.23	2.53	1.97	11.60	2.472	2.31	13.21
Li_2	2.82	0.141	1.46	2.99	0.185	0.61	2.692	1.029	1.55	2.673	1.057	1.59
Na_2	3.19	-0.033	1.02	3.62	0.082	0.23	3.174	0.710	0.98	3.079	0.742	1.07

a) R_e is the equilibrium internuclear separation, D_e is the dissociation energy, k_e is the harmonic force constant.
b) Calculations including many-body effects (electron correlation). Results for the noble metal dimers are taken from Reference [45] and results for the alkali metal dimers are taken from Reference [46].
c) The experimental results are taken from Reference [27] for the noble metal dimers and Reference [28] for the alkali metal dimers. R_e has not been measured for Ag_2; the listed value of 2.47 Å is the value recommended in Reference [27].
d) The UHF and HF total energies for Au_2 are equal for interatomic separations $R \leq 2.70$ Å.

Table 11. Hubbard Parameters based on high-spin ring clusters.[a)]

system	a (Å)	$\mathcal{U} = J_{11}^{\omega}$ (eV)	$\mathcal{B} = 4\lvert h_{12}^{\omega}\rvert$ (eV)	$\mathcal{B}/\mathcal{U}$
Ag_6	2.889	7.882	6.137	0.779
Ag_8	2.889	8.001	5.433	0.679
Ag_{10}	2.889	8.065	4.948	0.614
Li_6	3.014	8.079	3.999	0.495
Li_{10}	3.014	8.267	2.838	0.343
Li_{14}	3.014	8.325	2.334	0.280
Cu_{10}	2.556	8.639	6.314	0.731
Ag_{10}	2.889	8.065	4.948	0.614
Au_{10}	2.884	7.995	5.489	0.687
Li_{10}	3.014	8.267	2.838	0.343
Na_{10}	3.659	6.783	3.056	0.450

a) Results calculated with high-spin HF Wannier orbitals.

Table 12. Details of the UHF wavefunctions for symmetric ring clusters.

system	a (Å)	dimerization [a] energy (meV/atom)	$\langle \hat{S}^2 \rangle$	$\bar{S}$	valence [b] hybridization d	s	p	ΔE (meV/atom)
		bond-centered state						
Ag_6	2.889	153.8	1.515	0.828	0.002	0.684	0.314	
Ag_8	2.889	171.8	2.219	1.071	0.001	0.629	0.370	
Ag_{10}	2.889	180.8	2.789	1.243	0.001	0.594	0.404	
Li_6	3.014	269.1	2.306	1.099		0.595	0.405	
Li_{10}	3.014	305.6	3.973	1.555		0.494	0.506	
Li_{14}	3.014	316.3	5.618	1.922		0.433	0.567	
Cu_{10}	2.556	152.6	2.417	1.133	0.002	0.611	0.386	
Ag_{10}	2.889	180.8	2.789	1.243	0.001	0.594	0.404	
Au_{10}	2.884	138.6	2.343	1.110	0.007	0.835	0.158	
Li_{10}	3.014	305.6	3.973	1.555		0.494	0.506	
Na_{10}	3.659	136.5	3.541	1.447		0.649	0.351	
		atom-centered state						
Ag_6	2.889	70.9	0.842	0.545	0.002	0.829	0.196	82.9
Ag_8	2.889	62.3	1.626	0.870	0.002	0.804	0.194	109.6
Ag_{10}	2.889	66.1	1.870	0.956	0.002	0.771	0.228	114.7
Li_6	3.014	10.7	1.158	0.687		0.867	0.133	258.4
Li_{10}	3.014	6.3	2.150	1.049		0.752	0.248	299.3
Li_{14}	3.014	5.9	3.031	1.311		0.690	0.310	310.4
Cu_{10}	2.556	61.1	1.608	0.863	0.002	0.791	0.206	91.6
Ag_{10}	2.889	66.1	1.870	0.956	0.002	0.771	0.228	114.7
Au_{10}	2.884	92.9	1.977	0.992	0.007	0.928	0.064	45.7
Li_{10}	3.014	6.3	2.150	1.049		0.752	0.248	299.3
Na_{10}	3.659	14.5	2.712	1.221		0.959	0.041	122.0

a) The total cohesive energy with respect to diatomic molecules $M_N \rightarrow N/2\, M_2$ divided by N atoms (where the diatomic molecules are at equilibrium; see Table 10).
b) Atomic orbital populations calculated in the Mulliken approximation [19].

Table 13. Detailed energy data for selected Ag_8 wavefunctions.

wavefunction [a]	δa [b]	E^{CORE}	E^{ONE}	E^{TWO}	E^{TOTAL}
(undistorted ring)	(Å)	(hartree)	(hartree)	(hartree)	(hartree)
low-spin HF (C_s)	0.00	−294.22519	−8.33056	3.25950	−299.29625
low-spin HF (D_{4h})	0.00	−294.22519	−8.32737	3.26071	−299.29186
low-spin UHF (C_s)	0.00	−294.22519	−8.25960	3.12235	−299.36244
low-spin GVB (C_i)	0.00	−294.22519	−8.27990	3.11676	−299.38833
high-spin HF (D_{4h})	0.00	−294.22519	−7.93802	2.94002	−299.22320
			$E(\delta a) - E(\delta a = 0.00)$		
(distorted rings)	(Å)	(eV)	(eV)	(eV)	(eV)
low-spin HF (C_s)	±0.00	0.000	0.000	0.000	0.000
	±0.04	0.014	−0.046	0.010	−0.022
	±0.10	0.088	−0.243	0.030	−0.126
	±0.20	0.367	−0.595	0.027	−0.201
	±0.30	0.884	−0.968	0.022	−0.062
low-spin HF (D_{4h})	−0.30	0.884	0.804	0.015	1.703
	−0.20	0.367	0.569	0.013	0.949
	−0.10	0.088	0.301	0.007	0.395
	−0.04	0.014	0.124	0.002	0.141
	0.00	0.000	0.000	0.000	0.000
	0.04	0.014	−0.129	−0.002	−0.117
	0.10	0.088	−0.330	−0.003	−0.245
	0.20	0.367	−0.682	−0.005	−0.320
	0.30	0.884	−1.055	−0.010	−0.181
low-spin UHF (C_s)	0.00	0.000	0.000	0.000	0.000
	±0.04	0.014	−0.003	0.004	0.014
	±0.10	0.088	−0.019	0.021	0.090
	±0.20	0.367	−0.073	0.076	0.370
	±0.30	0.884	−0.163	0.159	0.879
low-spin GVB (C_i)	±0.00	0.000	0.000	0.000	0.000
	±0.04	0.014	−0.003	0.003	0.014
	±0.10	0.088	−0.016	0.018	0.090
	±0.20	0.367	−0.062	0.063	0.368
	±0.30	0.884	−0.222	0.208	0.870
high-spin HF (D_{4h})	±0.00	0.000	0.000	0.000	0.000
	±0.04	0.014	−0.004	0.004	0.014
	±0.10	0.088	−0.023	0.022	0.086
	±0.20	0.367	−0.075	0.071	0.363
	±0.30	0.884	−0.135	0.127	0.876

a) The orbital symmetry restriction is given in parenthesis.

b) The average nearest-neighbor internuclear separation is 2.889 Å.

Table 14. Detailed energy data for H_8.

wavefunction [a]	δa [b]	E^{CORE}	E^{ONE}	E^{TWO}	E^{TOTAL}
(undistorted ring)	(Å)	(hartree)	(hartree)	(hartree)	(hartree)
low-spin HF (D_{4h})	0.00	6.12818	−16.51837	6.40061	−3.98958
low-spin UHF (C_s)	0.00	6.12818	−16.42010	6.15824	−4.13368
low-spin GVB (C_i)	0.00	6.12818	−16.46687	6.12281	−4.21588
high-spin HF (D_{4h})	0.00	6.12818	−15.49309	5.72957	−3.63533
			$E(\delta a) - E(\delta a = 0.00)$		
(distorted rings)	(Å)	(eV)	(eV)	(eV)	(eV)
low-spin HF (D_{4h})	−0.05	0.084	0.946	−0.080	0.949
	0.00	0.000	0.000	0.000	0.000
	0.05	0.084	−1.230	0.154	−0.992
low-spin UHF (C_s)	0.00	0.000	0.000	0.000	0.000
	±0.05	0.084	−0.328	0.177	−0.067
low-spin GVB (C_i)	0.00	0.000	0.000	0.000	0.000
	±0.05	0.084	−0.645	0.211	−0.350
high-spin HF (D_{4h})	0.00	0.000	0.000	0.000	0.000
	±0.05	0.084	−0.017	−0.001	0.065

a) The orbital symmetry restriction is given in parenthesis.

b) The average nearest-neighbor internuclear separation is 1.483 Å.

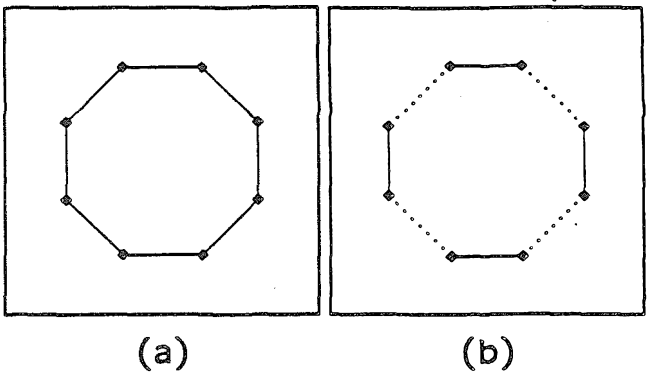

Figure 1. (a) The M_8 symmetric ring cluster as a model of the undistorted one-dimensional metal. (b) The M_8 distorted ring cluster (composed of alternating long and short bonds) as a model of the Peierls distorted one-dimensional metal.

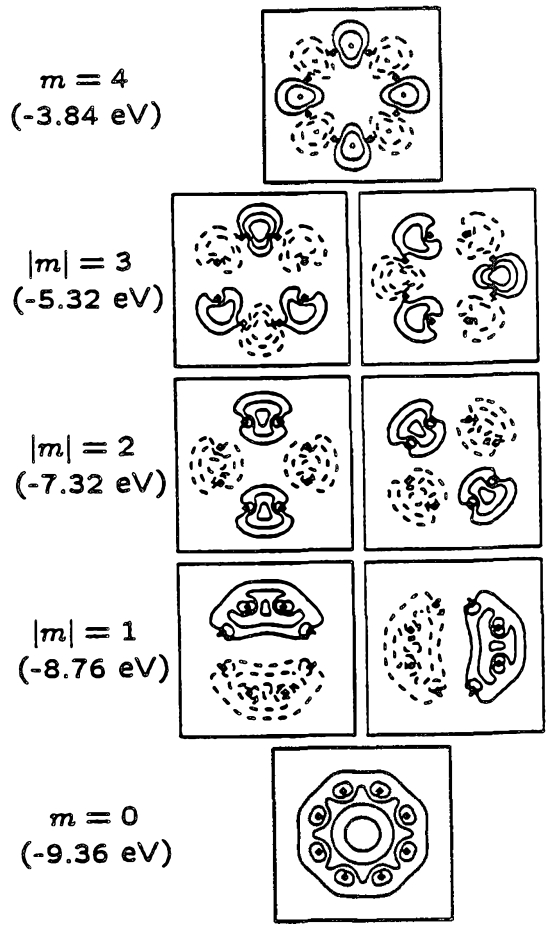

Figure 2. Real representations of the Bloch functions for the Ag_8 symmetric ring cluster. Note that the maximum absolute amplitudes are at *bond midpoints*. In this Figure and in similar figures that follow, contours are at uniform amplitude increments (0.015 au for Ag) and squares mark the atomic positions. Solid contours denote positive amplitudes and dashed contours denote negative amplitudes.

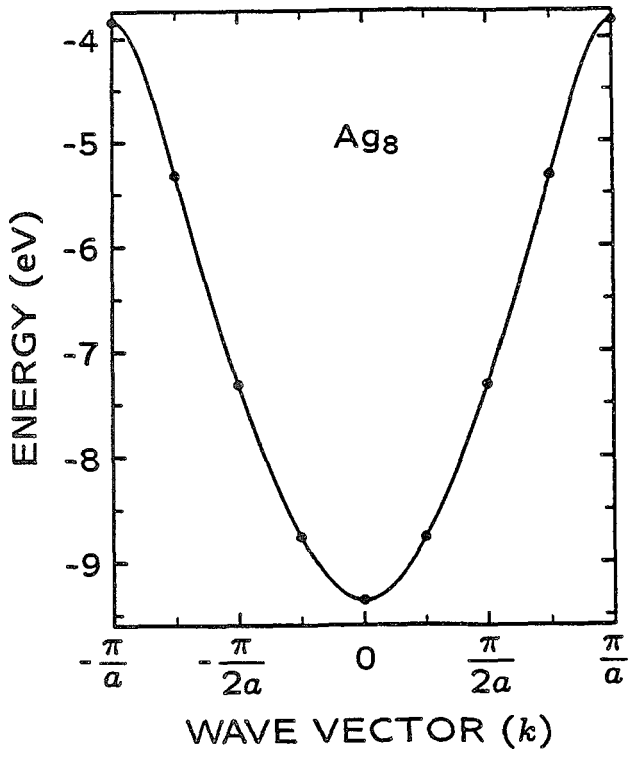

Figure 3. The valence energy band of the undistorted one-dimensional metal as defined by the valence high-spin state (where each Bloch function of Figure 2 is occupied by one up-spin electron). The discrete energy levels of Ag_8 (marked by the data points) are joined by the solid curve approximating the continuous energy band for the limit as N approaches infinity. The valence band is half filled in the HF description of the low-spin state of the one-dimensional metal, i.e., the one-electron states with $|k| < \pi/2a$ and one of the two degenerate $k = \pm\pi/2a$ states are double-occupied.

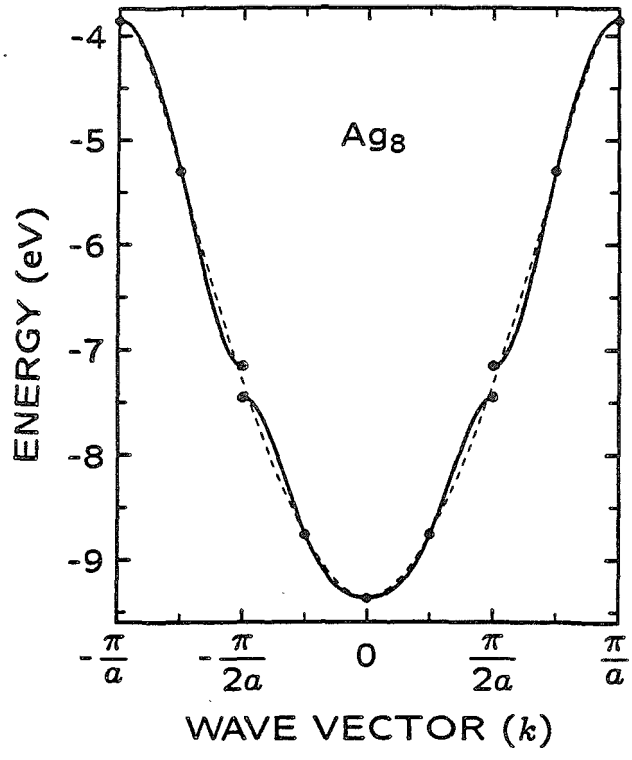

Figure 4. The valence ($-\pi/2a \leq k \leq \pi/2a$) and σ-conduction ($\pi/2a \leq |k| \leq \pi/a$) energy bands of the Peierls dimerized metal are shown by the solid curves. Data points mark the discrete energy levels for the Ag_8 distorted ring cluster ($a = 2.889$ Å, $\delta a = 0.1$ Å). The dashed curve shows the valence band for the undistorted one-dimensional metal. The distortion splits the states at $k = \pm\pi/2a$ by 0.011 eV. The lower half of the valence band is completely filled in the HF description of the low-spin state of the distorted one-dimensional metal.

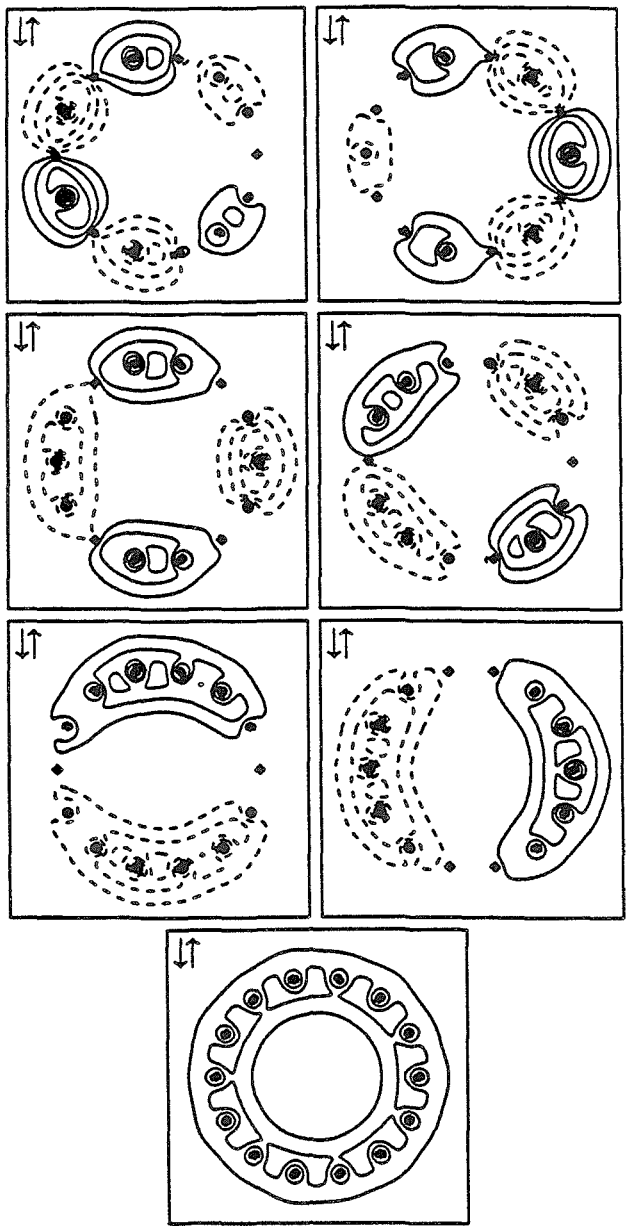

Figure 5. The HF valence orbitals for Li_{14} optimized with no orbital symmetry restrictions, leading to a charge density wave having maxima and minima centered about alternating atoms. All orbitals are doubly-occupied as indicated. The contour increment is 0.009 au.

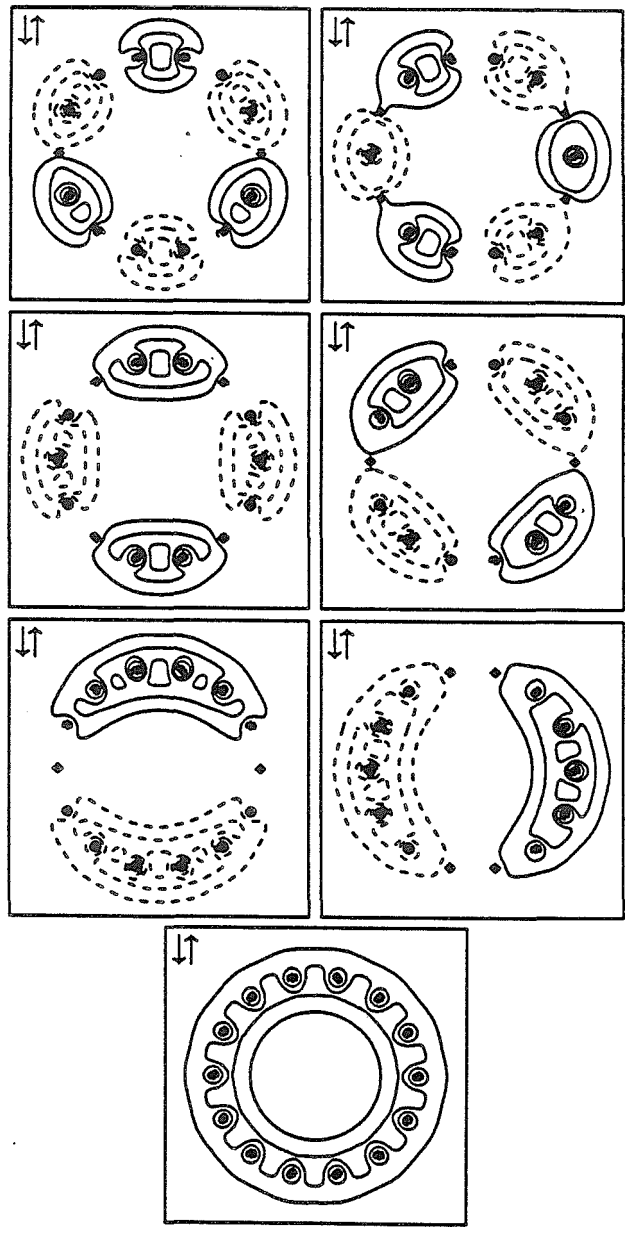

Figure 6. Real representations of the HF valence orbitals for Li_{14} optimized with full (D_{14h}) orbital symmetry restrictions. All orbitals are doubly-occupied as indicated.

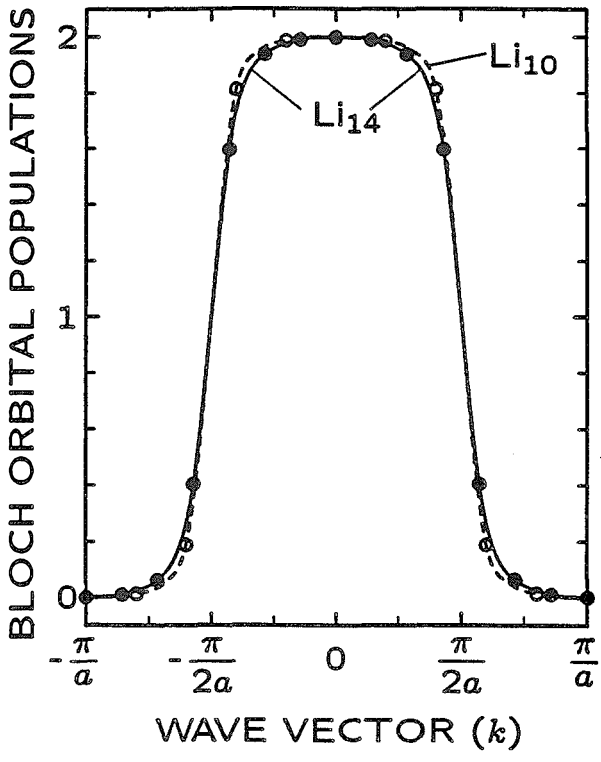

Figure 7. Bloch orbital populations for the HF low-spin charge density wave states of Li_{10} and Li_{14}. Populations are obtained by symmetry projecting the HF canonical (doubly-occupied) broken-symmetry orbitals (see Table 4).

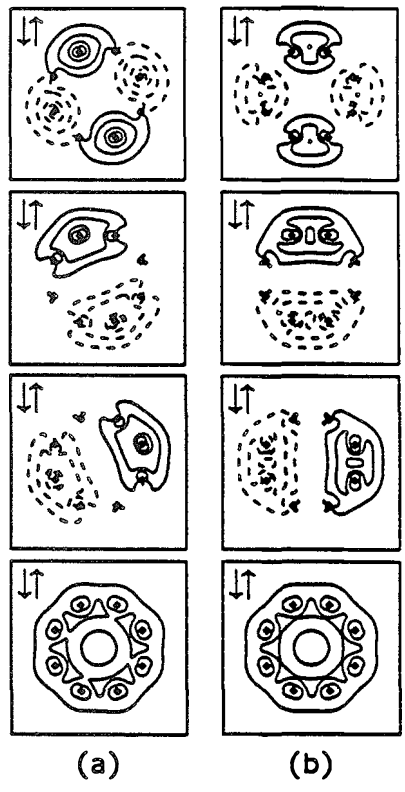

Figure 8. The HF valence orbitals optimized for the two distinct charge density wave states of the Ag_8 symmetric ring cluster. All orbitals are doubly-occupied as indicated. (a) Shows the orbitals for the state with charge density wave maxima *centered at the atoms.* (b) Shows the orbitals for the state with charge density wave maxima *centered at the bond midpoints.*

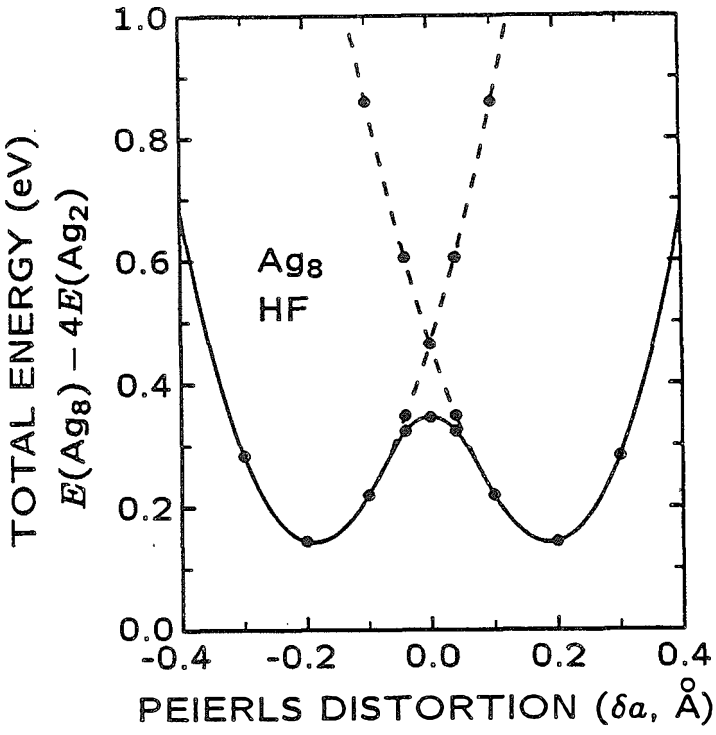

Figure 9. The HF total energy of low-spin Ag_8 as a function of the Peierls distortion (δa). The results calculated without orbital symmetry restrictions are indicated by the solid curve. The results calculated with D_{4h} orbital symmetry restrictions are indicated by the dashed curves.

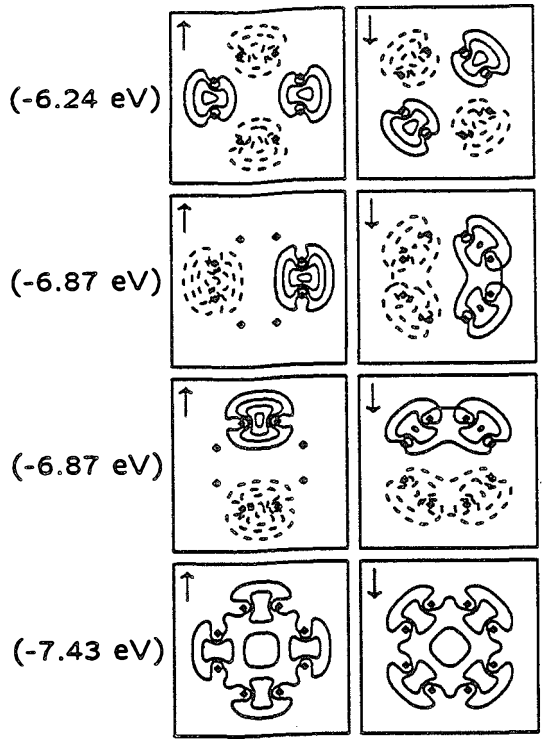

Figure 10. The UHF valence orbitals for the lowest-energy antiferromagnetic spin density wave state of Ag_8 optimized without orbital symmetry restrictions. All orbitals are singly-occupied as indicated.

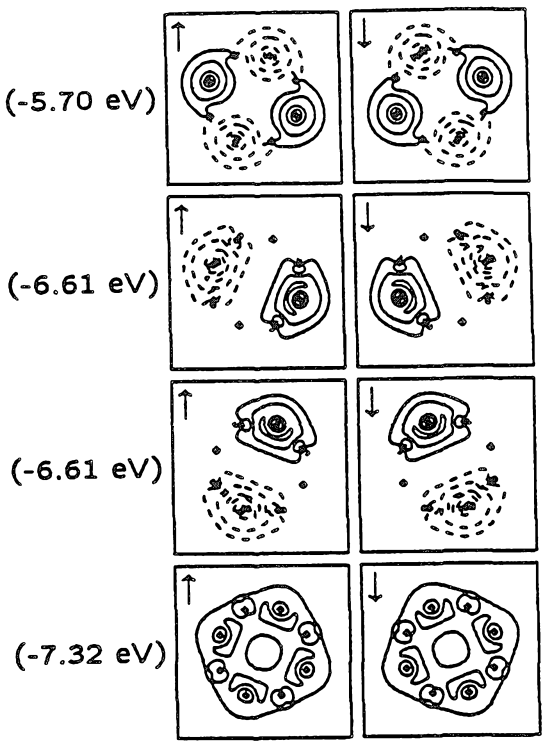

Figure 11. The UHF valence orbitals for the excited antiferromagnetic (phase-shifted) spin density wave state of Ag_8 optimized with orbital symmetry restrictions. All orbitals are singly-occupied as indicated.

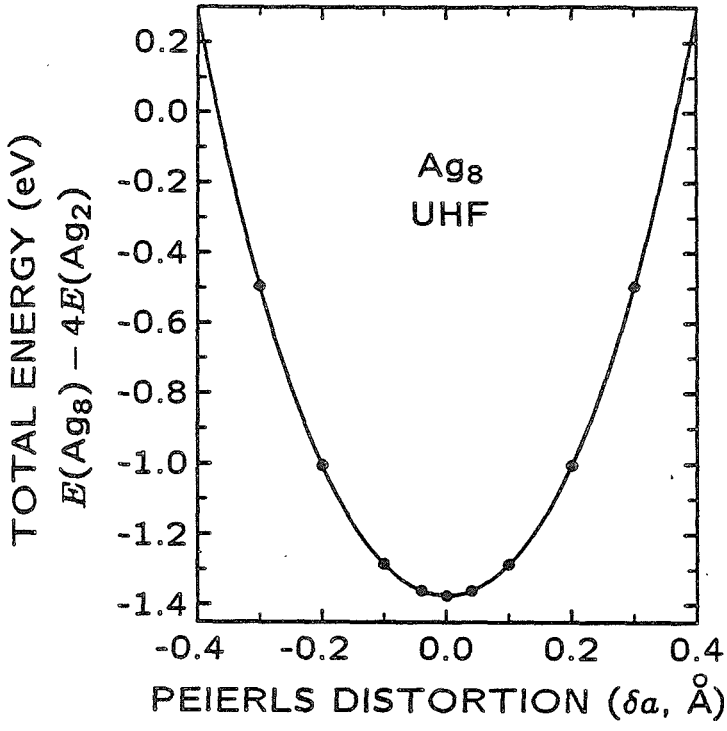

Figure 12. The UHF total energy of low-spin Ag_8 as a function of the Peierls distortion (δa).

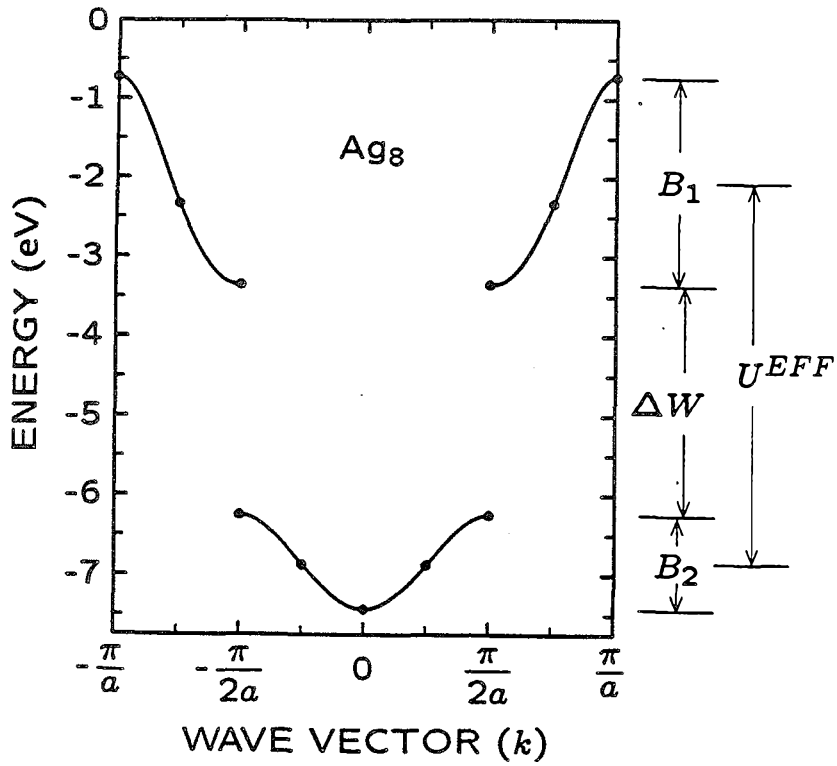

Figure 13. The UHF α-spin energy bands for the undistorted one-dimensional metal. Shown are the valence band ($-\pi/2a \leq k \leq \pi/2a$, occupied, band width $\mathcal{B}_2 = 1.187$ eV) and the σ-conduction band ($\pi/2a \leq |k| \leq \pi/a$, unoccupied, band width $\mathcal{B}_1 = 2.626$ eV) for the lowest energy antiferromagnetic state of the undistorted one-dimensional metal. The discrete α-spin energy levels of Ag_8 (marked by the data points) are joined by the curve approximating the continuous energy band for the limit as N approaches infinity. The β-spin energy bands are degenerate with the α-spin energy bands for the undistorted one-dimensional metal. The energy gap between the upper and lower bands is $\Delta W = 2.893$ eV. The effective intraatomic coulomb energy is $\mathcal{U}^{EFF} = 4.800$ eV (see Appendix C). The valence band is completely filled for the UHF antiferromagnetic ground state.

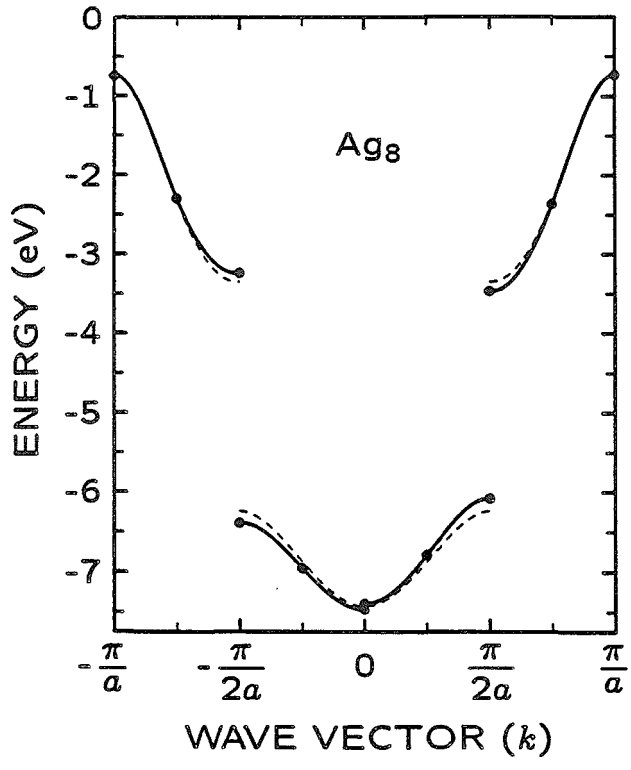

Figure 14. The UHF energy bands for the Peierls distorted one-dimensional metal. The α-spin valence ($-\pi/2a \leq k \leq 0$), β-spin valence ($0 \leq k \leq \pi/2a$), α-spin σ-conduction ($-\pi/a \leq k \leq -\pi/2a$), and β-spin σ-conduction ($\pi/2a \leq k \leq \pi/a$) energy bands for the lowest energy antiferromagnetic state of the Peierls distorted one-dimensional metal (solid curve). Data points mark the discrete energy levels for the Ag_8 distorted ring cluster ($\delta a = 0.1$ Å). The dashed curve shows analogous energy bands for the undistorted one-dimensional metal.

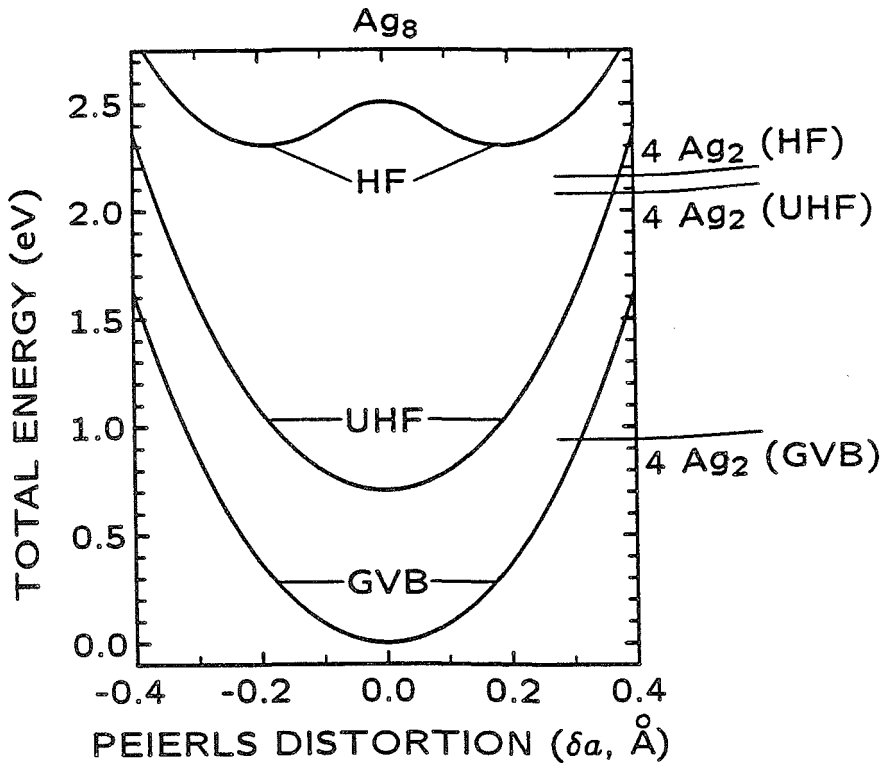

Figure 15. The total energy of Ag_8 as a function of the Peierls distortion (δa) calculated with the HF, UHF, and GVB wavefunctions, as indicated. The GVB energy of undistorted Ag_8 ($\delta a = 0$) is chosen as zero energy. The horizontal lines indicate the cohesive energy limits with respect to dissociation into four Ag_2 molecules (separate energies result from HF, UHF and GVB).

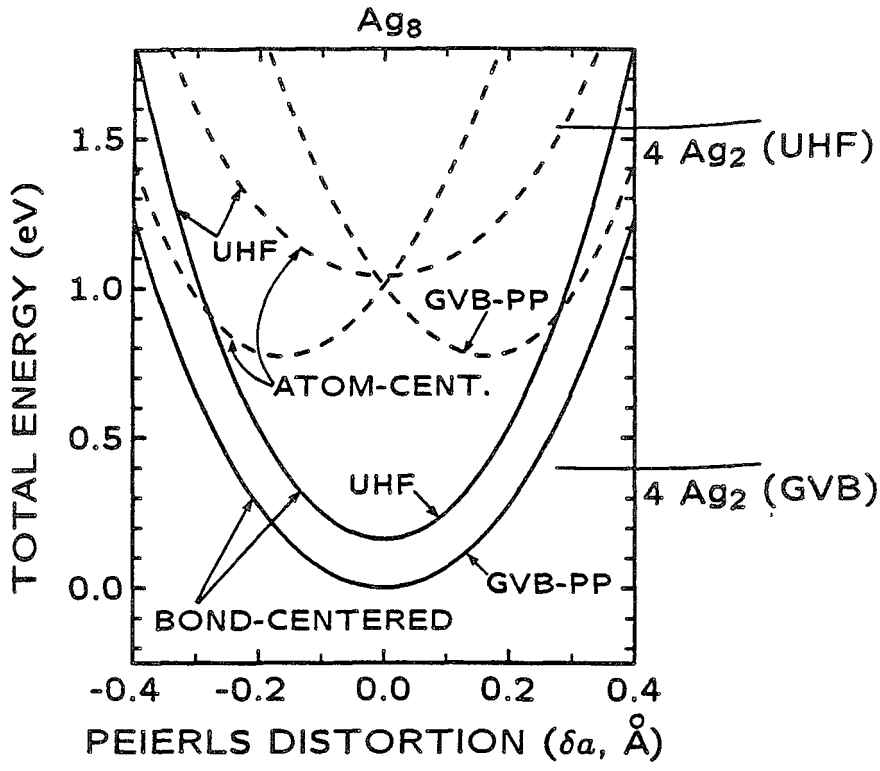

Figure 16. The total energy of Ag_8 as a function of the Peierls distortion (δa) calculated with the UHF and GVB–PP wavefunctions, as indicated. Solid curves denote the bond-centered states and dashed curves denote the atom-centered states. The GVB–PP energy of the Ag_8 bond-centered state (at $\delta a = 0$) is chosen as zero energy. The horizontal lines indicate the cohesive energy limits with respect to dissociation into four Ag_2 molecules (separate energies result from UHF and GVB–PP).

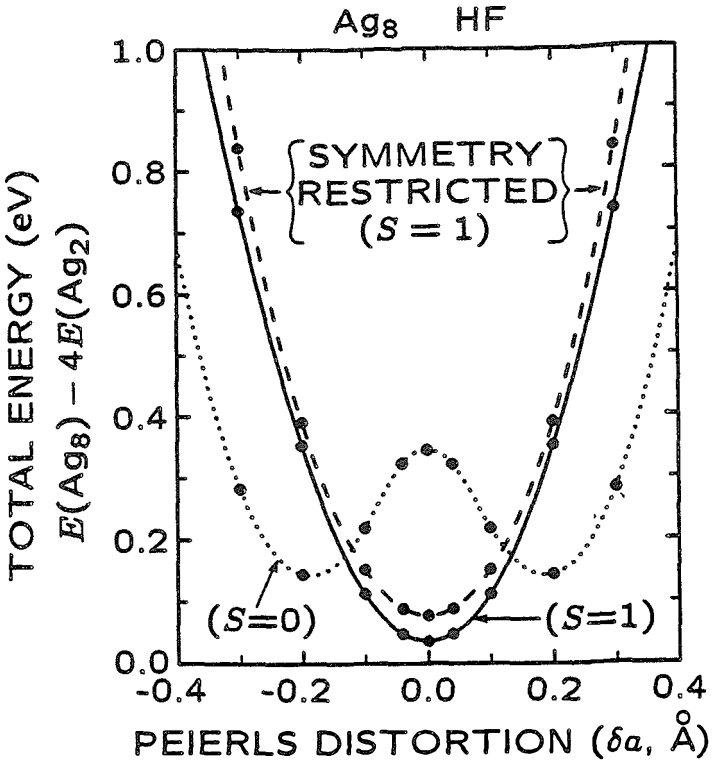

Figure 17. The HF total energy of Ag_8 as a function of the Peierls distortion (δa). Results for the triplet state with both spin and charge density waves (optimized without orbital symmetry restrictions) are indicated by the solid curve. Results for the triplet state with fully symmetrical spin and charge densities (optimized with D_{4h} orbital symmetry restrictions) are indicated by the dashed curve. Results for the singlet state with charge density waves (optimized without orbital symmetry restrictions) are indicated by the dotted curve.

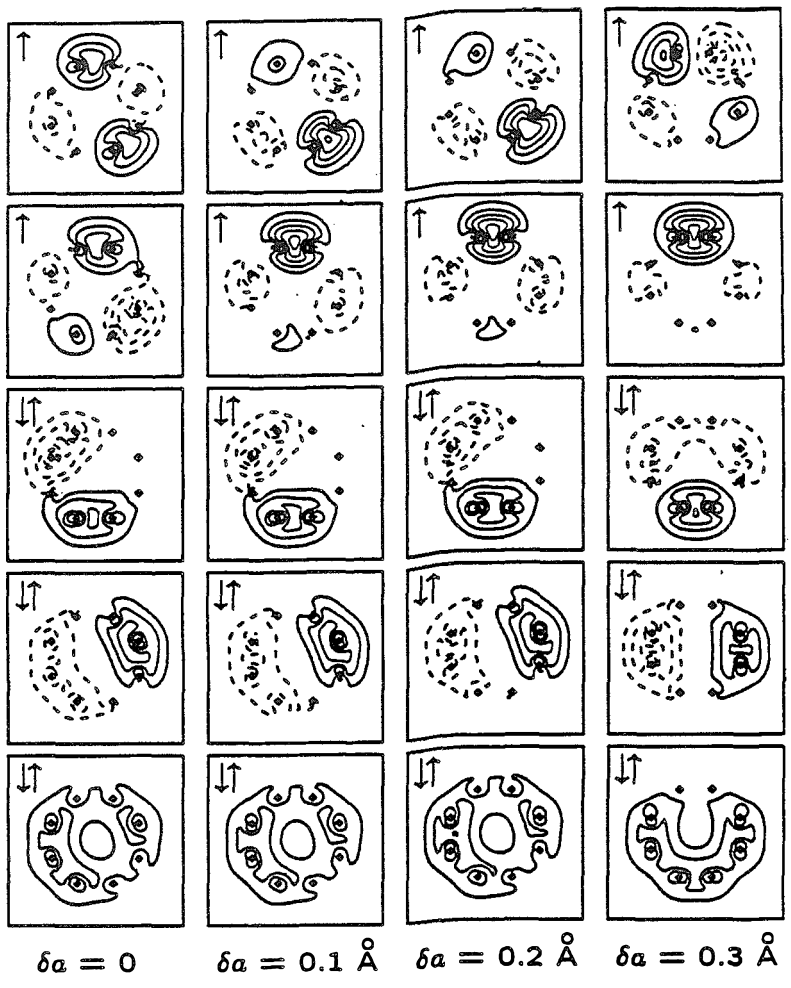

Figure 18. The HF valence orbitals optimized without symmetry restrictions for the Ag_8 triplet state, leading to spin and charge density waves that slide as a function of the Peierls distortion (δa). Orbital occupations are as indicated.

Chapter 2

Charge Density Waves, Spin Density Waves, and Peierls Distortions in One-Dimensional Metals: Generalized Valence Bond Studies of Cu, Ag, Au, Li, and Na

Chapter 2 consists of an article coauthored with William A. Goddard III that has been accepted for publication in the Journal of Physical Chemistry.

Charge Density Waves, Spin Density Waves, and Peierls Distortions in One-Dimensional Metals: II. Generalized Valence Bond Studies of Cu, Ag, Au, Li, and Na

Mark H. McAdon and William A. Goddard III

Contribution No. 7638 from the Arthur Amos Noyes Laboratory of Chemical Physics, California Institute of Technology, Pasadena, California 91125

(Received July 31, 1987)

Abstract: Ab initio generalized valence bond (GVB) calculations indicate that the one-dimensional elemental metals composed of Cu, Ag, Au, Li and Na are each *stable* with respect to the Peierls distortion. This results because of the strong cohesion resulting from two-center *one-electron* bonds (as opposed to two-center two-electron bonds). Hence, the Peierls distortion stretching and compressing alternate one-electron bonds is unfavorable. For each system, GVB leads to a singlet (low-spin) ground state having fully symmetrical charge and spin densities (no charge density wave and no spin density wave). Some of these GVB results are in complete disagreement with results calculated with less sophisticated wavefunctions such as restricted Hartree-Fock and unrestricted Hartree-Fock. Comparison of the GVB and Hartree-Fock wavefunctions reveals the origins of these errors in the Hartree-Fock descriptions.

I. Introduction

A common description of the electronic structures of crystalline solids is in terms of energy bands involving Bloch functions delocalized over the infinite lattice,[1,2,3] where each energy band can contain up to 2 electrons per primitive unit cell (one up-spin electron and one down-spin electron, e.g., doubly-occupied orbitals). The arrangement and occupation of the energy bands determine the electronic properties. Thus, for solids composed of monovalent atoms (alkali metals or noble metals), the classic metallic structures [face-centered cubic (*fcc*), hexagonal close-packed (*hcp*), and body-centered cubic (*bcc*)] all lead to a half-filled energy band, consistent with their metallic properties (e.g., low electrical resistivity).

Peierls[1] has shown that all *one-dimensional* metals with partially filled energy bands are susceptible to a distortion leading to an energy band gap at the Fermi level and hence a metal-to-insulator transition. Hence, linear metallic chains with equidistant adjacent atoms ("symmetical" chains) are predicted to distort such that the distances between adjacent atoms are not all equal.[1] For a homonuclear linear chain composed of monovalent atoms, the energy band description leads to a half-filled valence band and an instability pairing adjacent atoms to form a chain of diatomic molecules.[1]

Energy band theory [in both the restricted Hartree-Fock approximation (doubly-occupied orbitals) and the noninteracting electrons approximation including only one-electron terms in the hamiltonian] cannot account for the sharp metal-to-insulator transition that for all metals must occur for a sufficiently large uniform expansion of the crystalline lattice.[2] In order to account for a metal-to-insulator transition as a function of the lattice constant (a), Hubbard[4] introduced a hamiltonian for monova-

lent atoms including the normal one-electron terms and in addition, the intra-atomic coulomb repulsion energy

$$\mathcal{U} = \langle \omega_i(1)\omega_i(2)|r_{12}^{-1}|\omega_i(1)\omega_i(2)\rangle$$

that tends to prevent two electrons from occupying the *same* localized Wannier[3] orbital ω_1. Here r_{ij}^{-1} is the electrostatic interaction between electrons i and j (in atomic units where $e = 1$). The Hubbard hamiltonian presumably leads to a transition from antiferromagnetic insulator (large a or low-density) to metal (small a or high-density) when a is sufficiently small that[2,4]

$$\mathcal{B}/\mathcal{U} \geq \sqrt{4/3} \approx 1.15$$

[where $\mathcal{B}$ is the band width for $\mathcal{U} = 0$]. However, the critical ratio $\mathcal{B}/\mathcal{U} \approx 1.15$ is based on an approximate solution of the Hubbard hamiltonian,[2,4] and the exact solution[5] of the Hubbard hamiltonian for a *one-dimensional* lattice of monovalent atoms with a single band leads to a transition from antiferromagnetic insulator to metal only in the limit as $\mathcal{B}/\mathcal{U}$ approaches infinity.

In order to test these two contradictory models, we previously carried out ab initio[6] total energy calculations for various one-dimensional low-spin ring clusters composed of Cu, Ag, Au, Li, and Na, using single-determinant many-electron wavefunctions [restricted Hartree-Fock (HF, non spin polarized) and unrestricted Hartree-Fock (UHF, spin polarized)].[7]

For these one-dimensional metallic clusters, HF leads to half-filled energy bands, charge density waves, Peierls instabilities, and negative or very small cohesive energies with respect to dissociation into diatomic molecules.[7] UHF leads to large cohesive energies with respect to dissociation into diatomic molecules, stable symmetric

(undistorted) linear structures (in disagreement with the HF-Peierls model), and antiferromagnetic (non-metallic) ground states having spin density waves (consistent with the Hubbard hamiltonian at low density).[7]

Hence, the UHF and HF results are in complete disagreement with one another. Since the UHF total energy is lower than the HF total energy, the variational principle suggests that the UHF results are correct. However, unlike HF, the UHF wavefunctions are "spin-contaminated." The low-spin UHF wavefunction is not an eigenfunction of the many-electron spin operator ($\widehat{S}^2$) and hence contains contributions from not only the singlet ($S = 0$) but also from higher spin states such as triplet ($S = 1$), quintet ($S = 2$), etc., up to high-spin ($S = N/2$, where N is the number of atoms in the cluster).[7]

Because both HF and UHF have deficiencies (lack of cohesion for HF,[7] spin contamination for UHF), the HF and UHF results for these one-dimensional metals are not conclusive. Here we report the results of ab initio total energy calculations with multideterminant generalized valence bond (GVB) many-electron wavefunctions[8] removing the deficiencies in HF and UHF.

The GVB wavefunctions lead to the following conclusions concerning the ground electronic state of each of the Cu, Ag, Au, Li, and Na one-dimensional metal clusters. (*i*) The HF-Peierls description of the valence electronic structure (half-filled band) is fundamentally incorrect. The charge density waves and lack of cohesion for HF are artifacts of neglecting electron correlation effects. (*ii*) The UHF-Hubbard description of the electronic structure is basically correct except that the spin contamination and spin density wave are artifacts of the restricted nature of the UHF wavefunction. (*iii*) GVB leads to a singlet (antiferromagnetic)[9] ground state having fully symmetrical charge and spin densities (no charge density wave, no spin density

wave, and no spin contamination). Large cohesive energies with respect to dissociation into diatomic molecules result from two-center one-electron bonds similar to the two-center one-electron bonds of the diatomic molecular cations. Hence, the Peierls distortion stretching and compressing alternate one-electron bonds is unfavorable.

Details of the results are given in Section IV and details of the many-electron GVB wavefunction are given in Section III.

II. Qualitative aspects of the bonding

The *simple* valence bond (VB) description of bulk metals[10] is based upon two-center, two-electron covalent bonds between singly-occupied orbitals centered at adjacent atoms, as shown in Figure 1 for Cu_2, Ag_2, Au_2, Li_2, and Na_2. However, for Cu, Ag, Au, Li, and Na, the atomization energies of the bulk metals

$$M_{(s)} \rightarrow M_{(g)}$$

[(s) and (g) signify solid and gas, respectively] are 3.0-3.5 times larger than the two-center two-electron bond strengths of the respective homonuclear diatomic molecules

$$\frac{1}{2}M_2 \rightarrow M \qquad (1)$$

(experimental cohesive energies are given in Table 1).[11,12,13] Consequently, simple VB is not as useful for describing metallic systems as it is for describing nonmetallic systems.

On the other hand, the UHF and GVB many-electron wavefunctions for one-dimensional M_N ring clusters and one-dimensional M_N^+ chain clusters (M = Cu, Ag, Au, Li, and Na) lead in each case to singly-occupied orbitals having maximum absolute amplitudes *centered at the bond midpoints*, forming *two-center one-electron*

bonds as shown in Figures 2-3 for M_2^+ clusters, M_3^+ linear chains, and M_{10} rings (M = Cu, Ag, Au, Li, and Na; further details of these systems are presented in Section III and Appendices A-B). Hence, the UHF and GVB wavefunctions are not consistent with the *simple* valence bond (VB)[10] description of metals.[14]

This propensity for one-electron bonds vs. two-electron bonds is characteristic of metallic bonding[14] and is even manifest in the diatomic molecules. Thus, the cohesion per valence electron for the M_2^+ molecule

$$M_2^+ \rightarrow M + M^+,$$

is 1.83, 2.02, 2.46, and 2.65 times larger than the cohesion per valence electron for the M_2 molecule (1) for M = Cu,[11,15] Ag,[11,16] Li,[17] and Na,[18] respectively (see Table 1; the Au_2^+ bond strength is not known).

III. The GVB Many-Electron Wavefunction

The generalized valence bond (GVB)[8] valence wavefunction utilizes the hamiltonian

$$\begin{aligned}
\hat{\mathcal{H}} &= E_N^{CORE} + \sum_{i=1}^{N} \hat{h}(i) + \sum_{i>j}^{N} \frac{1}{r_{ij}} \\
\hat{h}(i) &= -\frac{1}{2}\hat{\nabla}_i^2 + \hat{V}(\vec{r}_i) + \hat{V}^{CORE} \\
\hat{V}^{CORE} &= \sum_c (2\hat{J}_c - \hat{K}_c)
\end{aligned}$$

where (i) E_N^{CORE} includes the nuclear repulsion energy and all one-electron and two-electron energy terms involving only the core electrons {the [Ar]$3d^{10}$, [Kr]$4d^{10}$, [Xe]$4f^{14}5d^{10}$, $1s^2$, and $1s^22s^22p^6$ shells for Cu, Ag, Au, Li, and Na,[19] respectively},[7] (ii) the "one-electron" operator $\hat{h}(i)$ includes the electronic kinetic energy ($-\frac{1}{2}\hat{\nabla}^2$), the electron-nuclear attraction [$\hat{V}(\vec{r}\,)$], and all two-electron interactions [coulomb

$(\hat{J}_c)$ and exchange $(\hat{K}_c)$] between core electrons and valence electrons $(\hat{V}^{CORE})$[20], and (iii) r_{ij}^{-1} is the electrostatic interaction between electrons i and j (r_{ij} is the distance between electrons i and j). This hamiltonian is identical to that utilized previously for UHF and HF calculations[7] and is based on the frozen core approximation presented elsewhere.[7]

The full (spin-optimized) generalized valence bond (SOGVB)[21] valence wavefunction for each of the various M_N ring clusters can be written in the general form

$$\Psi_{N,A} = \hat{\mathcal{A}}[\Phi_{N,A}\,\chi_{N,A}] \tag{2}$$

$$\Phi_{N,A} = \varphi_1(1)\varphi_2(2)\varphi_3(3)\cdots\varphi_N(N) \tag{3}$$

$$\chi_{N,A} = \sum_{i=1}^{n_f} c_i f_i^{N,S} \tag{4}$$

$$n_f = \frac{2S+1}{A+1}\binom{N}{A}$$

$$A = S + N/2$$

where $\hat{\mathcal{A}}$ is the antisymmetrizer or determinantal operator, $\Phi_{N,A}$ is the many-electron spatial product function, $\{\varphi_i\}$ are completely general one-electron valence orbitals optimized self-consistently for each state A without restrictions with respect to symmetry or overlap (the numbers in parentheses label the electronic coordinates),[22] and $\chi_{N,A}$ is a completely general N-electron spin function for total spin S where the coefficients c_i are optimized self-consistently and $\{f_i^{N,S}\}$ is a *complete set of spin eigenfunctions*. Thus, using the normal N-electron spin operators, the $\{f_i^{N,S}\}$ satisfy the eigenvalue equations

$$\hat{S}^2 = \hat{S}_x^2 + \hat{S}_y^2 + \hat{S}_z^2 = \hat{S}_z^2 + \hat{S}_z + \hat{S}^-\hat{S}^+$$

$$\hat{S}^2 f_i^{N,S} = S(S+1)\hbar^2 f_i^{N,S} \tag{5}$$

$$S = \frac{|A-B|}{2}$$

$$\begin{aligned} \hat{S}_z f_i^{N,S} &= M_S \hbar f_i^{N,S} \\ M_S &= \frac{A-B}{2} \end{aligned} \tag{6}$$

where S is the spin angular momentum quantum number, M_S is the spin angular momentum projection quantum number, and A and B are the number of valence electrons having spins α ($\uparrow$ or $m_s = +\frac{1}{2}$) and β ($\downarrow$ or $m_s = -\frac{1}{2}$), respectively ($A + B = N$). Optimizing χ in this fashion imposes no restriction[21] since $\hat{S}^2$ and $\hat{S}_z$ commute with one another and with $\hat{\mathcal{H}}$. Thus, the wavefunction (2) is a simultaneous eigenfunction of $\hat{S}^2$ and $\hat{S}_z$ and satisifies the Pauli principle for arbitrary $\{\varphi_i\}$ and χ.[21] The simultaneous self-consistent optimization of $\{\varphi_i\}$ and χ leads to the SOGVB wavefunction.[21]

For SOGVB, all N orbitals are allowed to overlap arbitrarily with one another, leading to an energy expression

$$E = \langle \Phi | \hat{\mathcal{H}} | \Psi \rangle / \langle \Phi | \Psi \rangle$$

involving $N!$ terms. As a result SOGVB is not practicable for large N.

Instead we use a procedure for obtaining a wavefunction mimicking SOGVB but optimizing N *orthogonal* orbitals in place of the N overlapping orbitals. This procedure is called self-consistent field full configuration interaction GVB [GVB–CI(SCF)] and is described in Appendix A.1. Using the GVB–CI(SCF) orthogonal orbitals as the basis, we obtain localized *non-orthogonal* orbitals typical of GVB with the Hartree localization method presented in Appendix A.2. These GVB–CI(SCF) results are labelled either full GVB or GVB.

An approximation to SOGVB is the perfect-pairing GVB wavefunction (GVB–PP)[23] having the form of Equations (2, 3) except that Φ is optimized for a *single*

spin eigenfunction

$$\chi_{N,A}^{PP} = (\alpha\beta - \beta\alpha)^B \alpha^{A-B}/\sqrt{2B}$$

dividing electrons into B "bond pairs" and $A - B$ "high-spin" electrons [this is called the "perfect-pairing" (PP) spin function].[22,23] Here, Φ is constrained so that the two orbitals of each bond pair maintain orthogonality with *all* other orbitals, e.g., orbitals φ_{2i-1} and φ_{2i} of the ith bond pair may overlap one another but are restricted to maintain orthogonality with all other orbitals. Both the GVB–PP wavefunction and the GVB–CI(SCF) wavefunction are simultaneous eigenfunctions of $\hat{S}^2$ and $\hat{S}_z$ and satisfy the Pauli principle.

The UHF wavefunction has the same general form (2, 3) except that the UHF spin function

$$\chi_{N,A}^{UHF} = \alpha^A \beta^B \tag{7}$$

is a simple product and is *not* an eigenfunction of $\hat{S}^2$ (except for $B = 0$). Since both Φ and χ are products of one-electron functions, the UHF wavefunction contains a single Slater determinant. Ψ^{UHF} is an eigenfunction of $\hat{S}_z$ but is not an eigenfunction of $\hat{S}^2$ unless the down-spin orbitals are identical to the up-spin orbitals (this leads to the restricted Hartree-Fock wavefunction, denoted simply HF herein).[7] For the general case where $\Psi^{UHF} \neq \Psi^{HF}$, $\Psi_{N,A}^{UHF}$ is "spin-contaminated", e.g., $\Psi_{N,A}^{UHF}$ contains a mixture of spins $|M_S| \leq S \leq N/2$.[7] The UHF orbitals are optimized without restrictions with respect to overlap or symmetry, resulting in a spin density wave for the ground state of each M_{10} ring cluster.[7]

For the high-spin state ($A = N$, $B = 0$), there is just one spin eigenfunction

$$\chi_{N,A=N} = f^{N,S=N/2} = \alpha^N$$

and hence the GVB and UHF wavefunctions are equivalent. However, for all other

spin states, GVB and UHF differ quite remarkably.

IV. Results

In the process of exploring the bonding in various metal clusters,[14,24] we performed extensive *ab initio* calculations for various one-dimensional ring and chain clusters of lithium atoms up to $N = 12$, where N is the number of atoms in the cluster, and have extrapolated various results to infinite N.[24] These studies show that the cohesive properties of the ring clusters converge rather quickly, and that the M_8 and M_{10} ring clusters are qualitatively correct and fairly accurate as models for the infinite chain (each is periodic in one dimension).

Here we examine M_N ring clusters composed of Cu, Ag, Au, Li, and Na, with lattice constants (a) for the undistorted (symmetric) clusters equal to the nearest-neighbor distances for the bulk metals.[25] The cohesive properties of the one-dimensional alkali and noble metals are dominated by the valence sp electrons,[7] and sp hybridization is crucial in describing the valence electronic structures.[7] However, in each case the $p\pi$ conduction bands are significantly higher in energy than the valence band, and hence the $p\pi$ conduction bands are unoccupied for the ground and low-lying excited electronic states.[7] For the ground and low-lying excited electronic states of the noble metal clusters, there is minimal hybridization of the d core orbitals with the sp valence orbitals, and hence the closed-shell d^{10} configurations are maintained.[7] These observations for both HF and UHF[7] are expected to hold also for GVB, and hence the same frozen core approximation for the core electrons (including the closed-shell d^{10} electrons of the noble metal rings) is employed for GVB as was previously employed for HF and UHF.[7]

Peierls[1] argued that the symmetric one-dimensional monovalent metal is unstable with respect to the geometric distortion pairing adjacent atoms to form a chain of diatomic molecules, because this distortion lowers the energies of the occupied one-electron states below the Fermi level (and raises the energies of the unoccupied one-electron states above the Fermi level).[1,7] To test for Peierls instability, we chose Ag_8.[26] The Ag_8 Peierls-distorted ring cluster contains alternating long and short internuclear separations $a \pm \delta a$, as shown in Figure 4, where the *average* nearest-neighbor distance is equal to that for the undistorted cluster.

The results presented here are calculated using the same geometries, hamiltonian, and basis sets as in our previous study,[7] but with different wavefunctions. First we present the GVB–PP results, and then we present results calculated with the more general GVB–CI(SCF) wavefunction.

A. GVB–PP

1. Cohesive Energies

The cohesive energies of the Cu_{10}, Ag_6, Ag_8, Ag_{10}, Au_{10}, Li_6, Li_{10}, Li_{14}, and Na_{10} low-spin symmetric ring clusters with respect to atomization

$$M_N \rightarrow N\,M \tag{8}$$

and dimerization

$$M_N \rightarrow N/2\,M_2 \tag{9}$$

(dissociation into diatomic molecules) calculated with GVB–PP wavefunctions are given in Table 2, where the total cohesive energies have been divided by N. These cohesive energies are calculated for low-spin ring clusters at fixed values of the lattice

constant (a). The dimerization energies are given with respect to similar calculations for diatomic molecules at their calculated equilibrium internuclear separations (R_e, see Appendix C.1).

At the GVB–PP level, the symmetric ring clusters are all stable with respect to both atomization and dimerization (see Table 2).

2. Charge Density Waves

For each of the Cu_{10}, Ag_6, Ag_8, Ag_{10}, Au_{10}, Li_6, Li_{10}, Li_{14}, and Na_{10} symmetric ring clusters, GVB–PP leads to a low-spin (antiferromagnetic) ground state described by N well-localized *singly-occupied* orbitals centered at the N bond midpoints (see Figures 3 and 5a). In each case, these are the orbitals obtained by optimizing the low-spin GVB–PP wavefunction without imposing any orbital symmetry restrictions. These *singly-occupied* orbitals are spin-coupled into $N/2$ equivalent bond pairs (as shown in Figures 3 and 5a). Each of the bond pairs for the M_N ring cluster is similar to the bond pair of linear M_3^+, as shown in Figures 2, 3, and 5a.

The GVB–PP ground state wavefunction of each of these systems leads to a charge density wave — the electronic charge density does not have the same periodicity as the lattice. In each case, the total electronic charge density can be decomposed into a fully symmetric component with periodicity a and a "wave" component with periodicity $2a$. The charge density wave maxima occur at atoms sharing the two overlapping orbitals of a bond pair. Thus, the charge density wave contains maxima and minima centered at alternate atoms — for Ag_8, electron density depleted from atoms 1, 3, 5, and 7 accumulates on atoms 2, 4, 6, and 8 as shown in Figure 5a.

For each of these systems, by applying local orbital symmetry restrictions, we solved self-consistently for an *excited* low-spin state having a charge density wave

with maxima and minima centered at alternate bond midpoints (we required that the orbitals of each bond pair be related by the symmetry plane bisecting a particular bond midpoint). Hence, the excited state charge density wave is "phase-shifted" by $a/2$ with respect to ground state charge density wave. For each of the Cu_{10}, Ag_6, Ag_8, Ag_{10}, Au_{10}, Li_6, Li_{10}, Li_{14}, and Na_{10} symmetric ring clusters, this GVB–PP excited state is described by N singly-occupied *atom-centered* orbitals, divided into $N/2$ equivalent bond pairs (as shown in Figure 5b for Ag_8). Each of the bond pairs for the M_N ring cluster is similar to the bond pair of M_2 (compare Figures 5b and 1 for Ag).

For brevity, we label these two distinct states "bond-centered" and "atom-centered", referring to the localization of the singly-occupied orbitals.

The bond pair overlaps, cohesive energies and energy splittings of these two distinct states are given in Table 3 for each of the nine symmetric ring clusters. In each case, the cohesive energy with with respect to dissociation into diatomic molecules (9) is *negative* for the atom-centered state *(this state is unstable).* For Ag_8, the dimerization energy (9) is -76.1 meV/atom for the atom-centered state (unstable) and $+49.8$ meV/atom for the bond-centered state (stable); the excitation energy between these two states is 1.007 eV (125.9 meV/atom; see Table 3). For each system, the cohesion of the ground state (bond-centered) is due to two-center one-electron bonding, similar to the bonding of M_2^+ and linear M_3^+ (compare Figures 2, 3, and 5a).

For each case, these two distinct charge density wave states are each doubly degenerate (for the symmetric ring cluster) in the sense that "translating" the valence orbitals by a (or rotating by $2\pi/N$) results in a new charge density wave state with the same energy (for finite N these many-electron states are *not* orthogonal). Each of

the four charge density wave states is invariant to translations by integral multiples of $2a$, hence each of these four states is consistent with D_{nh} symmetry for the M_N symmetric cluster ($n = N/2$).

3. Peierls Instability

The GVB–PP total energies of the low-spin states of Ag_8 as a function of the Peierls distortion (δa) are shown in Figure 6. The GVB–PP bond-centered wavefunctions (Figure 5a and Figure 6, solid curve) are optimized without orbital symmetry restrictions, leading to C_{4h} symmetry for $\delta a \neq 0$ (the lattice symmetry is D_{4h} for $\delta a \neq 0$). In order to obtain GVB–PP atom-centered wavefunctions (Figure 5b and Figure 6, dashed curve), we applied *local* orbital symmetry restrictions during the optimization (the two orbitals of each bond pair were restricted to be exact mirror images of one another), leading to D_{4h} symmetry for all δa.

The Peierls distortion breaks the degeneracy of the atom-centered states (Figure 5b). Numbering the *bond midpoints* as 1 through 8, the Peierls distortion compressing bonds 2, 4, 6, and 8 (and expanding bonds 1, 3, 5, and 7) lowers the energy of the atom-centered state having charge density wave maxima centered at bond midpoints 2, 4, 6, and 8, and raises the energy of the atom-centered state having charge density wave maxima centered at bond midpoints 1, 3, 5, and 7 (for small distortions δa). Hence, the atom-centered states are unstable. The optimum value of the Peierls distortion $|\delta a_{opt}| = 0.164$ Å leads to alternating internuclear separations of 2.725 and 3.053 Å. The optimum value of the compressed bond length is significantly smaller than the 2.801 Å equilibrium bond length calculated for Ag_2 at the GVB–PP level (see Appendix C.1), indicating that the interaction *between* dimers for the atom-centered state is repulsive [the total energy at $|\delta a_{opt}| = 0.164$ Å is higher than that

of four Ag_2 molecules (R_e = 2.801 Å) by 0.371 eV (46.4 meV/atom)].

However, Peierls distortions do not break the degeneracy of the bond-centered states (Figure 5a), and these states are stable. The Peierls distortion does cause a very minor sliding of the valence orbitals, leading to a very minor flow of charge from the expanded bond midpoints to the compressed bond midpoints, increasing as a function of $|\delta a|$ as shown in Figure 7. This results in a very minor sliding of the charge density wave maxima and minima towards the compressed and expanded bond midpoints, respectively. In addition, the bond pair overlaps increase slightly as a function of $|\delta a|$. However, these effects are rather small even for $|\delta a|$ = 0.30 Å.

In Figure 8 we show total energies calculated at the HF[7] and GVB–PP levels as a function of the Peierls distortion (δa) for low-spin Ag_8 (the dashed curves in both Figures 5 and 7 depict states with charge density wave maxima and minima centered at alternate bond midpoints). In the GVB–PP description, the cohesion of the Ag_8 ground state is due to two-center one-electron bonding, similar to the bonding of Ag_2^+ and linear Ag_3^+ (compare Figures 2 and 5a). The HF wavefunction leads to Peierls instability and lack of cohesion with respect to dissociation into diatomic molecules.[7] The lack of cohesion in the HF description of the Ag_8 ground state is due to the inaccuracy of describing *one-electron* bonds with *doubly-occupied* orbitals. Therefore, electron correlation effects (included in GVB–PP but excluded from HF) are responsible for the Peierls instability and lack of cohesion in the HF description of Ag_8.

B. Full GVB

1. Cohesive Energies

The GVB–CI(SCF) many-electron wavefunction mimics the full SOGVB[21] many-electron wavefunction (see Section III and Appendix A), and contains one orbital for each valence electron. At the full GVB level, the Cu_{10}, Ag_6, Ag_8, Ag_{10}, Au_{10}, Li_6, Li_{10}, and Na_{10} low-spin symmetric ring clusters are all quite stable with respect to dissociation into both atoms (8) and diatomic molecules (9) (see Table 2).

For the *three-dimensional* bulk noble metals, the experimental cohesive energies with respect to dimerization

$$M_{(s)} \rightarrow \frac{1}{2}M_2$$

follow the trend Au > Cu > Ag. This same trend (Au > Cu > Ag) is also followed by the atomization energies of the diatomic molecules (see Appendix C.1). However, for the *one-dimensional* noble metal ring clusters, the cohesive energies with respect to dimerization [Equation (9), calculated at both the GVB–PP and full GVB levels] follow the trend Ag > Cu > Au. This same trend for the one-dimensional noble metals was observed for the UHF calculations[7] and is consistent with both the atomic s-to-p experimental state splittings[27] and with the extent of p hybridization (smaller excitation energies lead to greater hybridization and stronger cohesion).[7] The same relationships between s-to-p excitation energies, p hybridization, and cohesion apply to Li and Na.[7] Hence, sp hybridization plays a crucial role in the cohesion of these one-dimensional metals.

2. Charge and Spin Densities

The GVB–CI(SCF) many-electron wavefunction for the ground state of each of the Cu_{10}, Ag_6, Ag_8, Ag_{10}, Au_{10}, Li_6, Li_{10}, and Na_{10} symmetric ring clusters leads to a fully-symmetrical (D_{Nh}) electronic charge distribution (no spin density wave or charge density wave; see Figures 3 and 9a, and see Appendix B for further details).

For each system, each localized valence orbital ϕ_i optimized for the ground state is symmetrically centered at a bond midpoint and is composed primarily of sp hybrids from the two adjacent atoms. Orbitals ϕ_i and ϕ_j are related by a rotation through $(j-i)$ bond midpoints and hence are equivalent. The high symmetry of the $\{\phi_i\}$ leads to a fully-symmetrical (D_{Nh}) electronic charge distribution (as shown in Figure 3 for Cu_{10}, Ag_{10}, Au_{10}, Li_{10}, and Na_{10} and in Figure 9a for Ag_8). Consequently, each GVB orbital has equal overlaps with the two adjacent orbitals (and with the two next-nearest neighbor orbitals, etc., see Appendix B).

The overlaps of adjacent GVB orbitals are compared with the GVB–PP bond pair overlaps in Table 3. The GVB–PP orbitals are also centered at the bond midpoints but each GVB–PP orbital has a non-zero overlap with one adjacent orbital and is orthogonal to the other adjacent orbital. Hence, the GVB–PP orbitals are skewed (leading to a charge density wave, as shown in Figure 3 for Cu_{10}, Ag_{10}, Au_{10}, Li_{10}, and Na_{10} and in Figure 5a for Ag_8). GVB–CI(SCF) corrects this GVB–PP deficiency.

Since the GVB ground state for each M_N symmetric ring cluster ($S = 0$, $A = B = N/2$)

$$\Psi_{N,S=0} = \hat{\mathcal{A}}[\Phi_N \, \chi_{N,S=0}] \tag{10}$$

$$\Phi_N = \phi_1\phi_2\phi_3\cdots\phi_N$$

contains a fully symmetrical spatial orbital product Φ_N, the many-electron sym-

metry is in each case determined by the symmetry of the spin function $\chi_{N,S=0}$ (in combination with $\hat{\mathcal{A}}$). The spin function $\chi_{N,S=0}$ can be written[24] as a "resonance combination" of two primary spin couplings

$$\begin{aligned}
\chi^{PP}_{N,S=0} &= (\alpha\beta - \beta\alpha)^A/\sqrt{N} \\
\chi^{\overline{PP}}_{N,S=0} &= [\alpha(\alpha\beta - \beta\alpha)^{A-1}\beta - \beta(\alpha\beta - \beta\alpha)^{A-1}\alpha]/\sqrt{N} \\
\chi_{N,S=0} &= c_1\left[\chi^{PP}_{N,S=0} - (-1)^A\chi^{\overline{PP}}_{N,S=0}\right] + \cdots
\end{aligned} \tag{11}$$

and numerous secondary spin couplings [there are $(A+1)^{-1}\binom{N}{A}$ linearly independent spin eigenfunctions for the N-electron singlet]. Here $\chi^{PP}_{N,S=0}$ and $\chi^{\overline{PP}}_{N,S=0}$ are the two perfect-pairing spin functions involved in the two degenerate GVB–PP charge-density wave states of M_N.

The ground state of the Ag_8 symmetric ring cluster (bond-centered orbitals, Figure 9a) has $^1B_{1g}$ symmetry, whereas the ground state of each of the Cu_{10}, Ag_6, Ag_{10}, Au_{10}, Li_6, Li_{10}, and Na_{10} symmetric ring clusters has $^1A_{1g}$ symmetry.[28]

In addition, for the Ag_8 symmetric ring cluster we carried out GVB–CI(SCF) calculations restricted so that the final (converged) orbitals would be atom-centered, leading to a $^1B_{2g}$ excited state (Figure 9b).[29] The orbitals optimized in this fashion (Figure 9b) also result in a fully-symmetrical (D_{8h}) electronic charge distribution, in contrast to the GVB–PP skewed orbitals for the Ag_8 atom-centered state (Figure 5b, leading to a charge density wave). Details of the Ag_8 atom-centered state are also given in Table 3.

The energy splitting between the atom-centered state ($^1B_{2g}$) and the bond-centered state ($^1B_{1g}$) is 1.043 eV (130.4 meV/atom) for the Ag_8 symmetric cluster. This is a measure of the very strong preference of the valence orbitals for centering about the bond midpoints (as opposed to centering about the atoms). The Ag_8

atom-centered state (Figure 9b) is unstable with respect to diatomic molecules (9) by 0.102 eV (12.7 meV/atom). The Ag_8 bond-centered state (Figure 9a) is stable with respect to diatomic molecules (9) by 0.941 eV (117.7 meV/atom).

These results show again that two-center one-electron bonding, similar to the bonding of M_2^+ and linear M_3^+ (compare Figures 2, 5a, and 9a), plays a crucial role in the cohesion of the M_N ring clusters.

3. Peierls Distortion

Again, we focus our attention on the Ag_8 ring cluster as the test for Peierls instability.[26] The Ag_8 ring is stable with respect to the Peierls distortion for both GVB and GVB–PP. Hence, the total energy of the Ag_8 ground state increases quadratically as a function of the Peierls distortion (δa; see Figure 10).

Although alternate bond midpoints are compressed and expanded for $\delta a \neq 0$, all the *nuclei* are equivalent by symmetry (D_{4h}). We tested for charge density waves in the GVB–CI(SCF) wavefunction by using the GVB–PP skewed orbitals as "starting-guess" orbitals (shown in Figure 7 for δa = 0.00, 0.10, 0.20 and 0.30 Å) and then solving iteratively for the *optimum* (self-consistent) orbitals (shown in Figure 11 for δa = 0.00, 0.10, 0.20 and 0.30 Å). The converged GVB–CI(SCF) wavefunction results in a fully symmetrical charge density for $|\delta a| \leq 0.20$ Å. For $|\delta a| \geq 0.30$ Å, the converged GVB–CI(SCF) wavefunction results in a charge density wave having C_{4h} symmetry [the GVB–PP charge density wave has C_{4h} symmetry for all $|\delta a| \neq 0$]. Hence, for δa = 0.30 Å the optimum GVB orbitals are slightly skewed. However, the GVB–CI(SCF) energy calculated with D_{4h} orbital symmetry restrictions (Figure 10, dashed line) at $|\delta a|$ = 0.30 Å is only 0.0049 eV (0.61 meV/atom) higher than that calculated without orbital symmetry restrictions (Figure 10, solid line).

The optimum GVB orbitals (shown in Figure 11) imply that the Peierls-distorted diatomic lattice is unfavorable because alternate one-electron bonds are stretched and compressed. As $|\delta a|$ increases, orbitals centered at expanded bond midpoints tend to delocalize somewhat over adjacent compressed bond midpoints, and orbitals centered at compressed bond midpoints tend to contract, resulting in increased gradients along the compressed bond axes.

V. Discussion

These ab initio calculations [GVB–PP and (full) GVB] indicate that the one-dimensional elemental metals composed of Cu, Ag, Au, Li, and Na have large cohesive energies with respect to both atomization and dissociation into diatomic molecules, and are *stable* with respect to the Peierls distortion (see Table 2 and Figure 12).

For each of the Cu_{10}, Ag_6, Ag_8, Ag_{10}, Au_{10}, Li_6, Li_{10}, and Na_{10} symmetric ring clusters, the GVB ground state wavefunction consists of singly-occupied valence orbitals centered at the bond midpoints, forming one-electron bonds similar to the bonds in the respective M_2^+ and linear M_3^+ molecules (compare Figures 2, 3, and 9a). Adjacent bond-centered orbitals overlap, leading to antiferromagnetic (singlet) ground states having fully symmetrical electronic charge densities (no charge density or spin density waves for full GVB).

The cohesion in each of these one-dimensional metals is dominated by these two-center one-electron bonds; hence, the Peierls distortion stretching and compressing alternate one-electron bonds is unfavorable.

For a correct description of the *cohesion* due to these one-electron bonds, the wavefunction must include the configuration occupying each localized nonorthogonal

valence orbital with only one valence electron. Hence, the wavefunction must include at least *one orbital for each valence electron*, as is the case for unrestricted Hartree-Fock (UHF, spin polarized), GVB–PP, and GVB, each including exactly one orbital per valence electron.

A. Restricted Hartree-Fock

The restricted Hartree-Fock wavefunction (HF, non spin polarized) describes each electron *pair* by a single orbital. Therefore, HF leads to spurious results such as (*i*) a charge density wave and Peierls instability for the Ag_8 symmetric ring cluster (see Figure 12),[7] (*ii*) a negative atomization energy for the low-spin Na_{10} ring cluster,[7] and (*iii*) a ferromagnetic (high-spin) ground state for the Li_{10} ring cluster.[14,24] The HF wavefunctions for the Cu_{10}, Ag_6, Ag_8, Ag_{10}, Au_{10}, Li_6, Li_{10}, Li_{14}, and Na_{10} low-spin symmetric ring clusters lead to cohesive energies with respect to dissociation into diatomic molecules that are very small or negative.[7] Thus, the HF results for these one-dimensional metals *are in absolute disagreement* with the more accurate UHF[7] and GVB results.

The HF-energy band arguments predicting instability for one-dimensional metals[1] have been generalized[1,30] to explain the Hume-Rothery rules.[31] These rules are based on an empirical correlation of particular alloy structures with particular valence-electron to atom ratios. For example, nearly all γ-brass alloys occur for electron/atom ratios of 1.54 - 1.70[31,32] [the ideal ratio is 21/13 as for Ag_5Zn_8, Cu_9Al_4, etc]. The present results raise doubts concerning this explanation of the stability of the Hume-Rothery phases, since it is based on doubly-occupied orbitals.

The absence of strong cohesion in the HF description of these systems is due to the inaccuracy of describing *one-electron* bonds with *doubly-occupied* orbitals. For the

Cu_{10}, Ag_6, Ag_8, Ag_{10}, Au_{10}, Li_6, Li_{10}, Li_{14}, and Na_{10} symmetric ring clusters, the local HF description of each electron pair involves an atom-centered orbital $[\varphi(\uparrow)\varphi(\downarrow)]$.[7,24] Expanding this atom-centered orbital φ as a sum of two adjacent orthogonal bond-centered orbitals

$$\varphi = (\omega_1 + \omega_2)/\sqrt{2}$$

leads to the two-electron spatial function

$$\Phi = \varphi\,\varphi = 0.5(\omega_1\omega_1 + \omega_2\omega_2) + 0.5(\omega_1\omega_2 + \omega_2\omega_1)$$

with equal components of "ionic" configurations (ω_i doubly-occupied) and "covalent" configurations.[33] The HF wavefunction *forces* the ionic and covalent configurations to have equal weights for each low-spin pair of electrons (no electron correlation), leading to the spurious results.

The relative weights of the covalent and ionic terms can be *optimized* for an electron pair by including the configuration placing both electrons in the antibonding orbital φ^*

$$\begin{aligned} \varphi^*\varphi^* &= 0.5(\omega_1\omega_1 + \omega_2\omega_2) - 0.5(\omega_1\omega_2 + \omega_2\omega_1) \\ \varphi^* &= (\omega_1 - \omega_2)/\sqrt{2}. \end{aligned}$$

The resultant configuration interaction (CI) spatial wavefunction

$$\begin{aligned} \Phi &= c_1\,\varphi\,\varphi - c_2\,\varphi^*\varphi^* \\ &= 0.5(c_1 - c_2)(\omega_1\omega_1 + \omega_2\omega_2) + 0.5(c_1 + c_2)(\omega_1\omega_2 + \omega_2\omega_1) \\ c_1^2 + c_2^2 &= 1 \end{aligned}$$

for

$$c_1 = \lambda^2 > 0, \quad \lambda > 0$$

$$c_2 = \bar{\lambda}^2 > 0, \quad \bar{\lambda} > 0$$

is equivalent to the GVB (correlated) wavefunction[23,34]

$$\begin{aligned}
\Phi &= \phi_1\phi_2 + \phi_2\phi_1 \\
\phi_1 &= (\lambda\varphi + \bar{\lambda}\varphi^*)/\sqrt{\lambda^2 + \bar{\lambda}^2} = [(\lambda + \bar{\lambda})\omega_1 + (\lambda - \bar{\lambda})\omega_2]/\sqrt{2(\lambda^2 + \bar{\lambda}^2)} \\
\phi_2 &= (\lambda\varphi - \bar{\lambda}\varphi^*)/\sqrt{\lambda^2 + \bar{\lambda}^2} = [(\lambda + \bar{\lambda})\omega_2 + (\lambda - \bar{\lambda})\omega_1]/\sqrt{2(\lambda^2 + \bar{\lambda}^2)} \\
\langle\phi_1|\phi_2\rangle &= \mathcal{S}_{12} = (\lambda^2 - \bar{\lambda}^2)/(\lambda^2 + \bar{\lambda}^2).
\end{aligned}$$

For the one-dimensional ring clusters composed of Cu, Ag, Au, Li, and Na, these GVB orbitals $\{\phi_i\}$ are centered at adjacent bond midpoints and overlap ($\mathcal{S}_{12} \neq 0$; see Figure 3 and Table 3).

The GVB total energy is always lower than the HF total energy (as shown in Figure 12 for the Ag_8 ring) because electron correlation is included in GVB but excluded in HF. Hence, the neglect of electron correlation is responsible for the spurious HF results.

B. Unrestricted Hartree-Fock

The UHF wavefunction is the simplest single-determinant wavefunction leading to strong cohesion for the low-spin M_N ring clusters composed of Cu, Ag, Au, Li, and Na.[7] The UHF total energy can be no higher than the HF total energy, since UHF allows a separate orbital for each valence electron. UHF leads to stability with respect to the Peierls distortion (in agreement with GVB), as shown in Figure 12 for Ag_8.

However, unlike HF and GVB, the low-spin UHF wavefunction is not an eigenfunction of the many-electron spin operator $\hat{S}^2$ and hence contains contributions from not only the singlet ($S = 0$) but also from higher spin states such as triplet ($S = 1$), quintet ($S = 2$), etc., up to high-spin ($S = N/2$, where N is the number of

atoms in the cluster).[7] As a result of this "spin contamination," the lack of Peierls instability for UHF does not imply a lack of Peierls instability for the exact ground state (which would be a properly described singlet state).

C. Generalized Valence Bond

The proper generalization of UHF yielding a wavefunction that is an eigenfunction of $\hat{S}^2$ is the GVB wavefunction.[8,35] GVB resolves the disagreement between the HF-Peierls model and the UHF-Hubbard model for these one-dimensional metals. The GVB total energy is always lower than the UHF and HF total energies, as shown in Figure 12 for the Ag_8 ring cluster. For Ag_8, GVB confirms the UHF result of stability with respect to the Peierls distortion (see Figure 12).

For the low-spin ground electronic states of the one-dimensional M_N ring clusters composed of Cu, Ag, Au, Li, and Na, GVB confirms that the HF-Peierls description is fundamentally incorrect due to the neglect of electron correlation effects, and that the UHF-Hubbard description is basically correct except that (unlike UHF) GVB does *not* lead to a spin density wave (or spin-contamination). Hence, both the spin contamination and the spin density wave resulting from UHF are due to an incomplete treatment of the electron correlation (forced by the use of a single determinant).

VI. Summary

For the ground electronic states of the one-dimensional metal clusters composed of Cu, Ag, Au, Li, and Na, the full GVB wavefunctions lead to the following results. (*i*) Electron correlation is crucial for a proper description of the valence electronic

structure. In each case the GVB ground state is singlet (antiferromagnetic),[9] consisting of *singly-occupied* nonorthogonal valence orbitals centered symmetrically at the bond midpoints (no charge density wave or spin density wave). (*ii*) The HF-Peierls description of the valence electronic structure (*doubly-occupied* orbitals, half-filled band) is fundamentally incorrect due to the neglect of electron correlation effects. (*iii*) The UHF-Hubbard description of the electronic structure is basically correct except that (*iv*) unlike UHF, the GVB antiferromagnetic (nonmetallic) ground state has neither spin-contamination nor a spin density wave. (*v*) GVB leads to large cohesive energies with respect to dissociation into diatomic molecules. The cohesion is due to two-center one-electron bonds similar to the two-center one-electron bonds describing the diatomic molecular cations. Hence, the Peierls distortion stretching and compressing alternate one-electron bonds is unfavorable.

Acknowledgement

This work was supported by the National Science Foundation - Materials Research Groups - Grant DMR-8421119 and by a grant (DMR-8215650) from the Division of Materials Research of the National Science Foundation.

Appendix A. Details of the Calculations

1. The GVB–CI(SCF) Wavefunction

The full (untruncated) configuration interaction GVB wavefunction (GVB–CI)[14,40] includes all possible N-electron spatial configurations (SC) within a fixed set of N orbitals (usually taken as the GVB–PP natural orbitals). Each SC consists of

orbitals occupied with zero, one, or two electrons, and is multiplied by all possible spin functions $\{f_i^{N,S}\}$. Here we call each (antisymmetrizable) product of a SC with a particular spin function $f_i^{N,S}$ a spin eigenfunction (SEF) [although each $f_i^{N,S}$ alone is also an eigenfunction of $\widehat{S}^2$]. Each SEF is multiplied by a separate CI coefficient optimized to give the lowest possible total energy.

For the full GVB–CI, the total number of SC, $f_i^{N,S}$, SEF, and Slater determinants (DET) are given as follows:

$$
\begin{aligned}
n_{SC} &= \sum_{i=A}^{N} \binom{N}{i} \binom{i}{2i-1} \\
n_f &= \frac{2S+1}{A+1} \binom{N}{A} \\
n_{SEF} &= \frac{2S+1}{A+1} \binom{N+1}{A+1} \binom{N}{A} \\
n_{DET} &= \binom{N}{A} \binom{N}{A}
\end{aligned}
$$

[note that n_{SEF} is much less than $n_f n_{SC}$ since a SC having D doubly occupied orbitals leads to $\frac{2S+1}{A+1}\binom{N-2D}{A}$ antisymmetrizable products]. These characteristics of the GVB–CI are given in Table 4 for even values of $N \leq 12$ (the above formulas are exact for all N and S).

For cases involving orbital symmetry, selecting configurations by symmetry reduces n_{SC}, n_{SEF}, and n_{DET} by approximately the factor F, where $F = 8$, 4, and 2 for D_{2h}, C_{2v}, and C_s, respectively [for planar cases without π orbitals, n_{SC}, n_{SEF}, and n_{DET} are reduced by $\approx F/2$; $F = 1$ for cases with no orbital symmetry (C_1)].

Since GVB–CI includes all possible SEF, the total energy is invariant to linear transformations of the orbitals and hence the orbitals can be taken as orthogonal without restriction.

Here the optimum set of GVB–CI orbitals are solved self-consistently by a two-

step iterative procedure where first (i) the CI coefficients[38] are optimized for the given orbitals and then (ii) the orbitals[39] are optimized for the given CI coefficients. This sequence is iterated until the orbitals, CI coefficients, and calculated total energy all converge (usually only three or four iterations are required), resulting in the self-consistent field full (untruncated) configuration interaction GVB wavefunction [GVB–CI(SCF)]. GVB–CI(SCF) is the most general wavefunction describing N electrons with N orbitals since it involves absolutely no restrictions other than the total number of orbitals.

The GVB–CI(SCF) wavefunction mimics the full SOGVB[21] wavefunction

$$\Psi_{N,A}^{SOGVB} = \hat{\mathcal{A}}[(\phi_1\,\phi_2\,\phi_3\,\cdots\,\phi_N)\;\chi_{N,A}]\,. \tag{A1}$$

SOGVB optimizes a separate orbital ϕ_i for each valence electron (without any restrictions with respect to overlap or symmetry) for a completely general many-electron spin function χ (see Section III). The SOGVB $\{\phi_i\}$ are uniquely defined and tend to be localized (and nonorthogonal).[8,21]

Since GVB–CI(SCF) includes all possible SEF, the total energy is invariant to linear transformations (both orthogonal and nonorthogonal) of the (orthogonal) GVB–CI(SCF) natural orbitals $\{\varphi_i\}$. A linear transformation of the $\{\varphi_i\}$ resulting in a unique set of localized overlapping orbitals $\{\phi_i\}$ is given by the Hartree-localization method of Appendix A.2.[33] These $\{\phi_i\}$ are used to discuss *qualitative* aspects of GVB–CI(SCF) in terms of (A1).

2. The Hartree Localization Method

We define the "classical" wavefunction

$$\Phi_{N,A}^{CL} = \phi_1\,\phi_2\,\phi_3\,\cdots\,\phi_N$$

as the Hartree product of the $\{\phi_i\}$. The classical wavefunction leads to the energy expression

$$\begin{aligned} E^{CL} &= \sum_{i=1}^{N} h_{ii} + \sum_{i>j}^{N} J_{ij} = \sum_{i=1}^{N} h_{ii} + 0.5 \sum_{i \neq j}^{N} J_{ij} \\ h_{ij} &= \langle \phi_i | \hat{h} | \phi_j \rangle \\ J_{ij} &= \langle \phi_i \phi_j | r_{12}^{-1} | \phi_i \phi_j \rangle \end{aligned}$$

where $\{h_{ij}\}$ are the one-electron integrals (including the electronic kinetic energy, the potential energy due to the nuclei, and all two-electron core-valence interactions),[7] and $\{J_{ij}\}$ are the two-electron "coulomb" integrals describing valence-valence electron repulsions (see Section III).

The classical energy expression can also be written as

$$E^{CL} = \Sigma_J + \sum_{i=1}^{N} (h_{ii} - 0.5 J_{ii}) \tag{A2}$$

$$\Sigma_J = 0.5 \sum_{i,j}^{N} J_{ij}. \tag{A3}$$

For a set of *orthogonal* orbitals, the quantity Σ_J is invariant to orthogonal tranformations of the orbitals, so that minimizing E^{CL} would correspond to minimizing the sum of $h_{ii} - 0.5 J_{ii}$. Our basic approximation in the Hartree localization method is that this is also true for the case of *overlapping* orbitals. The self-coulomb integral (J_{ii}) strongly favors localization, whereas h_{ii} effectively weights the transformation by the one-electron energies, favoring delocalization. Since Equation (A2) contains only diagonal integrals, we solve for each ϕ_i independently (using the GVB2P5[36] self-consistent field program).

Starting with the N optimum GVB–CI(SCF) orbitals $\{\varphi_i\}$ and solving for the transformation minimizing (A2) leads to the (nonorthogonal) Hartree-localized orbitals $\{\phi_i\}$.[33] Details of the Hartree-localized orbitals for Cu_{10}, Ag_6, Ag_8, Ag_{10}, Au_{10},

Li_6, Li_{10}, and Na_{10} are given in Appendix B (also see Figures 3, 9, and 11).

3. The Wannier Localization Method

Often it is useful[3,7,24,37] to obtain an *orthogonal* set of localized orbitals $\{\omega_j\}$ from a unitary transformation of the (delocalized) canonical or natural orbitals $\{\varphi_j\}$.[33]

For symmetric ring clusters where the $\{\varphi_j\}$ are a *full* set of one-electron Bloch functions $\{\psi_m\}$

$$\begin{aligned} \psi_m^{(\omega)} &= N^{-1/2} \sum_{j=1}^{N} \omega_j \exp(ikR_j) \\ k &= \frac{2\pi m}{aN} \\ R_j &= ja \end{aligned}$$

[where m is an integer ($|m| \leq N/2$), k is the wave vector, and R_j denotes the position of ω_j (going around the circumference)], the $\{\omega_j\}$ can be obtained by the Fourier transformation of the $\{\psi_m\}$.

However, for systems where the Fourier transformation method cannot be used (unfilled energy bands, low symmetry, etc.) a unique set of $\{\omega_j\}$ can be obtained[37] by minimizing the energy expression

$$E = -\sum_{i=1}^{N} J_{ii} \tag{A4}$$

within the $\{\varphi_j\}$ basis subject to orthogonality restrictions (we use the GVB2P5[36] self-consistent field program to solve for all the ω_j simultaneously).

For the M_N ring clusters, the $\{\omega_j\}$ by the self-localization method (A4) are identical to those obtained by the Fourier transformation method.

4. Basis Sets and Effective Potentials

The GVB–PP and GVB–CI(SCF) many-electron wavefunctions[36,38,39] were optimized using the same basis sets and hamiltonians as in our HF and UHF study;[7] hence, only a brief summary is given (further details are given elsewhere).[7]

For the ring clusters (Cu_{10}, Ag_6, Ag_8, Ag_{10}, Au_{10}, Li_6, Li_{10}, Li_{14}, and Na_{10}), all core electrons (including the subvalent d^{10} cores of the noble metals) are described using the core orbitals optimized for the valence electron high-spin state (one unpaired electron per atom).[7] Thus, only the valence orbitals are optimized for each state other than high-spin. For the diatomic molecules, all orbitals are optimized without restrictions.

For the noble metals, ab initio effective potentials[19] were utilized to include the effects of all electrons other than eleven electrons per atom ($d^{10}s^1$) described explicitly in the wavefunction. These effective potentials include relativistic effects for Ag and Au but not for Cu (relativistic effects are much less important for Cu in comparison to Ag and Au).[19] For the alkali metals, all electrons are treated explicitly in the wavefunction.

In each case, the basis set is composed of gaussian type orbitals contracted to give two s functions and two sets of p functions per atom for describing the valence orbitals. Hence, the basis sets chosen have sufficient flexibility to describe the valence polarization and hybridization effects crucial for describing the metallic cohesion.

Appendix B. Detailed Results for M_N Rings

1. GVB–CI(SCF) Wavefunctions

The GVB–CI(SCF) ground state wavefunction for each of the Cu_{10}, Ag_6, Ag_8, Ag_{10}, Au_{10}, Li_8, Li_{10}, and Na_{10} symmetric ring clusters leads to a fully-symmetrical (D_{Nh}) electronic charge distribution (no spin density wave or charge density wave, see Figures 3 and 9a) and can be constructed from a full set of one-electron Bloch functions

$$\begin{aligned} \psi_m^{(\phi)} &= c_m^{-1/2} \sum_{j=1}^{N} \phi_j \exp(ikR_j) \\ k &= \frac{2\pi m}{aN} \\ R_j &= ja \end{aligned}$$

where m is an integer ($|m| \leq N/2$), c_m is the normalization constant, $\{\phi_j\}$ is an optimal set of N equivalent real nonorthogonal localized orbitals, k is the wave vector, and R_j denotes the position of ϕ_j (going around the circumference). We use real representations of the $\{\psi_m\}$ except where otherwise noted. The $\{\phi_j\}$ are obtained from the $\{\psi_m\}$ by the Hartree-localization method presented in Appendix A.2.

For each of the M_{10} symmetric ring clusters, the $\{\psi_m\}$ optimized for the bond-centered state (Figure 3, $^1A_{1g}$ ground state) belong to the a_{1g}, e_{1u}, e_{2g}, e_{3u}, e_{4g}, and b_{2u}[28] representations of the point-symmetry group D_{10h}. The $\{\psi_m\}$ optimized for the Ag_8 bond-centered state (Figure 9a, $^1B_{1g}$ ground state) belong to the a_{1g}, e_{1u}, e_{2g}, e_{3u} and b_{2g} representations of D_{8h}. The $\{\psi_m\}$ optimized for the Ag_8 atom-centered state (Figure 9b, $^1B_{2g}$ excited state) belong to the a_{1g}, e_{1u}, e_{2g}, e_{3u} and b_{1g} representations of D_{8h}.

2. GVB–CI(SCF) Hartree Localized Orbitals

As a test of the Hartree-localization method, for the M_3^+ linear chain clusters we compare the GVB Hartree-localized orbitals $\{\phi_i\}$ with the unique GVB–PP canonical singly-occupied orbitals $\{\varphi_i\}$ (see Figure 2). Systems having two valence electrons such as M_3^+ are ideal test cases since the GVB–PP and GVB–CI(SCF) wavefunctions are identical. Hence we define

$$\delta(\phi_i) = 1 - \langle\phi_i|\varphi_i\rangle$$

to compare the $\{\phi_i\}$ and $\{\varphi_i\}$. Values of $\delta(\phi_i)$ for Cu_3^+, Ag_3^+, Au_3^+, Li_3^+, and Na_3^+ are 0.00258, 0.00104, 0.00154, 0.00022, and 0.00002, respectively. For comparison, values of

$$\delta(\omega_i) = 1 - \langle\omega_i|\varphi_i\rangle$$

[where $\{\omega_i\}$ are (orthogonal) GVB Wannier-localized orbitals] for Cu_3^+, Ag_3^+, Au_3^+, Li_3^+, and Na_3^+, are 0.01990, 0.01541, 0.01594, 0.00626, and 0.00838, respectively [the average $\delta(\phi_i)$ value (0.00108) is smaller than the average $\delta(\omega_i)$ value (0.01318) by a factor of 12]. As a further test, we also compare the overlaps $\langle\varphi_1|\varphi_2\rangle$ (GVB–PP) and $\langle\phi_1|\phi_2\rangle$ (GVB Hartree-localized) in Table 5. In comparison to the GVB–PP overlaps, the GVB Hartree-localized overlaps range from 18% too small (Li_3^+) to 33% too large (Cu_3^+). Overall, the comparison between the Hartree-localized orbitals and the GVB–PP orbitals for the linear M_3^+ clusters is satisfactory.

For each of the Cu_{10}, Ag_{10}, Au_{10}, Li_{10}, and Na_{10} ground state (bond-centered) symmetric ring clusters, the GVB Hartree-localized orbitals are quite similar to the GVB–PP singly-occupied orbitals (see Figure 3) except that they reflect the higher symmetry of GVB–CI(SCF) in comparision with GVB–PP. Each Hartree-localized GVB–CI(SCF) orbital overlaps both adjacent localized orbitals equally, leading to a

fully symmetrical charge density, whereas each GVB–PP orbital is allowed to overlap only one of the two neighboring orbitals, leading to a charge density wave. In comparison to the GVB–PP bond pair overlaps, the GVB Hartree-localized orbital nearest-neighbor overlaps range from smaller by 21% (Li_{10}) to larger by 6% (Cu_{10}; see Table 5).

Table 6 presents all the overlaps [$S_{ij} = S_{i+n\,j+n}$] between the GVB Hartree-localized orbitals. For the Cu_{10}, Ag_{10}, Au_{10}, Li_{10}, and Na_{10} low-spin ring clusters, the S_{ij} decrease with each succeeding increment of $1 \leq |i-j| \leq 4$ by factors of roughly 2.8, 3.3, 4.0, 4.2, and 6.2, respectively.

The overlaps S_{ij} for the Ag_8 bond-centered state are larger than the respective values for the Ag_{10} bond-centered state. Indeed, the distance between bond-centered orbitals i and $i+n$ is smaller for Ag_8 than for Ag_{10} — even for $n = 1$. This indicates a minor flaw in the GVB–PP bond pair overlaps since for the bond-centered state, the bond pair overlap for Ag_8 (0.542) is slightly smaller than that for Ag_{10} (0.546; see Table 3 or Table 5). But for the atom-centered state, the GVB–PP bond pair overlap for Ag_8 (0.657) is smaller than that for Ag_{10} (0.684; see Table 3).

For each of the M_3^+ linear chain clusters and each of the M_N ring clusters, the GVB Hartree-localized orbitals for the high-spin and low-spin (singlet) states are quite similar. Tables 5-6 present GVB Hartree-localized orbital overlaps for valence-electron high-spin states ($S = 1$ for M_3^+, $S = N/2$ for M_N). The GVB Hartree-localized orbital nearest-neighbor overlaps for the M_{10} high-spin states are 6 to 31% larger than values for respective M_{10} low-spin states (see Table 5). For each of these ring clusters, the fact that the nature of the localized valence orbitals does not change in going from low-spin to high-spin suggests that the magnon spectrum (the spectrum of excited spin states) can be described by the Heisenberg model[41]

involving local spin-spin exchange interactions.[14,24]

The Hartree localization method has not been tested for heteronuclear systems or for cases with very large overlaps [where the approximation of (A3) may tend to break down, possibly leading to orbitals that are not qualitatively correct]. However, the Hartree localization method is satisfactory for both the bond-centered and atom-centered states of Ag_8 (compare Figure 5a-b with Figure 9a-b) and for the bond-centered state of the Ag_8 Peierls-distorted ring cluster (compare Figure 7 with Figure 11).

Overall, the comparison between the Hartree-localized orbitals and the GVB–PP orbitals for the M_3^+ and M_N clusters is quite satisfactory.

3. UHF Hartree Localized Orbitals

For the ground state M_3^+ linear chains the canonical UHF orbitals $\{\varphi_i^{UHF}\}$ and the canonical GVB orbitals $\{\varphi_i^{GVB}\}$ are very similar (both sets of orbitals are singly-occupied and localized at bond midpoints). Values of

$$\delta(\varphi_i^{UHF}) = 1 - \langle \varphi_i^{UHF} | \varphi_i^{GVB} \rangle$$

for Cu_3^+, Ag_3^+, Au_3^+, Li_3^+, and Na_3^+, are 0.00079, 0.00050, 0.00044, 0.00010, and 0.00030, respectively [the average value of $\delta(\varphi_i^{UHF})$ is 0.00043]. For M_3^+, the UHF nearest-neighbor overlap integrals are 1-10% larger than the respective GVB–PP values (see Table 5).

For the M_N ring clusters, the $\{\varphi_i^{UHF}\}$ are delocalized although they do break symmetry (further details of these UHF wavefunctions are given elsewhere).[7,24] UHF wavefunctions are invariant to separate linear transformations of the up-spin and down-spin orbitals. Here, we compare UHF Hartree-localized orbitals $\{\phi_i^{UHF}\}$ (ob-

tained by separate transformations of the up-spin and down-spin valence orbitals) with the GVB Hartree-localized orbitals $\{\phi_i^{GVB}\}$.

Values of

$$\delta(\phi_i^{UHF}) = 1 - \langle \phi_i^{UHF} | \phi_i^{GVB} \rangle$$

for Cu_{10}, Ag_{10}, Au_{10}, Li_{10}, and Na_{10}, are 0.00098, 0.00033, 0.00026, 0.00112, and 0.00039, respectively [the average value of $\delta(\phi_i^{UHF})$ is 0.00062]. In comparison to the GVB Hartree-localized orbital nearest-neighbor overlaps, the UHF Hartree-localized orbital nearest-neighbor overlaps range from smaller by 5% (Cu_{10}) to larger by 21% (Li_{10}; see Table 5).

Table 6 presents all the overlaps $[\mathcal{S}_{ij} = \mathcal{S}_{i+n\,j+n}]$ for both the $\{\phi_i^{UHF}\}$ and the $\{\phi_i^{GVB}\}$. The UHF and GVB overlaps are in fairly good agreement up to the fourth-nearest neighbor ($\mathcal{S}_{15}$).

Appendix C. Results for the Diatomic Molecules

We calculated the optimum internuclear separations (R_e), dissociation energies (D_e) and force constants (k_e) at the full-valence GVB level for the ground state ($^1\Sigma_g^+$) Cu_2, Ag_2, Au_2, Li_2, and Na_2 molecules and for the ground state ($^2\Sigma_g^+$) Cu_2^+, Ag_2^+, Au_2^+, Li_2^+, and Na_2^+ molecules.

The frozen core approximation[7] is much less accurate for the diatomic molecules than it is for the M_N ring clusters; hence, we optimized both the core orbitals and the valence orbitals for all diatomic molecules.

The neutral diatomic molecules contain only two valence electrons so GVB–PP and GVB–CI(SCF) are identical for the $^1\Sigma_g^+$ ground states. The diatomic cations contain only one valence electron so HF, UHF, GVB–PP and GVB–CI(SCF) are

identical.

1. Cu_2, Ag_2, Au_2, Li_2, and Na_2

For Cu_2, Ag_2, Au_2, Li_2, and Na_2, the GVB results are compared with UHF results (calculated using the same basis sets and hamiltonians)[7] and with results obtained both from experiment and from calculations including more complete treatments of the electron correlation effects (see Table 7).[42,43] The errors in the various GVB results (in comparison to experiment) are due mainly to the neglect of dynamic electron correlation effects (GVB includes only "static" electron correlation effects) as opposed to the basis set truncation. Note that basis set truncation errors are generally much smaller for GVB than for the higher level wavefunctions including dynamic electron correlation effects.

The values of R_e and k_e calculated with UHF and GVB are of similar accuracy (except for Na_2 where UHF is especially poor). In each case, GVB leads to a cohesive energy (D_e) that is substantially larger than the UHF value.

Although atomization energies are seriously underestimated at the GVB level for both the M_2 diatomic molecules and the M_N ring clusters, the cohesive energies of the M_N ring clusters with respect to dissociation into diatomic molecules

$$M_N \rightarrow N/2\ M_2$$

should be much more accurate due to similar dynamic electron correlation energies (per atom or valence electron) for the M_N ring cluster and the M_2 diatomic molecule.

2. Cu_2^+, Ag_2^+, Au_2^+, Li_2^+, and Na_2^+

For Cu_2^+, Ag_2^+, Au_2^+, Li_2^+, and Na_2^+, the GVB results are compared with the available experiment results in Table 8.[11,15,16,17,18,27,44]

The GVB values of D_e for Cu_2^+, Ag_2^+, Li_2^+, and Na_2^+ are too small by $32 \pm 4\%$, $28 \pm 2\%$, 5.6%, and 5.9%, respectively (for Au_2^+, there is no available experimental data). Values of R_e and k_e have not been determined experimentally for Cu_2^+, Ag_2^+, or Au_2^+. The GVB values of k_e for Li_2^+ and Na_2^+ are too large by $1.6 \pm 1.1\%$ and $0.5 \pm 0.8\%$, respectively. The GVB values of R_e for Li_2^+ and Na_2^+ are too large by $2.2 \pm 0.4\%$ and $1.9 \pm 0.9\%$.

For Cu_2^+ and Ag_2^+, the errors in the GVB D_e values (in comparison to experiment) are mainly due to the neglect of core-core and core-valence electron correlation effects.[44] For Li_2^+, almost all of the discrepancy between the listed GVB results and the experimental results can be removed with basis set improvements (such as optimizing the p basis scale factor and adding a set of d functions).[14,45]

Appendix D. Localization transition for Li_8

The ground state local electronic structure of each of the Cu_{10}, Ag_6, Ag_8, Ag_{10}, Au_{10}, Li_6, Li_{10}, Li_{14}, and Na_{10} ring clusters involves valence orbitals centered at bond midpoints for lattice constants (a) equal to the respective bulk metal nearest-neighbor distances.[25] However, in each case, for sufficiently large uniform expansions of the lattice there is a sharp transition from the bond-centered state to the atom-centered state (having valence s orbitals centered at the atoms in the limit as a approaches infinity).

GVB–PP potential energy curves showing this localization transition for the Li_8

ring cluster are presented in Figure 13 for both the low-spin ($S = 0$) ground state and the valence electron high-spin state ($S = 4$). Results for these GVB–PP states and also for the UHF and GVB–CI(SCF) bond-centered (ground) states are given in Table 9 for Li_8. The localization transition occurs at $a = 1.42a_e = 4.424$ Å and at $a = 1.37a_e = 4.457$ Å for low-spin Li_8 and high-spin Li_8, respectively.

This localization transition is similar to the Mott[2] metal-insulator transition (both are sharp transitions as a function of a). For one-dimensional monovalent metals, the high-density (bond-centered) states are insulators since there is only one site (bond midpoint) per electron; hence all sites are filled. However, for two- and three-dimensional metals and alloys, analogous localization transitions — triangle-centered to atom-centered for 2D and tetrahedron-centered to atom-centered for 3D,[14] both occuring at $a \approx 1.4a_e$ for Li — are expected to be true metal-insulator transitions since in each case the number of sites per electron is greater than one (two sites/electron for 2D and up to five sites/electron for 3D).

References

[1] R. E. Peierls, *Quantum Theory of Solids*, (Oxford Univ. Press, London, 1956).

[2] N. F. Mott, *Metal-Insulator Transitions* (Barnes & Noble, New York, 1974).

[3] G. H. Wannier, *Elements of Solid State Theory* (Cambridge Univ. Press, London, 1959); G. Wannier, *Phys. Rev.* **52**, 191 (1937).

[4] J. Hubbard, *Proc. Roy. Soc. London* **A 276**, 238 (1963); *ibid* **A 277**, 237 (1964); *ibid* **A 281**, 401 (1964).

[5] E. H. Lieb and F. Y. Wu, *Phys. Rev. Lett.* **20**, 1445 (1968).

[6] The calculations for Li and Na are "ab initio" in the traditional definition in that the total energy expressions $\langle\Psi|\mathcal{H}|\Psi\rangle/\langle\Psi|\Psi\rangle$ include *all terms resulting from the true Hamiltonian* ($\widehat{\mathcal{H}}$) [within the usual Born-Oppenheimer approximation (frozen nuclei)] and no additional terms. The only approximations utilized in ab initio calculations are in the many-electron wavefunction (Ψ). "Exact" calculations would require Ψ to include essentially an infinite number of configurations within an infinite basis set and are generally unattainable; the configuration and basis set expansions are truncated in actual applications. For the M_N ring clusters (with monovalent M), GVB–CI(SCF) includes all configurations within N orbitals (see Appendix A). Both HF and UHF include only a single configuration. Local density functional calculations (such as $X\alpha$) are not ab initio in this traditional definition since the exchange integrals are replaced by a local "exchange-correlation" potential obtained from calculations on the free electron gas. The calculations for Cu, Ag and Au are ab initio for

eleven electrons per atom ($d^{10}s^1$), where "ab initio" effective potentials model all effects of the remaining core electrons. See Section III and Reference [19] for further details.

[7] M. H. McAdon and W. A. Goddard III, *J. Chem. Phys.,* accepted for publication.

[8] W. A. Goddard III, T. H. Dunning, Jr, W. J. Hunt, and P. J. Hay, *Accts. Chem. Res.* **6**, 368 (1973); W. A. Goddard III and L. B. Harding, *Ann. Rev. Phys. Chem.* **29**, 363 (1978).

[9] The GVB singlet ground state for each of the Cu_{10}, Ag_6, Ag_8, Ag_{10}, Au_{10}, Li_6, Li_{10}, and Na_{10} ring clusters is antiferromagnetic in the same sense that the singlet ground state of the H_2 molecule is antiferromagnetic. None of these systems has a spin density wave.

[10] L. Pauling, *The Nature of the Chemical Bond* (3rd edition, Cornell University Press, Ithaca, New York, 1960); L. Pauling, *Proc. Roy. Soc. (London)* A **196**, 343 (1949).

[11] M. D. Morse, *Chem. Rev.* **86**, 1049 (1986).

[12] M. M. Kappes, M. Schär and E. Schumacher, *J. Phys. Chem.* **89**, 1499 (1985).

[13] R. Hultgren, P. D. Desai, D. T. Hawkins, M. Gleiser, K. K. Kelley and D. D. Wagman, *Selected Values of the Thermodynamic Properties of the Elements* (American Society for Metals, Metals Park, Ohio, 1973).

[14] M. H. McAdon and W. A. Goddard III, *J. Phys. Chem.* **91**, 2607 (1987); M. H. McAdon and W. A. Goddard III, *J. Non-Cryst. Solids* **75**, 149 (1985); M.

H. McAdon and W. A. Goddard III, *Phys. Rev. Lett.* **55**, 2563 (1985).

[15] D. E. Powers, S. G. Hansen, M. E. Geusic, D. L. Michalopoulos, and R. E. Smalley, *J. Chem. Phys.* **78**, 2866 (1983).

[16] J. B. Hopkins, P. R. R. Langridge-Smith, M. D. Morse, and R. E. Smalley, unpublished results.

[17] R. A. Bernheim, L. P. Gold, and T. Tipton, *J. Chem. Phys.* **78**, 3635 (1983).

[18] S. Martin, J. Chevaleyre, M. Bordas, S. Valignat, M. Broyer, B. Cabaud, and A. Hoareau, *J. Chem. Phys.* **79**, 4132 (1983); N. W. Carlson, A. J. Taylor, and A. L. Schawlow, *Phys. Rev. Lett.* **45**, 18 (1980).

[19] P. J. Hay and W. R. Wadt, *J. Chem. Phys.* **82**, 270 (1985).

[20] L. G. Yaffe, LTRAN program, unpublished; see L. G. Yaffe and W. A. Goddard III, *Phys. Rev. A.* **13**, 1682 (1976). Also see W. J. Hunt, T. H. Dunning, Jr., and W. A. Goddard III, *Chem. Phys. Lett.* **3**, 606 (1969).

[21] W. A. Goddard III, *Int. J. Quantum Chem.* **IIIS**, 593 (1970); W. A. Goddard III and R. C. Ladner, *J. Chem. Phys.* **51**, 1073 (1969).

[22] For brevity, the electronic coordinates are omitted; by convention the electronic coordinates are sequential (and independent of the orbital subscripts), e.g., $\varphi_3\varphi_1\varphi_4\cdots \equiv \varphi_3(1)\varphi_1(2)\varphi_4(3)\cdots$ and $\alpha\beta\alpha\cdots \equiv \alpha(1)\beta(2)\alpha(3)\cdots$.

[23] W. J. Hunt, P. J. Hay, and W. A. Goddard III, *J. Chem. Phys.* **57**, 738 (1972).

[24] M. H. McAdon and W. A. Goddard III, unpublished.

[25] J. Donohue, *The Structure of the Elements* (Wiley, New York, 1974).

[26] Eight-atom ring clusters are more appropriate than six-atom or ten-atom clusters, since only M_N clusters where N is divisible by four have the degenerate one-electron states at $k_F = \pm\pi/2a$ that are split by the Peierls distortion ($k = \pm\pi/2a$ are not allowed states for M_N clusters with $N = 4i + 2$).[7] Hence, with respect to the Peierls instability, $N = 4i$ ring clusters are expected to be better models of the one-dimensional metal than $N = 4i + 2$ ring clusters, although the distinction between $N = 4i$ and $N = 4i + 2$ is expected to vanish in the limit as N approaches infinity. Since the valence electronic structures of the Cu_{10}, Ag_6, Ag_8, Ag_{10}, Au_{10}, Li_6, Li_{10}, Li_{14}, and Na_{10} ring clusters are similar, Ag_8 is suitable for testing for Peierls instability.

[27] C. E. Moore, *Atomic Energy Levels* (Nat. Stand. Rev. Data Ser., Nat. Bur. Stand. (U.S.), 1971).

[28] For each M_N symmetric ring cluster, the GVB-CI(SCF) natural orbitals are real Bloch functions $\{\psi_m\}$, forming irreducible representations of the point-symmetry group D_{Nh}. We follow the Mulliken convention [R. S. Mulliken, *J. Chem. Phys.* **23**, 1997 (1955)] for labeling the irreducible representations of the point-symmetry groups D_{Nh}, given for even N as follows. (*i*) a and b signify nondegenerate representations and label the symmetry with respect to the eight-fold (C_8) rotational symmetry axis [a for symmetric ($m = 0$) and b for antisymmetric ($m = N/2$)]. For nondegenerate representations, the numeric subscripts label the symmetry with respect to a set of C_2 rotation symmetry axes perpendicular to the C_N symmetry axis (1 for symmetric and 2 for antisymmetric; for M_N symmetric rings, the set of C_2 axes passing through opposite atoms of the ring are chosen). (*ii*) e signifies doubly-degenerate rep-

resentations with numeric subscripts equal to m. (*iii*) Subscripts g and u label the symmetry with respect to inversion [gerade (g, symmetric) and ungerade (u, antisymmetric)]. (*iv*) Lowercase labels (a, b and e) signify symmetries of one-electron orbitals. (*v*) Uppercase labels (A, B, and E) signify symmetries of many-electron state, where the numerical superscript preceding the label is equal to the $2S + 1$ spin degeneracy.

[29] For M_N symmetric ring clusters with $N = 4i$, the bond-centered and atom-centered states are $^1B_{1g}$ and $^1B_{2g}$, respectively. The $^1B_{2g}$ state cannot be described with singly-occupied orbitals centered at the bond midpoints. Likewise, the $^1B_{1g}$ state cannot be described with singly-occupied orbitals centered at the atoms. This is a property unique to M_N with $N = 4i$, since for the M_N symmetric ring clusters with $N = 4i + 2$, the bond-centered and atom-centered states are both $^1A_{1g}$.

[30] H. Jones, *Proc. Phys. Soc. (London)*, A49, 250 (1937); N. F. Mott and H. Jones, *Properties of Metals and Alloys* (Oxford Univ. Press, London, 1936); H. Jones, *The Theory of Brillouin Zones and Electronic States in Crystals* (North-Holland, Amsterdam, 1960).

[31] W. Hume-Rothery and G. V. Raynor, *The Structure of Metals and Alloys, 4th Ed.* (Institute of Metals, London, 1962).

[32] C. Barrett and T. B. Massalski, *Structure of Metals, Crystallographic Methods, Principles and Data, 3rd (revised) Ed.* (Pergamon Press, New York, 1980).

[33] To avoid confusion, we refer to canonical (natural) orbitals as $\{\varphi_i\}$, Bloch orbitals as $\{\psi_m\}$, localized non-orthogonal orbitals as $\{\phi_i\}$, and localized or-

thogonal orbitals as $\{\omega_i\}$ unless otherwise noted.

[34] F. W. Bobrowicz and W. A. Goddard III, in: "Modern Theoretical Chemistry: Methods of Electronic Structure Theory", edited by H. F. Schaefer III (Plenum, New York, 1977) Vol. III, Chap. 4.

[35] The UHF wavefunction can be spin-projected, leading to a wavefunction that is an eigenfunction of $\hat{S}^2$ (and eliminating the spin density wave). However, this leads to a particular spin eigenfunction which is not optimal for these M_N ring clusters. Optimizing the spin function leads to the full GVB wavefunction which is also an eigenfunction of $\hat{S}^2$.

[36] R. A. Bair, W. A. Goddard III, A. F. Voter, A. K. Rappé, L. G. Yaffe, F. W. Bobrowicz, W. R. Wadt, P. J. Hay and W. J. Hunt, GVB2P5 program, unpublished; see R. A. Bair, Ph. D. Thesis, California Institute of Technology, 1980 and Ref. [34].

[37] C. Edmiston and K. Ruedenberg, *Rev. Mod. Phys.* **35**, 457 (1963).

[38] CI3 program, unpublished; see F. W. Bobrowicz, Ph. D. Thesis, California Institute of Technology, 1974.

[39] GVB3P1 program; see L. G. Yaffe and W. A. Goddard III, *Phys. Rev. A.* **13**, 1682 (1976) and M. M. Goodgame, Ph. D. Thesis, California Institute of Technology, 1984.

[40] P. J. Hay, T. H. Dunning, Jr., and W. A. Goddard III, *J. Chem. Phys.* **62**, 3912 (1975).

[41] R. Orbach, Phys. Rev. **115**, 1181 (1958); L. F. Mattheiss, Phys. Rev. **123**, 1209 (1961); J. des Cloizeaux and J. J. Pearson, Phys. Rev. **128**, 2131 (1962); A. A. Ovchinnikov, Sov. Phys. JETP **29**, 727 (1969).

[42] S. R. Langhoff, C. W. Bauschlicher, Jr., S. P. Walch, and B. C. Laskowski, *J. Chem. Phys.* **85**, 7211 (1986); S. P. Walch, C. W. Bauschlicher, Jr. and S. R. Langhoff, *J. Chem. Phys.* **85**, 5900 (1986).

[43] D. D. Konowalow and M. L. Olson, *J. Chem. Phys.* **71**, 450 (1979); D. D. Konowalow, M. E. Rosenkrantz and M. L. Olson, *J. Chem. Phys.* **72**, 2612 (1980).

[44] E. A. Carter and W. A. Goddard III, unpublished.

[45] D. D. Konowalow and M. E. Rosenkrantz, *Chem. Phys. Lett.* **61**, 489 (1979).

Table 1. Cohesive energies for Cu, Ag, Au, Li and Na.

	Molecules		Bulk Solid	
system	M_2 [a] (eV/atom)	M_2^+ [b] (eV)	atomization [c] (eV/atom)	dimerization [d] (eV/atom)
Cu	1.02	1.87	3.49	2.47
Ag	0.84	1.69	2.94	2.11
Au	1.16	-	3.82	2.66
Li	0.53	1.30	1.64	1.11
Na	0.37	0.99	1.11	0.74

a) $1/2\ M_2 \rightarrow M$, References [11,12].
b) $M_2^+ \rightarrow M + M^+$, References [11,15,16,17,18]. See Table 8 for further details.
c) $M_{(s)} \rightarrow M_{(g)}$, Reference [13].
d) $M_{(s)} \rightarrow 1/2\ M_2$, e.g., cohesion with respect to M_2, References [11,12,13].

Table 2. Cohesive energies for low-spin ring clusters.[a)]

system	a (Å)	atomization energy[b)] (meV/atom) GVB–PP	GVB	dimerization energy[c)] (meV/atom) GVB–PP	GVB
Ag_6	2.889	401.7	480.3	60.5	139.1
Ag_8	2.889	391.0	458.9	49.8	117.7
Ag_{10}	2.889	406.8	479.0	65.6	137.7
Li_6	3.014	366.4	419.8	158.1	211.5
Li_{10}	3.014	402.1	447.6	193.8	239.3
Li_{14}	3.014	413.1		204.8	
Cu_{10}	2.556	425.4	509.1	38.1	121.8
Ag_{10}	2.889	406.8	479.0	65.6	137.7
Au_{10}	2.884	538.2	623.6	10.0	95.5
Li_{10}	3.014	402.1	447.6	193.8	239.3
Na_{10}	3.659	191.2	236.8	45.5	91.1

a) Results calculated for the lowest energy low-spin states (Section II). The frozen core approximation was used for the eight and ten-atom ring clusters.
b) The total atomization energy $M_N \rightarrow N\,M$ divided by N atoms.
c) The total cohesive energy with respect to diatomic molecules (at equilibrium), $M_N \rightarrow N/2\,M_2$, divided by N atoms.

Table 3. Details of GVB–PP and GVB–CI(SCF) wavefunctions for low-spin symmetric ring clusters.

system	a (Å)	dimerization energy (meV/atom)	nearest-neighbor overlap [a)]	ΔE (meV/atom)
		—— GVB–PP bond-centered state ——		
Ag_6	2.889	60.5	0.596	
Ag_8	2.889	49.8	0.542	
Ag_{10}	2.889	65.6	0.546	
Li_6	3.014	158.1	0.386	
Li_{10}	3.014	193.8	0.357	
Li_{14}	3.014	204.8	0.349	
Cu_{10}	2.556	38.1	0.597	
Ag_{10}	2.889	65.6	0.546	
Au_{10}	2.884	10.0	0.613	
Li_{10}	3.014	193.8	0.357	
Na_{10}	3.659	45.5	0.435	
		—— GVB–PP atom-centered state ——		
Ag_6	2.889	−15.5	0.714	76.0
Ag_8	2.889	−76.1	0.657	125.9
Ag_{10}	2.889	−53.4	0.684	119.0
Li_6	3.014	−65.2	0.683	223.3
Li_{10}	3.014	−93.2	0.651	287.0
Li_{14}	3.014	−97.1	0.644	301.9
Cu_{10}	2.556	−62.0	0.720	100.1
Ag_{10}	2.889	−53.4	0.684	119.0
Au_{10}	2.884	−37.9	0.668	47.9
Li_{10}	3.014	−93.2	0.651	287.0
Na_{10}	3.659	−73.1	0.558	118.6

Table 3. Details of GVB–PP and GVB–CI(SCF) wavefunctions for low-spin symmetric ring clusters, continued.

system	a (Å)	dimerization energy (meV/atom)	nearest-neighbor overlap [a]	ΔE (meV/atom)
		—— GVB–CI(SCF) bond-centered state ——		
Ag_6	2.889	139.1	0.818	
Ag_8	2.889	117.7	0.623	
Ag_{10}	2.889	137.7	0.548	
Li_6	3.014	211.5	0.536	
Li_{10}	3.014	239.3	0.282	
Cu_{10}	2.556	121.8	0.632	
Ag_{10}	2.889	137.7	0.548	
Au_{10}	2.884	95.5	0.593	
Li_{10}	3.014	239.3	0.282	
Na_{10}	3.659	91.1	0.382	
		—— GVB–CI(SCF) atom-centered state ——		
Ag_8	2.889	−12.7	0.755	130.4

a) For GVB–PP, the bond pair overlap is listed; each orbital overlaps one adjacent orbital (forming a bond pair) and is orthogonal to the other adjacent orbital.
b) For GVB–CI(SCF), each orbital has equal overlaps with both adjacent orbitals (see Table 6 for further details).

Table 4. Details of the full (untruncated) GVB–CI wavefunction.[a)]

N	S	A	n_f[b)]	n_{SC}	n_{SEF}	n_{DET}
2	0	1	1	3	3	4
2	1	2	1	1	1	1
4	0	2	2	19	20	36
4	1	3	3	13	15	16
4	2	4	1	1	1	1
6	0	3	5	141	175	400
6	1	4	9	121	189	225
6	2	5	5	31	35	36
6	3	6	1	1	1	1
8	0	4	14	1 107	1 764	4 900
8	1	5	28	1 037	2 352	3 136
8	2	6	20	477	720	784
8	3	7	7	57	63	64
8	4	8	1	1	1	1
10	0	5	42	8 953	19 404	63 504
10	1	6	90	8 701	29 700	44 100
10	2	7	75	5 551	12 375	14 400
10	3	8	35	1 351	1 925	2 025
10	4	9	9	91	99	100
10	5	10	1	1	1	1
12	0	6	132	73 789	226 512	853 776
12	1	7	297	72 865	382 239	627 264
12	2	8	275	56 233	196 625	245 025
12	3	9	154	21 583	44 044	48 400
12	4	10	54	3 103	4 212	4 356
12	5	11	11	133	143	144
12	6	12	1	1	1	1

a) Total numbers of spacial configurations (n_{SC}), spin eigenfunctions (n_{SEF}), and determinants (n_{DET}) for the GVB–CI wavefunction without symmetry restrictions.
b) Total number of spin eigenfunctions for the configuration having each orbital singly-occupied.

Table 5. Nearest-neighbor overlaps. [a)]

system	a (Å)	low-spin UHF	low-spin GVB–PP	low-spin GVB–CI(SCF)	high-spin GVB–CI(SCF)
Cu_3^+	2.556	0.429	0.389	0.517	0.654
Ag_3^+	2.889	0.367	0.344	0.428	0.544
Au_3^+	2.884	0.373	0.350	0.452	0.568
Li_3^+	3.014	0.224	0.222	0.181	0.227
Na_3^+	3.659	0.260	0.256	0.268	0.356
Ag_8 [f)]	2.889	0.692	0.657	0.755	0.755
Ag_6	2.889	0.658	0.596	0.818	0.862
Ag_8	2.889	0.562	0.542	0.623	0.680
Ag_{10}	2.889	0.535	0.546	0.548	0.609
Li_6	3.014	0.416	0.386	0.536	0.728
Li_{10}	3.014	0.341	0.357	0.282	0.369
Li_{14}	3.014	0.326	0.349		0.284
Cu_{10}	2.556	0.601	0.597	0.632	0.682
Ag_{10}	2.889	0.535	0.546	0.548	0.609
Au_{10}	2.884	0.589	0.613	0.593	0.631
Li_{10}	3.014	0.341	0.357	0.282	0.369
Na_{10}	3.659	0.408	0.435	0.382	0.477

a) Results are for the bond-centered state except where otherwise noted. See Table 6 for further details.
b) For UHF, the overlap is for adjacent Hartree-localized orbitals (obtained by separate localizations of the up-spin and down-spin orbitals).
c) For GVB–PP the bond pair overlap is listed.
d) For GVB–CI(SCF) the overlap is for adjacent Hartree-localized orbitals.
e) For the high-spin state ($S = N/2$, one unpaired electron per atom) HF, UHF, and GVB-CI(SCF) are identical.
f) Results for the atom-centered state.

Table 6. Hartree-localized orbital overlap integrals. [a]

system	a (Å)	S_{12}	S_{13}/S_{12}	S_{14}/S_{13}	S_{15}/S_{14}	S_{16}/S_{15} [b]
low-spin, UHF [c]						
Ag_8 [d]	2.889	0.692	0.478	0.439	0.668	
Ag_6	2.889	0.658	0.655	0.737		
Ag_8	2.889	0.562	0.391	0.356	0.655	
Ag_{10}	2.889	0.535	0.303	0.224	0.376	0.795
Li_6	3.014	0.416	0.564	0.611		
Li_{10}	3.014	0.341	0.199	0.165	0.362	0.625
Li_{14}	3.014	0.326	0.124	0.026	0.717	0.684
Cu_{10}	2.556	0.601	0.375	0.282	0.394	0.791
Ag_{10}	2.889	0.535	0.303	0.224	0.376	0.795
Au_{10}	2.884	0.589	0.300	0.183	0.253	1.062
Li_{10}	3.014	0.341	0.199	0.165	0.362	0.625
Na_{10}	3.659	0.408	0.179	0.107	0.157	1.057
low-spin, GVB–CI(SCF)						
Ag_8 [d]	2.889	0.755	0.499	0.455	0.668	
Ag_6	2.889	0.818	0.708	0.855		
Ag_8	2.889	0.623	0.397	0.403	0.619	
Ag_{10}	2.889	0.548	0.301	0.307	0.294	0.341
Li_6	3.014	0.536	0.547	0.813	0.000	0.000
Li_{10}	3.014	0.282	0.204	0.293	0.214	0.356
Cu_{10}	2.556	0.632	0.376	0.351	0.334	0.436
Ag_{10}	2.889	0.548	0.301	0.307	0.294	0.341
Au_{10}	2.884	0.593	0.298	0.257	0.193	−0.110
Li_{10}	3.014	0.282	0.204	0.293	0.214	0.356
Na_{10}	3.659	0.382	0.177	0.223	0.082	−1.476

Table 6. Hartree-localized orbital overlap integrals, continued. [a]

system	a (Å)	$\mathcal{S}_{12}$	$\mathcal{S}_{13}/\mathcal{S}_{12}$	$\mathcal{S}_{14}/\mathcal{S}_{13}$	$\mathcal{S}_{15}/\mathcal{S}_{14}$	$\mathcal{S}_{16}/\mathcal{S}_{15}$ [b]
high-spin, [e] GVB–CI(SCF)						
Ag_8 [d]	2.889	0.755	0.474	0.403	0.608	
Ag_8	2.889	0.862	0.742	0.856		
Ag_8	2.889	0.680	0.413	0.366	0.584	
Ag_{10}	2.889	0.609	0.316	0.235	0.209	0.329
Li_6	3.014	0.728	0.625	0.803	0.000	0.329
Li_{10}	3.014	0.369	0.216	0.189	0.262	0.534
Li_{14}	3.014	0.284	0.136	0.084	0.189	0.410
Cu_{10}	2.556	0.682	0.390	0.290	0.265	0.447
Ag_{10}	2.889	0.609	0.316	0.235	0.209	0.329
Au_{10}	2.884	0.631	0.308	0.198	0.042	−2.932
Li_{10}	3.014	0.369	0.216	0.189	0.262	0.534
Na_{10}	3.659	0.477	0.200	0.149	0.171	0.393

a) Results are for the bond-centered state except where otherwise noted.
b) For the M_{10} rings, the ratios $\mathcal{S}_{16}/\mathcal{S}_{15}$ vary somewhat haphazardly due to the small values of $\mathcal{S}_{16}$ and $\mathcal{S}_{15}$ [in each case $|\mathcal{S}_{15}| \leq 0.026$ and $|\mathcal{S}_{16}| \leq 0.020$].
c) UHF Hartree orbitals obtained by separate localizations of the up-spin and down-spin orbitals.
d) Results for the atom-centered state.
e) For the high-spin state ($S = N/2$, one unpaired electron per atom) the HF, UHF and GVB–CI(SCF) wavefunctions are identical.

Table 7. Comparison of calculated and experimental results for M_2 clusters.[a)]

	UHF			GVB			better theory[b)]			experiment[c)]		
system	R_e (Å)	D_e (eV)	k_e (eV/Å^2)	R_e (Å)	D_e (eV)	k_e (eV/Å^2)	R_e (Å)	D_e (eV)	k_e (eV/Å^2)	R_e (Å)	D_e (eV)	k_e (eV/Å^2)
Cu_2	2.48	0.47	3.03	2.51	0.77	3.00	2.25	1.97	7.64	2.220	2.04	8.10
Ag_2	2.78	0.40	2.56	2.80	0.68	2.83	2.59	1.48	6.29	2.47	1.67	7.34
Au_2	2.67	0.75	10.23	2.72	1.06	7.56	2.53	1.97	11.60	2.472	2.31	13.21
Li_2	2.99	0.19	0.61	2.98	0.42	0.88	2.692	1.029	1.55	2.673	1.057	1.59
Na_2	3.62	0.08	0.23	3.41	0.29	0.56	3.174	0.710	0.98	3.079	0.742	1.07

a) R_e is the equilibrium internuclear separation, D_e is the dissociation energy, k_e is the harmonic force constant.
b) Calculations which include many-body effects (electron correlation). Results for the noble metal dimers are taken from Reference [42] and results for the alkali metal dimers are taken from Reference [43].
c) The experimental results are taken from Reference [11] for the noble metal dimers and from Reference [12] for the alkali metal dimers. R_e has not been measured for Ag_2; the listed value of 2.47 Å is the value recommended in Reference [11].
d) The UHF and HF total energies for Au_2 are equal for interatomic separations $R \leq 2.70$ Å.

Table 8. Comparison of calculated and experimental results for M_2^+ clusters.[a)]

	GVB [b)]			experiment [c,d)]		
system	R_e (Å)	D_e (eV)	k_e (eV/Å^2)	R_e (Å)	D_e (eV)	k_e (eV/Å^2)
Cu_2^+	2.75	1.27	1.50		1.87 (10)	
Ag_2^+	2.99	1.22	1.63		1.69 (05)	
Au_2^+	2.85	1.44	4.39			
Li_2^+	3.18	1.225	0.901	3.11 (1)	1.298	0.887 (10)
Na_2^+	3.67	0.926	0.620	3.60 (3)	0.984	0.617 (05)

a) R_e is the equilibrium internuclear separation, D_e is the dissociation energy ($M_2^+ \rightarrow M + M^+$), k_e is the harmonic force constant.

b) Since these systems contain one valence electron, the HF (and also the UHF) results are identical.

c) D_e Values for Cu_2^+ and Ag_2^+ are based on the equation $D_e(M_2^+) = D_e(M_2) + IP(M) - IP(M_2)$ where D_e is the dissociation energy and IP is the ionization potential. We use $D_e(Cu_2) = 2.04 \pm .08$ eV and $D_e(Ag_2) = 1.67 \pm .03$ eV from Reference [11], $IP(Cu_2) = 7.894 \pm .015$ eV and $IP(Ag_2) = 7.56 \pm .02$ eV from References [11,15,16] and $IP(Cu) = 7.726$ eV and $IP(Ag) = 7.576$ eV from Reference [27]. $IP(Ag_2) = 7.56 \pm 0.02$ eV (based on an unpublished multiphoton experiment [11,16]), leads to $IP(Ag) - IP(Ag_2) = 0.016 \pm 0.020$ eV, in reasonably good agreement with unpublished theoretical results, $IP(Ag) - IP(Ag_2) = 0.09$ eV [44].

d) Values for Li_2^+ and Na_2^+ are from References [17,18].

Table 9. Calculated results for the Li_8 symmetric ring cluster.[a,b]

wavefunction	spin state	a_e (Å)	k_e (meV/atom·Å^2)	cohesive energies: atomization [c] (meV/atom)	cohesive energies: dimerization [d] (meV/atom)
atom-centered states					
GVB	$S = 4$			(no cohesion)	
GVB-PP	$S = 0$	3.317	375.8	124.9	−83.4
bond-centered states					
GVB	$S = 4$	3.249	734.7	246.1	37.8
UHF	$M_S = 0$	3.126	811.9	391.7	299.0
GVB–PP	$S = 0$	3.120	815.2	394.4	186.1
GVB–CI(SCF)	$S = 0$	3.097	840.2	439.6	231.3

a) a_e is the equilibrium lattice constant, k_e is the harmonic force constant.
b) For the $S = 4$ (valence electron high-spin) states, the HF, UHF, GVB–PP and GVB–CI(SCF) results are identical.
c) The total atomization energy $Li_8 \rightarrow 8$ Li divided by 8 atoms.
d) The total cohesive energy with respect to diatomic molecules (at equilibrium), $Li_8 \rightarrow 4\ Li_2$, divided by 8 atoms.

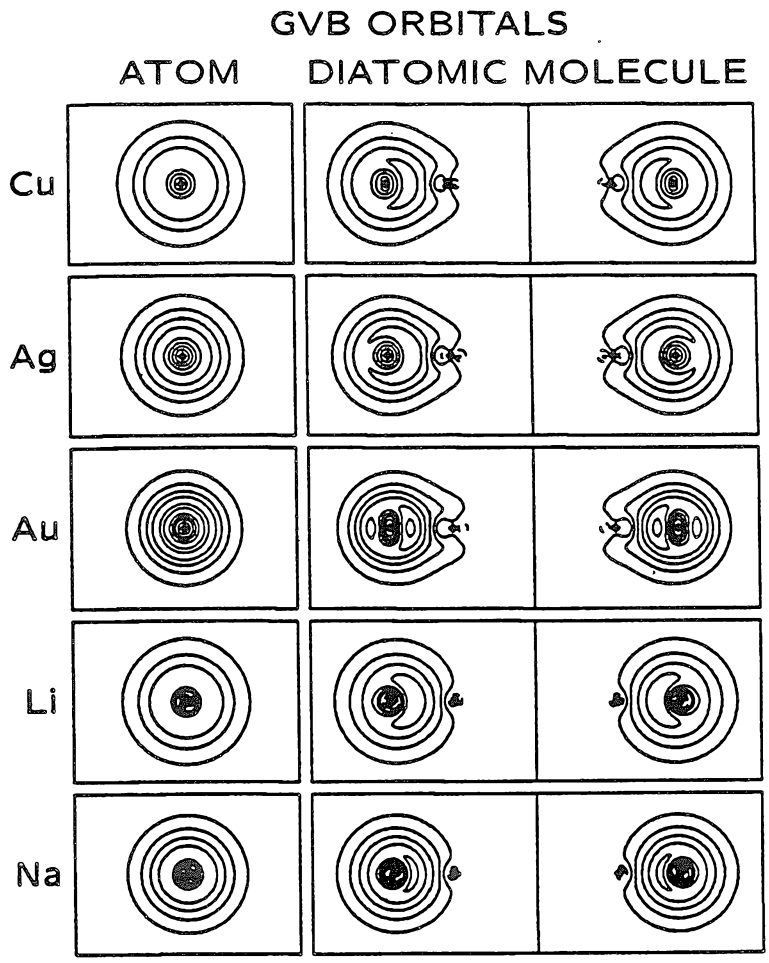

Figure 1. The optimum GVB valence orbitals for the Cu, Ag, Au, Li, and Na atoms (one orbital each) and homonuclear diatomic molecules (two orbitals each). Each orbital contains one electron. For Cu_2, Ag_2, Au_2, Li_2, and Na_2, the bond pair overlaps are 0.621, 0.596, 0.600, 0.593, and 0.496, respectively. For this figure and for all following figures showing orbital amplitude contours, the nearest-neighbor distance (a) is equal to that of the bulk metal (a = 2.556, 2.889, 2.884, 3.014, and 3.659 Å for Cu, Ag, Au, Li, and Na, respectively), and the boxes are scaled to a (for Figures 1-3, box width = 3.6 a). Squares mark the atomic positions. Contours mark even amplitude increments of $0.2a^{-3/2}$ unless noted otherwise. Solid and dashed contours denote positive and negative amplitudes, respectively.

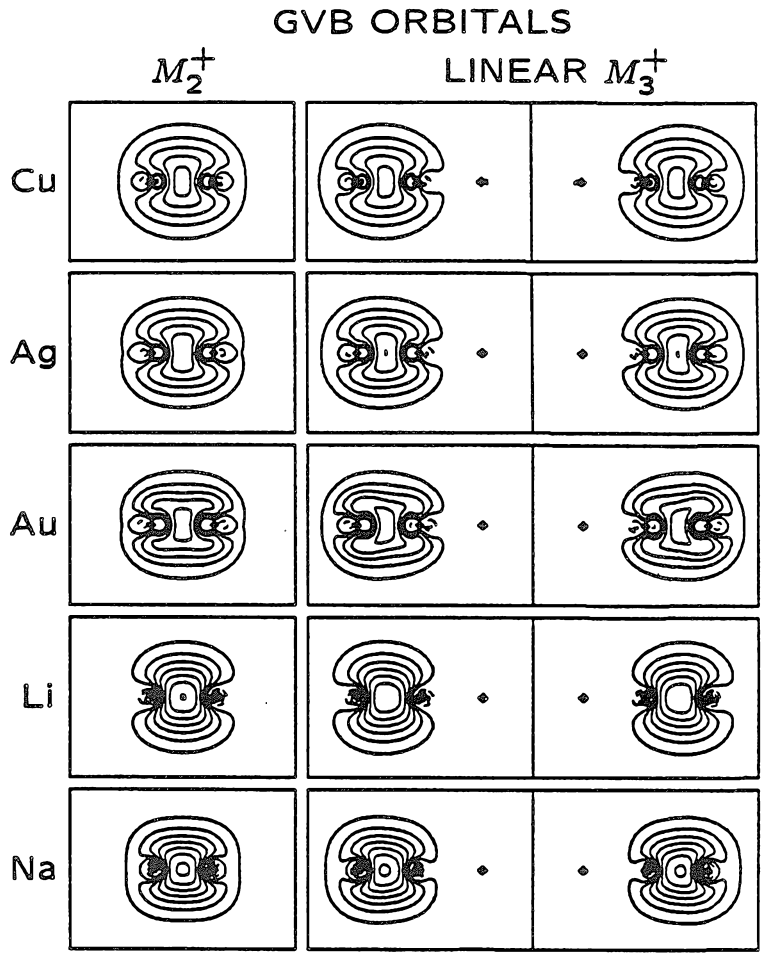

Figure 2. The optimum GVB valence orbitals for M_2^+ (one orbital each) and linear M_3^+ (two orbitals each), M = Cu, Ag, Au, Li, and Na. Each orbital contains one electron. For Cu_3^+, Ag_3^+, Au_3^+, Li_3^+, and Na_3^+, the bond pair overlaps are 0.389, 0.344, 0.350, 0.222, and 0.256, respectively. The GVB and UHF orbitals for the M_2^+ clusters are identical, since there is only one valence electron. For each of the linear M_3^+ clusters, the UHF orbitals are very similar to the GVB orbitals (the UHF spatial orbital overlaps for Cu_3^+, Ag_3^+, Au_3^+, Li_3^+, and Na_3^+ are 0.429, 0.367, 0.373, 0.224, and 0.260, respectively). However, UHF results in net spin densities for low-spin M_3^+, whereas GVB does not.

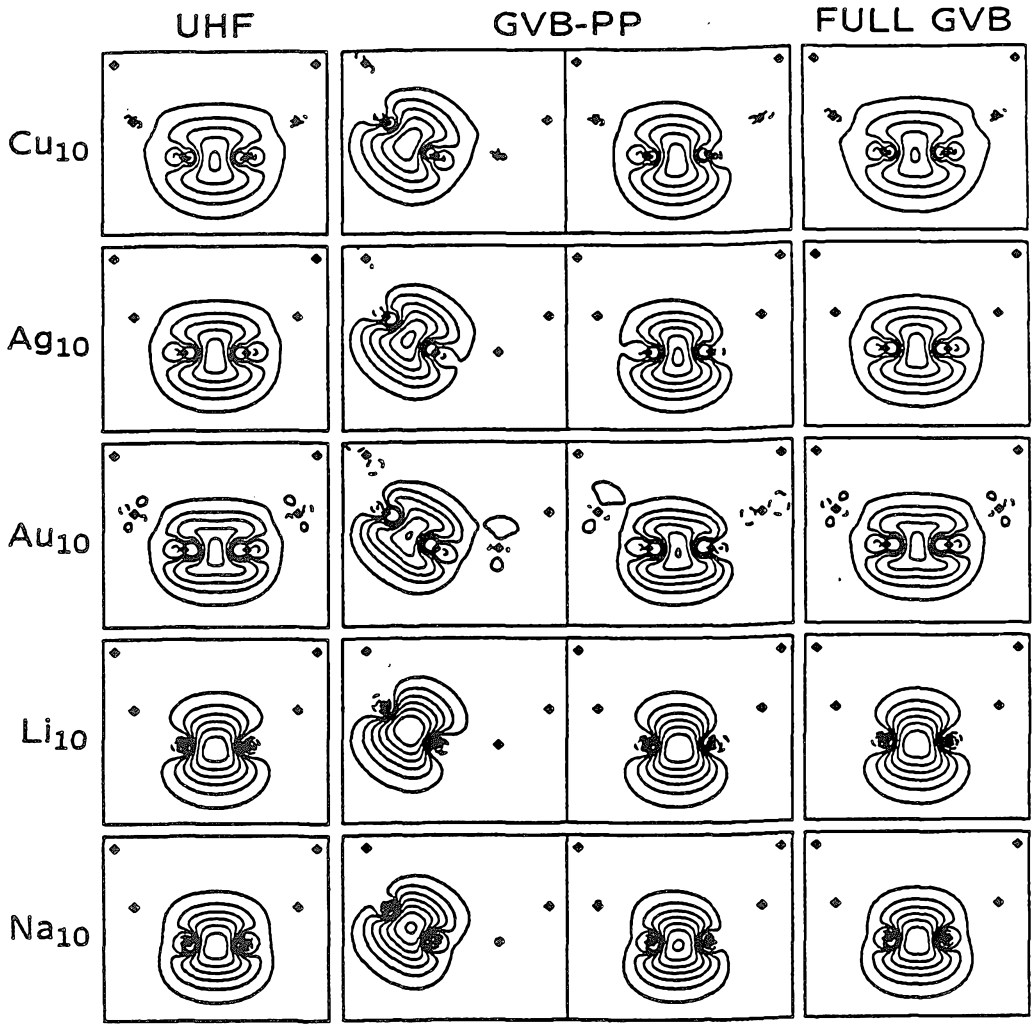

Figure 3. Valence orbitals for each of the Cu_{10}, Ag_{10}, Au_{10}, Li_{10}, and Na_{10} ring clusters (each orbital contains one electron; overlaps are given in Tables 3 and 5). Localized orbitals are shown for UHF (see Appendix B.3), GVB–PP (the two orbitals of a bond pair are shown), and full GVB (see Appendix B.2).

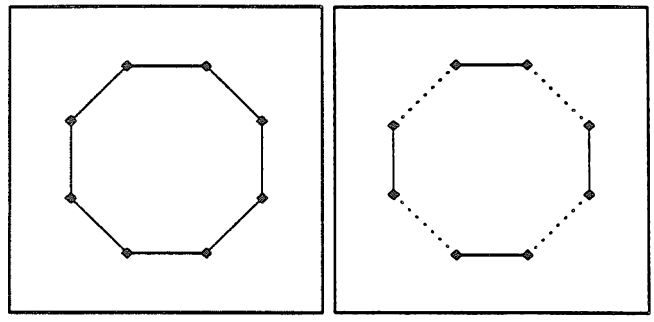

Figure 4. (a) The M_8 symmetric ring cluster as a model of the undistorted one-dimensional metal. (b) The M_8 distorted ring cluster (composed of alternating long and short bonds) as a model of the Peierls distorted one-dimensional metal.

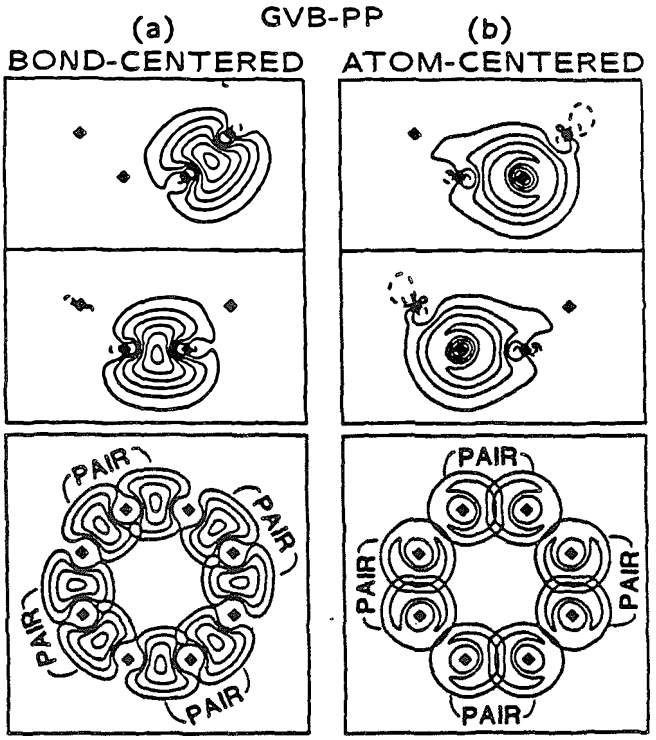

Figure 5. The GVB–PP (optimum) valence orbitals for (a) the bond-centered state of Ag_8, 0.542 overlap each bond pair, and (b) the atom-centered state of Ag_8, 0.657 overlap each bond pair. In each case, the superposition of all eight orbitals is shown at the bottom excluding contours $< 0.6a^{-3/2}$ for clarity. All orbitals are singly-occupied and spin-coupled into bond pairs as indicated. In each case, the four bond pairs are related by four-fold rotations about the eight-fold symmetry axis, leading to a charge density wave having D_{4h} symmetry.

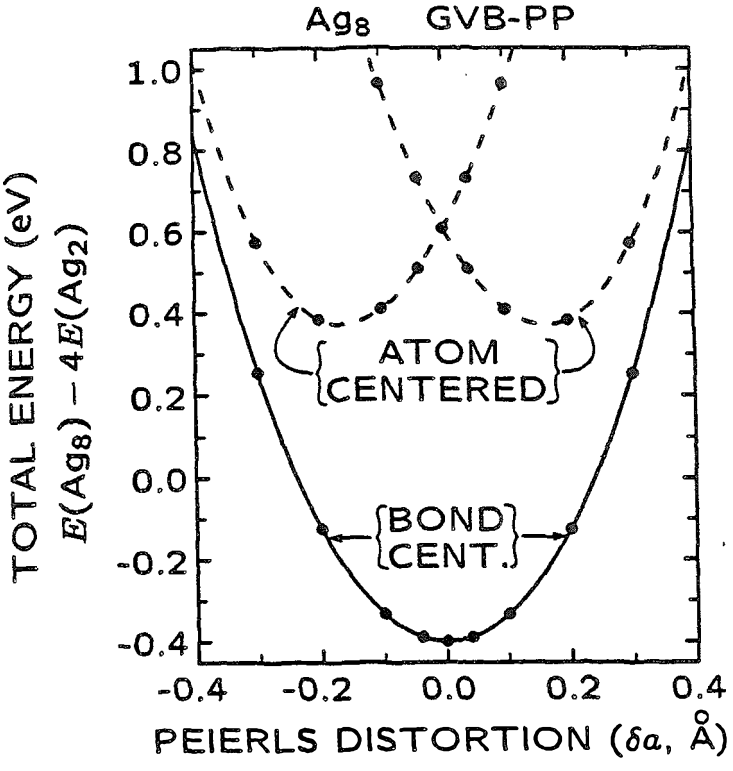

Figure 6. The total energy of low-spin Ag_8 as a function of the Peierls distortion (δa) calculated at the GVB–PP level. The solid curve depicts the bond-centered state (Figure 5a) and the dashed curves depict the atom-centered state (Figure 5b).

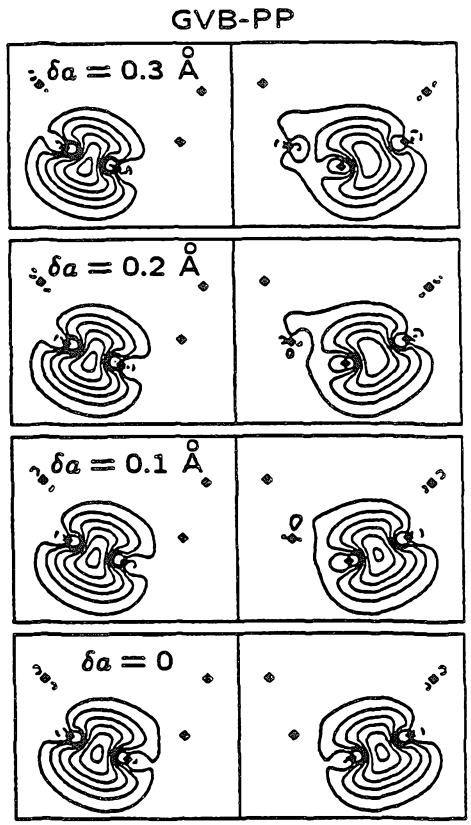

Figure 7. The GVB–PP valence orbitals for the Ag_8 bond-centered (ground) state as a function of the Peierls distortion (δa). All orbitals are singly-occupied and spin-coupled into bond pairs. In each case a single bond pair is shown (the other pairs are obtained by successive four-fold rotations). Bond pair overlaps are 0.542, 0.547, 0.562 and 0.589 for δ = 0.00, 0.10, 0.20 and 0.30 Å, respectively. The many-electron wavefunction symmetry for $\delta a \neq 0$ is C_{4h}.

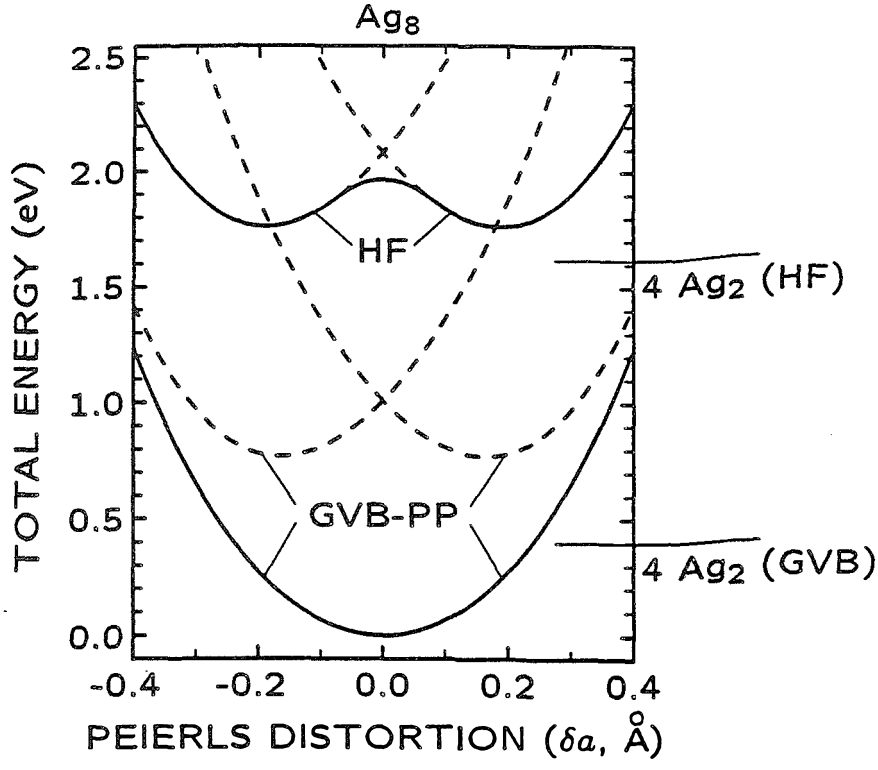

Figure 8. The total energy of low-spin Ag_8 as a function of the Peierls distortion (δa) calculated at the HF and GVB–PP levels. The results calculated without orbital symmetry restrictions are indicated by the solid curve (leading to charge density wave maxima centered at the atoms for all δa). The results calculated with D_{4h} orbital symmetry restrictions are indicated by the dashed curves (leading to charge density wave maxima centered at the bond midpoints for $\delta a = 0$).

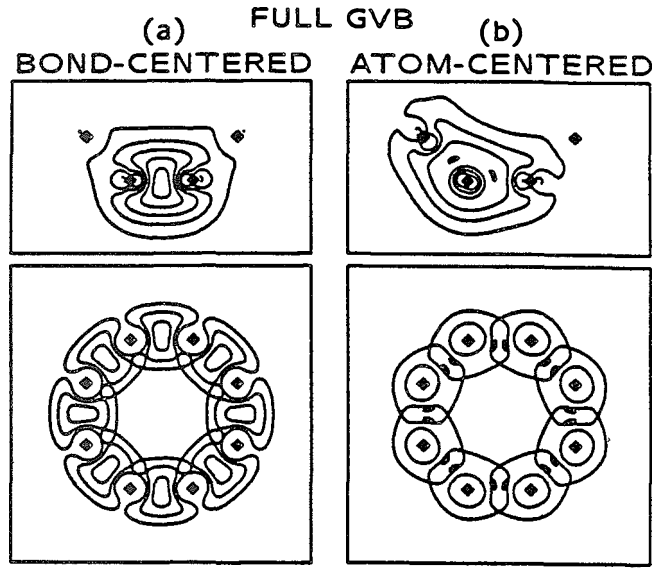

Figure 9. The GVB valence orbitals for (a) the bond-centered state of Ag_8 (ground state, $^1B_{1g}$) and (b) the atom-centered state of Ag_8 (excited state, $^1B_{2g}$). In each case, the superposition of all eight orbitals is shown at the bottom excluding contours $< 0.6a^{-3/2}$ for clarity. All orbitals are singly-occupied.

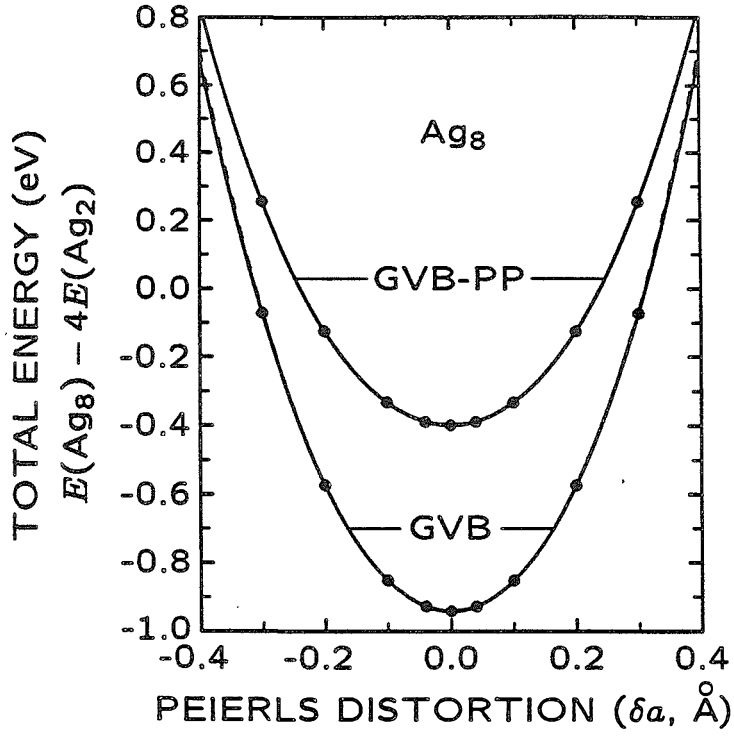

Figure 10. The total energy of the Ag_8 ground electronic state as a function of the Peierls distortion (δa) calculated at the GVB–PP and full GVB levels (solid curves). The GVB–CI(SCF) energy calculated with D_{4h} orbital symmetry restrictions (dashed curve, almost obscured by the solid curve) is equal to that calculated with no orbital symmetry restrictions (C_s, solid curve) for $|\delta a| \leq 0.20$ Å. For $|\delta a| = 0.30$ Å the D_{4h} energy is higher than the C_s energy by 0.0049 eV (0.61 meV/atom).

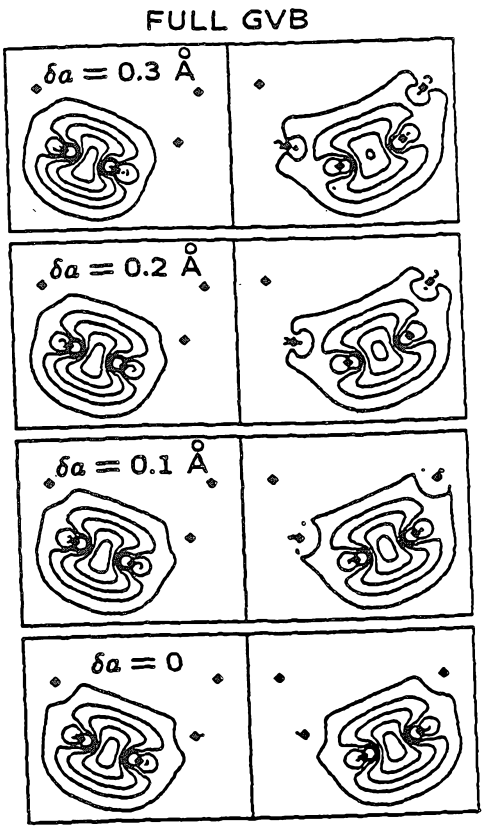

Figure 11. The GVB valence orbitals for the Ag_8 bond-centered (ground) state as a function of the Peierls distortion (δa). All orbitals are singly-occupied. In each case, two orbitals are shown (the other orbitals are obtained by successive four-fold rotations). For $|\delta a| \leq 0.20$ Å the optimum GVB orbitals lead to a fully symmetrical charge density (D_{8h} for $\delta a = 0$ and D_{4h} for $|\delta a| \leq 0.20$ Å). The adjacent-orbital overlaps are 0.623, 0.625, and 0.631 for $\delta a = 0.00$, 0.10, and 0.20 Å, respectively. For $|\delta a| = 0.30$ Å the optimum GVB orbitals are slightly skewed, leading to a C_{4h} symmetry charge density wave having very small amplitude. For $|\delta a| = 0.30$ Å, the adjacent-orbital overlaps alternate between 0.637 and 0.644 (the overlap of the orbitals shown is 0.637).

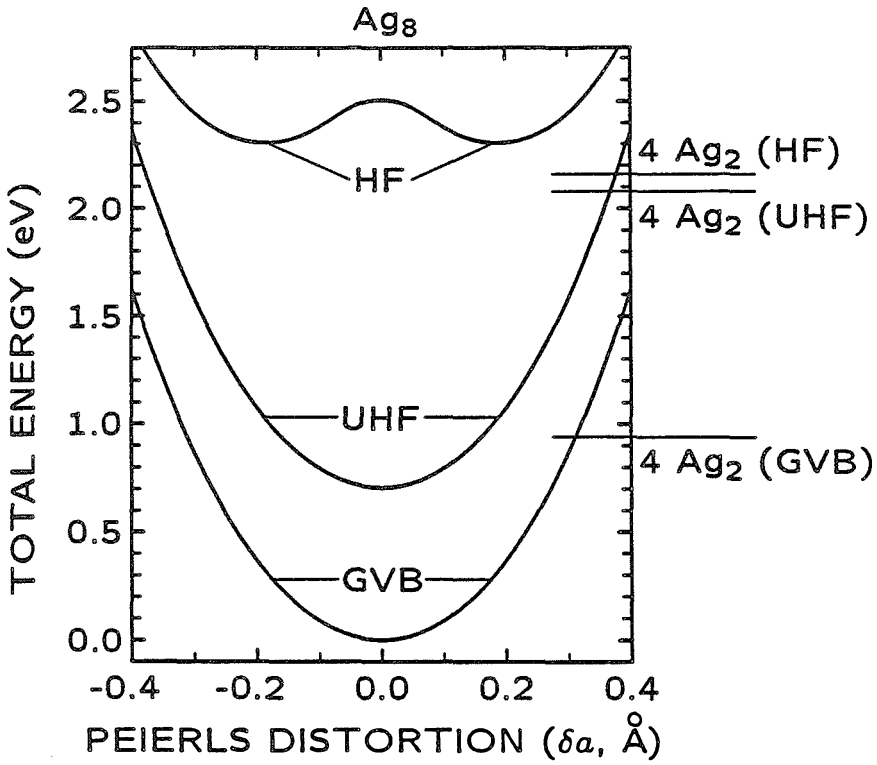

Figure 12. The total energy of the Ag_8 ground electronic state as a function of the Peierls distortion (δa) calculated without orbital symmetry restrictions at the HF, UHF and GVB levels.

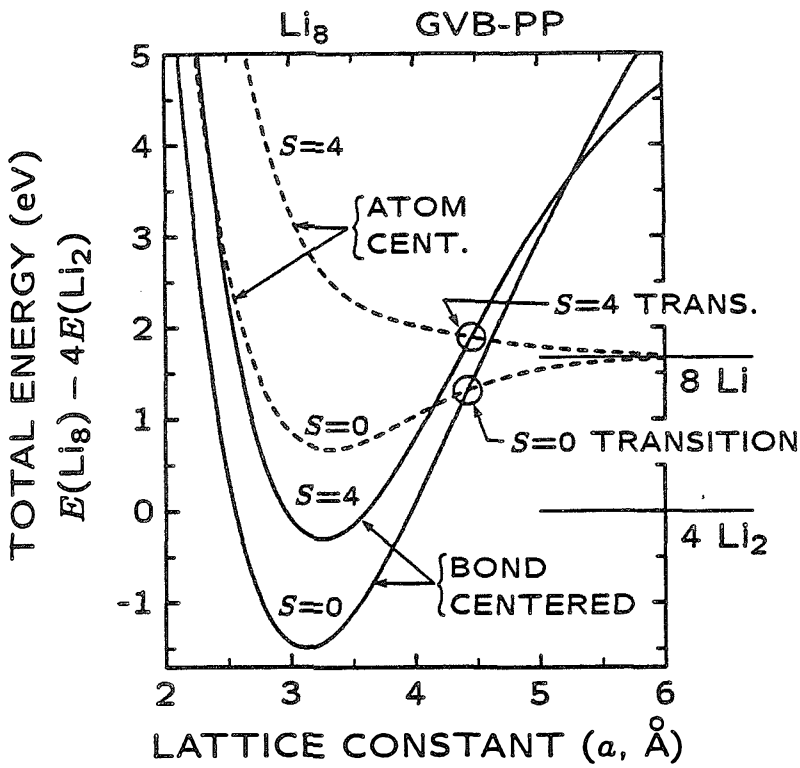

Figure 13. The GVB–PP total energy of the Li_8 symmetric ring cluster as a function of the lattice constant, showing localization transitions for the low-spin ($S = 0$) and high-spin ($S = 4$) states.

Chapter 3

Magnon Dispersion, Spin Density Waves, and Charge Density Waves in One-Dimensional Metals: Ab Initio HF and UHF Wavefunctions for Cu, Ag, Au, Li, and Na

I. Introduction

The properties of pseudo one-dimensional solids have long been a subject of considerable interest. Peierls[1] has shown that one-dimensional metals having partially filled energy bands are susceptible to a distortion leading to an energy band gap at the Fermi level and hence a metal-to-insulator transition. For a chain of monovalent atoms, the Peierls instability is often associated with a charge density wave having maxima and minima at alternating bond midpoints, leading to a Peierls distortion pairing up adjacent atoms to form a diatomic lattice.[1] However, for a chain of monovalent atoms, the exact solution[2] of the Hubbard hamiltonian[3,4] leads to an antiferromagnetic insulator (with a spin density wave).

These ideas of Peierls instability, charge density waves, antiferromagnetic insulators, and spin density waves have proved useful in characterizing pseudo-one-

dimensional inorganic and organic compounds[5,6] such as (*i*) $CuCl_2$ and $(CH_3)_4NMnCl_3$ antiferromagnetic insulators,[7] consisting of symmetric chains, (*ii*) organic polymers such as polyacetylene,[8] and (*iii*) organic charge transfer salts such as those based on the tetracyanoquinodimethane (TCNQ) anion.[5,6] Such pseudo-one-dimensional solids are believed to be likely candidates for high-temperature superconductivity.[6]

Testing these concepts of Peierls instability, charge density waves, antiferromagnetic insulators, and spin density waves with high quality ab initio[9] total energy calculations for one-dimensional metallic systems should prove valuable in understanding the properties of such pseudo-one-dimensional solids. In addition, such systems provide a sensitive test of various electronic structure techniques.

Hence, we have optimized restricted Hartree-Fock (HF, non-spin-polarized), unrestricted Hartree-Fock (UHF, spin-polarized) and generalized valence bond (GVB) wavefunctions for various one-dimensional ring clusters composed of Cu, Ag, Au, Li, and Na. Results for the low-spin states of these clusters are presented elsewhere in full detail.[10,11] The cohesion of these systems is due to two-center one-electron bonding,[11] as shown by the UHF valence orbitals for M_2^+, linear M_3^+, and M_{10} in Figures 1-2 [for these systems, the GVB and UHF (Hartree-localized) orbitals are similar].[11] At the highest level of theory (GVB),[11] these systems are antiferromagnetic insulators having fully symmetrical charge and spin densities, and do not lead to Peierls instabilities. UHF wavefunctions for these systems are consistent with the Hubbard hamiltonian.[10] However, both UHF and HF lead to incorrect results (in comparison to GVB), such as spin density waves (for UHF), charge density waves (for HF), and Peierls instabilities (for HF).[10,12]

Here, we present HF and UHF results calculated for all allowed magnetizations of the Cu_{10}, Ag_6, Ag_8, Ag_{10}, Au_{10}, Li_6, Li_{10}, Li_{14}, and Na_{10} ring clusters. An analogous

GVB study of these systems is presented in full detail elsewhere.[13] We show that the UHF magnon spectra are consistent with a nearest-neighbor Ising model.[14,15] However, HF leads to incorrect results (such as a ferromagnetic ground state for Li_N).

Section II presents details of these results, and additional details are given in the appendices. Speculations on Ising models for the valence electronic structures of two-dimensional and three-dimensional metals are given in Section III.D.

II. Results

A. Introduction

For each of the Cu_{10}, Ag_6, Ag_8, Ag_{10}, Au_{10}, Li_6, Li_{10}, Li_{14}, and Na_{10} ring clusters we report the total energy as a function of *magnetization* (or density of unpaired spins)

$$\mu = \frac{|A - B|}{N}$$

where A and B are the number of up-spin electrons ($\uparrow$ or α) and down-spin electrons ($\downarrow$ or β), respectively ($A + B = N$). We calculate both the UHF magnon spectrum and the HF magnon spectrum using the same geometries, hamiltonians, and basis sets as in our previous studies of the cohesive properties of these systems.[10,11] The bond lengths or lattice constants (a) for these symmetric ring clusters are taken equal to the nearest-neighbor distances for the respective bulk metals.[16] Further details of these ab initio calculations are given in Appendix A.

For each of these systems, the effect of valence magnetization changes on the core orbitals is small.[10] For Cu_{10}, Ag_6, Ag_8, Ag_{10}, and Au_{10}, calculations where both the core and valence orbitals are optimized self-consistently lead to minimal

hybridization between the d orbitals (core) and the valence sp orbitals for both the low-spin ($\mu = 0$) and high-spin ($\mu = 1$) states.[10] For these systems, the closed-shell d^{10} configurations are maintained for magnetizations of up to one unpaired electron per atom.[10] (In Appendix G, we show for Au_{10} that the lowest energy $5d$-excited $\mu = 1$ state is 2.46 eV higher in energy than the lowest energy $\mu = 1$ state at the HF level.)

Hence, the same frozen core approximation as utilized previously (including the closed-shell d^{10} electrons of the noble metal rings)[10,11] is expected to be reasonably accurate for magnetizations $0 \leq \mu \leq 1$.[10]

Incorporating this frozen core approximation, we solve for the UHF and HF valence wavefunctions

$$\Psi_{N,A}^{UHF} = \hat{\mathcal{A}}[(\varphi_1\varphi_2\cdots\varphi_A\varphi_{A+1}\varphi_{A+2}\cdots\varphi_N)\alpha^A\beta^B]$$

$$\Psi_{N,A}^{HF} = \hat{\mathcal{A}}[(\varphi_1\varphi_2\cdots\varphi_A\varphi_1\varphi_2\cdots\varphi_B)\alpha^A\beta^B]$$

where $\hat{\mathcal{A}}$ is the antisymmetrizer, $\{\varphi_j\}$ are the canonical one-electron orbitals optimized self-consistently for each case, and α and β are the up-spin and down-spin one-electron spin functions, respectively (see Appendix A for further details).

We first examine the electronic structure of the valence high-spin state ($\mu = 1$, one unpaired electron per atom) where HF and UHF are identical. However, for magnetizations $\mu < 1$, the UHF and HF wavefunctions differ dramatically.

B. The High-Spin State

For each of the Cu_{10}, Ag_6, Ag_8, Ag_{10}, Au_{10}, Li_6, Li_{10}, Li_{14}, and Na_{10} ring clusters, the optimum (real) canonical orbitals $\{\varphi_j\}$ for the lowest energy high-spin state (μ=1,

one unpaired electron per atom)

$$\Psi_{N,N} = \hat{\mathcal{A}}[(\varphi_1\varphi_2\varphi_3\cdots\varphi_N)(\alpha\alpha\alpha\cdots\alpha)] \tag{1}$$

can be combined[10] into (complex) Bloch functions[17]

$$\begin{aligned} \psi_m &= c_m^{-1/2}\sum_{j=1}^{N}\phi_j\exp(ikR_j),\ 0 \le |m| \le N/2 \\ k &= \frac{2\pi m}{aN} \\ R_j &= ja \end{aligned} \tag{2}$$

where c_m is the normalization constant for ψ_m, $\{\phi_j\}$ is a nonorthogonal set of N equivalent localized orbitals, k is the wave vector, and R_j denotes the position of ϕ_j (going around the circumference; ϕ_{1+j} is generated from ϕ_1 by j successive N-fold rotations). In terms of the $\{\psi_m\}$, the $\mu = 1$ wavefunction

$$\Psi^{\psi}_{N,N} = \hat{\mathcal{A}}[(\psi_0\psi_1\psi_{-1}\cdots\psi_{n-1}\,\psi_{-n+1}\,\psi_n)(\alpha\alpha\alpha\cdots\alpha\alpha\alpha)] \tag{3}$$

($n = N/2$) has the same form and total energy as wavefunction (1).

These two sets of orbitals [$\{\varphi_j\}$ and $\{\psi_m\}$] are not the only means of describing the high-spin state; e.g., the wavefunction written in terms of $\{\phi_j\}$

$$\Psi^{\phi}_{N,N} = \hat{\mathcal{A}}[(\phi_1\phi_2\phi_3\cdots\phi_N)(\alpha\alpha\alpha\cdots\alpha)] \tag{4}$$

has the same total energy as wavefunctions (1) and (3), since the $\{\varphi_j\}$, $\{\psi_m\}$, and $\{\phi_j\}$ are related by linear transformations [see Appendix A.3].

Figure 2b shows the optimum localized orbital ϕ_1 for each of the Cu_{10}, Ag_{10}, Au_{10}, Li_{10}, and Na_{10} ring clusters, where ϕ_1 is obtained from the $\{\varphi_j\}$ by Hartree localization.[11] For each case, ϕ_1 is centered at one of the bond midpoints and is composed primarily of a hybridization of s and $p\sigma$ functions from two adjacent atoms.

For each case, the ϕ_1 for the M_{10} high-spin cluster (Figure 2b) is remarkably similar to the valence orbital of the respective M_2^+ cluster (Figure 1a).

Incidentally, the $\{\psi_m\}$ can also be expanded in terms of a complete set of orthogonal localized Wannier[15,11] orbitals $\{\omega_j\}$

$$\psi_m = N^{-1/2} \sum_{j=1}^{N} \omega_j \exp(ikR_j)$$

and the high-spin wavefunction in terms of $\{\omega_j\}$

$$\Psi^{\omega}_{N,N} = \hat{\mathcal{A}}[(\omega_1\omega_2\omega_3\cdots\omega_N)(\alpha\alpha\alpha\cdots\alpha)] \tag{5}$$

has the same total energy[15] as wavefunctions (1), (3), and (4).

Figure 2c shows the optimum ω_1 for each of the Cu_{10}, Ag_{10}, Au_{10}, Li_{10}, and Na_{10} ring clusters. In each case, ω_1 (Figure 2c) is similar to ϕ_1 (Figure 2b) except for the negative amplitudes in the regions of adjacent orbitals (2 and 10) resulting since the $\{\omega_j\}$ are orthogonal whereas the $\{\phi_j\}$ are allowed to overlap one another.

The Hartree orbitals $\{\phi_j\}$ prove useful for describing the UHF wavefunctions for other magnetizations, and the Wannier orbitals $\{\omega_j\}$ prove useful for describing the HF wavefunctions for other magnetizations.

C. Unrestricted Hartree-Fock

1. Ab Initio Results

We optimized UHF wavefunctions for all allowed magnetizations $0 \leq \mu \leq 1$ of each of the Cu_{10}, Ag_6, Ag_8, Ag_{10}, Au_{10}, Li_6, Li_{10}, Li_{14}, and Na_{10} ring clusters. These UHF wavefunctions are optimized with real orbitals and with C_s orbital symmetry restrictions; however, reducing the orbital symmetry restriction to C_1 or raising the

orbital symmetry restriction to C_{2v} (with the C_2 axis bisecting two opposite bond midpoints of the ring) leads to identical results. The results are given in Tables 1-2.

For each case, UHF leads to a low spin (antiferromagnetic, $\mu = 0$) ground state with a monotonic increase in the total energy as μ is increased. Figure 3 presents the UHF magnon spectra for the M_{10} ring clusters. For M_{10}, the UHF magnon dispersion energies

$$\mathcal{D}_N = E_{N,\mu=1} - E_{N,\mu=0}$$

follow the trend Cu > Au > Ag $\gg$ Na > Li.

For each state A of each M_N ring cluster, the UHF wavefunction in terms of the optimum *canonical* orbitals $\{\varphi_i\}$ has an equivalent form in terms of nonorthogonal *localized* orbitals $\{\phi_i\}$ where ϕ_i and ϕ_{i+n} are nth nearest neighbors [ϕ_i and $\phi_{i\pm1}$ are adjacent (modulo N; see Figure 2)]. For each state A, the $\{\phi_i\}$ are obtained by separate Hartree localizations[11] of the up-spin canonical orbitals $\{\varphi_i, i = 1, 2, \ldots, A\}$ and the down-spin canonical orbitals $\{\varphi_i, i = A+1, A+2, \ldots, N\}$.

The key property of the $\{\phi_i\}$ is that they exhibit only minor variations as a function of μ for each of the Cu_{10}, Ag_6, Ag_8, Ag_{10}, Au_{10}, Li_6, Li_{10}, Li_{14}, and Na_{10} ring clusters (this is not true for the $\{\varphi_i\}$). Hence, the $\{\phi_i\}$ optimized for $\mu = 1$ (high-spin, Figure 2b) are very similar to the $\{\phi_i\}$ optimized for $\mu = 0$ (low-spin, Figure 2a). For Cu_{10}, Ag_{10}, Au_{10}, Li_{10}, and Na_{10}, the average value of

$$\delta\phi_1 = 1 - \langle\phi_1^{\mu=0}|\phi_1^{\mu=1}\rangle$$

is 0.00351 (individual values are listed in Table 2).

For M_{10}, values of the nearest-neighbor overlap integrals

$$S_{12} = \langle\phi_1|\phi_2\rangle$$

for $\mu = 1$ are 7-17% larger than those for $\mu = 0$ (see Table 2). These $\mathcal{S}_{12}$ values ($\mathcal{S}_{12}^{\mu=0}$, $\mathcal{S}_{12}^{\mu=1}$, and their average) follow the same trend as the $\mathcal{D}$ values (Cu > Au > Ag > Na > Li; see Figure 4 and Table 2).

The UHF wavefunctions in terms of the $\{\phi_i\}$ for magnetizations $0 \leq \mu \leq 1$ are outlined schematically in Figure 5 for M_{10}. UHF leads to a spin density wave for each magnetization except for $\mu = 1$. The UHF $\mu = 0$ spin density wave state is discussed elsewhere[10] in further detail.

For each magnetization of M_N, adjacent orbitals (ϕ_i and ϕ_{i+1}) prefer to be occupied with opposite spins (α-β or β-α) wherever possible [such as for the antiferromagnetic ($\mu = 0$) ground state; see Figure 5]. Hence, adjacent orbitals having parallel spins (α-α or β-β) lead to an antibonding nearest-neighbor exchange interaction (exchange coefficient $U = -1$; see Appendix B).

For M_N, $\Psi_{N,A}^{UHF}$ leads to $|A - B| = \mu N$ antibonding nearest-neighbor exchange interactions ($U = -1$) and $N(1 - \mu)$ nonbonding nearest-neighbor exchange interactions (α-β; $U = 0$). Ignoring all other interactions leads to the simple Ising[14] energy expression

$$E_{N,\mu} \approx E_{N,\mu=0} - \mu N \mathcal{J} \tag{6}$$

(where $\mathcal{J}$ is the exchange interaction), explaining the near linear increase of the total energy with increasing μ as shown in Figure 3 (therefore, $\mathcal{J}$ is negative; see Appendix B for further details).

The UHF magnon spectra for the series Ag_8, Ag_8, Ag_{10}, and for the series Li_6, Li_{10}, Li_{14} are presented in Figures 6 and 7, respectively. In agreement with (6), $\mathcal{D}$ increases almost linearly with increasing N.

For Ag_N and Li_N, $\mathcal{D}/N \approx |\mathcal{J}|$ decreases slightly with increasing N (see Table 2). The reason for this that $|\mathcal{J}|$ decreases as the distance between the two orbitals

increases. For M_N, the localized orbitals are centered at bond midpoints, and the distance between adjacent bond midpoints

$$R^{BM} = a\cos(\pi/N)$$

increases with increasing N, hence explaining the decrease in $\mathcal{D}/N$ with increasing N at fixed a. This also explains the decrease of the nearest-neighbor overlap ($\mathcal{S}_{12}$) with increasing N at fixed a.

2. Ising and Generalized Ising Models

For each of the Cu_{10}, Ag_6, Ag_8, Ag_{10}, Au_{10}, Li_6, Li_{10}, Li_{14}, and Na_{10} ring clusters, we fit the UHF total energies ($E^{UHF}_{N,A}$) to the Ising[14] model and generalized Ising models

$$\begin{aligned} E^{IM}_{N,\mu} &= E_{N,\mu=0} - \mu N\mathcal{J} \\ E^{GIM1}_{N,\mu} &= E_{N,\mu=0} - \frac{\mu N\mathcal{J}}{1-\mu N\mathcal{S}^2} \\ E^{GIM2}_{N,\mu} &= E_{N,\mu=0} - \mu N\mathcal{J}(1+\mu N\mathcal{S}^2) \end{aligned}$$

where $\mathcal{J}$ and $\mathcal{S}$ are the "effective" nearest-neighbor exchange energy and the "effective" nearest-neighbor overlap integral, respectively ($\mathcal{J} < 0$ leads to an antiferromagnetic ground state). These energy expressions are based exclusively on nearest-neighbor exchange interactions and are derived in Appendix B.

For each case, we take $E_{N,\mu=0}$ equal to the $\mu = 0$ UHF energy ($E_{10,\mu=0} = E^{UHF}_{10,5}$) and use $\mathcal{J}$ and $\mathcal{S}$ as least-squares parameters, e.g., $\mathcal{J}$ and $\mathcal{S}$ minimize root mean square (RMS) error

$$(\Delta E^{RMS})^2 = \frac{2}{N}\sum_{A=1+N/2}^{N}(E^{UHF}_{N,A} - E^{GIM}_{N,\mu})^2.$$

The results presented in Table 3 for M_{10} indicate that E^{GIM2} *is more accurate than* E^{IM} by factors of 6.3 to 13.8, and E^{GIM2} is more accurate than E^{GIM1} by

factors of 1.2 to 2.0; hence, E^{GIM2} is used to interpolate the calculated UHF total energies in Figure 3 and Figures 6-7.

For each of the M_N ring clusters, $\mathcal{J}$ and $\mathcal{S}$ values follow the patterns $-\mathcal{J}^{GIM2}| < |\mathcal{J}^{GIM1}| < |\mathcal{J}^{IM}|$ and $\mathcal{S}_{12} > \mathcal{S}^{GIM2} > \mathcal{S}^{GIM1} > \mathcal{S}^{IM} = 0$, respectively (where $\mathcal{S}_{12}$ is the average of the UHF values $\mathcal{S}_{12}^{\mu=0}$ and $\mathcal{S}_{12}^{\mu=1}$; see Table 2 and Figure 4).

The explanation of the trend $\mathcal{S}_{12} > \mathcal{S}^{GIM2} > \mathcal{S}^{GIM1}$ is as follows. GIM1 requires $\mathcal{S} < N^{-1/2}$ in order to avoid the singularity. GIM2 requires that $\mathcal{S}$ be proportional to $N^{-1/2}$ for large N in order to obtain a finite energy splitting between states A and $A+\delta$ in the limit as N approaches infinity (for finite δ)

$$\left|E^{GIM2}_{N,A+\delta} - E^{GIM2}_{N,A}\right| = \left|2\delta\mathcal{J}[1+2\bar{\mu}N\mathcal{S}^2]\right|$$
$$\bar{\mu} = |2A+\delta-N|/N$$

(where $\bar{\mu}$ is the magnetization of the average state $A+\delta/2$). Thus, GIM2 is somewhat less restrictive than GIM1, consistent with the superiority of GIM2 over GIM1.

Despite the restrictions, the $\mathcal{J}$ and $\mathcal{S}$ values from GIM are closely related to the $\mathcal{D}$ and $\mathcal{S}_{12}$ values from UHF, as shown in Figure 4 for M_{10}. Each set of values (see Figure 4) follows the trend Cu > Au > Ag > Na > Li except that (*i*) Au > Cu for $\mathcal{S}^{GIM1}$ and $\mathcal{S}^{GIM2}$, and (*ii*) Ag > Au for $\mathcal{J}^{GIM2}$.

D. Restricted Hartree-Fock

We optimized HF wavefunctions for all allowed magnetizations $0 \leq \mu$ of each of the Cu_{10}, Ag_8, Ag_8, Ag_{10}, Au_{10}, Li_6, Li_{10}, Li_{14}, and Na_{10} ring clusters. These HF wavefunctions are optimized using three different sets of orbital symmetry restrictions, as follows.

D_{Nh}: Complex orbitals restricted to transform according to the irreducible rep-

resentations of the point group D_{Nh} [e.g., Bloch orbitals (2)].[10,17] These HF(D_{Nh}) wavefunctions always lead to fully symmetrical charge densities[10] — even for degenerate open-shell states.

C_{2h}: Real orbitals restricted to transform according to the irreducible representations of C_{2h}. For M_{10}, raising the symmetry restriction to D_{2h} leads to identical results. For M_8, raising the symmetry restriction to D_{2h} is more complicated.[10,18]

C_s: Real orbitals restricted to be either symmetric or antisymmetric with respect to the plane of the ring. In each case, raising the symmetry restriction to C_{2v} (with the C_2 axis containing two opposite atoms of the ring) leads to identical results.

The results are given in Table 1 and Figures 8-17.

Optimizing HF wavefunctions with D_{Nh} or C_{2h} orbital symmetry restrictions leads to higher total energies and rather complicated magnon spectra in comparison to HF(C_s). Therefore, we first present the HF(C_s) magnon spectra, and then we discuss the HF(C_{2h}) and HF(D_{Nh}) magnon spectra. In Sections II.E-F we discuss symmetry-breaking effects (leading to charge and spin density waves).

1. HF Results Without Orbital Symmetry Restrictions

Unlike UHF, HF does not lead to $\mu = 0$ (low-spin, antiferromagnetic) ground states in all cases. Figure 8 presents the HF(C_s) magnon spectra for the M_{10} ring clusters. Although the HF and UHF magnon dispersion curves for M_{10} follow the same trend (Cu > Au > Ag $\gg$ Na > Li; compare Figures 3 and 8), the HF ground states for Na_{10} and Li_{10} contain 0.6 and 1.0 unpaired electrons per atom, respectively.

The HF magnon spectra for the series Ag_6, Ag_8, Ag_{10}, and for the series Li_6, Li_{10}, Li_{14} are presented in Figures 9 and 10, respectively. Unlike UHF, the HF magnon dispersion curves are not smooth and are not always monotonic (compare Figures 6

and 9 for Ag_N). Hence, HF leads to a $\mu = 0.25$ (triplet) ground state for Ag_8.[19] For Li_N, HF leads to a $\mu = 1$ (high-spin, ferromagnetic) ground state, with a monotonic increase in the energy with decreasing μ. Thus, for Li_N the HF and UHF results are in complete disagreement (compare Figures 7 and 10).

2. HF Results With Orbital Symmetry Restrictions

The HF magnon spectra calculated by imposing orbital symmetry restrictions are tabulated in Table 1 for each of the nine M_N ring clusters. For the Cu_{10}, Ag_8, Ag_{10}, Au_{10}, Li_{10}, Li_{14}, and Na_{10} ring clusters, the three sets of HF results (C_s, C_{2h}, and D_{Nh}) are presented in Figures 11-17, where the UHF results are included for comparision.

In general, the HF(D_{Nh}) and HF(C_{2h}) magnon dispersion curves are even less smooth and less monotonic than the HF(C_s) magnon dispersion curves, especially for Ag_{10}, Na_{10}, Li_{10} and Li_{14} (Figures 14-17). For each M_N cluster, the HF(D_{Nh}) energy is significantly higher than the HF(C_s) energy for all magnetizations $0 < \mu < 1$. In addition, the HF(C_{2h}) energy is significantly higher than the HF(C_s) energy for half of the allowed magnetizations $0 < \mu < 1$.

In each case, imposing orbital symmetry restrictions (D_{Nh} or C_{2h}) does not alter which magnetization has the minimum energy on the magnon dispersion curve. However, for Ag_{10}, Li_{10}, Li_{14}, and Na_{10}, imposing orbital symmetry restrictions *does* change which magnetization has the *maximum* energy on the magnon dispersion curve.

E. HF Charge Density Waves

For each magnetization μ where the reduced-symmetry (C_{2h} or C_s) HF total energy is lower than the HF(D_{Nh}) total energy, that reduced-symmetry HF wavefunction leads to a charge density wave (and also a spin density wave if $\mu \neq 0$). For these cases, the optimum HF canonical orbitals localize (break symmetry) — they do *not* have the symmetry of the lattice; i.e., they are not Bloch functions (2).

Figure 18 shows the energetic effects of allowing the full charge density wave

$$E^{CDW} = E^{HF(C_s)} - E^{HF(D_{10h})}$$

as a function of magnetization for each of the Cu_{10}, Ag_{10}, Au_{10}, Li_{10}, and Na_{10} ring clusters. These charge density wave effects follow the trend Li > Na > Ag > Cu > Au. These results for M_{10} are tabulated in Table 4, along with similar results for the other four clusters (Ag_6, Ag_8, Li_6, and Li_{14}).

1. Intermediate Magnetizations ($0 < \mu < 1$)

For each of these nine ring clusters, the HF(C_s) wavefunction leads to charge and spin density waves for all magnetizations $0 < \mu < 1$.

These charge density waves are a direct result of the HF doubly-occupied orbital restriction ($\mu = 1$ is unaffected since all valence orbitals are singly-occupied). For magnetization μ, the HF wavefunction contains $B = N(1-\mu)/2$ doubly occupied canonical orbitals. Each HF doubly-occupied orbital leads to substantial ionic character.[11] For HF, the amount of ionic character can be defined by expanding the wavefunction in terms of Wannier orbitals, resulting in a mixture of ionic and covalent configurations.[11]

In Appendices E-F we show that for HF, ionic character leads to a lowering

of the total one-electron energy (kinetic energy and electron - nuclear attraction energy) at the expense of raising the two-electron energy (due to electron - electron repulsions).[10]

The key measure of the ionic character is the average number of doubly-occupied Wannier orbitals per configuration, $\langle I \rangle$. Values of $\langle I \rangle$ are given by the formulas

$$\langle I \rangle_{D_{Nh}} = N(1-\mu^2)/4$$
$$\langle I \rangle_{C_s} = N(1-\mu)/4$$

(see Appendix D for further details). Hence, for $0 \leq \mu \leq 1$, allowing the valence orbitals to localize (C_s) reduces the amount of ionic character, leading to a lower total energy despite the charge density waves. The reduction in ionic character afforded by localization

$$\langle I \rangle_{D_{Nh}} - \langle I \rangle_{C_s} = N(\mu - \mu^2)/4 \tag{7}$$

depends quadratically on μ with the maximum at $\mu = 0.5$.

The results given in Figure 18 indicate that the reduction of ionic character (7) plays a major role in determining the charge density wave energy effects. Hence, for M_{10} the charge density wave effects peak at $\mu = 0.6$, and for Ag_8 the charge density wave effects peak at $\mu = 0.5$ (see Table 4).

2. Low Spin ($\mu = 0$)

For the $\mu = 0$ HF states of these systems, we have previously shown that charge density waves are enhanced by narrow valence energy bands, that they occur more readily for the $N = 4i$ clusters than for the $N = 4i + 2$ clusters, and that their magnitudes generally increase with increasing N.[10] For each of the Cu_{10}, Ag_6, Ag_{10}, Au_{10}, and Li_6 rings, the HF $\mu = 0$ (low-spin) state contains neither a charge density

wave nor a spin density wave. However, for each of the Ag_8, Li_{10}, Li_{14}, and Na_{10} rings, the HF $\mu = 0$ state contains a charge density wave — with maxima and minima centered at alternate atoms[10,11] — but no spin density wave. For Ag_8, Li_{10}, Li_{14}, and Na_{10}, the HF(D_{Nh}) energy is higher than the HF(C_s) energy by 0.222, 0.060, 0.325, and 0.007 eV, respectively.

F. Spin Density Waves and Spin Polarization

Figure 19 shows the energetic effects of allowing the full *spin* density wave (including spin polarization)

$$E^{SDW} = E^{UHF} - E^{HF(D_{10h})}$$

as a function of magnetization for each of the Cu_{10}, Ag_{10}, Au_{10}, Li_{10}, and Na_{10} ring clusters.

Figure 20 shows the energetic effects of allowing *spin polarization*

$$E^{SP} = E^{UHF} - E^{HF(C_s)}$$

as a function of magnetization for each of the Cu_{10}, Ag_{10}, Au_{10}, Li_{10}, and Na_{10} ring clusters. These spin polarization effects increase monotonically from $\mu = 1$ to $\mu = 0$.

Each of these effects (charge density wave, spin density wave, and spin polarization) follows the trend Li > Na > Ag > Cu > Au. This trend is almost the inverse of the Li < Na < Ag < Au < Cu trend followed by both the overlap and magnon dispersion energy for UHF (see Section II.C).

III. Discussion

A. Restricted Hartree-Fock

For the M_N ring clusters composed of Cu, Ag, Au, Li and Na, restricted Hartree-Fock (HF) leads to spurious results, such as (*i*) a charge density wave and Peierls instability for each of the Ag_8, Li_{10}, and Li_{14} $\mu = 0$ (low-spin) symmetric ring clusters,[10,11,12] (*ii*) a charge density wave and a negative atomization energy for the Na_{10} $\mu = 0$ ring cluster,[10] (*iii*) charge and spin density waves for all intermediate magnetizations ($0 < \mu < 1$) of Cu_{10}, Ag_6, Ag_8, Ag_{10}, Au_{10}, Li_6, Li_{10}, Li_{14}, and Na_{10} (see Section II.E), and (*iv*) ground states for Ag_8, Na_{10}, Li_6, Li_{10}, and Li_{14} having 0.25, 0.6, 1.0, 1.0, and 1.0 unpaired electrons per atom, respectively (see Table 1 and Figures 8-10).

This indicates a fundamental flaw in HF for these systems, and that flaw is the double occupation of valence orbitals for describing magnetizations $\mu < 1$. This is further discussed in Appendices D-E, where we show that the HF doubly-occupied orbitals lead to a *forced* mixture of covalent and ionic configurations in terms of the localized Wannier orbitals $\{\omega_j\}$.[15,11]

For magnetizations $0 \leq \mu < 1$, the charge and spin density waves are a direct result of minimizing the ionic character of the HF wavefunction (and hence the HF total energy) by allowing the orbitals to localize.

However, even with localized orbitals, each doubly-occupied HF valence orbital leads to 50% ionic character and 50% covalent character for each localized electron pair. Hence, the error in the HF energy due to the overemphasis of ionic character increases monotonically with decreasing magnetization (e.g., see Figure 20). Systems having narrow valence bands and large lattice constants (Li_N and Na_N) have a much lower tolerance of ionic character than those having wide valence bands and small

lattice constants (Cu_N, Ag_N, and Au_N). Thus, for Li_{10} and Na_{10}, the HF ground states are $\mu = 1.0$ and $\mu = 0.6$, respectively.

The obvious solution of these problems is to *optimize* the coefficients of all possible covalent and ionic configurations (electron correlation); however, the restricted form of the HF wavefunction does not allow this.

B. Unrestricted Hartree-Fock

Unrestricted Hartree-Fock (UHF) leads to a nonmetallic, antiferromagnetic ($\mu = 0$, low-spin) ground state for each of the M_N ring clusters composed of Cu, Ag, Au, Li and Na. UHF allows a full reduction of ionic character by providing a separate orbital for each electron, and allowing the orbitals to break symmetry (localize). Hence, for each magnetization $\mu < 1$, UHF leads to a spin density wave state (see Figure 5) having a lower total energy than the lowest energy HF state. The energy difference between UHF and HF ($|E^{HF(C_s)} - E^{UHF}|$; see Figure 20) increases monotonically with decreasing magnetization. Hence, for these systems, spin polarization is crucial for a Hartree Fock (single-determinant) description of the valence electronic structure.

In each case, the local valence electronic structure of the UHF ground state consists of singly-occupied orbitals centered at the bond midpoints with alternating spins (see Figures 2 and 5), e.g.,

$$\phi_1(\alpha)\phi_2(\beta)\phi_3(\alpha)\phi_4(\beta)\cdots\phi_{N-1}(\alpha)\phi_N(\beta)$$

(for even N). This leads to a spin density wave, although in each case the *net* electronic charge density (obtained by adding the up-spin and down-spin densities) is fully symmetrical.

For each magnetization, localized orbitals $\{\phi_i\}$ similar to those for $\mu = 0$ can be obtained by separate Hartree localizations[11] of the up-spin canonical UHF orbitals $\{\varphi_i,\ 1 \leq i \leq A\}$ and the down-spin canonical UHF orbitals $\{\varphi_i,\ A+1 \leq i \leq N\}$ (the UHF total energy is invariant to this orbital transformation).[11] In terms of the $\{\phi_i\}$, for UHF, the magnetization is increased by flipping down-spin (β) electrons to up-spin (α), as shown in Figure 5 for M_{10}.

The UHF energy increases monotonically with increasing magnetization, because the nearest-neighbor exchange interaction between adjacent parallel spins is antibonding ($U = -1$), as opposed to the nonbonding ($U = 0$) interaction between adjacent antiparallel spins (see Appendix B).

The UHF Hartree orbitals exhibit only minor variations as a function of μ for each of the Cu_{10}, Ag_8, Ag_8, Ag_{10}, Au_{10}, Li_8, Li_{10}, Li_{14}, and Na_{10} ring clusters (see Figure 2 and Table 2). As a result, the UHF total energies for the allowed magnetizations can be interpolated accurately with a generalized Ising Model

$$E_{N,\mu}^{GIM} = E_{N,\mu=0} - \mu N \mathcal{J}(1 + \mu N \mathcal{S}^2).$$

This generalized Ising energy expression includes effects due to the nearest-neighbor overlap ($\mathcal{S}$) to first order and results from the solutions of the nearest-neighbor Ising Hamiltonian[14,15]

$$\mathcal{H}^{ISING} = \mathcal{J} \sum_i \tfrac{1}{2} + 2\, s_{i\,z}\, s_{i+1\,z} \tag{8}$$

including only nearest-neighbor exchange interactions $\mathcal{J}$ where $s_{i\,z}$ is the z component of spin for lattice position i. This generalized Ising model reduces to the usual simple Ising model in the limit as $\mathcal{S}$ approaches zero (such as for a lattice of singly-occupied d or f orbitals).

The reason for the success of the generalized Ising model in fitting the UHF total

energies is that (i) the UHF wavefunctions for the various magnetizations of M_N can all be described fairly well in terms of a single set of N equivalent well-localized non-orthogonal orbitals $\{\phi_j\}$ (see Appendices B-C), and (ii) $\mathcal{J}$ and $\mathcal{S}$ decrease exponentially with increasing distance;[11,13] hence, non-nearest-neighbor overlaps and exchange interactions are negligible.

C. Generalized Valence Bond

The *optimum* wavefunction allowing an independent particle description of the electronic structure is the generalized valence bond wavefunction (GVB).[20,21] Both GVB and UHF include a separate spatial orbital for each valence electron, where the orbitals are energy-optimized without any restrictions. For UHF, the orbitals are optimized for a fixed many-electron spin function (χ) that is a simple product of one-electron spin functions ($\chi^{UHF} = \alpha^A\beta^B$). However, unlike UHF, for GVB, both the valence orbitals *and the many-electron spin function* are optimized simultaneously.[20,11] Hence, for $\mu < 1$, GVB always leads to a lower total energy than UHF.

We have optimized GVB wavefunctions for all allowed magnetizations of each of the Cu_{10}, Ag_8, Ag_8, Ag_{10}, Au_{10}, Li_8, Li_{10}, and Na_{10} ring clusters. Full details of these results are presented elsewhere.[13]

In agreement with UHF, GVB leads to a $\mu = 0$ ground state in each case. Also in agreement with UHF, GVB leads to localized orbitals centered at bond midpoints that exhibit only minor variations as a function of μ. However, unlike UHF, in each case GVB leads to fully symmetrical charge and spin densities for all magnetizations $0 \leq \mu \leq 1$. Therefore, for these systems, the spin density waves resulting from UHF are due to an incomplete treatment of the electron correlation forced by the use of a restricted (product) spin function.[11,13]

For each of the M_N ring clusters, the GVB total energies for the allowed magnetizations are in excellent agreement with the exact solutions of the nearest-neighbor Heisenberg Hamiltonian[15,22]

$$\mathcal{H}^{HEIS} = \mathcal{J} \sum_i \tfrac{1}{2} + 2\vec{s}_i \cdot \vec{s}_{i+1}. \tag{9}$$

The Heisenberg Hamiltonian leads to the energy expression

$$E_{N,\mu} = E^{IM}_{N,\mu=0} + \langle U_{N,\mu} \rangle N\mathcal{J}$$

where $E^{IM}_{N,\mu=0}$ is the Ising energy for $\mu = 0$, and $\langle U_{N,\mu} \rangle$ is average nearest-neighbor exchange coefficient (see Appendix B). The Ising model is an approximate solution of (9) leading to $\langle U_{N,\mu} \rangle = \mu$. Therefore, the exact solutions of (9) lead to $\langle U_{N,\mu} \rangle \leq \mu$.

As an example, for an M_2 antiferromagnetic chain, the exact $\mu = 0$ solution is simply $(\alpha\beta - \beta\alpha)/\sqrt{2}$, leading to $U = 1$ (bonding), and the UHF-Ising $\mu = 0$ solution is $\alpha\beta$, leading to $U = 0$ (nonbonding). For $\mu = 1$, the exact solution and the Ising solution are both $\alpha\alpha$, leading to $U = -1$ (antibonding).

For the M_N ring, the Ising solution for $\mu = 0$ leads to $\langle U^{IM}_{N,\mu=0} \rangle = 0$. However, for M_{10}, the exact solution leads to $\langle U_{N,\mu=0} \rangle = 0.403$ (bonding), and for M_∞, the exact solution leads to $\langle U_{N,\mu=0} \rangle = 2\ln 2 - 1 = 0.386$.[23]

The UHF-Ising description of the electronic structures of these systems can be useful as an approximation to the more exact GVB-Heisenberg description.

D. Ising Models for Simple Metals

Based on the success of the Ising model in approximating the UHF results for the one-dimensional metals composed of Cu, Ag, Au, Li, and Na, it is likely that the Ising model could prove useful for describing the valence electronic structures of two-dimensional metals (metal surfaces) and three-dimensional metals (bulk metals).

The classical model of antiferromagnetism is based on dividing the principal lattice into two sublattices $\{A\}$ and $\{B\}$ — occupied by up-spin and down-spin electrons, respectively — such that all nearest neighbors of sublattice $\{A\}$ belong to sublattice $\{B\}$ and vice versa.[15] However, this two-sublattice model of antiferromagnetism is impossible if the principal lattice contains triangles.[15]

The UHF results for the M_N rings are consistent with this classical model of antiferromagnetism; however, since the valence orbitals are centered at the bond midpoints, the principal lattice for describing the valence electrons is the lattice of bond midpoints — not the atomic lattice.

In general, for a n-dimensional atomic lattice, we expect that the "characteristic" localized valence orbital is composed of sp hybrid orbitals from $n+1$ adjacent atoms (for metallic systems). This expectation is based on UHF and generalized valence bond studies of small lithium clusters containing up to thirteen atoms.[24] Hence, the characteristic localized valence orbitals are centered at bond midpoints, triangular faces and tetrahedral hollows for 1D metals, 2D metals, and 3D metals, respectively.[24] Therefore, for 2D and 3D metals, *the lattice appropriate for simulating the valence electronic structure — based on interstices — need not have the same coordination as the atomic lattice!*

For 2D and 3D close-packed metals, we show in each case that the valence electronic lattice (based on orbitals centered at interstices) leads to the classical model of antiferromagnetism. Hence, the common belief that the classical model of antiferromagnetism cannot apply to the valence electrons of close-packed metals — because their atomic lattices contain triangles — is incorrect.

1. Planar Close-Packed Metals

For a planar close-packed metal, each atom has six nearest neighbors. If this lattice is filled with Cu^{2+} ($3d^9$) ions, then the atomic lattice is correct for describing the electronic structure of the hole states.

However, if this lattice is filled with Cu^{+} ($3d^{10}$) ions and one valence electron per ion is added, the honeycomb (hexagonal) lattice defined by the triangular hollows — where each lattice point has three nearest neighbors — should be used for describing the valence electronic structure.

For transition metals, such as Ni ($3d^9 4s^1$), the valence electronic lattice would interact with the atomic lattice, since the d electrons are atom-centered.

The honeycomb valence electronic lattice leads to the classical model of antiferromagnetism — where the two sublattices consist of the {B} and {N} sites of graphitelike BN.

Since there are two triangular hollows per atom, for monovalent metal atoms, this leads to a half-filled valence band for both the up-spin and the down-spin electrons, leading to a two-dimensional metal. For divalent simple metals (Be, Mn, Ca, etc. and Zn, Cd, Hg), the up-spin and down-spin valence bands are filled, leading to two-dimensional insulators.

2. Hexagonal Close-Packed Metals

For *hcp* metals, the "valence electronic lattice" consists of the centers of the tetrahedral hollows. For *hcp*, each tetrahedral hollow shares a face (three edges) with another tetrahedral hollow, and the three remaining edges are shared with three other tetrahedral hollows. Hence, for *hcp* the lattice of tetrahedral hollows corre-

sponds to the wurzite lattice (such as for hexagonal ZnS, where each lattice point has four neighbors).

The wurzite lattice leads to the classical model of antiferromagnetism — where the two sublattices consist of the {Zn} and {S} sites of hexagonal ZnS.

3. Face Centered Cubic Metals

For *fcc* metals, the electronic lattice also consists of the centers of tetrahedral hollows. For *fcc*, each tetrahedral hollow shares an edge with six other tetrahedral hollows; hence, for *fcc* the lattice of tetrahedral hollows corresponds to the rock salt lattice (NaCl).

The rock salt lattice leads to the classical model of antiferromagnetism — where the two sublattices consist of the {Na} and {Cl} sites of NaCl.

For both *fcc* and *hcp*, there are two tetrahedral hollows per atom. Hence, in each case the Ising model leads to a half-filled energy band for monovalent metal atoms and a completely filled energy band for divalent metal atoms. This is consistent with the observation that the monovalent metals tend to have higher electrical conductivities than the divalent metals.

IV. Summary

We optimized UHF and HF wavefunctions for all allowed magnetizations of each of the Cu_{10}, Ag_6, Ag_8, Ag_{10}, Au_{10}, Li_6, Li_{10}, Li_{14}, and Na_{10} ring clusters. The results for these one-dimensional metals — and speculations for two-dimensional metals and three-dimenstional metals — are summarized as follows.

Restricted Hartree-Fock leads to spurious results, such as (*i*) a charge density

wave for each of the Ag_8, Li_{10}, Li_{14}, and Na_{10} $\mu = 0$ (low-spin) symmetric ring clusters,[10,11] (*ii*) charge and spin density waves for all intermediate magnetizations ($0 < \mu < 1$) of each M_N ring cluster, and (*iii*) ground states for Ag_8, Na_{10}, and Li_{10} having 0.25, 0.6, and 1.0 unpaired electrons per atom, respectively. These spurious results indicate a fundamental flaw in HF for these systems — the double occupation of valence orbitals for describing magnetizations $\mu < 1$.

For each M_N ring cluster, unrestricted Hartree-Fock leads to an antiferromagnetic ($\mu = 0$) ground state that does not have a charge density wave. However, for each magnetization $\mu < 1$ (including $\mu = 0$), UHF leads to a spin density wave (orbital localization). The UHF total energy increases monotonically with increasing magnetization as long as spin density waves are allowed. The UHF magnon spectrum for each of the various M_N rings is described accurately in terms of a generalized Ising model including only effective nearest-neighbor exchange interactions.

However, for these systems, the spin density waves resulting from the UHF-Ising description are due to an incomplete treatment of the electron correlation.[11,13] Hence, generalized valence bond calculations[11,13] lead to lower total energies and fully symmetrical charge and spin densities for all magnetizations $0 \leq \mu \leq 1$.

For these one-dimensional ring clusters, the UHF-Ising model is consistent with the classical two-sublattice model of antiferromagnetism,[15] where the principal lattice is divided into two sublattices A and B — occupied by the up-spin and down-spin electrons, respectively — such that all nearest neighbors of one sublattice belong to the other sublattice. However, for these M_N rings, the valence orbitals are centered at the bond midpoints; hence, the principal lattice for describing the valence electrons is the lattice of bond midpoints — not the atomic lattice.

For close-packed metals, the valence orbitals are centered at interstitial hollows

— triangular hollows for two-dimensional metals and tetrahedral hollows for three dimensional metals.[24] For three cases (planar close-packed, *fcc* and *hcp*), we show that the lattice defined by the interstitial hollows is consistent with the two-sublattice model of antiferromagnetism. Each of these three close-packed metals contains two interstitial hollows per atom, leading (for monovalent metal atoms) to metallic properties resulting from a half-filled valence energy band. Therefore, the common belief that the classical (two sublattice) model of antiferromagnetism cannot apply to the valence electrons of close-packed metals — because their atomic lattices contain triangles — is incorrect.

Appendix A. Details of the Calculations

1. The Frozen Core Approximation

The frozen core approximation can be described briefly as follows (more detail is given elsewhere).[10]

First, both the core orbitals and the valence orbitals are optimized simultaneously for the valence high-spin state (chosen since the HF and UHF valence wavefunctions are identical for high-spin). The core orbitals optimized for the high-spin state are then used to construct the valence hamiltonian

$$\begin{aligned} \widehat{\mathcal{H}} &= E_N^{CORE} + \sum_{i=1}^{N} \hat{h}(i) + \sum_{i>j}^{N} \frac{1}{r_{ij}} \\ \hat{h}(i) &= -\frac{1}{2}\widehat{\nabla}_i^2 + \hat{V}(\vec{r}_i) + \hat{V}^{CORE} \\ \hat{V}^{CORE} &= \sum_c (2\hat{J}_c - \hat{K}_c) \end{aligned}$$

where (i) E_N^{CORE} includes the nuclear repulsion energy and all one-electron and two-electron energy terms involving only the core electrons {the [Ar]$3d^{10}$, [Kr]$4d^{10}$,

$[Xe]4f^{14}5d^{10}$, $1s^2$, and $1s^22s^22p^6$ shells for Cu, Ag, Au, Li, and Na,[25] respectively},[10] (*ii*) the "one-electron" operator $\hat{h}(i)$ includes the electronic kinetic energy ($-\frac{1}{2}\hat{\nabla}^2$), the electron-nuclear attraction [$\hat{V}(\vec{r}\,)$], and all two-electron interactions [coulomb ($\hat{J}$) and exchange ($\hat{K}$)] between core electrons and valence electrons ($\hat{V}^{CORE}$),[26] and (*iii*) r_{ij}^{-1} is the electrostatic interaction between electrons i and j (r_{ij} is the distance between electrons i and j).

This hamiltonian is then used for the self-consistent field (SCF) optimizations (energy minimization) of many-electron wavefunctions for the other magnetizations.

This frozen core approximation is exact for the high-spin state.[26] For the other magnetizations, total energies calculated with the frozen core approximation are somewhat higher than those calculated by the usual method of optimizing all orbitals self-consistently because the optimum core orbital shapes are not independent of the valence magnetization. However, the frozen core approximation is reasonably accurate for the low-spin states,[10] and hence, the frozen core approximation is expected to be reasonably accurate for magnetizations from zero to one unpaired valence electrons per atom ($0 \leq \mu \leq 1$).

2. Hartree-Fock Wavefunctions

The UHF and HF many-electron valence wavefunctions for the various M_N ring clusters can all be written in the general form

$$\begin{aligned} \Psi_{N,A} &= \hat{\mathcal{A}}[\Phi_{N,A}\,\chi_{N,A}] \qquad \text{(A1)} \\ \hat{\mathcal{A}} &= \sum_{\tau} \zeta_\tau \tau \\ \Phi_{N,A} &= \varphi_1(1)\varphi_2(2)\varphi_3(3)\cdots\varphi_N(N) \\ \chi_{N,A}^{HF} &= \chi_{N,A}^{UHF} = \alpha(1)\alpha(2)\cdots\alpha(A)\beta(A+1)\beta(A+2)\cdots\beta(N) \end{aligned}$$

where (i) $\hat{\mathcal{A}}$ is the antisymmetrizer or determinantal operator [where the summation is over all $N!$ permutations

$$\tau f(1,2,3,\ldots,N) = f(i_1,i_2,i_3,\ldots,i_N),\ 1 \leq i_j \leq N$$

of the electronic coordinates $(1,2,3,\ldots,N)$ and ζ_τ is the parity of permutation τ], (ii) $\Phi_{N,A}$ is the many-electron spatial product function, where $\{\varphi_i\}$ are the canonical valence one-electron orbitals (a separate set is optimized for each state A), and (iii) $\chi_{N,A}$ is the many-electron spin function, where α and β are the up-spin ($\uparrow$) and down-spin ($\downarrow$) one-electron spin functions, respectively (A and B are the number of valence electrons with spins α and β, respectively; $A+B=N$).

For wavefunctions such as (A1) where both Φ and χ are products of one-electron functions, $\hat{\mathcal{A}}$ forms a single Slater determinant. For brevity, the electron coordinates are often omitted. Hence, the orbital product is ordered such that the electron coordinates are sequential (the electron coordinates and the orbital subscripts are independent), e.g.,

$$\varphi_3\varphi_1\varphi_4\ldots \equiv \varphi_3(1)\varphi_1(2)\varphi_4(3)\ldots$$

$$\chi_{N,A}^{HF} = \chi_{N,A}^{UHF} = \alpha^A\beta^B.$$

The HF and UHF wavefunctions differ in the orbital restrictions as follows.

HF: Orbitals of opposite spin are forced to be equal

$$\varphi_{A+i} = \varphi_i,\ i = 1,2,\ldots,B$$

($A \geq B$; some orbitals are doubly-occupied). In addition, the $\{\varphi_i\}$ are restricted to be orthonormal

$$\langle\varphi_i|\varphi_j\rangle = \delta_{ij},\ i,j \leq A.$$

These restrictions ensure that the wavefunction is an eigenfunction of $\widehat{S}^2$

$$\begin{aligned} \widehat{S}^2\Psi^{HF}_{N,A} &= S(S+1)\hbar^2\Psi^{HF}_{N,A} \\ S &= \frac{|A-B|}{2} \end{aligned} \tag{A2}$$

where $\widehat{S}^2$ and S are the total (many-electron) spin angular momentum operator and quantum number, respectively.

UHF: Orbitals are optimized without any restrictions, generally leading to many-electron wavefunctions that are *not* eigenfunctions of $\widehat{S}^2$ (A2). However, both $\Psi^{UHF}_{N,A}$ and $\Psi^{HF}_{N,A}$ are eigenfunctions of $\widehat{S}_z$

$$\begin{aligned} \widehat{S}^2 &= \widehat{S}^2_x + \widehat{S}^2_y + \widehat{S}^2_z \\ \widehat{S}_z\Psi_{N,A} &= M_S\hbar\Psi_{N,A} \\ M_S &= \frac{A-B}{2} \end{aligned}$$

where $\widehat{S}_z$ and M_S are the total (many-electron) spin angular momentum projection operator and quantum number, respectively.

3. The Hartree-Fock Energy Expression

For determinantal wavefunctions (A1) the total energy expression

$$E_{N,A} = \frac{\langle\Psi_{N,A}|\widehat{\mathcal{H}}|\Psi_{N,A}\rangle}{\langle\Psi_{N,A}|\Psi_{N,A}\rangle}$$

can be simplified as

$$\begin{aligned} E_{N,A} &= \langle\Phi_{N,A}\,\chi_{N,A}|\widehat{\mathcal{H}}|\Psi_{N,A}\rangle = \sum_\tau \langle\Phi_{N,A}|\widehat{\mathcal{H}}|\tau\Phi_{N,A}\rangle U_\tau \\ U_\tau &= \zeta_\tau\langle\chi_{N,A}|\tau\chi_{N,A}\rangle \end{aligned} \tag{A3}$$

where the normalization of $\Psi_{N,A}$ is defined with respect to

$$\langle\Phi_{N,A}\,\chi_{N,A}|\Psi_{N,A}\rangle = \sum_\tau \langle\Phi_{N,A}|\tau\Phi_{N,A}\rangle U_\tau = 1.$$

For cases where the spin function is a product of single particle spin functions such as χ^{HF}, U_τ is zero for permutations that interchange α and β spin functions, and hence, the energy expression can be further simplified as

$$E_{N,A} = \sum_{\tau_A} \sum_{\tau_B} \langle \Phi_{N,A} | \widehat{\mathcal{H}} | \tau_A \tau_B \Phi_{N,A} \rangle U_{\tau_A} U_{\tau_B} \tag{A4}$$

where τ_A are permutations of the coordinates $\{1, 2, \ldots, A\}$, τ_B are permutations of the coordinates $\{A+1, A+2, \ldots, N\}$, and

$$U_{\tau_A} U_{\tau_B} = \zeta_{\tau_A} \zeta_{\tau_B} \langle \chi_{N,A} | \tau_A \tau_B \chi_{N,A} \rangle = \zeta_{\tau_A} \zeta_{\tau_B}.$$

Single determinant wavefunctions are invariant to separate linear transformations of the α-spin and β-spin orbitals (followed by renormalization), e.g.,

$$\widehat{\mathcal{A}} [\varphi_1(1) \cdots \varphi_i(i) \cdots \varphi_j(j) \cdots \varphi_N(N)\ \chi_{N,A}] =$$

$$\widehat{\mathcal{A}} [\varphi_1(1) \cdots [\varphi_i(i) + \lambda \varphi_j(i)] \cdots \varphi_j(j) \cdots \varphi_N(N)\ \chi_{N,A}] \tag{A5}$$

for $i < j \leq A$ or for $A+1 \leq i < j$. Hence, wavefunctions written in terms of delocalized canonical orbitals $\{\varphi_i\}$ have equivalent forms in terms of localized orbitals $\{\phi_i\}$.

The HF and UHF wavefunctions written in terms of the $\{\varphi_i\}$ lead to the same energy expression

$$\begin{aligned} E_{N,A} &= E_N^{CORE} + \sum_{i=1}^{N} h_{ii} + \sum_{i>j}^{N} J_{ij} - \sum_{i>j}^{A} K_{ij} - \sum_{i>j>A}^{N} K_{ij} \qquad \text{(A6)} \\ h_{ij} &= \langle \varphi_i(1) | \widehat{h}(1) | \varphi_j(1) \rangle \\ J_{ij} &= \langle \varphi_i(1) \varphi_j(2) | \frac{1}{r_{12}} | \varphi_i(1) \varphi_j(2) \rangle \\ K_{ij} &= \langle \varphi_i(1) \varphi_j(2) | \frac{1}{r_{12}} | \varphi_j(1) \varphi_i(2) \rangle \end{aligned}$$

where h_{ij} is the "one-electron" integral, and J_{ij} and K_{ij} are the two-electron coulomb and exchange integrals, respectively.

Appendix B. The Generalized Ising Energy Expression

Here we derive the generalized Ising energy expression providing an accurate fit of the UHF magnon spectrum for each of the Cu_{10}, Ag_6, Ag_8, Ag_{10}, Au_{10}, Li_6, Li_{10}, Li_{14}, and Na_{10} ring clusters. The generalized Ising energy expression is expected to be useful for any system where a range of magnetizations can be described by a single set of singly-occupied orbitals $\{\phi_i\}$. Hence, the M_N ring clusters are ideal cases since the Hartree orbitals[11] $\{\phi_i\}$ optimized for low-spin ($\mu = 0$, Figure 2a) are very similar to those optimized for high-spin ($\mu = 1$, Figure 2b).

1. Two Electrons

For a system having two valence electrons ($N = 2$) such as the Cu_3^+, Ag_3^+, Au_3^+, Li_3^+, and Na_3^+ linear chain clusters, the UHF wavefunctions

$$\Psi_{2,2}^{UHF} = \hat{\mathcal{A}}[(\phi_1\phi_2)(\alpha\alpha)] = (\phi_1\phi_2 - \phi_2\phi_1)(\alpha\alpha)/\sqrt{2-2\mathcal{S}_{12}^2}$$

$$\Psi_{2,1}^{UHF} = \hat{\mathcal{A}}[(\phi_1\phi_2)(\alpha\beta)] = (\phi_1\phi_2)(\alpha\beta) - (\phi_2\phi_1)(\beta\alpha)$$

and the generalized valence bond (GVB) wavefunctions

$$\Psi_{2,S=1}^{GVB} = \hat{\mathcal{A}}[(\phi_1\phi_2)(\alpha\beta+\beta\alpha)] = (\phi_1\phi_2 - \phi_2\phi_1)(\alpha\beta+\beta\alpha)/\sqrt{2-2\mathcal{S}_{12}^2}$$

$$\Psi_{2,S=0}^{GVB} = \hat{\mathcal{A}}[(\phi_1\phi_2)(\alpha\beta-\beta\alpha)] = (\phi_1\phi_2 + \phi_2\phi_1)(\alpha\beta-\beta\alpha)/\sqrt{2+2\mathcal{S}_{12}^2}$$

can all be described fairly accurately with the *same* product of two overlapping valence orbitals

$$\Phi = \phi_1\phi_2$$

$$\mathcal{S}_{ij} = \langle\phi_i|\phi_j\rangle.$$

For each of the Cu_3^+, Ag_3^+, Au_3^+, Li_3^+, and Na_3^+ linear chain clusters, ϕ_1 and ϕ_2 are localized at the left and right bond midpoints, respectively (see Figure 1b), and the optimum shapes of ϕ_1 and ϕ_2 do not depend crucially on the spin function, χ (as shown quantitatively in Appendix C, Table 5).

These wavefunctions all lead to the energy expression[27]

$$E_2 = E^{CORE} + E^{CL} + \frac{U_{12}\mathcal{J}_{12}}{1 + U_{12}S_{12}^2} \tag{B1}$$

$$E^{CL} = \langle\phi_i\phi_j|\widehat{\mathcal{H}}|\phi_i\phi_j\rangle - E^{CORE} = h_{11} + h_{22} + J_{12}$$

$$\mathcal{J}_{ij} = \langle\phi_i\phi_j|\widehat{\mathcal{H}}|\phi_j\phi_i\rangle - S_{ij}^2 E^{CORE} - S_{ij}^2 E^{CL} \tag{B2}$$

$$= 2S_{ij}h_{ij} + K_{ij} - S_{ij}^2 E^{CL}$$

where E^{CL} is the electronic energy of the classical (Hartree product) wavefunction,[27] U_{ij} is the coefficient for the exchange of orbitals i and j and is the only spin-dependent term ($U_{12} = -1$, 0, -1, and $+1$ for $\Psi_{2,2}^{UHF}$, $\Psi_{2,1}^{UHF}$, $\Psi_{2,S=1}^{GVB}$, and $\Psi_{2,S=0}^{GVB}$, respectively), and $\mathcal{J}_{ij}$ is the *valence bond exchange term*[27] (h_{ij}, J_{ij}, and K_{ij} have the same definitions as in Appendix A.3 except that the $\{\phi_i\}$ are used in place of the $\{\varphi_i\}$).

A singlet ground state results if $\mathcal{J}_{12}$ is negative, occurring for nearly all cases where $S_{12} \neq 0$ (as in bonding). If $S_{12} = 0$, then $\mathcal{J}_{12} = K_{12}$ is positive, leading to a triplet ground state. [These conditions are consistent with Hund's rule, which states that the lowest energy state for a configuration containing orthogonal (non-overlapping) singly-occupied orbitals is the state of highest spin multiplicity (e.g., for the $1s^2 2s^2 2p^2$ carbon atom, the lowest energy state is triplet).] Note that for $S_{ij} \neq 0$ the valence bond exchange term $\mathcal{J}_{ij}$ is not equal to the two-electron exchange integral K_{ij}. Also, for $S_{12} = 1$ ($\phi_1 = \phi_2$, $K_{12} = J_{12}$), we obtain $\Psi_{2,S=0}^{GVB} = \Psi_{2,1}^{UHF} = \Psi_{2,1}^{HF}$ and $E_2 = E_2^{HF} = E_2^{CL}$ for all U_{12}.

2. M_N Ring Clusters

The $\Psi_{N,A}^{UHF}$ for the various magnetizations (μ) of the M_N ring clusters can all be described fairly accurately with the same spatial configuration

$$\Phi = \phi_1\phi_2\phi_3\cdots\phi_N \tag{B3}$$

but with the one-electron spin functions flipped from α to β as μ is decreased, as follows (for M_{10}; also see Figure 5).

$$\begin{aligned}
\chi_{10,10} &= \alpha^{10} \qquad\qquad (B4)\\
\chi_{10,9} &= \alpha^9\beta\\
\chi_{10,8} &= (\alpha^4\beta)(\alpha^4\beta)\\
\chi_{10,7} &= (\alpha^2\beta)(\alpha^2\beta)(\alpha^3\beta)\\
\chi_{10,6} &= (\alpha^2\beta)(\alpha\beta)(\alpha^2\beta)(\alpha\beta)\\
\chi_{10,5} &= (\alpha\beta)^5
\end{aligned}$$

Hence, except for high-spin ($A = N$), UHF leads to a spin density wave.

In terms of the $\{\phi_i\}$, the α-spin orbitals and the β-spin orbitals of $\Psi_{N,A}^{UHF}$ are configured in such a manner that $|A - B| = \mu N$ nearest-neighbor exchange interactions are α-α (or β-β; $U_{i,i+1} = -1$, antibonding) and $N - |A - B|$ nearest-neighbor exchange interactions are α-β ($U_{i,i+1} = 0$, nonbonding).

Applying the general energy expression (A3) of Appendix A.3 to (B3, B4) with the assumptions that (i) non-nearest neighbor overlap and exchange integrals are zero, e.g.,

$$\begin{aligned}
S_{i,i\pm1} &\gg S_{i,i\pm j} \approx 0,\ |j| \geq 2\\
\mathcal{J}_{i,i\pm1} &\gg \mathcal{J}_{i,i\pm j} \approx 0,\ |j| \geq 2
\end{aligned}$$

and (ii) the ϕ_i are all equivalent, e.g.,

$$\begin{aligned} \phi_j &= \widehat{C}_N^{(j-i)}\phi_i \\ \mathcal{J}_{i,i\pm1} &= \mathcal{J}_{12},\ i = 1,2,\ldots,N \\ \mathcal{S}_{i,i\pm1} &= \mathcal{S}_{12},\ i = 1,2,\ldots,N \end{aligned}$$

where $\widehat{C}_N$ perfoms a rotation of $\theta = 2\pi/N$ about the C_N rotational symmetry axis, leads to the approximate energy expression

$$E_{N,A} = E^{CORE} + E_N^{CL} - \frac{\mu N \mathcal{J}_{12}[1+\mathcal{R}]}{1-\mu N \mathcal{S}_{12}^2[1+\mathcal{R}]} \tag{B5}$$

$$E_N^{CL} = \langle\Phi|\widehat{\mathcal{H}}|\Phi\rangle - E^{CORE} = \sum_{i=1}^{N} h_{ii} + \sum_{i\neq j}^{N} J_{ij}$$

$$\mathcal{R} \approx \sum_{i=1}^{N/2-1} \mathcal{O}[\mu^i (N-2i)^i \mathcal{S}_{12}^{2i}] \tag{B6}$$

where $\mathcal{R}$ represents the approximate dependence of the higher order terms.

Since the exchange operator

$$\tau_{ij}\ \chi(1,2,\ldots,i,\ldots,j,\ldots,N) = \chi(1,2,\ldots,j,\ldots,i,\ldots,N)$$

is equivalent to the spin operator $1/2 + 2\vec{s}_i \cdot \vec{s}_j$,[28] Equation (B5) leads to a generalization of the nearest-neighbor *Ising model* (IM)[15]

$$E_{N,A}^{IM} = E_N^{CORE} + E_N^{CL} - \mathcal{J}\sum_{i=1}^{N} 1/2 + 2s_{z_i}s_{z_{i+1}}$$

where the s_{z_i} is the z-component of $\vec{s}_i$ ($s_{z_i} = m_{s_i} = \pm 1/2$ for UHF).

The untruncated energy expression Equation (B5) is not useful for large N because of the importance of the higher order terms (B6). In addition, $\mathcal{J}_{12}$ as defined by Equation (B2) is not a useful quantity for large N, e.g.,

$$\lim_{N\to\infty} \mathcal{J}_{12} = \lim_{N\to\infty} -\mathcal{S}_{12}^2 E_N^{CL} = +\infty.$$

Hence, we have employed the following truncations of Equation (B5) for fitting UHF results for the various M_{10} ring clusters:

$$\begin{aligned} E_{N,A}^{IM} &= E^{CORE} + E^{CL} - \mu N \mathcal{J} \\ E_{N,A}^{GIM1} &= E^{CORE} + E^{CL} - \frac{\mu N \mathcal{J}}{1 - \mu N \mathcal{S}^2} \\ E_{N,A}^{GIM2} &= E^{CORE} + E^{CL} - \mu N \mathcal{J}(1 + \mu N \mathcal{S}^2) \end{aligned}$$

where E^{CL}, $\mathcal{S}$ and $\mathcal{J}$ (without subscripts) refer to "effective" values of the classical energy, nearest-neighbor overlap integral, and nearest-neighbor exchange energy, respectively, and are assumed to have values that are independent of μ and include relaxation effects. E^{IM} (Ising model) is obtained from (B5) by taking $\mathcal{S} = 0$. The generalized Ising models (GIM) result from $\mathcal{S} \neq 0$. E^{GIM1} is obtained by truncating (B5) (taking $\mathcal{R} = 0$; E^{GIM1} is "exact" for $N = 2$), and E^{GIM2} is a truncated Taylor's expansion of (B5) (for $\mathcal{S} = 0$, $E^{IM} = E^{GIM1} = E^{GIM2}$).

Appendix C. UHF Results for Linear M_3^+ Clusters

Here we present results for the Cu_3^+, Ag_3^+, Au_3^+, Li_3^+, and Na_3^+ linear chain clusters, since (*i*) they are rather simple models of the respective infinite linear chains — in each case the localized orbitals for linear M_3^+ (Figure 1b) and for M_{10} (Figures 2a-b) are remarkably similar — and (*ii*) they each contain two valence electrons, hence the higher order terms ($\mathcal{R}$) in the general energy expression (B5) are avoided; see Equation (B1).

For each of these M_3^+ linear chain clusters, Table 5 presents the overlap of adjacent localized orbitals ($\mathcal{S}_{12}$) and the magnon dispersion energy

$$\mathcal{D} = E_{2,\mu=1}^{UHF} - E_{2,\mu=0}^{UHF}$$

(i.e., the "singlet-triplet gap").

In order to evaluate the usefulness of Equation (B1) for linear M_3^+, we compare the fully self-consistent UHF values of $\mathcal{D}$ (where valence orbitals are optimized separately for each state) with the "frozen orbital" UHF magnon dispersion energies

$$\mathcal{D}^{FROZEN} = \frac{-\mathcal{J}_{12}}{1 - \mathcal{S}_{12}^2}$$

(where the localized valence orbitals optimized for $\mu = 0$ are used to describe the $\mu = 1$ state). The self-consistent $\mathcal{D}$ values are smaller than the frozen orbital $\mathcal{D}$ values by only 5 - 11%; hence, both magnetizations can be described fairly well using a single set of localized orbitals.

Figure 21 shows that the values of $\mathcal{D}$ and $\mathcal{S}_{12}$ for M_3^+ follow the same overall trend (Cu > Au > Ag > Na > Li) as the values of $\mathcal{D}/10$ and $\mathcal{S}_{12}$ for M_{10} (with one exception — $\mathcal{D}$ for Au_3^+ and Ag_3^+ are reversed). In order to compare values of $\mathcal{D}$ for linear M_3^+ and for the M_N ring, we divide each value by the number of nearest-neighbor exchange interactions (one for M_3^+ and N for M_N).

The values $\mathcal{D}$ and $\mathcal{S}_{12}$ for M_3^+ are somewhat smaller than the respective values $\mathcal{D}/10$ and $\mathcal{S}_{12}$ for M_{10}. This is because (*i*) $\mathcal{D}$ and $\mathcal{S}_{12}$ both decrease as the distance between adjacent orbitals increases, and (*ii*) the effective distance between adjacent orbitals is larger for M_3^+ than for the M_N ring (for constant a). For M_3^+, the orbitals are not centered at the exact bond midpoints but are polarized somewhat away from one another (see Figure 2b); hence, for M_3^+ the effective distance between adjacent orbitals is somewhat larger than a. However, for the M_N ring, the effective distance between adjacent orbitals is somewhat smaller than a since the orbitals are centered at the bond midpoints and the distance between adjacent bond midpoints $[R^{BM} = a\cos(\pi/N)]$ is somewhat smaller than a for finite N. Hence, for the M_N

ring, both $\mathcal{D}/N$ and $\mathcal{S}_{12}$ decrease somewhat with increasing N (for constant a; see Table 2).

Appendix D. Ionic Character of HF wavefunctions

For magnetizations $0 \leq \mu < 1$, restricted Hartree-Fock (HF) leads to incorrect results such as (*i*) a charge density wave and Peierls instability for each of the Ag_8, Li_{10}, and Li_{14} $\mu = 0$ (low-spin) symmetric ring clusters,[10,11,12] (*ii*) a charge density wave and a negative atomization energy for the Na_{10} $\mu = 0$ ring cluster,[10] (*iii*) charge and spin density waves for all intermediate magnetizations ($0 < \mu < 1$) of Cu_{10}, Ag_6, Ag_8, Ag_{10}, Au_{10}, Li_6, Li_{10}, Li_{14}, and Na_{10} (see Section II.E), and (*iv*) ground states for Ag_8, Na_{10}, Li_6, Li_{10}, and Li_{14} having 0.25, 0.6, 1.0, 1.0, and 1.0 unpaired electrons per atom, respectively (see Table 1 and Figures 8-10).

These problems indicate a fundamental flaw in HF for these systems, and that flaw is the double occupation of valence orbitals for describing magnetizations $0 \leq \mu < 1$. To elucidate problems with HF, we expand the HF wavefunctions in terms of the localized Wannier orbitals $\{\omega_j\}$.[15,11]

The HF $\mu = 1$ (high-spin) wavefunction can be described by a single covalent configuration in terms of the $\{\omega_j\}$,

$$\omega_1(\uparrow)\omega_2(\uparrow)\omega_3(\uparrow)\omega_4(\uparrow)\omega_5(\uparrow)\omega_6(\uparrow)\omega_7(\uparrow)\omega_8(\uparrow)\omega_9(\uparrow)\omega_{10}(\uparrow)$$

(see Section II.A). For $0 \leq \mu < 1$, doubly-occupied valence orbitals present in the HF wavefunction lead to a mixture of covalent configurations (having each ω_j singly-occupied) and ionic configurations[11] — configurations containing doubly-occupied and empty ω_j such as

$$\omega_1(\uparrow\downarrow)\omega_2(\ \ )\omega_3(\uparrow)\omega_4(\downarrow)\omega_5(\uparrow)\omega_6(\uparrow)\omega_7(\uparrow)\omega_8(\downarrow)\omega_9(\uparrow)\omega_{10}(\uparrow)$$

where ω_1 is doubly occupied and ω_2 is empty (for each neutral ionic configuration, the number of doubly-occupied orbitals and holes is equal).

For magnetization μ, HF has $B = N(1-\mu)/2$ doubly-occupied valence canonical orbitals, leading to configurations (in terms of $\{\omega_j\}$) having $0 \leq I \leq B$ doubly-occupied orbitals. The distributions of covalent and ionic configurations depend on the orbital symmetry restriction, and are given in Table 6 for all allowed magnetizations of M_N (for even values of $N \leq 10$).

For $0 < \mu < 1$, allowing the valence orbitals to localize reduces the average number of doubly-occupied ω_j per configuration ($\langle I \rangle$; see Table 6) leading to a lower total energy even though this results in charge and spin density waves (orbital symmetry breaking).

1. HF Without Symmetry Restrictions

The HF wavefunctions optimized without orbital symmetry restrictions lead to charge density waves (broken symmetry orbitals) for all intermediate magnetizations $0 < \mu < 1$ of the Ag_6, Ag_8, Cu_{10}, Ag_{10}, Au_{10}, Li_6, Li_{10}, Li_{14}, and Na_{10} ring clusters, and also for $\mu = 0$ states of Ag_8, Li_{10}, Li_{14}, and Na_{10} (see Table 4 and Figures 11-18).

The HF wavefunctions containing charge density waves [labelled $\Psi_{N,A}^{HF(C_s)}$] can be written in terms of localized orthogonal (Wannier-like) orbitals $\{\omega_i\}$ by performing separate orthogonal localizations[11] of the singly-occupied and doubly-occupied canonical orbitals. In terms of the $\{\omega_i\}$, the HF(C_s) wavefunctions for the various magnetizations of M_{10} are

$$\Psi_{10,9}^{HF(C_s)} = \hat{\mathcal{A}}\left[(\omega_{1+2}\omega_3\omega_4\omega_5\omega_6\omega_7\omega_8\omega_9\omega_{10}\omega_{1+2})(\alpha^9\beta)\right]$$

$$\Psi_{10,8}^{HF(C_s)} = \hat{\mathcal{A}}\left[(\omega_{1+2}\omega_{6+7}\omega_3\omega_4\omega_5\omega_8\omega_9\omega_{10}\omega_{1+2}\omega_{6+7})(\alpha^8\beta^2)\right]$$

$$\Psi_{10,7}^{HF(C_s)} = \hat{\mathcal{A}}\left[(\omega_{1+2}\omega_{4+5}\omega_{8+9}\omega_3\omega_6\omega_7\omega_{10}\omega_{1+2}\omega_{4+5}\omega_{8+9})(\alpha^7\beta^3)\right]$$

$$\Psi_{10,6}^{HF(C_s)} = \hat{\mathcal{A}}\left[(\omega_{1+2}\omega_{3+4}\omega_{6+7}\omega_{8+9}\omega_5\omega_{10}\omega_{1+2}\omega_{3+4}\omega_{6+7}\omega_{8+9})(\alpha^6\beta^4)\right]$$

$$\Psi_{10,5}^{HF(C_s)} = \hat{\mathcal{A}}\left[(\omega_{1+2}\omega_{3+4}\omega_{5+6}\omega_{7+8}\omega_{9+10}\omega_{1+2}\omega_{3+4}\omega_{5+6}\omega_{7+8}\omega_{9+10})(\alpha^5\beta^5)\right]$$

where

$$\omega_{i\pm j} \equiv \frac{\omega_i \pm \omega_j}{\sqrt{2}}$$

$$\omega_{i\pm j}\omega_{i\pm j} = \frac{(\omega_i\omega_i + \omega_j\omega_j) \pm (\omega_i\omega_j + \omega_j\omega_i)}{2}.$$

Hence, for $\Psi_{N,A}^{HF(C_s)}$, the doubly-occupied orbitals break symmetry in such a manner that (*i*) each doubly-occupied canonical orbital leads to 50% ionic and 50% covalent *local* character, and (*ii*) each ionic configuration has the property that each doubly-occupied orbital is adjacent to at least one hole.

For $\Psi_{N,A}^{HF(C_s)}$, expanding the B doubly-occupied orbitals in terms of the $\{\omega_i\}$ results in 2^{2B} configurations all of which survive antisymmetrization. The number of configurations having I doubly-occupied ω_i is

$$n_I = \binom{B}{I} 2^B$$

and the average number of doubly-occupied orbitals per configuration is

$$\langle I \rangle = \frac{B}{2} = \frac{N(1-\mu)}{4}$$

(values of n_I and $\langle I \rangle$ are given in Table 6 for $B \leq 5$).

2. D_{Nh} symmetry-restricted HF

For M_N, the D_{Nh} symmetry restricted HF wavefunctions are composed of complex Bloch orbitals (2),[17] leading always to fully symmetrical charge densities.[10] For the

various magnetizations of M_{10}, the HF(D_{10h}) wavefunctions are as follows.

$$\begin{aligned}
\Psi_{10,10}^{HF(D_{10h})} &= \hat{\mathcal{A}}\left[(\psi_0\psi_1\psi_{-1}\psi_2\psi_{-2}\psi_3\psi_{-3}\psi_4\psi_{-4}\psi_5)(\alpha^{10})\right] \\
\Psi_{10,9}^{HF(D_{10h})} &= \hat{\mathcal{A}}\left[(\psi_0\psi_1\psi_{-1}\psi_2\psi_{-2}\psi_3\psi_{-3}\psi_4\psi_{-4}\psi_0)(\alpha^{9}\beta)\right] \\
\Psi_{10,8}^{HF(D_{10h})} &= \hat{\mathcal{A}}\left[(\psi_0\psi_1\psi_{-1}\psi_2\psi_{-2}\psi_3\psi_{-3}\psi_4\psi_0\psi_1)(\alpha^{8}\beta^{2})\right] \\
\Psi_{10,7}^{HF(D_{10h})} &= \hat{\mathcal{A}}\left[(\psi_0\psi_1\psi_{-1}\psi_2\psi_{-2}\psi_3\psi_{-3}\psi_0\psi_1\psi_{-1})(\alpha^{7}\beta^{3})\right] \\
\Psi_{10,6}^{HF(D_{10h})} &= \hat{\mathcal{A}}\left[(\psi_0\psi_1\psi_{-1}\psi_2\psi_{-2}\psi_3\psi_0\psi_1\psi_{-1}\psi_2)(\alpha^{6}\beta^{4})\right] \\
\Psi_{10,5}^{HF(D_{10h})} &= \hat{\mathcal{A}}\left[(\psi_0\psi_1\psi_{-1}\psi_2\psi_{-2}\psi_0\psi_1\psi_{-1}\psi_2\psi_{-2})(\alpha^{5}\beta^{5})\right].
\end{aligned}$$

For $\Psi_{N,A}^{HF(D_{Nh})}$, each Bloch orbital ψ_m contains equal contributions from all N Wannier orbitals $\{\omega_i\}$; hence, expanding each ψ_m in terms of the $\{\omega_i\}$ results in N^N configurations of which $\binom{N}{A}\,N!$ survive antisymmetrization — configurations where two electrons of the same spin occupy the same orbital such as

$$(\omega_1\alpha)\cdots(\omega_j\alpha)\cdots(\omega_j\alpha)\cdots(\omega_N\alpha)$$

are deleted by the antisymmetrizer. The number of configurations having I doubly-occupied ω_i is

$$n_I = \binom{A}{I}\binom{B}{I}N!$$

and the average number of doubly-occupied orbitals per configuration is

$$\langle I\rangle = \frac{NB - B^2}{N} = \frac{N(1-\mu^2)}{4}$$

(values of n_I and $\langle I\rangle$ are given in Table 6 for even values of $N \leq 10$).

In comparison to HF with no symmetry restrictions, imposing full (D_{Nh}) orbital symmetry restrictions results in a substantial increase of $\langle I\rangle$ for $0 < \mu < 1$, and, in addition, the orientations of the doubly-occupied orbitals and holes are no longer favorably correlated.

Appendix E. HF States with a Single Reversed Spin

In this appendix, we analyse the HF states having $(N-1)$ up-spin electrons and one down-spin electron ($A = N-1$; $B = 1$). The HF valence wavefunctions for these states contain $(N-2)$ singly-occupied orbitals and one doubly-occupied orbital. Allowing the valence orbitals to localize reduces the amount of ionic character (*vide infra*) leading to a lower total energy even though this results in a charge density wave (orbital symmetry breaking).

1. The Wavefunctions

The HF wavefunctions for the $B = 1$ ($A = 9$) state of M_{10} can be written as follows.

$$\Psi_{10,9}^{HF(C_s)} = \hat{\mathcal{A}}\left[(\omega_{1+2}\omega_3\omega_4\omega_5\omega_6\omega_7\omega_8\omega_9\omega_{10}\omega_{1+2})(\alpha^9\beta)\right] \quad \text{(E1)}$$

$$\Psi_{10,9}^{HF(C_{2h})} = \hat{\mathcal{A}}\left[(\omega_{1+6}\omega_2\omega_3\omega_4\omega_5\omega_7\omega_8\omega_9\omega_{10}\omega_{1+6})(\alpha^9\beta)\right] \quad \text{(E2)}$$

$$\Psi_{10,9}^{HF(D_{10h})} = \hat{\mathcal{A}}\left[(\psi_0\psi_1\psi_{-1}\psi_2\psi_{-2}\psi_3\psi_{-3}\psi_4\psi_{-4}\psi_0)(\alpha^9\beta)\right] \quad \text{(E3)}$$

Wavefunctions $\Psi_{10,9}^{HF(C_s)}$ and $\Psi_{10,9}^{HF(C_{2h})}$ each involve a doubly-occupied orbital spread out over two bond midpoints, leading to $\langle I \rangle = 0.5$ (50% ionic character and 50% covalent character; see Appendix D).

Wavefunction $\Psi_{10,9}^{HF(D_{10h})}$ is obtained from $\Psi_{10,10}^{HF(D_{10h})}$ (3) by removing the electron from the highest energy band orbital (ψ_5), reversing its spin, and placing it into the lowest energy band orbital (ψ_0). Expanding the product of the first nine orbitals of $\Psi_{10,9}^{HF(D_{10h})}$ in terms of the $\{\omega_j\}$ results in a total of 10^9 configurations, of which 10! (3,628,800) survive antisymmetrization. Each of these 10! configurations involves

nine singly-occupied ω_j and one hole, thus multiplying by $\psi_0\beta$ results in $\langle I \rangle = 0.9$ (90% ionic configurations and 10% covalent configurations, all surviving $\widehat{\mathcal{A}}$).

2. Energy Analysis for M_{10}

Here, we analyse the energetic effects of the ionic configurations for M_{10}, using the high-spin $\{\omega_i\}$ to describe both the high-spin ($B = 0,\ A = 10$) and the next-highest-spin ($B = 1,\ A = 9$) HF states.

The energy of the high-spin state (5) is

$$E^{HF}_{10,10} = \sum_{i=1}^{10} h^{\omega}_{ii} + \frac{1}{2}\sum_{i\neq j}^{10} J^{\omega}_{ij} - K^{\omega}_{ij}$$

where h^{ω}_{ij} is the one-electron integral, and J^{ω}_{ij} and K^{ω}_{ij} are the two-electron coulomb and exchange integrals, respectively (h^{ω}_{ij}, J^{ω}_{ij}, and K^{ω}_{ij} have the same definitions as in Appendix A.3 except that the integrals are over the $\{\omega_j\}$; values are tabulated in Tables 7-8 for the various ring clusters). Because of the cyclical nature of the $\{\omega_j\}$, the energy expression can be simplified as

$$\begin{aligned} E^{HF}_{10,10} &= 10h^{\omega}_{11} + 5\sum_{j=2}^{10} J^{\omega}_{1j} - K^{\omega}_{1j} \\ &\approx 10h^{\omega}_{11} + 5\sum_{j=2}^{10} J^{\omega}_{1j} - 10K^{\omega}_{12} \end{aligned}$$

where non-nearest neighbor exchange integrals are neglected (for Cu_{10}, Ag_{10}, Au_{10}, Li_{10}, and Na_{10}, $0.021 \leq K^{\omega}_{13}/K^{\omega}_{12} \leq 0.134$; see Table 8).

For each of the $B = 1$ states, the ionic configurations stabilize the total one-electron energy (relative to that of the $B = 0$ state) as follows.

$$\begin{aligned} E^{ONE(C_3)}_{10,9} - E^{ONE}_{10,10} &= 2h^{\omega}_{12} \\ E^{ONE(C_{2h})}_{10,9} - E^{ONE}_{10,10} &= 2h^{\omega}_{16} \end{aligned}$$

$$E_{10,9}^{ONE(D_{10h})} - E_{10,10}^{ONE} = \langle\psi_0|\hat{h}|\psi_0\rangle - \langle\psi_5|\hat{h}|\psi_5\rangle$$
$$= 4h_{12}^{\omega} + 4h_{14}^{\omega} + 2h_{16}^{\omega}$$

Since the relation $|h_{12}^{\omega}| \gg |h_{14}^{\omega}| > |h_{16}^{\omega}|$ holds true for all cases that we considered (see Table 7), the one-electron contributions to the total energy strongly favor the fully symmetrical state (D_{10h}) over the charge density wave states (C_s or C_{2h}).

However, ionic configurations destabilize the total two-electron energy (relative to that of the $B = 0$ state). The total energy of a covalent $B = 1$ configuration is higher than the total energy of the $B = 0$ configuration by two nearest-neighbor exchange integrals

$$E_{10,9}^{COV} - E_{10,10} \approx 2K_{12}^{\omega}.$$

The total energy of an ionic $B = 1$ configuration is

$$E_{10,9}^{IONIC} - E_{10,10} \approx 2K_{12}^{\omega} + J_{11}^{\omega} - J_{kl}^{\omega}$$

where k and l denote the doubly-occupied and empty orbitals, respectively.

Since the HF wavefunctions in terms of the $\{\omega_j\}$ each contain more than one configuration, the resultant energy expressions each contain cross terms. The cross terms between the covalent and ionic configurations lead to the stabilization of the total one-electron energy, as discussed above. Two-electron contributions in the energy expression resulting from such cross terms are generally small and are neglected for the purpose of this appendix.

The total two-electron energies for the various $B = 1$ HF states can be estimated by

$$E_{10,9}^{TWO} - E_{10,10}^{TWO} \approx 2K_{12}^{\omega} + \langle I\rangle \left[J_{11}^{\omega} - e^2\langle R_{IONIC}^{-1}\rangle\right]$$

$$
\begin{aligned}
e^2\langle R^{-1}_{IONIC}\rangle &= J^{\omega}_{12} && \text{for } C_s \\
e^2\langle R^{-1}_{IONIC}\rangle &= J^{\omega}_{16} && \text{for } C_{2h} \\
e^2\langle R^{-1}_{IONIC}\rangle &= \frac{1}{9}\sum_{i=2}^{10} J^{\omega}_{1i} && \text{for } D_{10h}
\end{aligned}
$$

where e is the fundamental electronic charge ($e = 1$ in atomic units) and $\langle R^{-1}_{IONIC}\rangle$ is the reciprocal distance between the doubly-occupied Wannier orbital and the empty Wannier orbital (averaged over all ionic configurations). J^{ω}_{11} is related to the ionization potential (IP) and electron affinity (EA) associated with ω_1, e.g.,

$$J^{\omega}_{11} = IP - EA,$$

and $e^2\langle R^{-1}_{IONIC}\rangle$ results from the effective coulombic attraction between the doubly-occupied Wannier orbital and the empty Wannier orbital.

3. Approximate Energy Expression for M_N

The analysis for M_{10} is generalized as follows. For M_N, the HF $B = 1$ ($A = N - 1$) state leads to the energy expression

$$E^{HF}_{N,N-1} - E^{HF}_{N,N} \approx f_{12}h^{\omega}_{12} + 2K^{\omega}_{12} + \langle I\rangle\left[J^{\omega}_{11} - \langle R^{-1}_{IONIC}\rangle\right] \qquad \text{(E4)}$$

where

$$
\left.
\begin{aligned}
f_{12} &= 2 \\
\langle I\rangle &= 0.5 \\
\langle R^{-1}_{IONIC}\rangle &= J^{\omega}_{12} \approx a^{-1}
\end{aligned}
\right\} \text{for } C_s
$$

$$
\left.
\begin{aligned}
f_{12} &= 0 \\
\langle I\rangle &= 0.5 \\
\langle R^{-1}_{IONIC}\rangle &= J^{\omega}_{1\,n+1} \approx a^{-1}\sin(\pi/N) \\
(n &= N/2)
\end{aligned}
\right\} \text{for } C_{2h}
$$

$$\left.\begin{aligned} f_{12} &= 4 \\ \langle I \rangle &= 1 - N^{-1} \\ \langle R^{-1}_{IONIC} \rangle &= \frac{1}{N-1} \sum_{i=2}^{N} J_{1i} \\ &\approx \frac{a^{-1}}{(N-1)} \sin\left(\frac{\pi}{N}\right) \sum_{i=1}^{N-1} \frac{1}{\sin\left(i\pi/N\right)} \\ &\approx \frac{2a^{-1}}{(N-1)} \ln \frac{2N}{\pi} \\ \lim_{N\to\infty} \langle R^{-1}_{IONIC} \rangle &= 0 \end{aligned}\right\} \text{for } D_{Nh}.$$

Hence, in the limit as N approaches infinity, a charge density wave (C_s) occurs if

$$4|h^{\omega}_{12}| < J^{\omega}_{11} + J^{\omega}_{12}.$$

Hence, a charge density wave occurs when the band width ($\mathcal{B} = 4|h^{\omega}_{12}|$) is smaller than the sum of (i) the difference between the ionization potential and electron affinity associated with a localized Wannier orbital ($J_{11} = IP - EA$), and (ii) the coulomb repulsion between adjacent localized Wannier orbitals.

4. Failure of Simple Energy Band Theory

The assumption of simple energy band theory [or molecular orbital (MO) theory, both of which ignore electron-electron repulsions] is that the difference in *total* energy between two states can be obtained by summing up the *one-electron* energy levels (weighted by occupation) for each of the two states and taking the difference. Hence, for M_{10}, the difference in total energy between the $B = 0$ ($A = 10$, high-spin) and $B = 1$ ($A = 9$, next-highest-spin) HF(D_{10h}) states is

$$E^{MO}_{10,9} - E^{MO}_{10,10} = \langle \psi_0 | \hat{h} | \psi_0 \rangle - \langle \psi_5 | \hat{h} | \psi_5 \rangle \approx 4h^{\omega}_{12}. \qquad \text{(E5)}$$

However, the HF results — including all the one-electron *and two-electron* contributions to the total energy (*ab initio*) — are in serious disagreement with Equa-

tion (E5). Thus, the values of $E_{10,9}^{HF(D_{10h})} - E_{10,10}^{HF}$ (-0.63, $+0.13$, -1.11, $+2.33$, and $+1.15$ eV for Cu_{10}, Ag_{10}, Au_{10}, Li_{10}, and Na_{10}, respectively; see Table 1) are 4.4-5.7 eV higher than the respective values of $E_{10,9}^{MO} - E_{10,10}^{MO}$ (values of $4h_{12}^{\omega}$ are -6.31, -4.95, -5.49, -2.84, and -3.06 eV for Cu_{10}, Ag_{10}, Au_{10}, Li_{10}, and Na_{10}, respectively; see Table 7).

5. Detailed Results for Cu_{10} and Li_{10}

First we present the total energies of the three $B = 1$ frozen-orbital wavefunctions (i.e., energies for $B = 1$ calculated with the $B = 0$ orbitals), and then we describe the relaxation effects. In the remainder of this appendix, we focus on Cu_{10} and Li_{10}; results for the other ring clusters are very similar. Detailed results are given in Table 9 for Cu_{10} and in Table 10 for Li_{10}.

For the three $B = 1$ frozen-orbital states [C_s (E1), C_{2h} (E2), and D_{10h} (E3)], Equation (E4) is accurate to 0.63 eV for Cu_{10} and to 0.13 eV for Li_{10} (in comparison to the frozen-orbital total energy; see Tables 9-10). The calculated $\langle R_{IONIC}^{-1} \rangle$ values are in reasonable agreement with expectation based on simple geometrical arguments — $(1.000\ a)^{-1}$, $(3.236\ a)^{-1}$, and $(1.885\ a)^{-1}$ for C_s, C_{2h}, and D_{10h}, respectively, based on the nearest-neighbor distance, the diameter of the M_{10} ring, and the average reciprical distance between a given atom and the remaining atoms, respectively.

In comparison to the $B = 1$ (D_{10h}) frozen state, the $B = 1$ (C_s) and $B = 1$ (C_{2h}) frozen states lead to a stabilization of the two-electron energy (E^{TWO}) at the expense of destabilizing the one-electron energy (E^{ONE}). This is due to the reduction of ionic character in the wavefunction afforded by the localization of the doubly-occupied orbital (leading to a charge density wave). Such orbital localization is most favorable for cases having narrow band widths (for M_{10}, the band widths

$\mathcal{B} = 4|h_{12}^{\omega}|$ follow the trend Cu > Au > Ag $\gg$ Na > Li; see Table 7).

Relaxation effects (optimizing the $B = 1$ orbitals within the given symmetry restrictions) are as follows.

(*i*) The doubly-occupied orbital can partially delocalize, stabilizing E^{ONE} at the expense of destabilizing E^{TWO} [this cannot occur for the $B = 1$ (D_{10h}) state (E3) since ψ_0 is fully delocalized]. Cases where this is the primary effect are the $B = 1$ (C_{2h}) and the $B = 1$ (C_s) states for Cu_{10}.

(*ii*) The doubly-occupied orbital can become more diffuse, stabilizing E^{TWO} at the expense of destabilizing E^{ONE}. Cases where this is the primary effect are the $B = 1$ (D_{10h}) state for both Cu_{10} and Li_{10}, and the $B = 1$ (C_s) state for Li_{10}.

The lowest energy $B = 1$ *relaxed* state — for both Cu_{10} and Li_{10} — is the $B = 1$ (C_s) state, leading to a charge density wave. The $B = 1$ (C_s) state is lower in *total* energy than the $B = 1$ (D_{10h}) state by 0.98 eV for Cu_{10} and by 2.01 eV for Li_{10}. The $B = 1$ (D_{10h}) state leads to a fully symmetrical charge density.

For the Li_{10} $B = 1$ (C_{2h}) state, both relaxation effects play a major role, stabilizing both E^{ONE} and E^{TWO}.

For the Cu_{10} $B = 1$ (C_{2h}) state, relaxation leads to a fully delocalized doubly-occupied orbital; hence, for Cu_{10} the $B = 1$ (C_{2h}) and $B = 1$ (D_{10h}) fully relaxed states are equivalent (neither leads to a charge density wave).

Appendix F. Detailed Comparison of the UHF and HF Energies

Here we compare the total energy (E^{TOTAL}), the one-electron energy (E^{ONE}), and the two-electron energy (E^{TWO}) for UHF, HF(C_s), HF(C_{2h}), and HF(D_{Nh}), as a

function of magnetization (μ). Results are given in Table 11 for the Na_{10} ring cluster (results for the other clusters are fairly similar).

For $\mu = 1$ (high-spin), UHF, HF(C_s), HF(C_{2h}), and HF(D_{Nh}) lead to identical results.

For $\mu < 1$, each of the HF wavefunctions contains doubly-occupied valence orbitals, leading to a *forced* mixture of covalent and ionic configurations (in terms of the ω_j; see Appendices D-E). The UHF wavefunction does not contain doubly-occupied valence orbitals and hence the weights of the ionic configurations are determined variationally [within the restricted (single-determinant) form of Ψ^{UHF}].

For each allowed magnetization $\mu < 1$, E^{ONE} follows the trend UHF $\gg$ HF(C_s) $>$ HF(D_{Nh}), whereas E^{TWO} follows the trend UHF $\ll$ HF(C_s) $<$ HF(D_{Nh}). Since ionic configurations stabilize the total one-electron energy but destabilize the total two-electron energy, the total amount of ionic character in the wavefunction follows the trend UHF $\ll$ HF(C_s) $<$ HF(D_{Nh}). The net result is that the UHF total energy is much lower than the HF(C_s) total energy, and the HF(C_s) total energy is lower than the HF(D_{Nh}) total energy (for all magnetizations other than $\mu = 1$).

Appendix G. Core-Excited States of Au_{10}

Since this appendix is concerned with core-excited states, we optimize both the core orbitals and the valence orbitals self-consistently (no frozen core approximation).

1. One-Electron Energy Bands

Figures 22-23 show the energy band structure of the Au_{10} ring, as defined by the orbital energies (Koopmans' theorem)[29] for the lowest energy $\mu = 1$ state (3), where

the valence band orbitals are each occupied with an up-spin electron and the $5d$ band orbitals are each doubly occupied.

We label the $5d$ bands and band orbitals according to the symmetry of the orbitals, as follows.

(*i*) Symmetry with respect to the plane of the ring (single-prime for symmetric; double-prime for antisymmetric).

(*ii*) Local symmetry with respect to rotation about each bond axis [using the standard ($D_{\infty h}$) notation — σ, π, and δ]. For an M_N ring cluster with finite N, this is not an exact symmetry due to the curvature of the ring. However, we find for Au_{10} that the $5d$ band orbitals (having D_{10h} symmetry) can be classified as σ, π, or δ rather easily by inspection (orbitals having wave vectors near $k = \pi/2a$ are somewhat harder to classify, since the orbital energies all cross near $k = \pi/2a$, resulting in rather strong orbital mixing effects — these mixing effects vanish in the limit as N approaches infinity, since rotation about the bond axis is an exact symmetry in the limit as N approaches infinity).

Hence, the $5d$ energy levels split into five bands — $d\sigma'$, $d\pi'$, $d\pi''$, $d\delta'$, and $d\delta''$. In the limit as N approaches infinity, the two $d\pi$ bands become degenerate, and the two $d\delta$ bands become degenerate. For finite N, the nondegeneracy of the two $d\pi$ bands is a sensitive indication of the ring curvature (see Figure 23).

For each band, the band widths ($\mathcal{B}$) and mean values of the orbital energies are listed in Table 12. The trend of the band widths ($\sigma > \pi > \delta$) is exactly that expected by the orbital overlaps ($\sigma > \pi > \delta$).

2. HF States Involving $5d$ Excitations

We solved for $5d$-excited HF $\mu = 1$ states of Au_{10} with (i) D_{10h} orbital symmetry restrictions and (ii) C_{2v} orbital symmetry restrictions (with the C_{2v} symmetry axis passing through two opposite atoms of the Au_{10} ring).

The one-electron energy levels (Figures 22-23) suggest that the lowest energy $5d$-excited $\mu = 1$ state of Au_{10} involves promoting an electron from the highest energy $5d$ orbital ($5d\sigma'$, $k = \pi/a$) to the lowest energy valence orbital ($k = 0$). This HF (D_{10h}) $\mu = 1$ state is 6.01 eV higher in energy than the lowest energy $\mu = 1$ state (3). This illustrates a weakness of the HF Koopmans' theorem orbital energies, since the $5d$ – valence indirect gap obtained from Figure 22 is only 0.78 eV.

At the HF level, the lowest energy $5d$-excited $\mu = 1$ state of Au_{10} involves a *localized "core hole"* — a singly-occupied $5d$ orbital localized at a single atom — inducing a local $5d^9 6s^2$ configuration at that atom (cancelling the +1 charge left by the core hole).

We constructed starting-guess orbitals for the $5d$-excited $\mu = 1$ state having a singly-occupied $d\sigma'$ orbital localized at a single atom. However, solving for the orbitals self-consistently (with no symmetry restrictions) resulted in convergence to the lowest energy $\mu = 1$ state (3).

Using C_{2v} orbital symmetry restrictions, we optimized orbitals for a similar $5d$-excited $\mu = 1$ state having a $5d\pi''$ hole localized at one atom. The total energy of this state is just 2.46 eV higher than that of (3).

The various HF $\mu = 1$ states each having one localized $5d\sigma$ core hole (σ, π, δ) should all be within approximately 0.19 eV in energy from one another (based on the average band energies given in Table 12).

For comparison, the $5d^{10}6s^1$ - $5d^96s^2$ state splitting for the isolated Au atom (using the same Au basis set as for the Au_{10} calculation) is 3.11 eV at the HF level. A much more flexible basis set (and the same ab initio relativistic effective potential) leads to a $5d^{10}6s^1$ - $5d^96s^2$ atomic state splitting of 2.14 eV at the HF level.[25] The experimental $5d^{10}6s^1$ - $5d^96s^2$ atomic energy splitting is 1.74 eV.[30]

Our HF calculations indicate that the $5d$ core hole of $\mu = 1$ Au_{10} is stabilized by 0.65 eV with respect to that of the Au atom.

Appendix H. Results for Hydrogen Ring Clusters

Often, ideas concerning the electronic structures of one-dimensional metals have been tested with calculations on symmetric ring clusters composed of hydrogen atoms.[31,32]

In this appendix we present UHF and HF calculations for the H_6, H_8, H_{10}, and H_{20} symmetric ring clusters using Huzinaga's[33] (5s) primitive set of gaussian-type orbitals (unscaled) contracted triple-ζ.[10] For each of these H_N rings, we chose a lattice constant (a = 1.483 Å) equal to twice the H_2 equilibrium bond length.[34] For H_{10}, we also optimized UHF and HF wavefunctions for many other lattice constants, including a = 1.112 Å, a = 1.186 Å, and a = 1.260 Å, equal to factors of 1.5, 1.6, and 1.7 times the H_2 equilibrium bond length.[34]

The topologies of the various wavefunctions for H_N and M_N (M = Cu, Ag, Au, Li, and Na) are similar, except that the localized orbitals ($\{\omega_j\}$ and $\{\phi_j\}$) are centered at the atoms for H_N as opposed to the bond midpoints for M_N (see Figure 2).

We find (for UHF and HF) that H_N ring clusters (at the extended lattice constant a = 1.483 Å) can model some aspects of the M_N ring clusters. However, the H_N results are rather sensitive to the lattice constant.

1. UHF Results and the Ising Models

Table 13 summarizes the UHF results for each of the H_N rings. For H_{10}, the magnon dispersion (for $1.112 \leq a \leq 1.483$ Å) is a factor of 2.7 to 7.0 greater than that for Cu_{10} (at $a = 2.556$ Å). Also, for H_{10}, the nearest-neighbor overlap (for $1.112 \leq a \leq 1.483$ Å) is a factor of 0.93 to 1.30 times that for Cu_{10} (at $a = 2.556$ Å).

The large magnon dispersion for H_N results from the large antibonding exchange interactions for the $\mu > 0$ states. For H_{10}, the $\mu = 1$ state is so strongly antibonding that for $a \leq 1.195$ Å, UHF leads to a positive orbital energy for the highest occupied orbital ($m = 5$). Hence, for $a \leq 1.195$ Å, the UHF $\mu = 1$ state is unstable with respect to ionization (forming $\mu = 1$ $H_{10}^+ + e^-$). In order to compare UHF results for $a > 1.195$ Å with those for $1.112 \leq a \leq 1.195$ Å, we optimize the UHF $\mu = 1$ wavefunction (3) with D_{10h} orbital symmetry restrictions (this is no restriction for $a > 1.195$ Å; however, for $a < 1.195$ Å, the UHF(D_{10h}) $\mu = 1$ state (3) is not the lowest energy UHF solution).

Table 14 summarizes the results of fitting the Ising model (IM) and the generalized Ising models (GIM1 and GIM2) to the UHF total energies (following the same least-squares procedure as for the M_N rings; see Section II.C.2). The results for the H_N rings (for $1.112 \leq a \leq 1.483$ Å) are of similar quality to those for the M_N rings (for M = Cu, Ag, Au, Li, and Na; see Table 3). For H_N (as well as for M_N; see Tables 3 and 14), GIM2 gives the best fit to the UHF energies, as shown in Figure 24 for H_{20}.

For small enough a, the Ising model is not expected to provide an accurate fit to the lowest energy UHF states.

(i) Due to the large antibonding exchange interactions for $\mu > 0$ (especially for the higher magnetizations), for small enough a the UHF states involving 1s-like

orbitals become unstable with respect to ionization. For $\mu = 1$ H_{10}, this occurs for $a \leq 1.195$ Å, and for $\mu = 0.8$ H_{10}, this occurs for $a \leq 1.046$ Å.

(*ii*) Due to the UHF spin contamination for $\mu < 1$,[10] for small enough a, the spin polarization vanishes. For $\mu = 0$ H_{10}, this occurs for $a \leq 1.048$ Å.

2. HF Results and Symmetry Breaking Effects

Figure 25 presents the magnon spectrum for H_{10} (at $a = 1.483$ Å) calculated with the various wavefunctions [UHF, HF(C_s), HF (C_{2h}), and HF (D_{10h})]. The results for H_{10} at $a = 1.483$ Å are qualitatively similar to the results for Cu_{10} at $a = 2.556$ Å (Figure 11) — the energetic magnitudes of orbital symmetry breaking effects (charge density waves, spin density waves, and spin polarization) relative to the magnon dispersion ($\mathcal{D}$) are remarkably similar for H_{10} at $a = 1.483$ Å and Cu_{10} at $a = 2.556$ Å.

However, for H_{10}, as a decreases, the energetic magnitudes of the orbital symmetry breaking effects (relative to $\mathcal{D}$) decrease rather rapidly. As an example, for $\mu = 0.6$, the energetic magnitude of the charge density wave ($|E^{HF(C_s)} - E^{HF(D_{10h})}|$) is 0.1879 $\mathcal{D}$, 0.0747 $\mathcal{D}$, 0.0540 $\mathcal{D}$, and 0.0385 $\mathcal{D}$ for H_{10} at $a = 1.483$, 1.260, 1.186, and 1.112 Å, respectively (compare to 0.2028 $\mathcal{D}$ for Cu_{10} at $a = 2.556$ Å; Table 13 lists values of $\mathcal{D}$ for H_{10}). For $\mu = 0$, the energetic magnitude of the spin density wave ($|E^{UHF} - E^{HF(D_{10h})}|$) is 0.1759 $\mathcal{D}$, 0.0292 $\mathcal{D}$, 0.0116 $\mathcal{D}$, and 0.0026 $\mathcal{D}$ for H_{10} at $a = 1.483$, 1.260, 1.186, and 1.112 Å, respectively (compare to 0.2310 $\mathcal{D}$ for Cu_{10} at $a = 2.556$ Å; for H_{10}, the UHF $\mu = 0$ spin density wave vanishes for $a \leq 1.048$ Å).

References

[1] R. E. Peierls, *Quantum Theory of Solids* (Oxford Univ. Press, London, 1956).

[2] E. H. Lieb and F. Y. Wu, *Phys. Rev. Lett.* **20**, 1445 (1968).

[3] J. Hubbard, *Proc. Roy. Soc. London* **A 276**, 238 (1963); *ibid* **A 277**, 237 (1964); *ibid* **A 281**, 401 (1964).

[4] N. F. Mott, *Metal-Insulator Transitions* (Barnes & Noble, New York, 1974).

[5] M.-H. Whangbo, *Acc. Chem. Res.* **16**, 95 (1983); F. Wudl, *Acc. Chem. Res.* **17**, 227 (1984).

[6] *Low-Dimensional Cooperative Phenomena. The Possibility of High-Temperature Superconductivity*, edited by H. J. Keller (Plenum, New York, 1974); *Chemistry and Physics of One-Dimensional Metals*, edited by H. J. Keller (Plenum, New York, 1977); *One-Dimensional Conductors*, edited by H. G. Schuster (Springer-Verlag, New York, 1975); *Extended Linear Chain Compounds*, edited by J. S. Miller (Plenum, New York, 1982, 1982, 1983), Vols. 1-3.

[7] Z. G. Soos, in *Low-Dimensional Cooperative Phenomena. The Possibility of High-Temperature Superconductivity*, edited by H. J. Keller (Plenum, New York, 1974).

[8] C. Castiglioni, G. Zerbi, and M. Gussoni, *Solid State Commun.* **56**, 863 (1985); K. A. Chao and S. Stafstroem, *Mol. Cryst. Liq. Cryst.* **118**, 45 (1985); I. Bozovic, *Phys. Rev.* **B 32**, 8136 (1985); M. Kertesz and R. Hoffmann, *Solid State Commun.* **47**, 97 (1983).

[9] The calculations for Li and Na are "ab initio" in the traditional definition in that the total energy expressions $\langle\Psi|\mathcal{H}|\Psi\rangle/\langle\Psi|\Psi\rangle$ include *all terms that result from the true Hamiltonian* ($\mathcal{H}$) [within the usual Born-Oppenheimer approximation (frozen nuclei)] and no additional terms. The only approximations utilized in ab initio calculations are in the many-electron wavefunction (Ψ), e.g., "exact" calculations where Ψ includes essentially an infinite number of configurations within an infinite basis set are generally unattainable, and hence the configuration and basis set expansions are truncated. Both the HF and UHF wavefunctions include only a single configuration. Local density functional calculations (such as $X\alpha$) are not ab initio in this traditional definition since the exchange integrals are replaced by adding an extra term (the local "exchange-correlation" potential) to the true Hamiltonian. The calculations for Cu, Ag and Au are ab initio for eleven electrons per atom ($d^{10}s^1$), where "ab initio" effective potentials model all effects of the remaining core electrons. See Appendix A and Reference [25] for further details.

[10] M. H. McAdon and W. A. Goddard III, *J. Chem. Phys.*, accepted for publication. See Chapter 1 of this thesis.

[11] M. H. McAdon and W. A. Goddard III, *J. Phys. Chem.*, accepted for publication. See Chapter 2 of this thesis.

[12] W. Förner and M. Seel, *J. Chem. Phys.* **87**, 443 (1987).

[13] See Chapter 4 of this thesis.

[14] E. Ising, *Z. Phys.* **31**, 253 (1925).

[15] G. H. Wannier, *Elements of Solid State Theory* (Cambridge Univ. Press, London, 1959); G. Wannier, *Phys. Rev.* **52**, 191 (1937).

[16] J. Donohue, *The Structure of the Elements* (Wiley, New York, 1974).

[17] The real and imaginary components of the complex Bloch functions are identical to what is commonly referred to as molecular orbitals (MO).

[18] For the symmetric (D_{8h}) M_8 ring cluster, there are two distinct choices for lowering the symmetry to D_{2h} — (i) choosing the x and y axes (C_2 axes) bisecting two sets of opposite atoms, and (ii) choosing the x and y axes bisecting two sets of opposite bond midpoints. This is the case for all $N = 4i$ ring clusters. Thus, for $N = 4i$, HF wavefunctions optimized with D_{2h} orbital symmetry restrictions depend on the choice of the coordinate system! This is not a problem for $N = 4i + 2$ ring clusters, since one axis bisects a pair of opposite atoms, while the other axis bisects a pair of opposite bond midpoints. Reducing the orbital symmetry restrictions to C_{2h} and choosing the principal (C_N) symmetry axis as the C_2 symmetry axis avoids this problem.

[19] The lowest energy HF triplet state of Ag_8 leads to charge and spin density waves (see Figure 13). More details of the HF triplet state of Ag_8 are given in Reference [10].

[20] W. A. Goddard III, *Int. J. Quantum Chem.* **IIIS**, 593 (1970); R. C. Ladner and W. A. Goddard III, *J. Chem. Phys.* **51**, 1073 (1969).

[21] W. A. Goddard III, T. H. Dunning, Jr, W. J. Hunt, and P. J. Hay, *Accts. Chem. Res.* **6**, 368 (1973); W. A. Goddard III and L. B. Harding, *Ann. Rev. Phys. Chem.* **29**, 363 (1978).

[22] W. Heisenberg, *Z. Phys.* **49**, 619 (1928).

[23] L. Hulthén, *Ark. Mat. Astr. Fys.* **26A**, 1 (1938).

[24] M. H. McAdon and W. A. Goddard III, *J. Phys. Chem.* **91**, 2607 (1987); M. H. McAdon and W. A. Goddard III, *J. Non-Cryst. Solids* **75**, 149 (1985); M. H. McAdon and W. A. Goddard III, *Phys. Rev. Lett.* **55**, 2563 (1985). See Chapter 5 of this thesis.

[25] P. J. Hay and W. R. Wadt, *J. Chem. Phys.* **82**, 270 (1985).

[26] L. G. Yaffe, LTRAN program, unpublished; see L. G. Yaffe and W. A. Goddard III, *Phys. Rev. A.* **13**, 1682 (1976). Also see W. J. Hunt, T. H. Dunning, Jr., and W. A. Goddard III, *Chem. Phys. Lett.* **3**, 606 (1969).

[27] C. W. Wilson, Jr. and W. A. Goddard III, *Chem. Phys. Lett.*, **5**, 45 (1970); C. W. Wilson, Jr. and W. A. Goddard III, *Theor. Chim. Acta,* **26**, 195 (1972); W. A. Goddard III and C. W. Wilson, Jr., *Theor. Chim. Acta,* **26**, 211 (1972).

[28] P. A. M. Dirac, *Proc. Roy. Soc. A* **123**, 714 (1929).

[29] T. Koopmans, *Physica* **1**, 104 (1933).

[30] C. E. Moore, *Atomic Energy Levels* (Nat. Stand. Rev. Data Ser., Nat. Bur. Stand. (U.S.), 1971). Values of atomic excitation energies are obtained weighting the various J values for each configuration by the $2J+1$ degeneracy, e.g., for Cu, Ag, and Au, the d-to-s excitation energy involves the $d^{10}s^1$ ($J=0$) and d^9s^2 ($J=5/2$, and $J=3/2$) atomic states.

[31] L. F. Mattheiss, Phys. Rev. **123**, 1209 (1961).

[32] R. D. Poshusta and D. J. Klein, *Phys. Rev. Lett.* **48**, 1555 (1982); M. Seel, P. S. Bagus and J. Ladik, *J. Chem. Phys.* **77**, 3123 (1982); A. Karpfen, *Chem. Phys. Lett.* **61**, 363 (1979); M. Kertesz, J. Koller, and A. Azman, *Phys. Rev.* **B 14**, 76 (1976); S. P. Ionov, I. I. Amelin, V. S. Lyubimov, G. V. Ionova, and E. F. Makarov, *Physica Status Solidi* **B 77**, 441 (1976).

[33] S. Huzinaga, *J. Chem. Phys.* **42**, 1293 (1965).

[34] K. P. Huber and G. Herzberg, *Molecular Spectra and Molecular Structure: IV. Constants of Diatomic Molecules* (Van Nostrand Reinhold, New York, 1979).

Table 1. UHF and HF magnon spectra. [a)]

A	B	μ	$E_\mu - E_{\mu=1}$ (eV) UHF	HF(C_s)	HF(C_{2h})	HF(D_{Nh})
Cu_{10}		$a = 2.556$ Å		$E_{\mu=1} = -504.28277$ Hartree		
5	5	0.000	−6.448	−4.959	−4.959	−4.959
6	4	0.200	−5.646	−4.550	−4.550	−4.062
7	3	0.400	−4.709	−4.141	−3.707	−3.707
8	2	0.600	−3.334	−3.025	−3.025	−1.717
9	1	0.800	−1.739	−1.610	−0.631	−0.631
10	0	1.000	0.000	0.000	0.000	0.000
Ag_6		$a = 2.889$ Å		$E_{\mu=1} = -224.40832$ Hartree		
3	3	0.000	−2.981	−2.342	−2.342	−2.342
4	2	0.333	−2.282	−1.736	−1.736	−1.259
5	1	0.667	−1.368	−1.253	−1.101	−1.101
6	0	1.000	0.000	0.000	0.000	0.000
Ag_8		$a = 2.889$ Å		$E_{\mu=1} = -299.22320$ Hartree		
4	4	0.000	−3.789	−1.988	−1.988	−1.766
5	3	0.250	−3.151	−2.297	−2.256	−2.256
6	2	0.500	−2.308	−1.820	−1.820	−0.894
7	1	0.750	−1.233	−1.049	−0.391	−0.391
8	0	1.000	0.000	0.000	0.000	0.000
Ag_{10}		$a = 2.889$ Å		$E_{\mu=1} = -374.03507$ Hartree		
5	5	0.000	−4.661	−2.775	−2.775	−2.775
6	4	0.200	−4.024	−2.616	−2.616	−2.073
7	3	0.400	−3.299	−2.478	−1.891	−1.891
8	2	0.600	−2.315	−1.843	−1.843	−0.440
9	1	0.800	−1.194	−0.985	0.129	0.129
10	0	1.000	0.000	0.000	0.000	0.000
Au_{10}		$a = 2.884$ Å		$E_{\mu=1} = -333.83386$ Hartree		
5	5	0.000	−6.220	−4.846	−4.846	−4.846
6	4	0.200	−5.501	−4.485	−4.485	−4.066
7	3	0.400	−4.661	−4.176	−3.838	−3.838
8	2	0.600	−3.362	−3.097	−3.097	−2.054
9	1	0.800	−1.857	−1.771	−1.115	−1.115
10	0	1.000	0.000	0.000	0.000	0.000

Table 1. UHF and HF magnon spectra, continued. [a)]

			$E_\mu - E_{\mu=1}$ (eV)			
A	B	μ	UHF	HF(C_s)	HF(C_{2h})	HF(D_{Nh})
Li_6		$a = 3.014$ Å		$E_{\mu=1} = -44.63264$ Hartree		
3	3	0.000	−1.021	0.786	0.786	0.786
4	2	0.333	−0.726	0.520	0.520	1.338
5	1	0.667	−0.380	0.182	0.930	0.930
6	0	1.000	0.000	0.000	0.000	0.000
Li_{10}		$a = 3.014$ Å		$E_{\mu=1} = -74.40442$ Hartree		
5	5	0.000	−1.613	2.219	2.279	2.279
6	4	0.200	−1.329	1.627	1.627	2.676
7	3	0.400	−1.032	1.043	2.450	2.575
8	2	0.600	−0.699	0.636	0.636	3.003
9	1	0.800	−0.351	0.311	2.193	2.325
10	0	1.000	0.000	0.000	0.000	0.000
Li_{14}		$a = 3.014$ Å		$E_{\mu=1} = -104.17273$ Hartree		
7	7	0.000	−2.230	3.360	3.685	3.685
8	6	0.143	−1.951	2.690	2.690	3.982
9	5	0.286	−1.658	2.025	3.768	3.944
10	4	0.429	−1.363	1.485	1.485	4.386
11	3	0.571	−1.034	1.051	3.234	4.314
12	2	0.714	−0.692	0.683	0.683	4.313
13	1	0.857	−0.346	0.340	2.542	3.061
14	0	1.000	0.000	0.000	0.000	0.000
Na_{10}		$a = 3.659$ Å		$E_{\mu=1} = -1617.94206$ Hartree		
5	5	0.000	−2.074	0.431	0.438	0.438
6	4	0.200	−1.746	0.159	0.159	0.818
7	3	0.400	−1.389	−0.128	0.725	0.776
8	2	0.600	−0.960	−0.191	−0.191	1.339
9	1	0.800	−0.489	−0.123	1.108	1.147
10	0	1.000	0.000	0.000	0.000	0.000

a) For $\mu = 1$, the UHF and various HF wavefunctions are identical (see Section II.B).

Table 2. Details of the UHF results. [a]

system	a (Å)	$\mathcal{D}/N$ (eV/atom)	S_{12} $\mu=0$	S_{12} $\mu=1$	S_{12} average [b]	$\delta\phi_1$
Ag_6	2.889	0.497	0.658	0.862	0.760	0.03427
Ag_8	2.889	0.474	0.562	0.680	0.621	0.00956
Ag_{10}	2.889	0.466	0.535	0.609	0.572	0.00422
Li_6	3.014	0.170	0.416	0.728	0.572	0.04058
Li_{10}	3.014	0.161	0.341	0.369	0.355	0.00130
Li_{14}	3.014	0.159	0.326	0.284	0.305	0.00131
Cu_{10}	2.556	0.645	0.601	0.682	0.642	0.00631
Ag_{10}	2.889	0.466	0.535	0.609	0.572	0.00422
Au_{10}	2.884	0.622	0.589	0.631	0.610	0.00224
Li_{10}	3.014	0.161	0.341	0.369	0.355	0.00130
Na_{10}	3.659	0.207	0.408	0.477	0.442	0.00348

a) $\mathcal{D}$ is the magnon dispersion, S_{12} is the nearest-neighbor overlap integral, and $\delta\phi_1$ measures the difference between orbitals $\phi_1^{\mu=0}$ and $\phi_1^{\mu=1}$ (see Section II.C.1).
b) $(S_{12}^{\mu=0} + S_{12}^{\mu=1})/2$

Table 3. Fits of the Ising and generalized Ising models to $E^{UHF}_{N,A}$.[a)]

System	a (Å)	Ising $-\mathcal{J}$ (eV)	Ising $\mathcal{S}$	Ising error (%)	gen. Ising 1 $-\mathcal{J}$ (eV)	gen. Ising 1 $\mathcal{S}$	gen. Ising 1 error (%)	gen. Ising 2 [b)] $-\mathcal{J}$ (eV)	gen. Ising 2 $\mathcal{S}$	gen. Ising 2 error (%)
Ag_6	2.889	0.459	0.000	7.49	0.297	0.259	0.31	0.248	0.407	1.06
Ag_8	2.889	0.440	0.000	6.13	0.309	0.209	0.81	0.270	0.307	0.26
Ag_{10}	2.889	0.432	0.000	5.78	0.308	0.185	1.01	0.272	0.268	0.57
Li_8	3.014	0.166	0.000	2.85	0.141	0.170	0.32	0.138	0.198	0.22
Li_{10}	3.014	0.157	0.000	2.11	0.139	0.119	0.38	0.137	0.134	0.32
Li_{14}	3.014	0.155	0.000	1.98	0.138	0.100	0.33	0.136	0.112	0.28
Cu_{10}	2.556	0.588	0.000	6.97	0.392	0.199	1.29	0.321	0.319	0.65
Ag_{10}	2.889	0.432	0.000	5.78	0.308	0.185	1.01	0.272	0.268	0.57
Au_{10}	2.884	0.554	0.000	8.09	0.342	0.213	1.05	0.254	0.380	0.59
Li_{10}	3.014	0.157	0.000	2.11	0.139	0.119	0.38	0.137	0.134	0.32
Na_{10}	3.659	0.198	0.000	3.76	0.159	0.155	0.57	0.151	0.193	0.39

a) $\mathcal{J}$ and $\mathcal{S}$ are the effective nearest-neighbor exchange and overlap determined by least-squares fits [see Section II.C.2]. The error is $\Delta E^{RMS}/\mathcal{D}$, where $\mathcal{D}$ is the UHF magnon dispersion (see Table 2).

b) For E^{GIM2}, including $E_{N,0}$ as a least-squares parameter reduces the listed ΔE^{RMS} values by factors of only 1.01 to 1.05.

Table 4. Charge density wave (CDW), spin density wave (SDW), and spin polarization (SP) effects.

system	a (Å)	A	B	μ	$a)$ E^{CDW} (eV)	$b)$ $E^{CDW(C_{2k})}$ (eV)	$c)$ E^{SDW} (eV)	$d)$ E^{SP} (eV)
Cu_{10}	2.556	5	5	0.000	0.000	0.000	−1.490	−1.490
		6	4	0.200	−0.488	−0.488	−1.584	−1.096
		7	3	0.400	−0.434	0.000	−1.001	−0.568
		8	2	0.600	−1.308	−1.308	−1.618	−0.310
		9	1	0.800	−0.980	0.000	−1.108	−0.129
		10	0	1.000	0.000	0.000	0.000	0.000
Ag_8	2.889	3	3	0.000	0.000	0.000	−0.638	−0.638
		4	2	0.333	−0.478	−0.478	−1.024	−0.546
		5	1	0.667	−0.152	0.000	−0.267	−0.115
		6	0	1.000	0.000	0.000	0.000	0.000
Ag_8	2.889	4	4	0.000	−0.222	−0.222	−2.023	−1.801
		5	3	0.250	−0.041	0.000	−0.894	−0.854
		6	2	0.500	−0.926	−0.926	−1.414	−0.488
		7	1	0.750	−0.657	0.000	−0.842	−0.184
		8	0	1.000	0.000	0.000	0.000	0.000
Ag_{10}	2.889	5	5	0.000	0.000	0.000	−1.885	−1.885
		6	4	0.200	−0.543	−0.543	−1.950	−1.407
		7	3	0.400	−0.588	0.000	−1.408	−0.821
		8	2	0.600	−1.403	−1.403	−1.875	−0.472
		9	1	0.800	−1.114	0.000	−1.323	−0.209
		10	0	1.000	0.000	0.000	0.000	0.000
Au_{10}	2.884	5	5	0.000	0.000	0.000	−1.375	−1.375
		6	4	0.200	−0.419	−0.419	−1.435	−1.016
		7	3	0.400	−0.338	0.000	−0.823	−0.485
		8	2	0.600	−1.043	−1.043	−1.308	−0.265
		9	1	0.800	−0.656	0.000	−0.742	−0.086
		10	0	1.000	0.000	0.000	0.000	0.000

Table 4. Charge density wave (CDW), spin density wave (SDW), and spin polarization (SP) effects, continued.

system	a (Å)	A	B	μ	E^{CDW} (eV) [a]	$E^{CDW(C_{2h})}$ (eV) [b]	E^{SDW} (eV) [c]	E^{SP} (eV) [d]
Li_6	3.014	3	3	0.000	0.000	0.000	−1.808	−1.808
		4	2	0.333	−0.819	−0.819	−2.065	−1.246
		5	1	0.667	−0.748	0.000	−1.311	−0.562
		6	0	1.000	0.000	0.000	0.000	0.000
Li_{10}	3.014	5	5	0.000	−0.060	0.000	−3.892	−3.832
		6	4	0.200	−1.049	−1.049	−4.005	−2.956
		7	3	0.400	−1.532	−0.125	−3.607	−2.075
		8	2	0.600	−2.367	−2.367	−3.702	−1.335
		9	1	0.800	−2.014	−0.132	−2.676	−0.662
		10	0	1.000	0.000	0.000	0.000	0.000
Li_{14}	3.014	7	7	0.000	−0.325	0.000	−5.915	−5.590
		8	6	0.143	−1.292	−1.292	−5.933	−4.641
		9	5	0.286	−1.919	−0.176	−5.602	−3.683
		10	4	0.429	−2.901	−2.901	−5.750	−2.849
		11	3	0.571	−3.263	−1.079	−5.348	−2.085
		12	2	0.714	−3.630	−3.630	−5.005	−1.375
		13	1	0.857	−2.721	−0.519	−3.407	−0.686
		14	0	1.000	0.000	0.000	0.000	0.000
Na_{10}	3.659	5	5	0.000	−0.007	0.000	−2.512	−2.505
		6	4	0.200	−0.659	−0.659	−2.564	−1.905
		7	3	0.400	−0.904	−0.051	−2.166	−1.262
		8	2	0.600	−1.530	−1.530	−2.299	−0.769
		9	1	0.800	−1.270	−0.039	−1.635	−0.365
		10	0	1.000	0.000	0.000	0.000	0.000

a) $E^{CDW} = E^{HF(C_s)} - E^{HF(D_{Nh})}$.
b) $E^{CDW(C_{2h})} = E^{HF(C_{2h})} - E^{HF(D_{Nh})}$.
c) $E^{SDW} = E^{UHF} - E^{HF(D_{Nh})}$.
d) $E^{SP} = E^{UHF} - E^{HF(C_s)}$.

Table 5. UHF results for selected two-electron systems.

system	a (Å)	$\Psi_{2,1}^{UHF}$ [a] $-\mathcal{J}_{12}$ (eV)	$\Psi_{2,1}^{UHF}$ [a] $\mathcal{S}_{12}$	$E_{2,2} - E_{2,1}$ [b] frozen (eV)	$E_{2,2} - E_{2,1}$ [b] relaxed (eV)	$\delta\phi_1$ [c]
Cu_3^+	2.556	0.226	0.429	0.277	0.260	0.00948
Ag_3^+	2.889	0.154	0.367	0.178	0.166	0.00530
Au_3^+	2.884	0.133	0.373	0.154	0.143	0.00648
Li_3^+	3.014	0.069	0.224	0.073	0.069	0.00016
Na_3^+	3.659	0.075	0.260	0.080	0.071	0.00173

a) Values calculated with the UHF low-spin canonical orbitals.
b) Energy splitting between the low-spin and high-spin states. The frozen orbital values are calculated using a single set of orbitals — the low-spin orbitals — to describe both states (see Appendix C). The relaxed orbital values are calculated using the UHF (SCF) total energies for both states.
c) $\delta\phi_1 = 1 - \langle\phi_1^{\mu=0}|\phi_1^{\mu=1}\rangle$.

Table 6. Ionic character of HF wavefunctions. [a)]

N	A	B	n_0	n_1	n_2	n_3	n_4	n_5	$\langle I \rangle$
HF(C_s) [b)]					$n_I/2^B$				
		5	1	5	10	10	5	1	2.500
		4	1	4	6	4	1		2.000
		3	1	3	3	1			1.500
		2	1	2	1				1.000
		1	1	1					0.500
		0	1						0.000
HF(D_{Nh})					$n_I/N!$				
2	1	1	1	1					0.500
2	2	0	1						0.000
4	2	2	1	4	1				1.000
4	3	1	1	3					0.750
4	4	0	1						0.000
6	3	3	1	9	9	1			1.500
6	4	2	1	8	6				1.333
6	5	1	1	5					0.833
6	6	0	1						0.000
8	4	4	1	16	36	16	1		2.000
8	5	3	1	15	30	10			1.875
8	6	2	1	12	15				1.500
8	7	1	1	7					0.875
8	8	0	1						0.000
10	5	5	1	25	100	100	25	1	2.500
10	6	4	1	24	90	80	15		2.400
10	7	3	1	21	63	35			2.100
10	8	2	1	16	28				1.600
10	9	1	1	9					0.900
10	10	0	1						0.000

a) n_I is the number of configurations (in terms of Wannier orbitals) having I doubly occupied orbitals. $\langle I \rangle$ is the average number of doubly occupied orbitals per configuration.

b) For HF(C_s), n_I and $\langle I \rangle$ depend only on B.

Table 7. One-electron integrals over Wannier orbitals.

System	a (Å)	h^{ω}_{11} (eV)	h^{ω}_{12} (eV)	$h^{\omega}_{13}/h^{\omega}_{12}$	$h^{\omega}_{14}/h^{\omega}_{12}$	$h^{\omega}_{15}/h^{\omega}_{12}$	$h^{\omega}_{16}/h^{\omega}_{12}$
Ag_6	2.889	−23.702	−1.534	−0.038	0.133		
Ag_8	2.889	−27.001	−1.358	−0.108	0.071	−0.037	
Ag_{10}	2.889	−29.468	−1.237	−0.149	0.064	−0.029	0.022
Li_6	3.014	−22.444	−1.000	0.133	0.105		
Li_{10}	3.014	−27.851	−0.710	−0.012	0.014	0.002	0.004
Li_{14}	3.014	−31.253	−0.584	−0.058	0.011	−0.001	0.001
Cu_{10}	2.556	−32.196	−1.579	−0.147	0.066	−0.031	0.025
Ag_{10}	2.889	−29.468	−1.237	−0.149	0.064	−0.029	0.022
Au_{10}	2.884	−31.106	−1.372	−0.221	0.109	−0.070	0.051
Li_{10}	3.014	−27.851	−0.710	−0.012	0.014	0.002	0.004
Na_{10}	3.659	−23.313	−0.764	−0.156	0.056	−0.022	0.017

Table 8. Two-electron integrals over Wannier orbitals.

System	a (Å)	J^{ω}_{11} (eV)	J^{ω}_{12} (eV)	$J^{\omega}_{13}/J^{\omega}_{12}$	$J^{\omega}_{14}/J^{\omega}_{12}$	$J^{\omega}_{15}/J^{\omega}_{12}$	$J^{\omega}_{16}/J^{\omega}_{12}$
Ag_6	2.889	7.882	4.513	0.622	0.536		
Ag_8	2.889	8.001	4.536	0.587	0.447	0.412	
Ag_{10}	2.889	8.065	4.549	0.572	0.415	0.351	0.334
Li_6	3.014	8.079	4.404	0.615	0.535		
Li_{10}	3.014	8.267	4.399	0.562	0.411	0.350	0.333
Li_{14}	3.014	8.325	4.398	0.549	0.385	0.307	0.267
Cu_{10}	2.556	8.639	5.004	0.580	0.422	0.358	0.340
Ag_{10}	2.889	8.065	4.549	0.572	0.415	0.351	0.334
Au_{10}	2.884	7.995	4.705	0.571	0.410	0.345	0.327
Li_{10}	3.014	8.267	4.399	0.562	0.411	0.350	0.333
Na_{10}	3.659	6.783	3.661	0.563	0.409	0.347	0.330

System	a (Å)	K^{ω}_{11} (eV)	K^{ω}_{12} (eV)	$K^{\omega}_{13}/K^{\omega}_{12}$	$K^{\omega}_{14}/K^{\omega}_{12}$	$K^{\omega}_{15}/K^{\omega}_{12}$	$K^{\omega}_{16}/K^{\omega}_{12}$
Ag_6	2.889	7.882	0.159	0.068	0.019		
Ag_8	2.889	8.001	0.148	0.081	0.013	0.002	
Ag_{10}	2.889	8.065	0.141	0.088	0.015	0.003	0.001
Li_6	3.014	8.079	0.093	0.032	0.012		
Li_{10}	3.014	8.267	0.069	0.021	0.002	0.000	0.000
Li_{14}	3.014	8.325	0.061	0.026	0.002	0.000	0.000
Cu_{10}	2.556	8.639	0.164	0.093	0.017	0.003	0.001
Ag_{10}	2.889	8.065	0.141	0.088	0.015	0.003	0.001
Au_{10}	2.884	7.995	0.206	0.134	0.031	0.007	0.004
Li_{10}	3.014	8.267	0.069	0.021	0.002	0.000	0.000
Na_{10}	3.659	6.783	0.091	0.076	0.012	0.002	0.001

Table 9. Details of $B = 0$ and $B = 1$ HF wavefunctions for Cu_{10}. [a]

A	B	Orbital Symmetry Restriction	E^{TOTAL} (eV)	E^{ONE} (eV)	E^{TWO} (eV)	[b] $\langle I \rangle$	[c] R_{IONIC} (a)	Relaxation Energy (eV)	[d] Overlap
10	0	D_{10h}, relaxed	−13722.35	−321.96	124.74		0.0		
			—— Energy relative to $E_{B=0}$ ——						
9	1	C_s, Eq. (E4)	−1.01	−3.16	2.15	0.5	1.126		
9	1	C_s, frozen	−0.38	−3.16	2.78	0.5	1.126		
9	1	C_s, relaxed	−1.61	−4.56	2.95	0.5		1.23	0.947
9	1	C_{2h}, Eq. (E4)	3.80	0.00	3.80	0.5	3.312		
9	1	C_{2h}, frozen	3.76	−0.08	3.84	0.5	3.312		
9	1	C_{2h}, relaxed	−0.63	−5.82	5.19	0.9		4.39	0.447
9	1	D_{10h}, Eq. (E4)	−0.74	−6.31	5.57	0.9	2.003		
9	1	D_{10h}, frozen	−0.39	−6.81	6.42	0.9	2.003		
9	1	D_{10h}, relaxed	−0.63	−5.82	5.19	0.9		0.24	0.999

a) $E_{10}^{CORE} = -13525.13$ eV; $a = 2.556$ Å.

b) Average number of doubly-occupied ω_j per configuration.

c) Reciprocal of the average reciprocal distance between doubly-occupied and empty ω_j. Values are given in units of the lattice constant, a.

d) Overlap of the doubly-occupied frozen orbital with the doubly-occupied relaxed orbital.

Table 10. Details of $B = 0$ and $B = 1$ HF wavefunctions for Li_{10}. [a)]

A	B	Orbital Symmetry Restriction	E^{TOTAL} (eV)	E^{ONE} (eV)	E^{TWO} (eV)	b) $\langle I \rangle$	c) R_{IONIC} (a)	Relaxation Energy (eV)	d) Overlap
10	0	D_{10h}, relaxed	−2024.66	−278.51	108.82		0.0		
			—— Energy relative to $E_{B=0}$ ——						
9	1	C_s, Eq. (E4)	0.65	−1.42	2.07	0.5	1.086		
9	1	C_s, frozen	0.78	−1.42	2.20	0.5	1.086		
9	1	C_s, relaxed	0.31	−1.09	1.40	0.5		0.47	0.976
9	1	C_{2h}, Eq. (E4)	3.54	0.00	3.54	0.5	3.259		
9	1	C_{2h}, frozen	3.53	−0.01	3.54	0.5	3.259		
9	1	C_{2h}, relaxed	2.19	−0.81	3.01	0.5		1.34	0.840
9	1	D_{10h}, Eq. (E4)	2.55	−2.84	5.39	0.9	1.963		
9	1	D_{10h}, frozen	2.63	−2.88	5.51	0.9	1.963		
9	1	D_{10h}, relaxed	2.33	−1.50	3.82	0.9		0.30	0.993

a) $E_{10}^{CORE} = -1854.97$ eV; $a = 3.014$ Å.

b) Average number of doubly-occupied ω_j per configuration.

c) Reciprocal of the average reciprocal distance between doubly-occupied and empty ω_j. Values are given in units of the lattice constant, a.

d) Overlap of the doubly-occupied frozen orbital with the doubly-occupied relaxed orbital.

Table 11. Detailed Energy Data for Na_{10}. [a)]

A	B	μ	UHF	HF(C_s)	HF(C_{2h})	HF(D_{Nh})
			$E_\mu^{TOTAL} - E_{\mu=1}^{TOTAL}$ (eV)			
5	5	0.0	−2.074	0.431	0.438	0.438
6	4	0.2	−1.746	0.159	0.159	0.818
7	3	0.4	−1.389	−0.128	0.725	0.776
8	2	0.6	−0.960	−0.191	−0.191	1.339
9	1	0.8	−0.489	−0.123	1.108	1.147
10	0	1.0	0.000	0.000	0.000	0.000
			$E_\mu^{ONE} - E_{\mu=1}^{ONE}$ (eV)			
5	5	0.0	−4.742	−7.140	−7.240	−7.240
6	4	0.2	−4.093	−5.976	−5.976	−6.559
7	3	0.4	−3.348	−4.881	−5.642	−5.987
8	2	0.6	−2.336	−3.354	−3.354	−4.122
9	1	0.8	−1.194	−1.704	−2.097	−2.408
10	0	1.0	0.000	0.000	0.000	0.000
			$E_\mu^{TWO} - E_{\mu=1}^{TWO}$ (eV)			
5	5	0.0	2.668	7.571	7.678	7.678
6	4	0.2	2.347	6.135	6.135	7.377
7	3	0.4	1.959	4.754	6.366	6.763
8	2	0.6	1.376	3.163	3.163	5.461
9	1	0.8	0.705	1.581	3.205	3.554
10	0	1.0	0.000	0.000	0.000	0.000

a) $a = 3.659$ Å. For $\mu = 1$, the UHF and various HF wavefunctions are identical (see Section II.B). $E_{\mu=1}^{TOTAL} = -1617.94206$ Hartree; $E^{CORE} = -1612.67937$ Hartree; $E_{\mu=1}^{ONE} = -8.56735$ Hartree; $E_{\mu=1}^{TWO} = 3.30467$ Hartree.

Table 12. HF one-electron energy bands for Au_{10}. [a)]

symmetry	mean energy (eV)	band width ($\mathcal{B}$, eV)
$d\sigma'$	12.98	3.04
$d\pi'$	12.90	2.20
$d\pi''$	12.87	1.76
$d\delta'$	12.80	0.47
$d\delta''$	12.79	0.45
(d band, overall)	12.87	3.04
(valence)	8.16	6.82

a) Energy bands based on orbital energies for the lowest energy $\mu = 1$ state of Au_{10} ($a = 2.884$ Å).

Table 13. Details of UHF results for H_N rings. [a]

system	a (Å)	$\mathcal{D}/N$ (eV/atom)	S_{12} $\mu = 0$	S_{12} $\mu = 1$	S_{12} average [b]	$\delta\phi_1$
H_6	1.483	1.630	0.646	0.710	0.678	0.00542
H_8	1.483	1.695	0.599	0.634	0.616	0.00311
H_{10}	1.483	1.744	0.594	0.603	0.598	0.00241
H_{20}	1.483	1.810	0.580	0.549	0.564	0.00272
H_{10}	1.483	1.744	0.594	0.603	0.598	0.00241
H_{10}	1.260	3.115	0.749	0.759	0.754	0.00381
H_{10}	1.186	3.750	0.800	0.796	0.798	0.00419
H_{10}	1.112	4.497	0.849	0.825	0.837	0.00552

a) $\mathcal{D}$ is the magnon dispersion, S_{12} is the nearest-neighbor overlap integral, and $\delta\phi_1$ measures the difference between orbitals $\phi_1^{\mu=0}$ and $\phi_1^{\mu=1}$ (see Section II.C.1).
b) $(S_{12}^{\mu=0} + S_{12}^{\mu=1})/2$

Table 14. Fits of the Ising and generalized Ising models to $E^{UHF}_{N,A}$ for H_N rings.[a)]

System	a (Å)	Ising $-\mathcal{J}$ (eV)	Ising $\mathcal{S}$	Ising error (%)	gen. Ising 1 $-\mathcal{J}$ (eV)	gen. Ising 1 $\mathcal{S}$	gen. Ising 1 error (%)	gen. Ising 2 [b)] $-\mathcal{J}$ (eV)	gen. Ising 2 $\mathcal{S}$	gen. Ising 2 error (%)
H_6	1.483	1.540	0.000	5.75	1.107	0.231	0.36	1.003	0.323	0.08
H_8	1.483	1.583	0.000	6.25	1.116	0.208	1.52	0.969	0.308	0.94
H_{10}	1.483	1.620	0.000	6.10	1.144	0.187	1.51	0.991	0.278	0.97
H_{20}	1.483	1.648	0.000	6.15	1.140	0.138	1.55	0.957	0.214	0.92
H_{10}	1.483	1.620	0.000	6.10	1.144	0.187	1.51	0.991	0.278	0.97
H_{10}	1.260	2.771	0.000	9.21	1.654	0.218	2.58	1.076	0.439	1.37
H_{10}	1.186	3.295	0.000	10.03	1.882	0.225	2.91	1.074	0.503	1.53
H_{10}	1.112	3.915	0.000	10.60	2.166	0.229	3.10	1.100	0.559	1.64

a) $\mathcal{J}$ and $\mathcal{S}$ are the effective nearest-neighbor exchange and overlap determined by least-squares fits [see Section II.C.2]. The error is $\Delta E^{RMS}/\mathcal{D}$, where $\mathcal{D}$ is the UHF magnon dispersion (see Table 13).

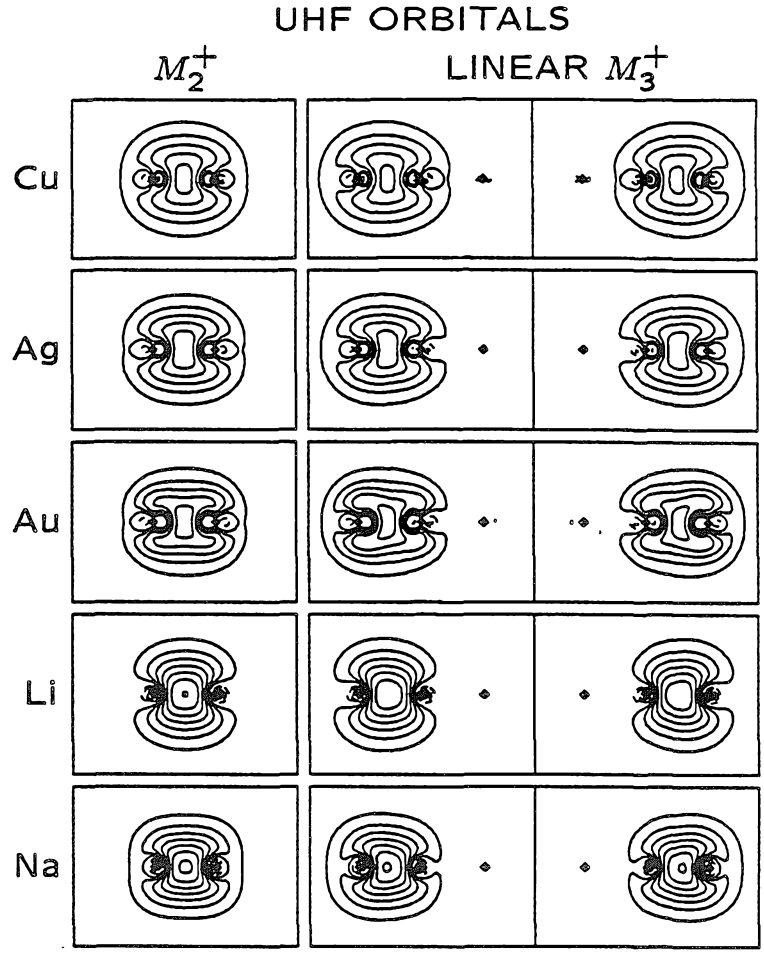

Figure 1. The optimum UHF valence orbitals for M_2^+ and linear M_3^+ (low spin), M = Cu, Ag, Au, Li, and Na. Each orbital contains one electron (one orbital for M_2^+ and two orbitals for M_3^+; overlaps for M_3^+ are given in Table 5). For Figures 1-2, the nearest-neighbor distance (a) is equal to that of the bulk metal (a = 2.556, 2.889, 2.884, 3.014, and 3.659 Å for Cu, Ag, Au, Li, and Na, respectively), and the boxes are scaled to a (box width = 3.6 a). Squares mark the atomic positions. Contours mark even amplitude increments of $0.2a^{-3/2}$. Solid and dashed contours denote positive and negative amplitudes, respectively. For M_2^+, the GVB and UHF orbitals are identical, since there is only one valence electron. For each of the linear M_3^+ clusters, the GVB orbitals are very similar to the UHF orbitals. However, for low-spin M_3^+, UHF leads to net spin densities whereas GVB does not.

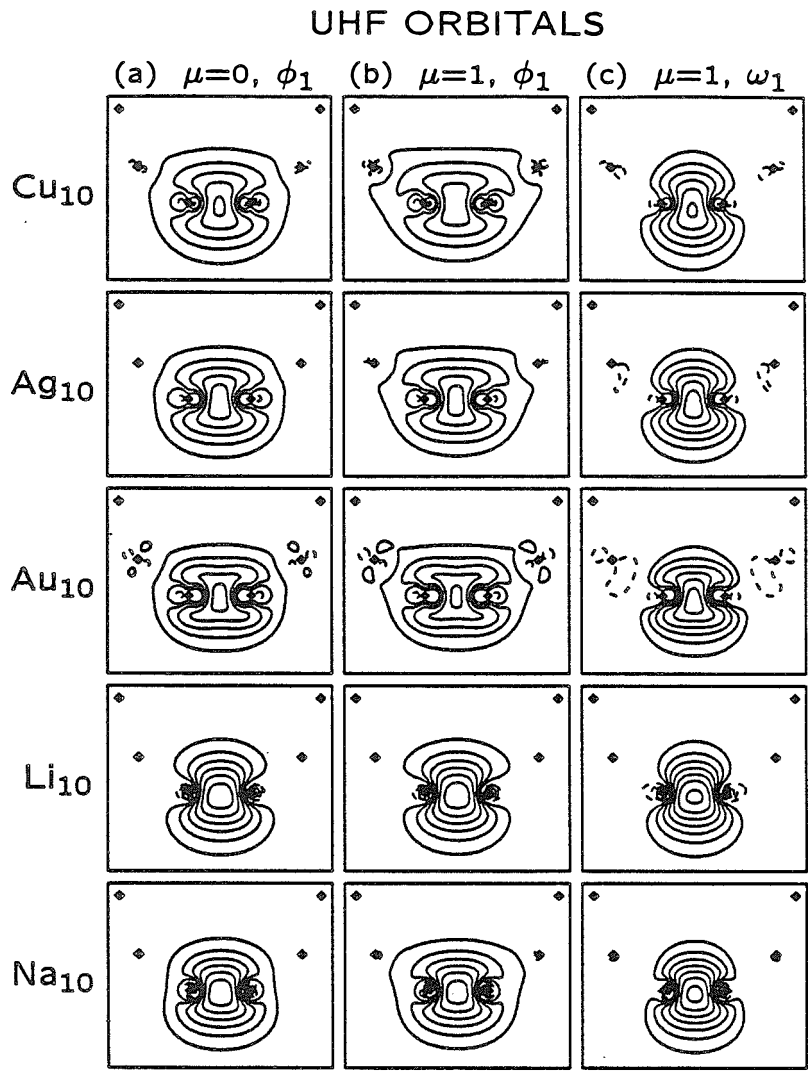

Figure 2. UHF valence orbitals for each of the Cu_{10}, Ag_{10}, Au_{10}, Li_{10}, and Na_{10} ring clusters (overlaps are given in Table 2). (a) Shows the low-spin ($\mu = 0$) UHF Hartree-localized orbital. (b) Shows the high-spin ($\mu = 1$) UHF Hartree-localized orbital. (c) Shows the high-spin UHF Wannier orbital.

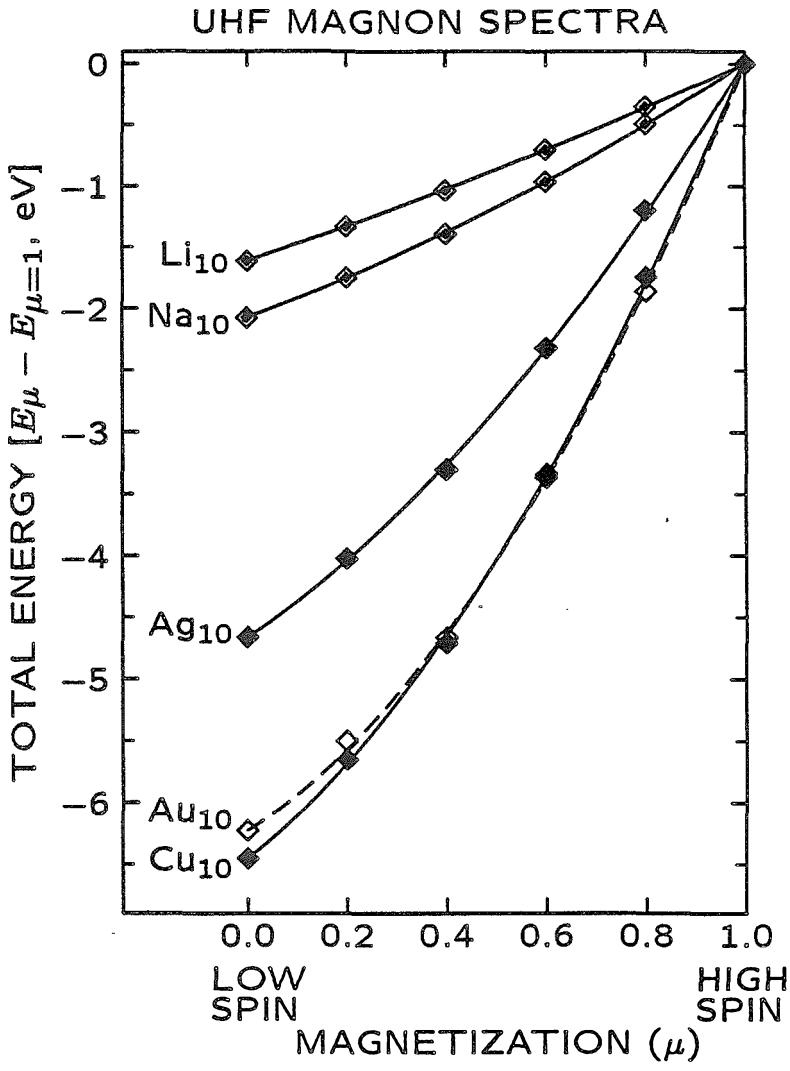

Figure 3. The UHF magnon spectra for the Cu_{10}, Ag_{10}, Au_{10}, Li_{10}, and Na_{10} ring clusters. In each case, (*i*) data points show the UHF total energy as a function of the magnetization (see Table 1), (*ii*) a curve shows the fit of the generalized Ising model to the UHF total energies (GIM2; see Table 3), and (*iii*) the UHF total energy for $\mu = 1$ is chosen as zero energy. Analogous figures all follow this convention for UHF (Figures 4-5, Figures 8-17, and Figures 24-25).

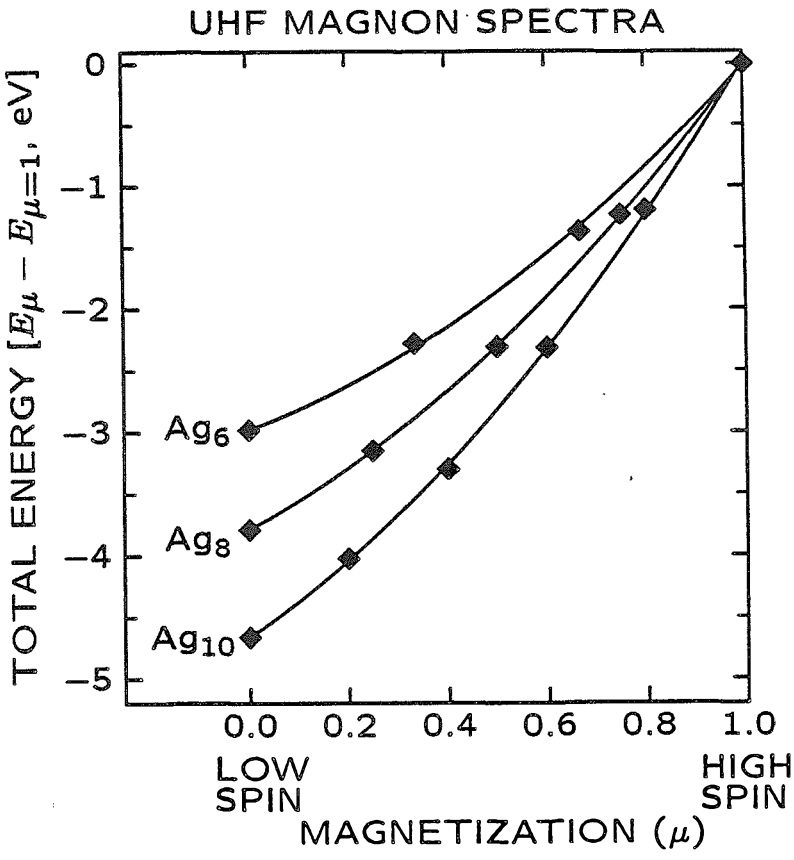

Figure 4. The UHF magnon spectra for Ag_6, Ag_8, and Ag_{10}. Data points show the UHF total energies, and the curves show the fits of the generalized Ising model to the UHF total energies (GIM2, see Table 3).

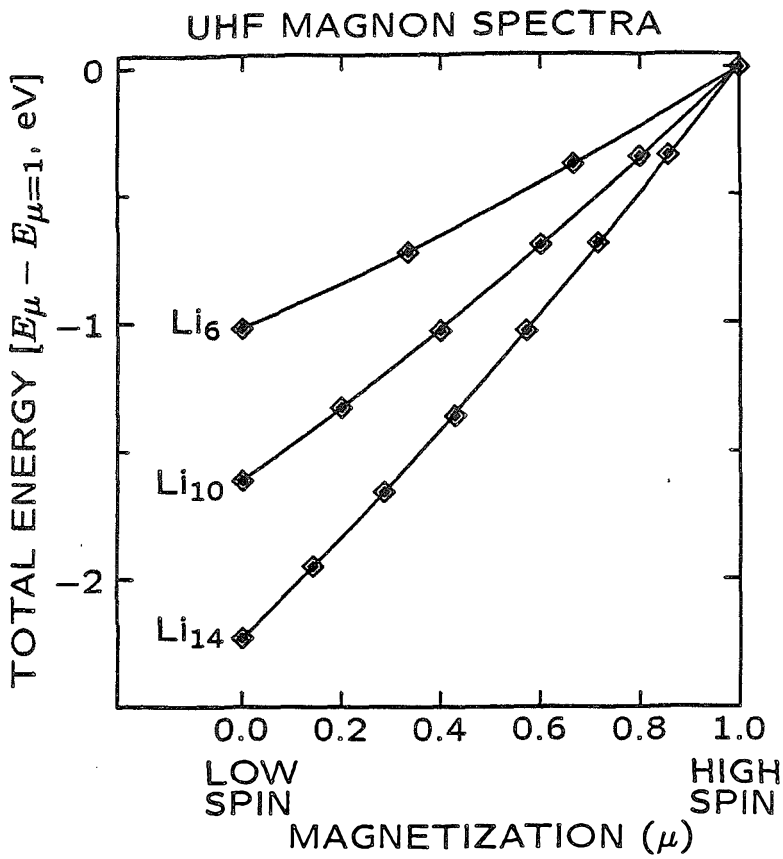

Figure 5. The UHF magnon spectra for Li_6, Li_{10}, and Li_{14}. Data points show the UHF total energies, and the curves show the fits of the generalized Ising model to the UHF total energies (GIM2, see Table 3).

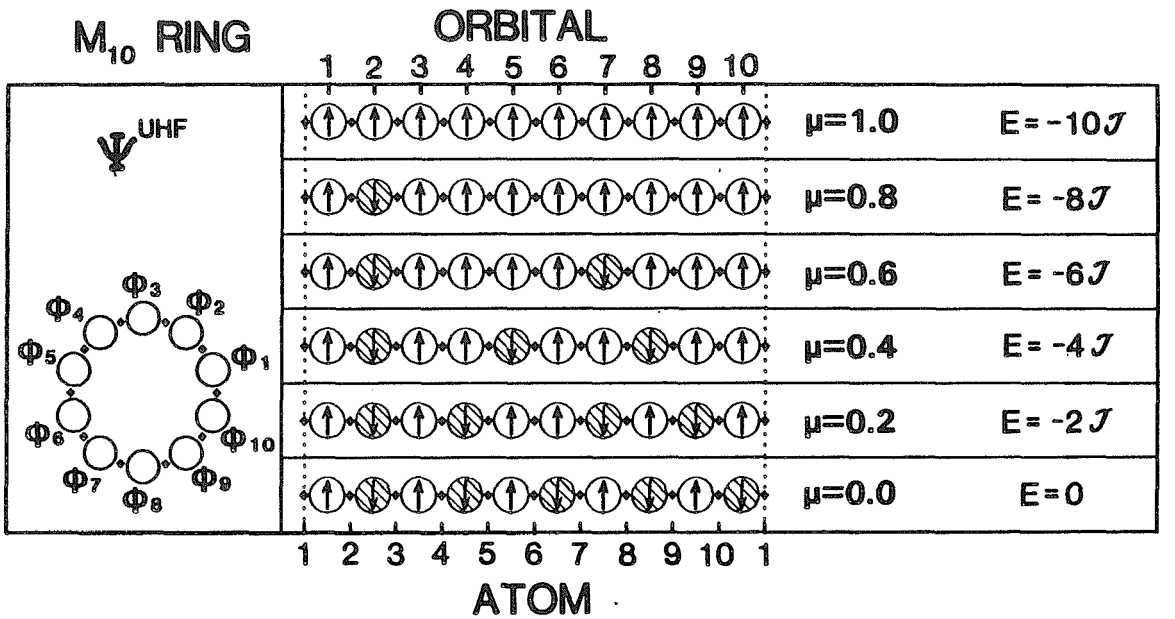

Figure 6. UHF wavefunctions for M_{10} as a function of magnetization. Left: The M_{10} ring — squares mark the atomic positions, and large circles represent the Hartree-localized orbitals (ϕ_i) centered at each bond midpoint (see Figure 2). Center: The M_{10} ring unraveled (dotted lines denote periodic boundaries). Occupations of the localized orbitals are given as a functon of magnetization (μ). Each orbital is occupied with one electron ($\uparrow$ for up-spin, $\downarrow$ for down-spin; down-spin orbitals are shaded). Right: The Ising energy as a function of magnetization. Each pair of adjacent up-spin electrons leads to an antibonding nearest-neighbor exchange interaction ($-\mathcal{J}$).

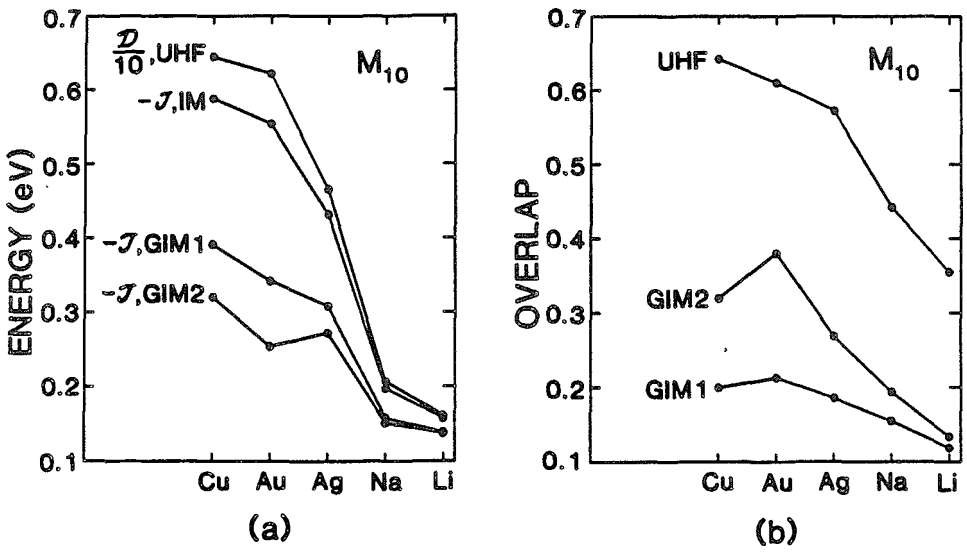

Figure 7. (a) Effective nearest-neighbor exchange energies ($\mathcal{J}$) and (b) effective nearest-neighbor overlap integrals (S), obtained by fitting the Ising Model and Generalized Ising models to the UHF total energies for Cu_{10}, Au_{10}, Ag_{10}, Na_{10}, and Li_{10} (see Table 3). Also shown are the UHF magnon dispersion energy $\mathcal{D}$ and the UHF nearest-neighbor overlap integral (see Table 2; the UHF overlap shown is the average of the values for $\mu = 0$ and $\mu = 1$).

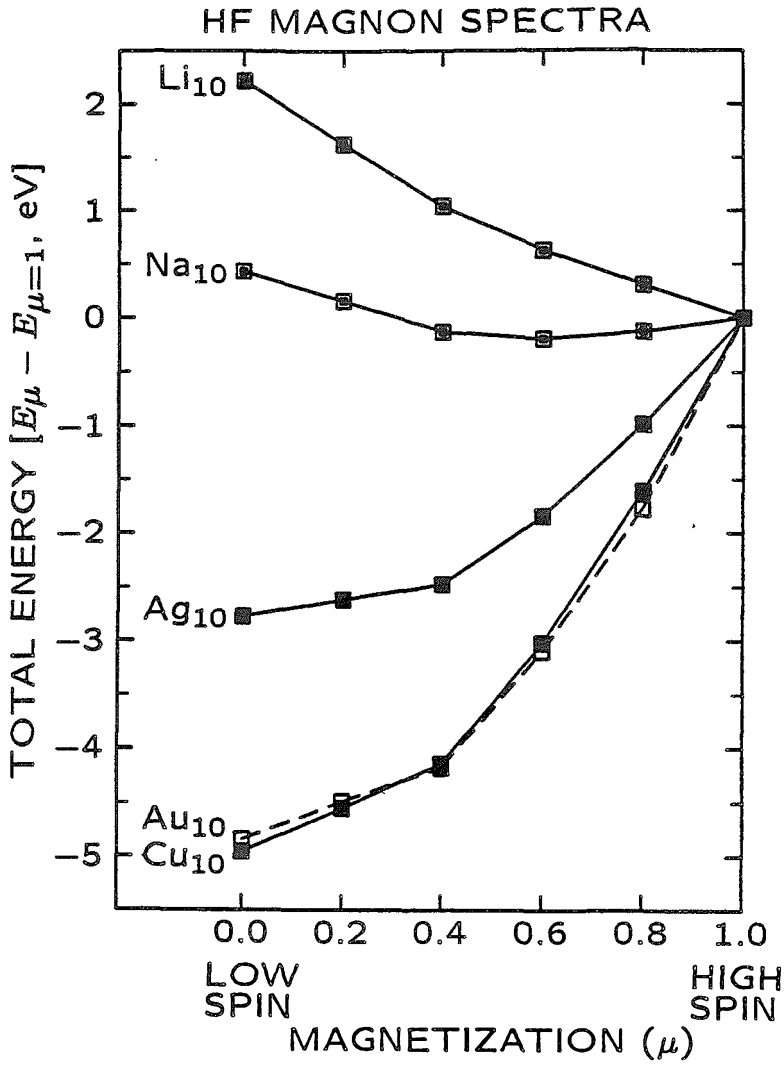

Figure 8. The HF(C_s) magnon spectra for Cu_{10}, Ag_{10}, Au_{10}, Li_{10}, and Na_{10}. In each case, (*i*) data points show the HF total energy as a function of the magnetization (see Table 1), (*ii*) line segments joining the data points serve as a guide to the eye, and (*iii*) the HF total energy for $\mu = 1$ is chosen as zero energy. Analogous figures all follow this convention for HF (Figures 9-17 and Figure 25).

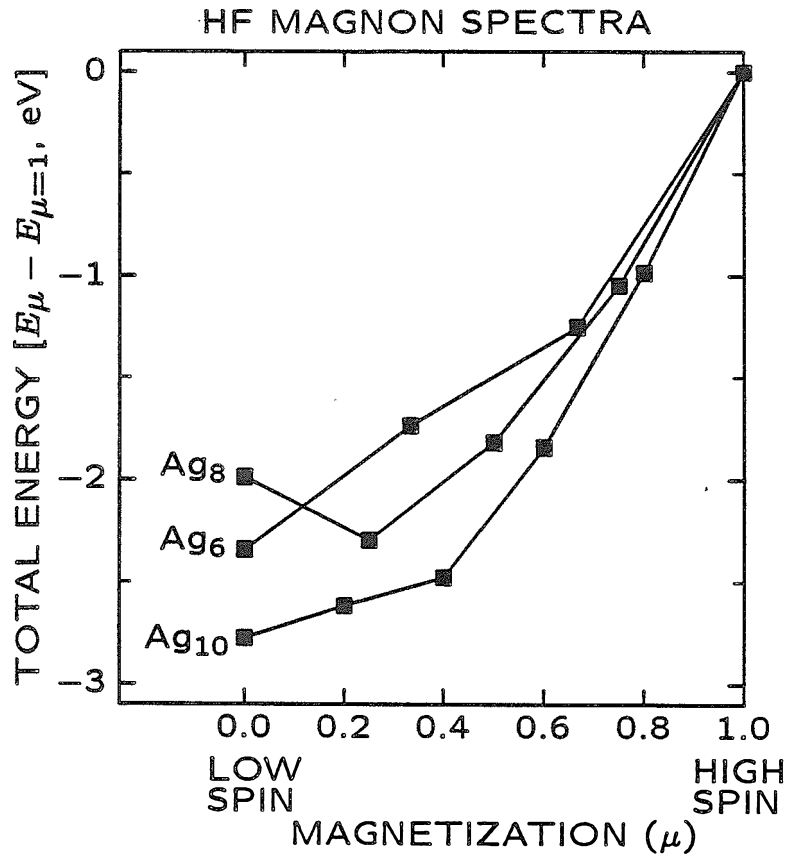

Figure 9. The HF(C_s) magnon spectra for Ag_6, Ag_8, and Ag_{10} (see Table 1).

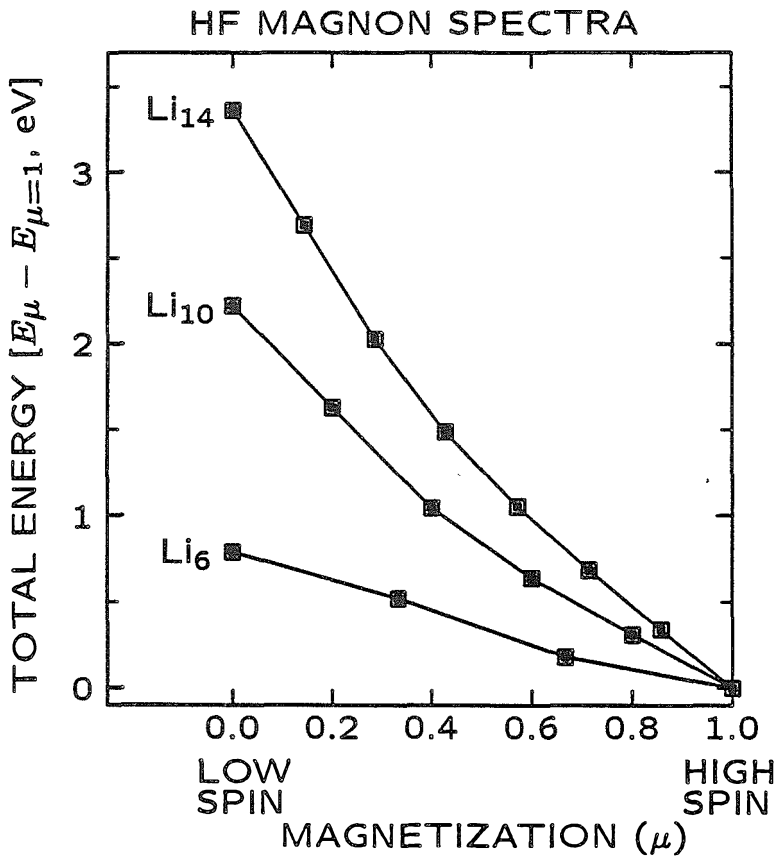

Figure 10. The HF(C_s) magnon spectra for Li_6, Li_{10}, and Li_{14} (see Table 1).

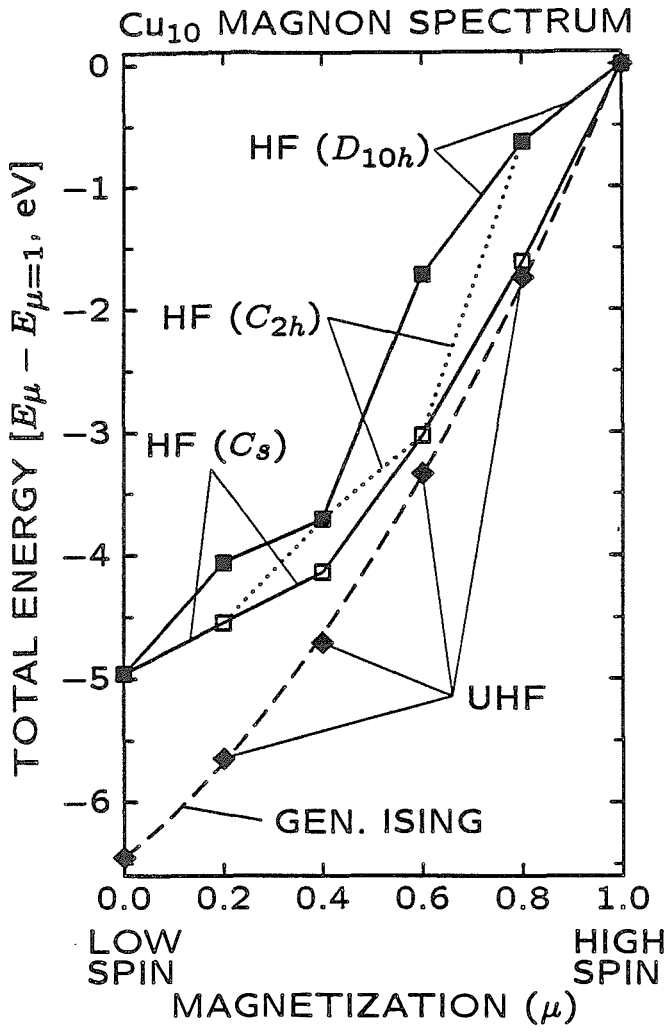

Figure 11. The Cu_{10} magnon spectrum. Data points show the total energy as a function of the magnetization for UHF, HF(C_s), HF(C_{2h}), and HF(D_{10h}), as indicated (see Table 1). The UHF results are interpolated by the generalized Ising model (GIM2, dashed line; see Table 3). Each of these four Hartree-Fock wavefunctions gives the same total energy for $\mu = 1$ (see Section II.B); hence, the total energy for $\mu = 1$ is chosen as zero energy. Analogous figures all follow this convention (Figures 12-17 and Figure 25).

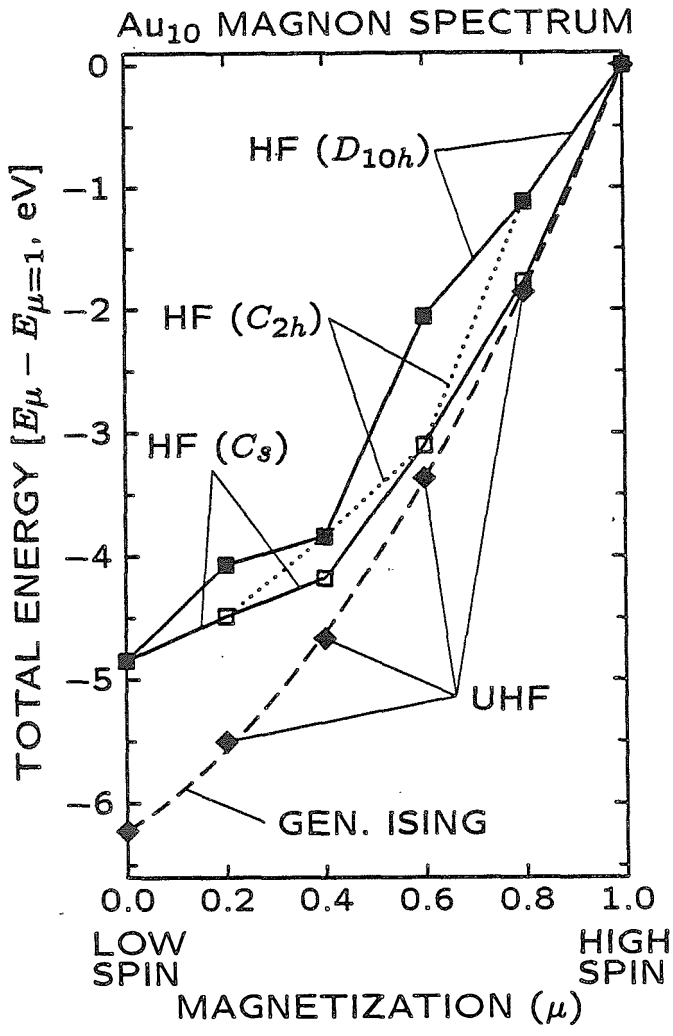

Figure 12. The Au_{10} magnon spectrum, as calculated with UHF, HF(C_s), HF(C_{2h}), and HF(D_{10h}), as indicated (see Table 1).

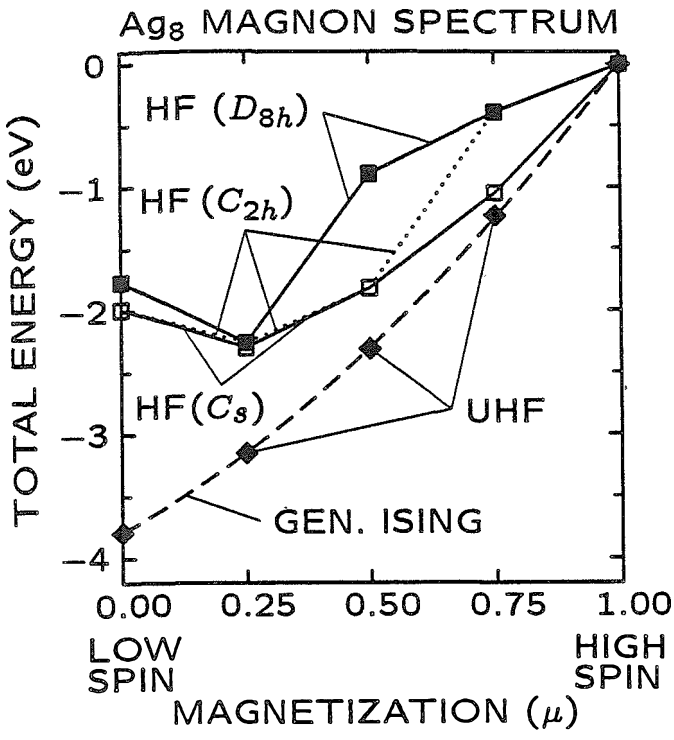

Figure 13. The Ag_8 magnon spectrum, as calculated with UHF, HF(C_s), HF(C_{2h}), and HF(D_{8h}), as indicated. The UHF results are interpolated by the generalized Ising model (GIM2, dashed line; see Table 3).

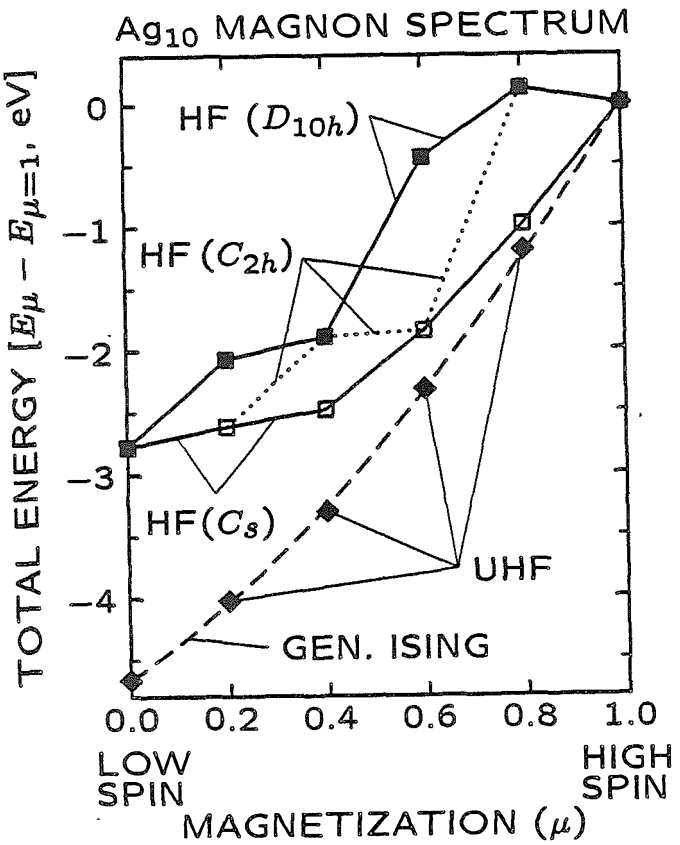

Figure 14. The Ag_{10} magnon spectrum, as calculated with UHF, HF(C_s), HF(C_{2h}), and HF(D_{10h}), as indicated (see Table 1).

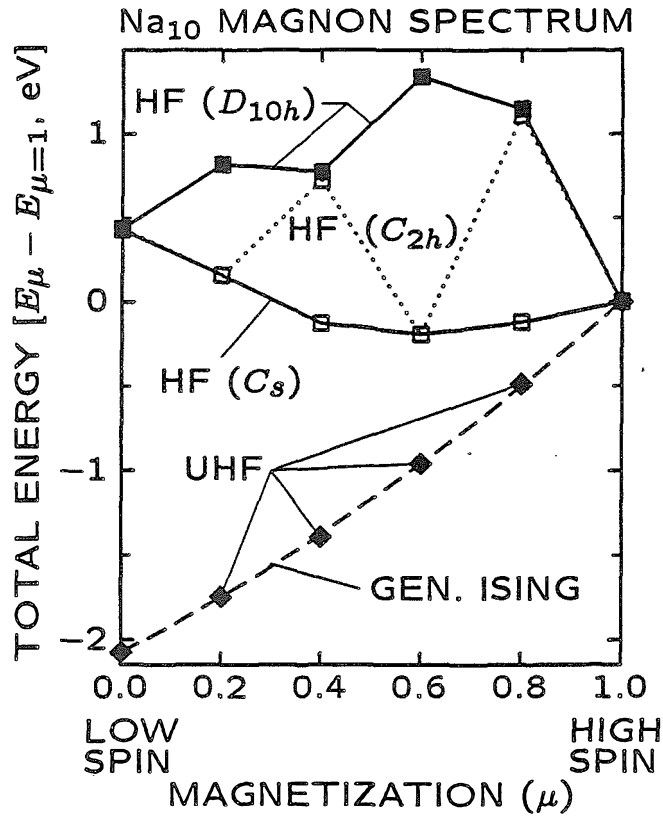

Figure 15. The Na_{10} magnon spectrum, as calculated with UHF, HF(C_s), HF(C_{2h}), and HF(D_{10h}), as indicated. The UHF results are interpolated by the generalized Ising model (GIM2, dashed line; see Table 3).

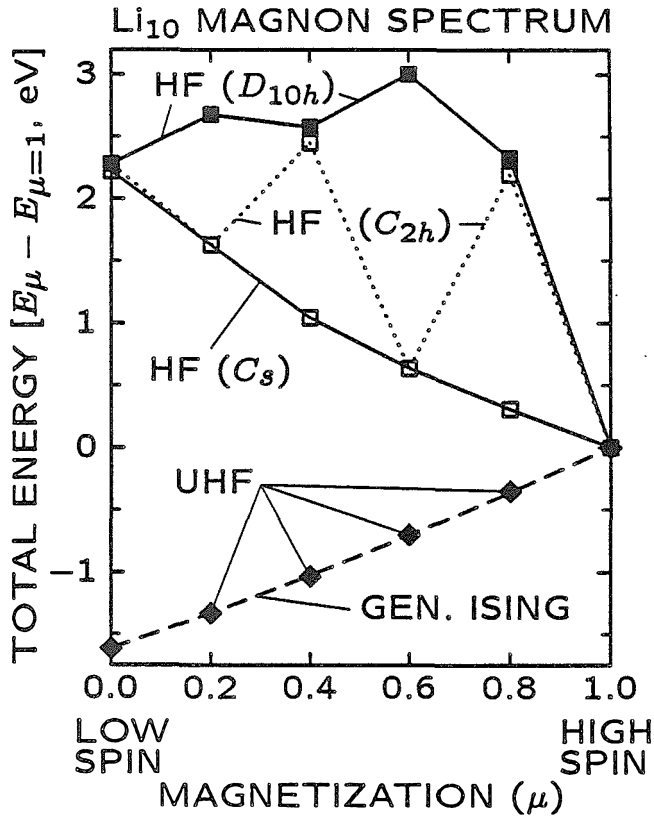

Figure 16. The Li_{10} magnon spectrum, as calculated with UHF, HF(C_s), HF(C_{2h}), and HF(D_{10h}), as indicated (see Table 1).

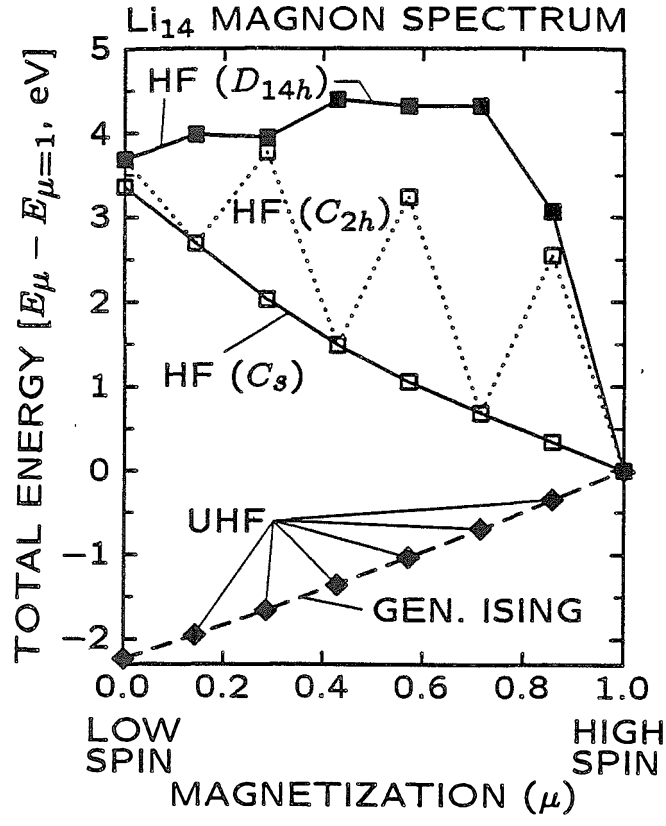

Figure 17. The Li_{14} magnon spectrum, as calculated with UHF, HF(C_s), HF(C_{2h}), and HF(D_{14h}), as indicated. The UHF results are interpolated by the generalized Ising model (GIM2, dashed line; see Table 3).

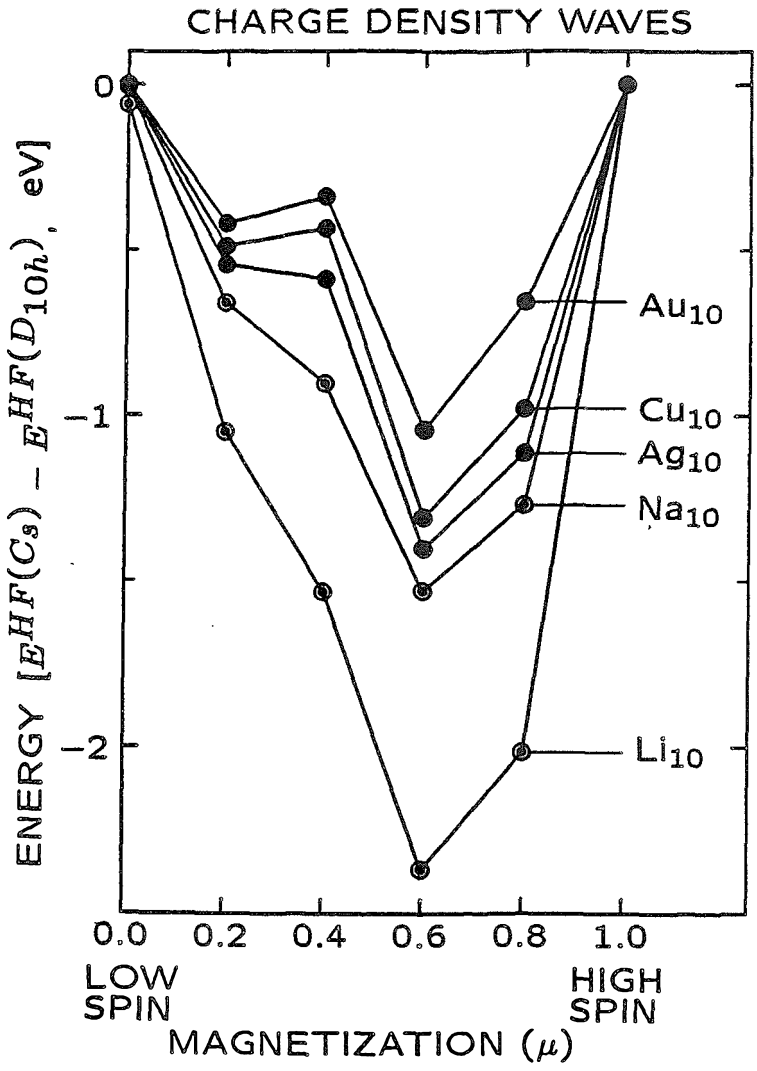

Figure 18. Energetic magnitudes of charge density wave effects $[E^{HF(C_s)} - E^{HF(D_{10h})}]$ as a function of magnetization for the various M_{10} ring clusters (see Table 4).

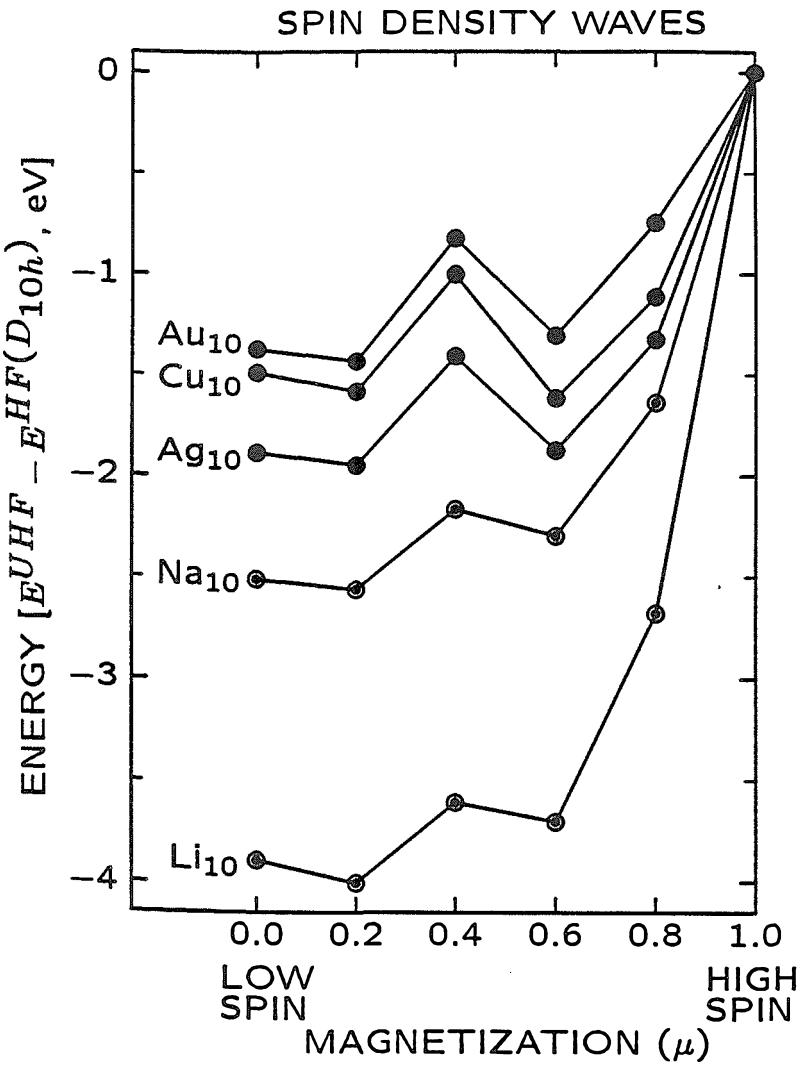

Figure 19. Energetic magnitudes of spin density wave effects $[E^{UHF} - E^{HF(D_{10h})}]$ as a function of magnetization for the various M_{10} ring clusters (see Table 4).

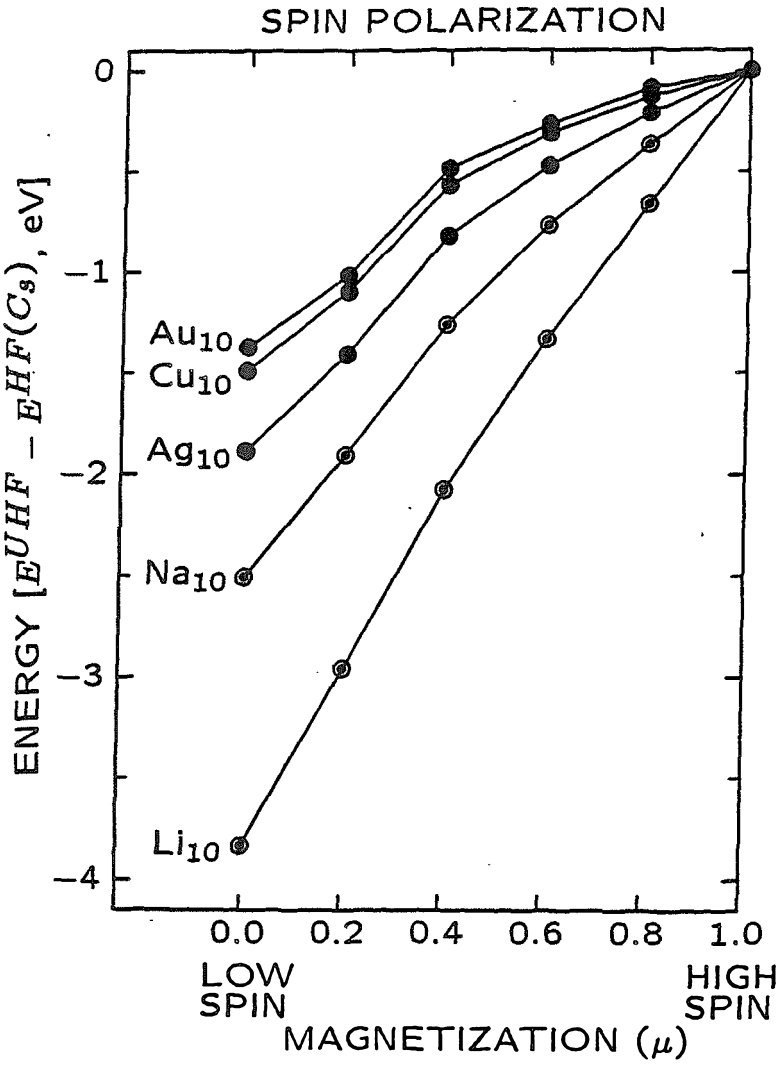

Figure 20. Energetic magnitudes of spin polarization effects $[E^{UHF} - E^{HF(C_s)}]$ as a function of magnetization for the various M_{10} ring clusters (see Table 4).

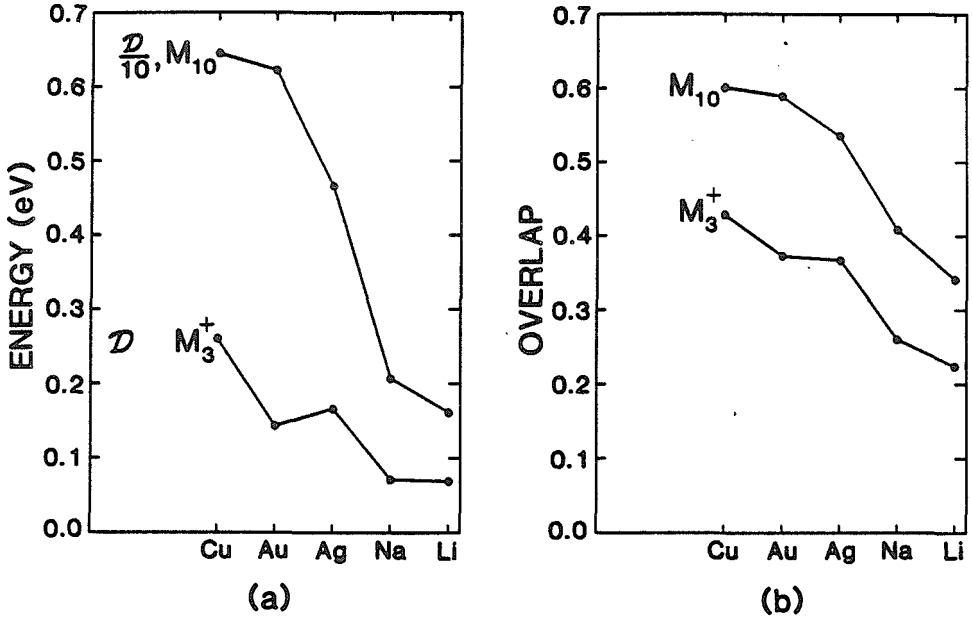

Figure 21. (a) The UHF magnon dispersion energy ($\mathcal{D}$) divided by the number of nearest-neighbor exchange interactions — ten for M_{10} and one for linear M_3^+. (b) The UHF nearest-neighbor overlap integral for M_{10} and M_3^+ ($\mu = 0$; Hartree-localized orbitals — see Figures 1-2, Table 2, and Table 5).

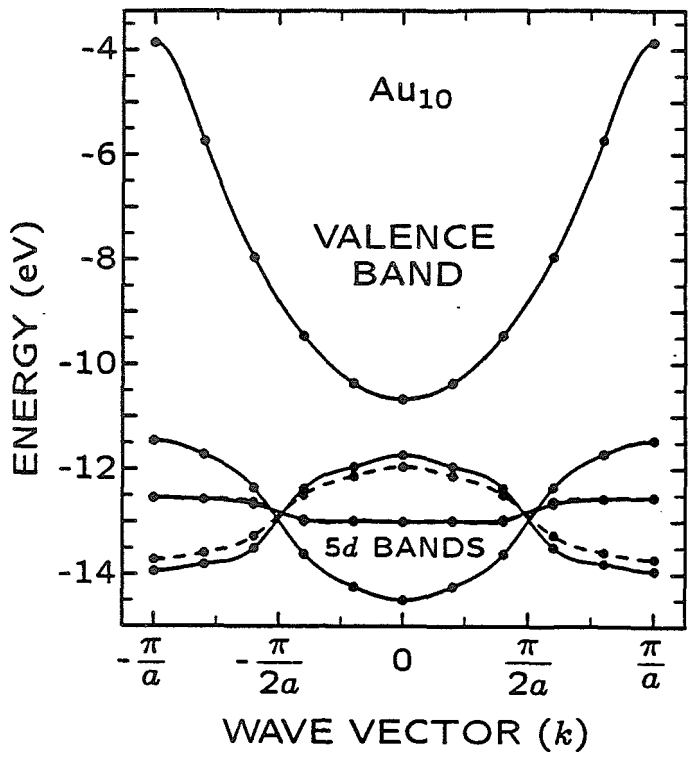

Figure 22. The Au_{10} one-electron energy bands. Data points show the orbital energies (Koopmans' theorem) for the $\mu = 1$ state as a function of wave vector (k). The valence energy levels are each singly-occupied and the $5d$ (core) energy levels are each doubly-occupied. Curves joining the data points approximate the band of continuous energy levels for the infinite ring. Figure 23 shows the $5d$ energy bands in greater detail (also see Table 12).

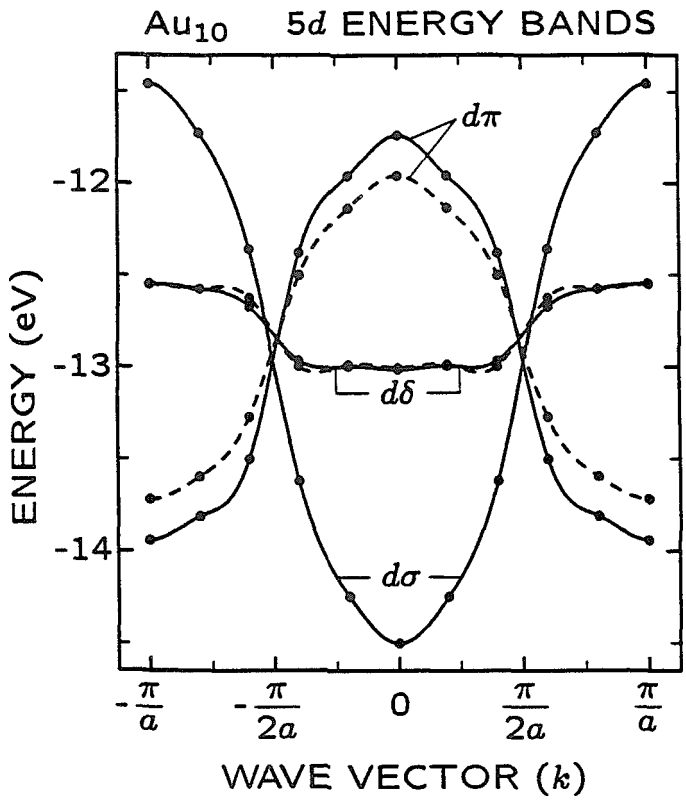

Figure 23. The Au_{10} $5d$ one-electron energy bands. The $5d$ energy levels split into five bands — $d\sigma'$, $d\pi'$, $d\pi''$, $d\delta'$, and $d\delta''$, as indicated (dashed curves join the double-prime energy levels). Figure 22 shows the valence band (also see Table 12).

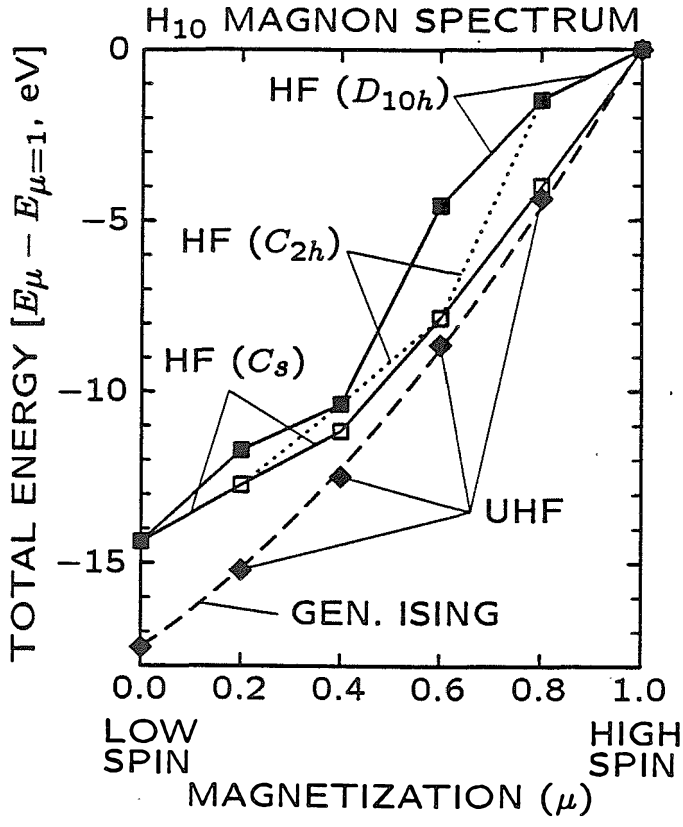

Figure 24. The H_{20} magnon spectrum. Data points show the UHF total energy as a function of the magnetization. The UHF results are interpolated by the Ising model, and the generalized Ising models — GIM1 (dashed line) and GIM2 (solid line) — as indicated (also see Tables 13-14). The UHF total energy for $\mu = 1$ is chosen as zero energy.

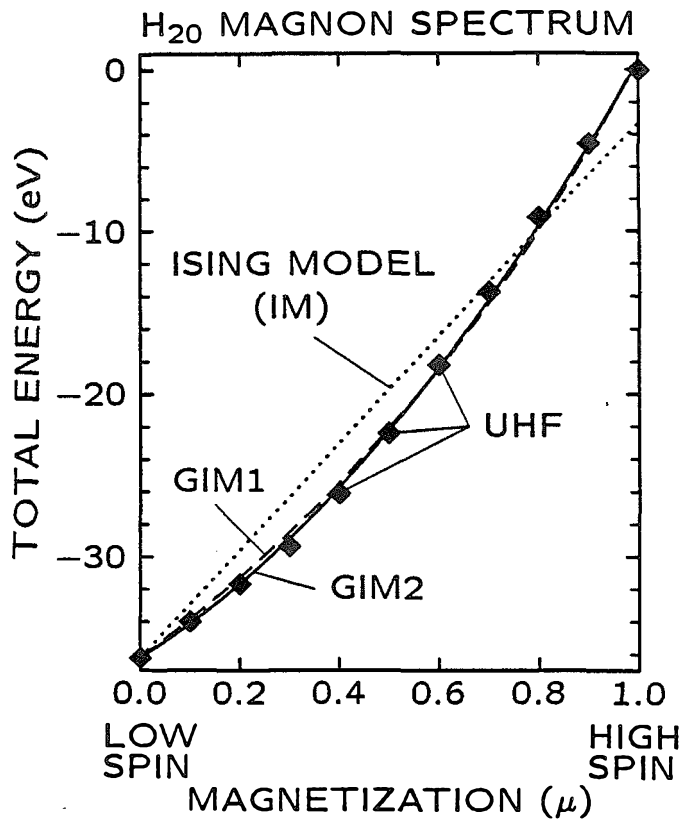

Figure 25. The H_{10} magnon spectrum. Data points show the total energy as a function of the magnetization for UHF, HF(C_s), HF(C_{2h}), and HF(D_{10h}), as indicated. The UHF results are interpolated by the generalized Ising model (GIM2, dashed line; see Table 14). Each of these four Hartree-Fock wavefunctions gives the same total energy for $\mu = 1$; hence, the total energy for $\mu = 1$ is chosen as zero energy.

Chapter 4

Magnon Dispersion, Spin Density Waves, and Charge Density Waves in One-Dimensional Metals: Ab Initio GVB Wavefunctions for Cu, Ag, Au, Li, and Na

I. Introduction

One-dimensional monovalent metals have long served as bench marks for electronic structure theories of metals.[1,2,3,4,5,6,7]

For example, for a one-dimensional chain of monovalent atoms, simple energy band theory leads to a half-filled energy band. However, Peierls[6] showed that the half-filled energy band is susceptible to a distortion pairing up adjacent atoms, leading to a band gap at the Fermi level and hence a metal to insulator transition. However, the Hubbard hamiltonian[7,8] leads to an antiferromagnetic insulator for the undistorted chain.

We have carried out *ab initio*[9,10] total energy calculations[11,12,13] for M_N ring clusters composed of Cu, Ag, Au, Li, and Na using three distinct types of wavefunctions — restricted Hartree-Fock (HF, non-spin-polarized) unrestricted Hartree-Fock (UHF, spin-polarized) and generalized valence bond (GVB). These studies show that,

for normal lattice constants, the one-dimensional metals composed of Cu, Ag, Au, Li, and Na are all in the "low-density limit" with respect to the treatment of the electron-electron interactions. Hence, simple energy band theory leads to incorrect results for these systems.[11,12,13]

At the highest level of theory (GVB),[12] these systems are antiferromagnetic insulators having fully symmetrical charge and spin densities, and do not lead to Peierls instabilities.[14] These systems lead to strong cohesion due to two-center one-electron bonding,[12] as shown by the GVB valence orbitals for M_2^+, linear M_3^+, and M_{10} in Figures 1-2. However, both UHF and HF lead to incorrect results (in comparison to GVB), such as spin density waves (for UHF), charge density waves (for HF), and Peierls instabilities (for HF).[11,15]

Here, we present GVB results calculated for all allowed magnetizations of the Cu_{10}, Ag_6, Ag_8, Ag_{10}, Au_{10}, Li_6, Li_{10}, and Na_{10} ring clusters. We show that the GVB magnon spectra are consistent with a nearest-neighbor Heisenberg model.[1,16] An analogous HF and UHF study of these systems is presented in full detail elsewhere.[13]

II. Details of the Calculations

For each of the Cu_{10}, Ag_6, Ag_8, Ag_{10}, Au_{10}, Li_6, Li_{10}, and Na_{10} ring clusters we optimize the GVB wavefunction for the lowest energy state of each allowed magnetization (or density of unpaired spins)

$$\mu = \frac{|A - B|}{N}$$

where A and B are the number of up-spin electrons ($\uparrow$ or α) and down-spin electrons ($\downarrow$ or β), respectively ($A+B = N$). The magnon spectrum is simply the total energy as a function of magnetization.

These magnon spectra are calculated using the same geometries, hamiltonians, and basis sets as in previous studies.[11,12,13] The bond lengths or lattice constants (a) are taken equal to the nearest-neighbor distances for the respective bulk metals[17] (except where noted otherwise — for lithium, in addition to $a = 3.014$ Å[17] we also include results for $a = 2.50$ Å and for $a = 3.10$ Å).

For each of these systems, the effect of valence magnetization changes on the core orbitals is small.[11] For Cu_{10}, Ag_6, Ag_8, Ag_{10}, and Au_{10}, optimizing all orbitals self-consistently leads to minimal hybridization between the d orbitals (core) and the valence sp orbitals for both the low-spin ($\mu = 0$) and high-spin ($\mu = 1$) states.[11] In addition, the closed-shell d^{10} configurations are maintained for magnetizations $0 \leq \mu \leq 1$.[11,13] Hence, we incorporate the same frozen core approximation as utilized previously (including the closed-shell d^{10} electrons of the noble metal rings).[11,12,13] This frozen core approximation is expected to be reasonably accurate for magnetizations $0 \leq \mu \leq 1$.[11]

The full (spin-optimized) generalized valence bond (SOGVB)[18] valence wavefunction for M_N (monovalent M) can be written in the general form

$$\begin{aligned} \Psi_{N,A} &= \hat{\mathcal{A}}[\Phi_{N,A}\,\chi_{N,A}] \\ \Phi_{N,A} &= \varphi_1(1)\varphi_2(2)\varphi_3(3)\cdots\varphi_N(N) \qquad (1) \\ \chi_{N,A} &= \sum_{i=1}^{n_f} c_i f_i^{N,S} \qquad (2) \\ n_f &= \frac{2S+1}{A+1}\binom{N}{A} \\ A &= S + N/2 \end{aligned}$$

where $\hat{\mathcal{A}}$ is the antisymmetrizer or determinantal operator, $\Phi_{N,A}$ is the many-electron spatial product function, $\{\varphi_i\}$ are completely general one-electron valence orbitals optimized self-consistently for each state A without restrictions with respect to sym-

metry or overlap (the numbers in parentheses label the electronic coordinates),[19] and $\chi_{N,A}$ is a completely general N-electron spin function for total spin S where the coefficients c_i are optimized self-consistently and $\{f_i^{N,S}\}$ is a *complete set of spin eigenfunctions*. Thus, using the normal N-electron spin operators, the $\{f_i^{N,S}\}$ satisfy the eigenvalue equations

$$\begin{aligned}
\widehat{S}^2 &= \widehat{S}_x^2 + \widehat{S}_y^2 + \widehat{S}_z^2 = \widehat{S}_z^2 + \widehat{S}_z + \widehat{S}^- \widehat{S}^+ \\
\widehat{S}^2 f_i^{N,S} &= S(S+1)\hbar^2 f_i^{N,S} \\
S &= \frac{|A-B|}{2} \\
\widehat{S}_z f_i^{N,S} &= M_S \hbar f_i^{N,S} \\
M_S &= \frac{A-B}{2}
\end{aligned}$$

where S is the spin angular momentum quantum number, and M_S is the spin angular momentum projection quantum number. As long as the complete set of spin eigenfunctions is used, optimizing χ in this fashion imposes no restriction[18] since $\widehat{S}^2$ and $\widehat{S}_z$ commute with one another and with the Hamiltonian. Thus, the wavefunction (1, 2) is a simultaneous eigenfunction of $\widehat{S}^2$ and $\widehat{S}_z$ and satisfies the Pauli principle for arbitrary $\{\varphi_i\}$ and χ.[18] The simultaneous self-consistent optimization of $\{\varphi_i\}$ and χ leads to the SOGVB wavefunction.[18]

For SOGVB, all N orbitals are allowed to overlap arbitrarily with one another, leading to an energy expression

$$E = \langle \Phi | \widehat{\mathcal{H}} | \Psi \rangle / \langle \Phi | \Psi \rangle$$

involving $N!$ terms. As a result SOGVB is not practicable for large N.

Instead we use a procedure for obtaining a wavefunction mimicking SOGVB but optimizing N *orthogonal* orbitals in place of the N overlapping orbitals. This proce-

dure leads to the self-consistent field full configuration interaction GVB wavefunction [GVB–CI(SCF)]. Using the GVB–CI(SCF) orthogonal orbitals as the basis, localized *non-orthogonal* orbitals $\{\phi_i\}$ mimicking the SOGVB orbitals $\{\varphi_i\}$ are obtained with the Hartree localization method. The GVB–CI(SCF) and Hartree-localization methods are fully described elsewhere.[12] The GVB–CI(SCF) results are labelled either full GVB or GVB.

The UHF wavefunction has the same general form (1, 2) except that the UHF spin function

$$\chi_{N,A}^{UHF} = \alpha^A \beta^B$$

is a simple product. $\chi_{N,A}^{UHF}$ is an eigenfunction of $\hat{S}_z$ but is *not* an eigenfunction of $\hat{S}^2$ (except for $B = 0$). The UHF wavefunction is not an eigenfunction of $\hat{S}^2$ unless each down-spin orbital is equal to an up-spin orbital, e.g.,

$$\varphi_{i+A} = \varphi_i,\ 1 \leq i \leq B$$

(this leads to the restricted Hartree-Fock wavefunction, denoted simply HF herein).[11] For the general case where $\Psi^{UHF} \neq \Psi^{HF}$, $\Psi_{N,A}^{UHF}$ is "spin-contaminated" — $\Psi_{N,A}^{UHF}$ contains a mixture of spins $|M_S| \leq S \leq N/2$.[11]

For $\mu = 1$ (high-spin; $B = 0$), there is just one spin eigenfunction

$$\chi_{N,A=N} = f^{N,S=N/2} = \alpha^N$$

and hence the GVB, UHF, and HF wavefunctions are equivalent.

Here, we present magnon spectra calculated with GVB wavefunctions, and compare the GVB results with results calculated with HF and UHF wavefunctions. For magnetizations $\mu < 1$, GVB, UHF, and HF differ dramatically. The HF and UHF magnon spectra are discussed in full detail elsewhere.[13]

III. Results and Discussion

A. Ab Initio (GVB) Magnon Spectra

The GVB magnon spectra for the Cu_{10}, Ag_6, Ag_8, Ag_{10}, Au_{10}, Li_6, Li_{10}, and Na_{10} ring clusters are given in Table 1 and Figures 3-4.

For each case, GVB leads to a low-spin (antiferromagnetic, $\mu = 0$) ground state with a monotonic increase in the total energy as μ is increased. The magnon dispersion energies

$$\mathcal{D}_N = E_{N,\mu=1} - E_{N,\mu=0}$$

follow the trend Cu > Au > Ag $\gg$ Na > Li for M_{10} (see Figure 3).

For each magnetization $0 \leq \mu \leq 1$ of each M_N ring cluster, GVB leads to a fully symmetrical charge density and a fully symmetrical spin density. Hence, the Hartree-localized orbitals $\{\phi_i\}$ exhibit the full symmetry of the molecule. In each case, ϕ_1 is centered symmetrically at bond midpoint number 1, as shown in Figure 2 for the $\mu = 0$ and $\mu = 1$ states of each M_{10} ring cluster. Orbitals ϕ_1 and ϕ_{1+i} are related by a rotation through i bond midpoints.

For each of the Cu_{10}, Ag_6, Ag_8, Ag_{10}, Au_{10}, Li_6, Li_{10}, and Na_{10} ring clusters, the $\{\phi_i\}$ exhibit only minor variations as a function of μ. Hence, the $\{\phi_i\}$ optimized for $\mu = 1$ (high-spin, Figure 2b) are very similar to the $\{\phi_i\}$ optimized for $\mu = 0$ (low-spin, Figure 2a). For Cu_{10}, Ag_{10}, Au_{10}, Li_{10}, and Na_{10}, the average value of

$$\delta\phi_1 = 1 - \langle \phi_1^{\mu=0} | \phi_1^{\mu=1} \rangle$$

is 0.00384 (individual values are listed in Table 2).

For M_{10}, values of the nearest-neighbor overlap integrals

$$S_{12} = \langle \phi_1 | \phi_2 \rangle$$

for $\mu = 1$ are 6-31% larger than those for $\mu = 0$ (see Table 2). These $\mathcal{S}_{12}$ values ($\mathcal{S}_{12}^{\mu=0}$, $\mathcal{S}_{12}^{\mu=1}$, and their average) follow the same trend as the $\mathcal{D}$ values (Cu > Au > Ag $\gg$ Na > Li; see Table 2).

For M_N, the orbitals are centered at bond midpoints, and the distance between adjacent bond midpoints

$$R^{BM} = a \cos(\pi/N) \tag{3}$$

increases with increasing N (for fixed a). This explains the decrease of the nearest-neighbor overlap ($\mathcal{S}_{12}$) with increasing N for the series Ag_6, Ag_8, Ag_{10} (see Table 2).

For each of the M_N ring clusters, the GVB magnon spectrum is in fairly accurate agreement with that given by the exact solutions of the nearest-neighbor Heisenberg model (HM)[1,16] (see Table 3 and Figures 3-4). Details of the Heisenberg model are given in Section III.B. Here we discuss further details of the GVB results using the effective nearest-neighbor exchange energies ($\mathcal{J}$) determined by (i) the GVB values of $\mathcal{D}$ and (ii) the HM values of the nearest-neighbor exchange coefficients (U; see Section III.B for further details).

For Li_8, results for $a = 3.10$ Å and for $a = 2.50$ Å indicate that both $\mathcal{J}$ and $\mathcal{D}/N$ decrease as the distance between adjacent orbitals decreases (see Appendix D for further details).

Since the distance between adjacent orbitals increases with increasing N (for fixed a), a decrease in $\mathcal{J}$ with increasing N is expected. This is observed for the series Li_3, Li_5, Li_7, Li_9 (see Table 3). However, the series Li_4, Li_6, Li_8, Li_{10} indicates that a small $N = 4i$ / $N = 4i + 2$ oscillation also plays a minor role. This $N = 4i$ / $N = 4i + 2$ oscillation is more pronounced in the $\mathcal{J}$ values for the series Ag_6, Ag_8, Ag_{10}, and is also apparent in the cohesive energies of this series.[12]

We have not determined the origin of this subtle $N = 4i$ / $N = 4i+2$ oscillation. However, the many-electron symmetry of the $\mu = 0$ state also exhibits a $N = 4i$ / $N = 4i + 2$ oscillation.[11]

B. The Heisenberg Model

The nearest-neighbor Heisenberg Hamiltonian[1,16]

$$\mathcal{H}^{HM} = \mathcal{J} \sum_i \tfrac{1}{2} + 2\vec{s}_i \cdot \vec{s}_{i+1} \tag{4}$$

is based exclusively on nearest-neighbor exchange interactions where (i) $\vec{s}_i$ is the one-electron spin operator for lattice point i, (ii) $\frac{1}{2} + 2\vec{s}_i \cdot \vec{s}_j$ is equivalent to the two-electron exchange operator τ_{ij},[20] and (iii) $\mathcal{J}$ is the effective nearest-neighbor exchange energy.

The exact solutions of $\mathcal{H}^{HM}$ $(\chi^{HM}_{N,A})$ depend only on the sign of $\mathcal{J}$. $\mathcal{J} < 0$ leads to a $\mu = 0$ ground state (antiferromagnetism) and $\mathcal{J} > 0$ leads to a $\mu = 1$ ground state (ferromagnetism).

For the M_N ring, the Heisenberg Hamiltonian leads to the energy expression

$$\begin{aligned} E^{HM}_{N,A} &= E_{N,A=N} + N\mathcal{J}\left(\bar{U}_{N,A} + 1\right) \\ \bar{U}_{N,A} &= N^{-1} \sum_i U_{i\,i+1} \\ U_{i\,j} &= -\langle \chi | \tau_{ij} | \chi \rangle \end{aligned} \tag{5}$$

where $U_{i\,j}$ is the coefficient for exchanging spins i and j, and $\bar{U}_{N,A}$ is the average nearest-neighbor exchange coefficient (see Appendices A-B). The relationship of (5) and the GVB energy expression is derived in Appendix A.

For infinite N, Bethe[4] obtained the exact $\mu = 0$ eigenvector, and Hulthén[5] ob-

tained the exact $\mu = 0$ eigenvalue

$$\lim_{N\to\infty} \bar{U}_{N,\mu=0} = 2\ln 2 - 1 = 0.38629.$$

Cloizeaux and Pearson[21] showed that (4) leads to a zero singlet-triplet gap in the limit as N approaches infinity, e.g.,

$$\lim_{N\to\infty} E^{HM}_{N,A} - E^{HM}_{N,A+\delta A}\Big|_{\mu=0} = 0$$

$$\lim_{N\to\infty} \frac{d\bar{U}_{N,\mu}}{d\mu}\Big|_{\mu=0} = 0.$$

For $N = 4$, 6, 8, 10,[22] 16, and 48,[21] exact solutions have been obtained for various magnetizations. We solved (4) for the exact eigenvectors and eigenvalues for the five lowest-energy states of each allowed magnetization for $N \leq 12$. Results for the lowest-energy state of each magnetization are given in Table 4 for even values of $N \leq 12$.

As an example, for an M_2 antiferromagnetic chain, the exact solutions are

$$\mu = 0: \chi^{HM}_{2,1} = (\alpha\beta - \beta\alpha)/\sqrt{2}$$

$$\bar{U}^{HM}_{2,1} = 1 \quad \text{(bonding)}$$

$$\mu = 1: \chi^{HM}_{2,2} = \alpha\alpha$$

$$\bar{U}^{HM}_{2,2} = -1 \quad \text{(antibonding)}.$$

Each of these exact solutions leads to a fully symmetrical spin density and each is nondegenerate.[23] In contrast, for $\mu = 0$, the UHF spin functions $\alpha\beta$ and $\beta\alpha$ are degenerate (each leads to $U = 0$; nonbonding), and each leads to a spin density wave. These UHF spin functions are not eigenvectors of (4).

In agreement with GVB, for even N, the lowest-energy state of each magnetization is nondegenerate and leads to a fully symmetrical spin density — in each

case, $U_{i\,i+1} = \bar{U}_{N,A}$ for all i. However, for each magnetization $\mu < 1$, higher-energy eigenvectors of (4) exist that are doubly degenerate and do lead to a spin density wave.[23]

For each of the Cu_{10}, Ag_6, Ag_8, Ag_{10}, Au_{10}, Li_6, Li_{10}, and Na_{10} ring clusters, we fit the Heisenberg model (5) to the GVB total energies ($E^{GVB}_{N,A}$) using the exact $\bar{U}_{N,A}$ (see Table 4). For each case, $E_{N,A=N}$ and $\mathcal{J}$ are obtained by matching the GVB total energies for magnetizations $\mu = 1$ and $\mu = 0$. The agreement of HM with GVB for $0 < \mu < 1$ is evaluated by calculating the root mean square (RMS) error

$$(\Delta E^{RMS})^2 = \frac{2}{N-2} \sum_{A=1+N/2}^{N-1} (E^{GVB}_{N,A} - E^{HM}_{N,A})^2 \quad \text{for even } N.$$

The results presented in Table 3 indicate that for M_{10}, E^{HM} is accurate to $0.028\mathcal{D}$ or better. For M_{10}, the trend of the RMS errors (Au > Cu > Ag > Na > Li) is almost the same as the trend followed by the $\mathcal{D}$ values and the S_{12} values (Cu and Au are switched).

The results for the series Ag_6, Ag_8, Ag_{10} (see Table 3 and Figure 4), for the series Li_4, Li_6, Li_8, Li_{10}, and for the series Li_5, Li_7, Li_9 (see Table 3) show that (*i*) the agreement of HM with GVB is just as good for odd N as it is for even N, and (*ii*) the agreement of HM with GVB improves with increasing N.

An explanation of the increased accuracy of HM with increasing N is that the distance between next-nearest-neighbor orbitals

$$R_{13} = 2R_{12}\cos(\pi/N)$$

(where R_{ij} is the distance between orbitals ϕ_i and ϕ_j) increases as N increases, due to the curvature of the M_N ring. Hence, for the M_N rings, the HM error due to the neglect of next-nearest-neighbor interactions decreases with increasing N.

The reason for the success of the Heisenberg model in fitting the GVB total energies is that (*i*) the GVB wavefunctions for the various magnetizations of M_N can all be described fairly well in terms of a single set of N equivalent well-localized nonorthogonal orbitals $\{\phi_j\}$ (see Appendix A and Appendix C), and (*ii*) $\mathcal{J}$ decreases exponentially with increasing distance (see Appendix D); hence, non-nearest-neighbor exchange interactions are negligible (for large N).

C. Comparison of GVB with Hartree-Fock

The GVB wavefunction is the *optimum* wavefunction allowing an independent particle description of the electronic structure.[18,24] Here we compare the GVB results with results obtained with less sophisticated wavefunctions (UHF and HF).

The GVB magnon spectra are compared with UHF and HF magnon spectra in Figures 5-10 for Cu_{10}, Au_{10}, Ag_8, Ag_{10}, Na_{10}, and Li_{10}. For $\mu = 1$, the total energy is the same for GVB, UHF, and HF. For $\mu < 1$, the total energies obey the relation $E^{GVB} < E^{UHF} < E^{HF}$. In Figures 5-10, the GVB magnon spectra are interpolated by the Heisenberg model, and the UHF magnon spectra are interpolated by the generalized Ising model.[13] Full details of the HF and UHF results are given elsewhere.[13]

1. UHF

In each case, the UHF ground state is $\mu = 0$, in agreement with GVB. However, UHF leads to spin density waves for all magnetizations $\mu < 1$, whereas GVB leads to fully symmetrical charge and spin densities for all magnetizations $0 \leq \mu \leq 1$. In addition, the UHF magnon dispersion curves are significantly different than those for GVB. For GVB, the magnon dispersion curve has zero slope at $\mu = 0$; hence,

the single-triplet splitting is expected to approach zero in the limit as N approaches infinity.[21] For UHF, the magnon dispersion curve has nonzero slope at $\mu = 0$, leading to a single-triplet splitting of approximately $2|\mathcal{J}|$ for all N.[13]

Both GVB and UHF lead to valence orbitals centered at bond midpoints, exhibiting only minor variations as a function of μ. For GVB, both the orbitals *and the many-electron spin function* are optimized simultaneously.[18,12] For UHF, the orbitals are optimized for a many-electron spin function that is a simple product of one-electron spin functions ($\chi^{UHF} = \alpha^A\beta^B$). Therefore, for these systems, differences between the GVB and UHF results are due to an incomplete treatment of the electron correlation forced by the use of a restricted (product) spin function.[12]

Figure 11 shows the energetic effects of allowing *spin optimization*

$$E^{SOPT} = E^{GVB} - E^{UHF}$$

as a function of magnetization for each of the Cu_{10}, Ag_{10}, Au_{10}, Li_{10}, and Na_{10} ring clusters (see Table 5 for $N \neq 10$). These spin optimization effects follow the same trend as the magnon dispersion energy (Cu > Au > Ag $\gg$ Na > Li).

2. HF

For Ag_8, Na_{10}, and Li_{10}, the HF ground state contains 0.25, 0.6, and 1.0 unpaired electrons per atom, respectively — in serious disagreement with both GVB and UHF.

The *total* error in the HF energy due to the neglect of electron correlation effects can be divided into static and dynamic (instantaneous) contributions. Splitting each HF doubly-occupied orbital into a pair of overlapping singly-occupied orbitals allows the two electrons on the average to stay further apart. GVB includes a separate orbital for each valence electron, leading to the optimum *static* (independent particle)

description of the electronic structure.[18,24] Hence,

$$E^{CORR} = E^{GVB} - E^{HF}$$

is a reasonable definition of the static electron correlation energy. For each of the eight M_N ring clusters, the static electron correlation energy increases monotonically with decreasing magnetization, as shown in Figure 12 for Cu_{10}, Ag_{10}, Au_{10}, Li_{10}, and Na_{10} (see Table 5 for $N \neq 10$).

The near linear dependence of the static correlation energy — especially for $0.2 \leq \mu \leq 1$ — suggests a simple explanation for the error in HF (in comparison to GVB). For HF, ionic character is forced into the wavefunction by the restriction of doubly-occupied valence orbitals — and the amount of ionic character increases linearly with decreasing magnetization.[13] GVB includes one orbital for each valence electron, allowing an *optimization* of the amount of ionic character.

The static correlation energies are remarkably similar for Cu_{10}, Ag_{10}, Au_{10}, and Na_{10}. For $\mu = 0$, the static correlation energy follows the trend Li $\gg$ Na $>$ Ag $>$ Cu $>$ Au. This trend is almost the inverse of the Li $<$ Na $<$ Ag $<$ Au $<$ Cu trend followed by both the overlap and magnon dispersion energy for GVB (see Section III.A). This inverse relation between the correlation energy and the magnon dispersion energy explains why HF leads incorrect ground state magnetizations for Li_{10} and Na_{10} but not for Ag_{10}, Au_{10}, and Cu_{10}.

IV. Summary

We optimized GVB, UHF and HF wavefunctions for all allowed magnetizations of each of the Cu_{10}, Ag_8, Ag_8, Ag_{10}, Au_{10}, Li_8, Li_{10}, and Na_{10} ring clusters. The results for these one-dimensional metals are summarized as follows.

For each case, GVB leads to leads to an antiferromagnetic ($\mu = 0$) ground state, and fully symmetrical charge and spin densities for all magnetizations $0 \leq \mu \leq 1$. The GVB magnon spectrum can be fit fairly accurately with the nearest-neighbor Heisenberg Hamiltonian. This suggests that the singlet-triplet energy splitting approaches zero in the limit a N approaches infinity for each of these systems.[21]

In agreement with GVB, UHF leads to an antiferromagnetic ($\mu = 0$) ground state for each case. The UHF magnon spectrum can be fit fairly accurately with a nearest-neighbor generalized Ising model.[13] However, the UHF magnon dispersion curve does not have the correct form, and UHF leads to spin density waves for all magnetizations $\mu < 1$. This disagreement of UHF with GVB is due to an incomplete treatment of the electron correlation (for UHF).

Restricted Hartree-Fock leads to spurious results, such as (i) incorrect ground state magnetizations for Ag_8 ($\mu = 0.25$), Na_{10} ($\mu = 0.6$), and Li_{10} ($\mu = 1.0$), and (ii) charge and spin density waves for all intermediate magnetizations ($0 < \mu < 1$) of each M_N ring cluster. These spurious results indicate a fundamental flaw in HF for these systems — the double occupation of valence orbitals for describing magnetizations $\mu < 1$.

Appendix A. The Heisenberg Energy Expression

Here we show the relationship between the Heisenberg energy expression and the full GVB energy expression.

The Heisenberg energy expression is expected to be useful for any system where a range of magnetizations can be described by a single set of singly-occupied orbitals $\{\phi_i\}$. For the M_N ring clusters, the GVB orbitals $\{\phi_i\}$ optimized for $\mu = 0$ (Figure

2a) are very similar to those optimized for $\mu = 1$ (Figure 2b); hence, the Heisenberg energy expression provides an accurate fit of the GVB magnon spectrum for each of the Cu_{10}, Ag_6, Ag_8, Ag_{10}, Au_{10}, Li_6, Li_{10}, and Na_{10} ring clusters.

1. The GVB Energy Expression

For determinantal wavefunctions (1, 2) the total energy expression

$$E_{N,A} = \frac{\langle \Psi_{N,A} | \widehat{\mathcal{H}} | \Psi_{N,A} \rangle}{\langle \Psi_{N,A} | \Psi_{N,A} \rangle}$$

can be simplified as

$$\begin{aligned} E_{N,A} &= \langle \Phi_{N,A}\, \chi_{N,A} | \widehat{\mathcal{H}} | \Psi_{N,A} \rangle = \sum_{\tau} \langle \Phi_{N,A} | \widehat{\mathcal{H}} | \tau \Phi_{N,A} \rangle U_{\tau} \qquad \text{(A1)} \\ U_{\tau} &= \zeta_{\tau} \langle \chi_{N,A} | \tau \chi_{N,A} \rangle \end{aligned}$$

where the summation is over all $N!$ permutations

$$\tau f(1,2,3,\ldots,N) = f(i_1,i_2,i_3,\ldots,i_N),\ 1 \le i_j \le N$$

of the electronic coordinates $(1,2,3,\ldots,N)$, ζ_{τ} is the parity of permutation τ, and the normalization of $\Psi_{N,A}$ is defined with respect to

$$\langle \Phi_{N,A}\, \chi_{N,A} | \Psi_{N,A} \rangle = \sum_{\tau} \langle \Phi_{N,A} | \tau \Phi_{N,A} \rangle U_{\tau} = 1.$$

2. Two Electrons

For a system having two valence electrons ($N = 2$) such as the Cu_3^+, Ag_3^+, Au_3^+, Li_3^+, and Na_3^+ linear chain clusters, the generalized valence bond (GVB) wavefunctions for the two allowed magnetizations

$$\begin{aligned} \Psi^{GVB}_{2,\mu=1} &= \widehat{\mathcal{A}}[(\phi_1\phi_2)(\alpha\alpha)] &&= \frac{(\phi_1\phi_2 - \phi_2\phi_1)(\alpha\alpha)}{\sqrt{1 - \mathcal{S}_{12}^2}} \\ \Psi^{GVB}_{2,\mu=0} &= \widehat{\mathcal{A}}[(\phi_1\phi_2)(\alpha\beta - \beta\alpha)] &&= \frac{(\phi_1\phi_2 + \phi_2\phi_1)(\alpha\beta - \beta\alpha)}{\sqrt{2 + 2\mathcal{S}_{12}^2}} \end{aligned}$$

can each be described fairly accurately with the *same* product of two overlapping valence orbitals

$$\Phi = \phi_1\phi_2$$

$$S_{ij} = \langle\phi_i|\phi_j\rangle.$$

For each of the Cu_3^+, Ag_3^+, Au_3^+, Li_3^+, and Na_3^+ linear chain clusters, ϕ_1 and ϕ_2 are localized at the left and right bond midpoints, respectively (see Figure 1b), and the optimum shapes of ϕ_1 and ϕ_2 do not depend crucially on the spin function, χ (as shown quantitatively in Appendix C, Table 6).

These wavefunctions lead to the energy expression[25,13]

$$\begin{aligned} E_2 &= E^{CORE} + E^{CL} + \frac{U_{12}\mathcal{J}_{12}}{1 + U_{12}S_{12}^2} \qquad \text{(A2)} \\ E^{CL} &= \langle\phi_i\phi_j|\widehat{\mathcal{H}}|\phi_i\phi_j\rangle - E^{CORE} = h_{11} + h_{22} + J_{12} \\ \mathcal{J}_{ij} &= \langle\phi_i\phi_j|\widehat{\mathcal{H}}|\phi_j\phi_i\rangle - S_{ij}^2E^{CORE} - S_{ij}^2E^{CL} \\ &= 2S_{ij}h_{ij} + K_{ij} - S_{ij}^2E^{CL} \end{aligned}$$

where (i) E^{CORE} is the total energy excluding the two valence electrons, (ii) E^{CL} is the electronic energy of the classical (Hartree product) valence wavefunction[25] — E^{CL} includes valence-core interactions,[13] (iii) U_{ij} is the coefficient for the exchange of orbitals i and j and is the only magnetization-dependent term ($U_{12} = -1$ for $\mu = 1$ and $U_{12} = +1$ for $\mu = 0$), (iv) $\mathcal{J}_{ij}$ is the *valence bond exchange energy*,[25] and (v) h_{ij} is the one-electron integral, and J_{ij} and K_{ij} are the two-electron coulomb and exchange integrals, respectively.[11]

For nearly all cases where $S_{12} \neq 0$ (as in bonding), $\mathcal{J}_{12} < 0$, leading to a $\mu = 0$ ground state (antiferromagnetism). If $S_{12} = 0$, then $\mathcal{J}_{12} = K_{12} > 0$, leading to a $\mu = 1$ ground state (ferromagnetism). [These conditions are consistent with Hund's

rule, stating that the lowest energy state for a configuration containing orthogonal (non-overlapping) singly-occupied orbitals is the state of highest spin multiplicity (e.g., for the $1s^2 2s^2 2p^2$ carbon atom, the lowest energy state is triplet). Note that for $\mathcal{S}_{ij} \neq 0$ the valence bond exchange energy $\mathcal{J}_{ij}$ is not equal to the two-electron exchange integral K_{ij}].

3. M_N Ring Clusters

The $\Psi_{N,A}^{GVB}$ for the various magnetizations (μ) of the M_N ring clusters can all be described fairly accurately with the same spatial configuration

$$\Phi = \phi_1 \phi_2 \phi_3 \cdots \phi_N .$$

Hence, the many-electron spin function $\chi_{N,A}^{GVB}$ plays the major role in describing the various magnetizations.

Applying the general energy expression (A1) to the GVB wavefunction (1, 2) with the assumptions that (i) the nearest-neighbor exchange energies are all equal

$$\mathcal{J}_{i,i\pm1} = \mathcal{J}_{12} \quad \text{for all } i,$$

(ii) non-nearest-neighbor exchange integrals are zero, e.g.,

$$\mathcal{J}_{i,i\pm1} \gg \mathcal{J}_{i,i\pm j} \approx 0 \quad \text{for } |j| \geq 2,$$

and (iii) $\mathcal{S}_{ij}^2$ terms and higher-order terms can be neglected, leads to the approximate energy expression

$$\begin{aligned} E_{N,A} &= E_N^{CORE} + E_N^{CL} + N\mathcal{J}_{12}\bar{U}_{N,A} \\ \bar{U}_{N,A} &= N^{-1}\sum_i U_{i\,i+1} \\ U_{i\,j} &= -\langle\chi|\tau_{ij}|\chi\rangle \end{aligned}$$

which is equivalent to the HM energy expression (5).

Appendix B. Approximate Solutions of the Heisenberg Hamiltonian

For M_N ring clusters, this appendix compares values of the average nearest-neighbor exchange coefficient ($\bar{U}_{N,\mu}$) obtained with various many-electron spin functions. The exact solutions to the Heisenberg Hamiltonian maximize ($\bar{U}_{N,\mu}$) for each pair of values (N, μ). Hence, approximate solutions lead to values of $\bar{U}_{N,\mu}$ smaller than the exact Heisenberg values.

Values of $\bar{U}_{N,\mu}$ for various spin functions are presented in Table 4 (for even values of $N \leq 12$).

1. Exact HM Solutions

We solved for the exact HM eigenvectors and eigenvalues using a general configuration interaction program[26] where (*i*) we included only the configuration having all N orbitals singly-occupied — but including the full set of spin eigenfunctions, (*ii*) the overlap integrals (S_{ij}) were taken as the unit matrix, (*iii*) all one-electron and two-electron integrals were set equal to zero, except that (*iv*) all nearest-neighbor exchange integrals ($K_{i\,i+1}$) were set equal to -1.

2. Normal UHF (Ising)

Elsewhere[13] we showed for the M_N ring that UHF leads to $|A-B| = \mu N$ antibonding exchanges ($\alpha\alpha$; $U = -1$) and $N(1-\mu)$ nonbonding exchanges ($\alpha\beta$; $U = 0$). Hence, UHF leads to

$$\bar{U}_{N,\mu} = -\mu$$

regardless of whether N is even or odd. This UHF solution is identical to the Ising solution.[13]

3. Spin Projected UHF

The two definitions of magnetization

$$\mu = \frac{|A-B|}{N} = \frac{|M_S|}{N}$$

$$\mu = \frac{2S}{N}$$

are equivalent as long as (i) the spin function is an eigenfunction of the $\hat{S}^2$ operator, and (ii) the $M_S = S$ spin function component is chosen.

The rigorous definition of the magnetization (density of unpaired spins) is the one based on S. However, for $\mu < 1$, the UHF spin function is not an eigenfunction of $\hat{S}^2$; hence, for UHF, μ is defined in terms of M_S.

For even N, spin-projecting the $M_S = 0$ UHF spin function[27] leads to

$$\bar{U}_{N,\mu} = -\mu^2 + 2\,\frac{(1-\mu)}{N}$$

(where μ is defined in terms of S). For odd N, spin-projecting the $M_S = \frac{1}{2}$ UHF spin function[27] leads to

$$\bar{U}_{N,\mu} = -\mu^2 + \frac{(1-\mu)^2}{N+1}\,.$$

4. Simple Valence Bond

Values of $U_{N,\mu}$ for simple valence bond (perfect pairing) are also given in Table 4. For $\mu = 0$, the VB spin function

$$\chi^{VB} = (\alpha\beta - \beta\alpha)^n/(2)^{n/2}$$

($n = N/2$) leads to alternating exchanges of $U = 1$ (intrapair) and $U = -\frac{1}{2}$ (interpair), leading to $\bar{U}_{N,\mu=0} = -0.25$.

5. Resonating Valence Bond

For $\mu = 0$, an equivalent VB spin function is

$$\begin{aligned}\bar{\chi}^{VB} &= \tau_{12}\tau_{23}\cdots\tau_{N-1\,N}\,\chi^{VB} \\ &= [\beta(\alpha\beta-\beta\alpha)^{n-1}\alpha - \alpha(\alpha\beta-\beta\alpha)^{n-1}\beta]/2^{n/2}.\end{aligned}$$

Hence, the resonating VB spin function is

$$\chi^{RVB} = \chi^{VB} \pm \bar{\chi}^{VB}.$$

RVB leads to

$$\begin{aligned}\bar{U} = U_{12} &= \frac{\langle\chi^{RVB}|-\tau_{12}|\chi^{RVB}\rangle}{\langle\chi^{RVB}|\chi^{RVB}\rangle} \\ &= \frac{1-0.5\pm 2\langle\bar{\chi}^{VB}|-\tau_{12}|\chi^{VB}\rangle}{2\pm 2\langle\bar{\chi}^{VB}|\chi^{VB}\rangle} \\ &= \frac{0.5\pm(-1)^{n-1}(2)^{2-n}}{2\pm(-1)^{n-1}(2)^{2-n}}.\end{aligned}$$

Hence, RVB leads to a resonant state

$$\chi^{RVB} = \chi^{VB} - (-1)^n\,\bar{\chi}^{VB} \qquad \bar{U} = \frac{2^{n-3}+1}{2^{n-1}+1}$$

and an antiresonant state

$$\chi^{AVB} = \chi^{VB} + (-1)^n\,\bar{\chi}^{VB} \qquad \bar{U} = \frac{2^{n-3}-1}{2^{n-1}-1}.$$

However, both states lead to $\bar{U} = 0.25$ in the limit as N approaches infinity.

Appendix C. GVB Results for Linear M_3^+ Clusters

Here we present results for the Cu_3^+, Ag_3^+, Au_3^+, Li_3^+, and Na_3^+ linear chain clusters, since they are rather simple models of the respective infinite linear chains — in each case the localized orbitals for linear M_3^+ (Figure 1b) and for M_{10} (Figures 2a-b) are remarkably similar. Since these systems each contain two valence electrons, SOGVB and GVB–CI(SCF) are identical; hence, (*i*) we obtain the localized orbitals directly from GVB (avoiding the Hartree-localization method), and (*ii*) we compare the GVB results to the "exact" energy expression (A2).

For each of these M_3^+ linear chain clusters, Table 6 presents the GVB orbital overlap ($\mathcal{S}_{12} = \langle\varphi_1|\varphi_2\rangle$) and the magnon dispersion energy

$$\mathcal{D} = E_{2,\mu=1}^{GVB} - E_{2,\mu=0}^{GVB}$$

(i.e., the "singlet-triplet gap").

In order to evaluate the usefulness of Equation (A2) for linear M_3^+, we compare the fully self-consistent GVB values of $\mathcal{D}$ (where valence orbitals are optimized separately for each state) with the "frozen orbital" GVB magnon dispersion energies

$$\mathcal{D}^{FROZEN} = \frac{-2\mathcal{J}_{12}}{1-\mathcal{S}_{12}^4}$$

(where the GVB orbitals optimized for $\mu = 0$ are used to describe $\mu = 1$). The self-consistent $\mathcal{D}$ values are smaller than the frozen orbital $\mathcal{D}$ values by only 7 - 17%; hence, both magnetizations can be described fairly well using a single set of localized orbitals.

The values $\mathcal{J}_{12}$ and $\mathcal{S}_{12}$ for M_3^+ (Table 6) are somewhat smaller than the respective values $\mathcal{J}$ and $\mathcal{S}_{12}$ for M_{10} (see Tables 2-3). This is because (*i*) $\mathcal{J}$ and $\mathcal{S}_{12}$ both decrease as the distance between adjacent orbitals increases, and (*ii*) the effective

distance between adjacent orbitals is larger for M_3^+ than for the M_N ring (for constant a). For M_3^+, the orbitals are not centered at the exact bond midpoints but are polarized somewhat away from one another (see Figure 1b); hence, for M_3^+ the effective distance between adjacent orbitals is somewhat larger than a. However, for the M_N ring, the effective distance between adjacent orbitals is somewhat smaller than a since the orbitals are centered at the bond midpoints and the distance between adjacent bond midpoints (3) is somewhat smaller than a for finite N. Hence, for the M_N ring, both $\mathcal{J}$ and $\mathcal{S}_{12}$ decrease somewhat with increasing N (for constant a; see Table 2-3 and Appendix D).

Appendix D. The Dependence of $\mathcal{J}$ on a and N

Figure 13 shows the dependence of the effective exchange energy on a for Li_5, Li_6, Li_7, and Li_8. Here, $\mathcal{J}$ is obtained from GVB total energies in the same manner as in Section III.B. Figure 13 shows an exponential decrease in $\mathcal{J}$ with increasing a (for constant N).

In addition, $\mathcal{J}$ decreases with increasing N (for constant a). This is because the orbitals are centered at the bond midpoints (see Figure 2), and the distance between adjacent bond midpoints

$$R^{BM} = a\cos(\pi/N)$$

increases with increasing N (for constant a), approaching a in the limit as N approaches infinity.

The effective distance between adjacent orbitals

$$R^{EFF} = \lambda a + (1-\lambda)R^{BM}$$

is midway between a and R^{BM} because the orbitals are slightly polarized outwards from the center of the ring.

Hence, we fit the data of Figure 13 (24 data points) to the exponential

$$\mathcal{J}(R^{EFF}) = C \exp\left[-\gamma R^{EFF}\right] \tag{D1}$$

using λ, C, and γ as least-square parameters [the resultant values are $\lambda = 0.5480$, $C = -0.8736$ eV, and $\gamma = -0.6010$ Å^{-1}, leading to a root mean square error of 0.00143 eV]. The results are given in Figure 14, showing that the 24 data points all fit on one curve!

Since R^{EFF} approaches a in the limit as N approaches infinity, (D1) gives $\mathcal{J}$ as a function of a for the infinite lithium chain.

Appendix E. Results for Hydrogen Ring Clusters

Often, ideas concerning the electronic structures of one-dimensional metals have been tested with calculations on symmetric ring clusters composed of hydrogen atoms.[28,29]

In this appendix we present GVB results for H_6, H_8, and H_{10} using Huzinaga's[30] (5s) primitive set of gaussian-type orbitals (unscaled) contracted triple-ζ.[11] For each of these H_N rings, we chose a lattice constant ($a = 1.483$ Å) equal to twice the H_2 equilibrium bond length.[31] For H_{10}, we also chose $a = 1.112$ Å, $a = 1.186$ Å, and $a = 1.260$ Å, equal to factors of 1.5, 1.6, and 1.7 times the H_2 equilibrium bond length.[31]

The GVB wavefunctions for H_N and M_N (M = Cu, Ag, Au, Li, and Na) are similar, except that the $\{\phi_j\}$ are centered at the atoms for H_N as opposed to the bond midpoints for M_N (see Figure 2).

Table 7 summarizes the GVB results. For H_{10}, the magnon dispersion (for $1.112 \leq a \leq 1.483$ Å) is a factor of 4.6 to 6.4 greater than that for Cu_{10} (at $a = 2.556$ Å). Also, for H_{10}, the nearest-neighbor overlap (for $1.112 \leq a \leq 1.483$ Å) is a factor of 1.14 to 1.26 times that for Cu_{10} (at $a = 2.556$ Å).

The large magnon dispersion for H_N results from the large antibonding exchange interactions for magnetizations $\mu > 0.5$ (see Table 4). For H_{10}, the $\mu = 1$ state is so strongly antibonding that for $a \leq 1.195$ Å, the $\mu = 1$ state is unstable with respect to ionization (forming $\mu = 1$ $H_{10}^{+} + e^{-}$).[13] In order to compare GVB results for $a > 1.195$ Å with those for $1.112 \leq a \leq 1.195$ Å, we optimize the $\mu = 1$ GVB wavefunction with D_{10h} orbital symmetry restrictions.[13]

Table 8 summarizes the results of fitting the Heisenberg model (HM) to the GVB total energies (following the same procedure as for the M_N rings; see Section III.B). The results for the H_{10} rings (for $1.112 \leq a \leq 1.483$ Å) are of similar quality to those for the M_{10} rings (for M = Cu, Ag, Au, Li, and Na; see Table 3).

Results for the series H_6, H_8, H_{10} compare favorably with results for the series Ag_6, Ag_8, Ag_{10} except that $|\mathcal{J}|$ increases with increasing N for hydrogen, whereas $|\mathcal{J}|$ decreases with increasing N for silver (see Tables 3 and 8).

For small enough a, the Heisenberg model is not expected to provide an accurate fit to the lowest energy GVB states, due to the large antibonding exchange interactions for $\mu > 0.5$. For small enough a, $\mu > 0.5$ states involving $1s$-like orbitals become unstable with respect to ionization.[13] Hence, Mattheiss' result[28] that HM is inaccurate for H_6 at $a = 0.529$ Å — leading to an RMS error of $0.21\mathcal{D}$ — is not the least bit surprising.

References

[1] W. Heisenberg, *Z. Phys.* **49**, 619 (1928).

[2] F. Bloch, *Z. Phys.* **61**, 206 (1930).

[3] J. C. Slater, *Phys. Rev.* **35**, 509 (1931).

[4] H. Bethe, Z. Physik **71**, 205 (1931).

[5] L. Hulthén, *Ark. Mat. Astr. Fys.* **26A**, 1 (1938).

[6] R. Peierls, *Quantum Theory of Solids* (Clarendon Press, Oxford, 1955).

[7] J. Hubbard, *Proc. Roy. Soc. London* **A 276**, 238 (1963); *ibid* **A 277**, 237 (1964); *ibid* **A 281**, 401 (1964).

[8] E. H. Lieb and F. Y. Wu, *Phys. Rev. Lett.* **20**, 1445 (1968). (Cornell University Press, Ithaca, New York, 1960).

[9] The calculations for Li and Na are "ab initio" in the traditional definition in that the total energy expressions $\langle\Psi|\mathcal{H}|\Psi\rangle/\langle\Psi|\Psi\rangle$ include *all terms resulting from the true Hamiltonian* ($\widehat{\mathcal{H}}$) [within the usual Born-Oppenheimer approximation (frozen nuclei)] and no additional terms. The only approximations utilized in ab initio calculations are in the many-electron wavefunction (Ψ). "Exact" calculations would require Ψ to include essentially an infinite number of configurations within an infinite basis set and are generally unattainable; the configuration and basis set expansions are truncated in actual applications. For the M_N ring clusters (with monovalent M), GVB–CI(SCF) includes all configurations within N orbitals (see Appendix A). Both HF and UHF include only a

single configuration. Local density functional calculations (such as $X\alpha$) are not ab initio in this traditional definition since the exchange integrals are replaced by a local "exchange-correlation" potential obtained from calculations on the free electron gas. The calculations for Cu, Ag and Au are ab initio for eleven electrons per atom ($d^{10}s^1$), where "ab initio" effective potentials model all effects of the remaining core electrons. See References [10,11,12,13] for further details.

[10] P. J. Hay and W. R. Wadt, *J. Chem. Phys.* **82**, 270 (1985).

[11] M. H. McAdon and W. A. Goddard III, *J. Chem. Phys.*, accepted for publication. See Chapter 1 of this thesis.

[12] M. H. McAdon and W. A. Goddard III, *J. Phys. Chem.*, accepted for publication. See Chapter 2 of this thesis.

[13] See Chapter 3 of this thesis.

[14] The GVB singlet ground state for each of the Cu_{10}, Ag_6, Ag_8, Ag_{10}, Au_{10}, Li_6, Li_{10}, and Na_{10} ring clusters is antiferromagnetic in the same sense that the singlet ground state of the H_2 molecule is antiferromagnetic. None of these systems has a spin density wave.

[15] W. Förner and M. Seel, *J. Chem. Phys.* **87**, 443 (1987).

[16] G. Wannier, Phys. Rev. **52**, 191 (1937).

[17] J. Donohue, *The Structure of the Elements* (Wiley, New York, 1974).

[18] W. A. Goddard III, *Int. J. Quantum Chem.* **IIIS**, 593 (1970); R. C. Ladner and W. A. Goddard III, *J. Chem. Phys.* **51**, 1073 (1969).

[19] For brevity, the electron coordinates are often omitted. By standard convention, orbital products are ordered such that the electron coordinates are sequential.

[20] P. A. M. Dirac, *Proc. Roy. Soc. A* **123**, 714 (1929).

[21] J. des Cloizeaux and J. J. Pearson, Phys. Rev. **128**, 2131 (1962).

[22] R. Orbach, Phys. Rev. **115**, 1181 (1958).

[23] For spin eigenfunctions, we ignore the usual $2S+1$ spin multiplicity in defining a nondegenerate state. Hence, by an n-fold degeneracy we refer to n orthogonal states having the same energy and the same S and M_S quantum numbers.

[24] W. A. Goddard III, T. H. Dunning, Jr, W. J. Hunt, and P. J. Hay, *Accts. Chem. Res.* **6**, 368 (1973); W. A. Goddard III and L. B. Harding, *Ann. Rev. Phys. Chem.* **29**, 363 (1978).

[25] C. W. Wilson, Jr. and W. A. Goddard III, *Chem. Phys. Lett.*, **5**, 45 (1970); C. W. Wilson, Jr. and W. A. Goddard III, *Theor. Chim. Acta*, **26**, 195 (1972); W. A. Goddard III and C. W. Wilson, Jr., *Theor. Chim. Acta*, **26**, 211 (1972).

[26] CI3 program, unpublished; see F. W. Bobrowicz, Ph. D. Thesis, California Institute of Technology, 1974.

[27] W. A. Goddard III, *J. Chem. Phys.* **48**, 450 (1968) and *ibid*, **48**, 5337 (1968); A. F. Voter, M. M. Goodgame, and W. A. Goddard III, *Chem. Phys.* **98**, 7 (1985).

[28] L. F. Mattheiss, *Phys. Rev.* **123**, 1209 (1961).

[29] R. D. Poshusta and D. J. Klein, *Phys. Rev. Lett.* **48**, 1555 (1982); M. Seel, P. S. Bagus and J. Ladik, *J. Chem. Phys.* **77**, 3123 (1982); A. Karpfen, *Chem. Phys. Lett.* **61**, 363 (1979); M. Kertesz, J. Koller, and A. Azman, *Phys. Rev.* **B 14**, 76 (1976); S. P. Ionov, I. I. Amelin, V. S. Lyubimov, G. V. Ionova, and E. F. Makarov, *Physica Status Solidi* **B 77**, 441 (1976).

[30] S. Huzinaga, *J. Chem. Phys.* **42**, 1293 (1965).

[31] K. P. Huber and G. Herzberg, *Molecular Spectra and Molecular Structure: IV. Constants of Diatomic Molecules* (Van Nostrand Reinhold, New York, 1979).

Table 1. GVB, UHF, and HF magnon spectra. [a)]

A	B	μ	$E_\mu - E_{\mu=1}$ (eV) GVB	UHF	HF
Cu_{10}	$a = 2.556$ Å			$E_{\mu=1} = -504.28277$ Hartree	
5	5	0.000	−7.652	−6.448	−4.959
6	4	0.200	−7.098	−5.646	−4.550
7	3	0.400	−6.123	−4.709	−4.141
8	2	0.600	−4.329	−3.334	−3.025
9	1	0.800	−2.286	−1.739	−1.610
10	0	1.000	0.000	0.000	0.000
Ag_6	$a = 2.889$ Å			$E_{\mu=1} = -224.40832$ Hartree	
3	3	0.000	−3.746	−2.981	−2.342
4	2	0.333	−2.936	−2.282	−1.736
5	1	0.667	−1.949	−1.368	−1.253
6	0	1.000	0.000	0.000	0.000
Ag_8	$a = 2.889$ Å			$E_{\mu=1} = -299.22320$ Hartree	
4	4	0.000	−4.494	−3.789	−1.988
5	3	0.250	−4.274	−3.151	−2.297
6	2	0.500	−3.124	−2.308	−1.820
7	1	0.750	−1.740	−1.233	−1.049
8	0	1.000	0.000	0.000	0.000
Ag_{10}	$a = 2.889$ Å			$E_{\mu=1} = -374.03507$ Hartree	
5	5	0.000	−5.652	−4.661	−2.775
6	4	0.200	−5.268	−4.024	−2.616
7	3	0.400	−4.501	−3.299	−2.478
8	2	0.600	−3.188	−2.315	−1.843
9	1	0.800	−1.668	−1.194	−0.985
10	0	1.000	0.000	0.000	0.000
Au_{10}	$a = 2.884$ Å			$E_{\mu=1} = -333.83386$ Hartree	
5	5	0.000	−7.342	−6.220	−4.846
6	4	0.200	−6.814	−5.501	−4.485
7	3	0.400	−5.981	−4.661	−4.176
8	2	0.600	−4.253	−3.362	−3.097
9	1	0.800	−2.344	−1.857	−1.771
10	0	1.000	0.000	0.000	0.000

Table 1. GVB, UHF, and HF magnon spectra, continued. [a)]

			$E_\mu - E_{\mu=1}$ (eV)		
A	B	μ	GVB	UHF	HF
Li_6	$a = 3.014$ Å			$E_{\mu=1} = -44.63264$ Hartree	
3	3	0.000	−1.369	−1.021	0.786
4	2	0.333	−1.123	−0.726	0.520
5	1	0.667	−0.648	−0.380	0.182
6	0	1.000	0.000	0.000	0.000
Li_{10}	$a = 3.014$ Å			$E_{\mu=1} = -74.40442$ Hartree	
5	5	0.000	−2.107	−1.613	2.219
6	4	0.200	−1.978	−1.329	1.627
7	3	0.400	−1.643	−1.032	1.043
8	2	0.600	−1.155	−0.699	0.636
9	1	0.800	−0.586	−0.351	0.311
10	0	1.000	0.000	0.000	0.000
Na_{10}	$a = 3.659$ Å			$E_{\mu=1} = -1617.94206$ Hartree	
5	5	0.000	−2.666	−2.074	0.431
6	4	0.200	−2.493	−1.746	0.159
7	3	0.400	−2.077	−1.389	−0.128
8	2	0.600	−1.454	−0.960	−0.191
9	1	0.800	−0.738	−0.489	−0.123
10	0	1.000	0.000	0.000	0.000

a) For $\mu = 1$, the GVB, UHF, and HF wavefunctions are identical (see Section II).

Table 2. Details of the GVB results. [a)]

system	a (Å)	$\mathcal{D}/N$ (eV/atom)	S_{12} $\mu=0$	S_{12} $\mu=1$	S_{12} average [b)]	$\delta\phi_1$
Ag_6	2.889	0.624	0.818	0.862	0.840	0.00462
Ag_8	2.889	0.562	0.623	0.680	0.652	0.00392
Ag_{10}	2.889	0.565	0.548	0.609	0.579	0.00373
Li_6	3.014	0.228	0.536	0.728	0.632	0.01993
Li_{10}	3.014	0.211	0.282	0.369	0.325	0.00371
Cu_{10}	2.556	0.765	0.632	0.682	0.657	0.00390
Ag_{10}	2.889	0.565	0.548	0.609	0.579	0.00373
Au_{10}	2.884	0.734	0.593	0.631	0.612	0.00219
Li_{10}	3.014	0.211	0.282	0.369	0.325	0.00371
Na_{10}	3.659	0.267	0.382	0.477	0.429	0.00568

a) $\mathcal{D}$ is the magnon dispersion, S_{12} is the nearest-neighbor overlap integral, and $\delta\phi_1$ measures the difference between orbitals $\phi_1^{\mu=0}$ and $\phi_1^{\mu=1}$ (see Section III.A).
b) $(S_{12}^{\mu=0} + S_{12}^{\mu=1})/2$

Table 3. Fit of the Heisenberg model to $E_{N,A}^{GVB}$.[a)]

system	a (Å)	$\mathcal{D}/N$ [b)] (eV)	$-\mathcal{J}$ (eV)	error (%)
Ag_6	2.889	0.624	0.435	5.62
Ag_8	2.889	0.562	0.398	3.42
Ag_{10}	2.889	0.565	0.403	1.15
Cu_{10}	2.556	0.765	0.545	1.48
Ag_{10}	2.889	0.565	0.403	1.15
Au_{10}	2.884	0.734	0.523	2.81
Li_{10}	3.014	0.211	0.150	0.43
Na_{10}	3.659	0.267	0.190	0.62
Li_6	3.014	0.228	0.159	1.59
Li_{10}	3.014	0.211	0.150	0.43
Li_4	3.100	0.229	0.153	20.56
Li_6	3.100	0.218	0.152	1.64
Li_8	3.100	0.202	0.143	0.47
Li_{10}	3.100	0.199	0.142	0.48
Li_∞ [c)]	3.100	0.188	0.135	
Li_9	3.100	0.192	0.143	0.25
Li_7	3.100	0.193	0.147	0.62
Li_5	3.100	0.198	0.159	2.12
Li_3	3.100	0.205	0.205	*d*)
Li_8	2.500	0.309	0.219	1.21

a) $\mathcal{D}$ is the GVB magnon dispersion, and $\mathcal{J}$ is the effective nearest-neighbor exchange (see Section III.B). The error is $\Delta E^{RMS}/\mathcal{D}$ (see Section III.B).
b) For odd N, HM is fit to the GVB energies for magnetizations $\mu = 1/N$ and $\mu = 1$, and the magnon dispersion is defined as $\mathcal{D} = E_{\mu=1} - E_{\mu=1/N}$ ($\mu = 0$ is not allowed for odd N).
c) Obtained by extrapolation; Appendix C.
d) For Li_3, there are only two allowed magnetizations ($\mu = 0.333$ and $\mu = 1.000$); hence, ΔE^{RMS} is undefined.

Table 4. Average nearest-neighbor exchange coefficients.

N	A	B	μ	Heisenberg	simple VB	spin projected UHF	normal UHF [a]
2	1	1	0.000	1.00000	1.00000	1.00000	0.00000
2	2	0	1.000	−1.00000	−1.00000	−1.00000	−1.00000
4	2	2	0.000	0.50000	0.25000	0.50000	0.00000
4	3	1	0.500	0.00000	−0.25000	0.00000	−0.50000
4	4	0	1.000	−1.00000	−1.00000	−1.00000	−1.00000
6	3	3	0.000	0.43426	0.25000	0.33333	0.00000
6	4	2	0.333	0.20601	0.00000	0.11111	−0.33333
6	5	1	0.667	−0.33333	−0.50000	−0.33333	−0.66667
6	6	0	1.000	−1.00000	−1.00000	−1.00000	−1.00000
8	4	4	0.000	0.41277	0.25000	0.25000	0.00000
8	5	3	0.250	0.28210	0.06250	0.12500	−0.25000
8	6	2	0.500	−0.04952	−0.25000	−0.12500	−0.50000
8	7	1	0.750	−0.50000	−0.62500	−0.50000	−0.75000
8	8	0	1.000	−1.00000	−1.00000	−1.00000	−1.00000
10	5	5	0.000	0.40309	0.25000	0.20000	0.00000
10	6	4	0.200	0.31844	0.10000	0.12000	−0.20000
10	7	3	0.400	0.09519	−0.10000	−0.04000	−0.40000
10	8	2	0.600	−0.22412	−0.40000	−0.28000	−0.60000
10	9	1	0.800	−0.60000	−0.70000	−0.60000	−0.80000
10	10	0	1.000	−1.00000	−1.00000	−1.00000	−1.00000
12	6	6	0.000	0.39790	0.25000	0.16667	0.00000
12	7	5	0.167	0.33859	0.12500	0.11111	−0.16667
12	8	4	0.333	0.17842	0.00000	0.00000	−0.33333
12	9	3	0.500	−0.05804	−0.25000	−0.16667	−0.50000
12	10	2	0.667	−0.34684	−0.50000	−0.38889	−0.66667
12	11	1	0.833	−0.66667	−0.75000	−0.66667	−0.83333
12	12	0	1.000	−1.00000	−1.00000	−1.00000	−1.00000
∞	[b]		0.000	0.38629	0.25000	0.00000	0.00000

a) The Ising Hamiltonian gives the same values as normal UHF.
b) Reference [5].

Table 5. Electron correlation and spin optimization effects.

system	a (Å)	A	B	μ	electron [a] correlation (eV)	spin [b] optimization (eV)
Cu_{10}	2.556	5	5	0.000	−2.694	−1.204
		6	4	0.200	−2.548	−1.452
		7	3	0.400	−1.981	−1.414
		8	2	0.600	−1.304	−0.994
		9	1	0.800	−0.675	−0.547
		10	0	1.000	0.000	0.000
Ag_6	2.889	3	3	0.000	−1.404	−0.765
		4	2	0.333	−1.200	−0.654
		5	1	0.667	−0.696	−0.581
		6	0	1.000	0.000	0.000
Ag_8	2.889	4	4	0.000	−2.506	−0.705
		5	3	0.250	−1.976	−1.123
		6	2	0.500	−1.304	−0.816
		7	1	0.750	−0.692	−0.507
		8	0	1.000	0.000	0.000
Ag_{10}	2.889	5	5	0.000	−2.877	−0.992
		6	4	0.200	−2.652	−1.244
		7	3	0.400	−2.023	−1.203
		8	2	0.600	−1.345	−0.872
		9	1	0.800	−0.683	−0.474
		10	0	1.000	0.000	0.000
Au_{10}	2.884	5	5	0.000	−2.497	−1.122
		6	4	0.200	−2.329	−1.313
		7	3	0.400	−1.805	−1.320
		8	2	0.600	−1.156	−0.891
		9	1	0.800	−0.573	−0.488
		10	0	1.000	0.000	0.000

Table 5. Electron correlation and spin optimization effects, continued.

system	a (Å)	A	B	μ	electron [a] correlation (eV)	spin [b] optimization (eV)
Li_6	3.014	3	3	0.000	−2.156	−0.348
		4	2	0.333	−1.642	−0.396
		5	1	0.667	−0.830	−0.267
		6	0	1.000	0.000	0.000
Li_{10}	3.014	5	5	0.000	−4.326	−0.494
		6	4	0.200	−3.605	−0.649
		7	3	0.400	−2.686	−0.611
		8	2	0.600	−1.791	−0.456
		9	1	0.800	−0.897	−0.235
		10	0	1.000	0.000	0.000
Na_{10}	3.659	5	5	0.000	−3.097	−0.592
		6	4	0.200	−2.652	−0.747
		7	3	0.400	−1.950	−0.688
		8	2	0.600	−1.263	−0.494
		9	1	0.800	−0.614	−0.249
		10	0	1.000	0.000	0.000

a) $E^{CORR} = E^{GVB} - E^{HF}$.
b) $E^{SOPT} = E^{GVB} - E^{UHF}$.

Table 6. GVB results for selected two-electron systems.

system	a (Å)	$\Psi^{GVB}_{2,\mu=0}$ [a] $-\mathcal{J}_{12}$ (eV)	$\Psi^{GVB}_{2,\mu=0}$ [a] $\mathcal{S}_{12}$	$E_{2,\mu=1} - E_{2,\mu=0}$ [b] frozen (eV)	$E_{2,\mu=1} - E_{2,\mu=0}$ [b] relaxed (eV)
Cu_3^+	2.556	0.267	0.389	0.547	0.471
Ag_3^+	2.889	0.181	0.344	0.366	0.314
Au_3^+	2.884	0.159	0.350	0.322	0.271
Li_3^+	3.014	0.074	0.222	0.149	0.138
Na_3^+	3.659	0.089	0.256	0.178	0.148

a) Values calculated with the $\mu = 0$ GVB canonical orbitals.
b) Energy splitting between $\mu = 0$ and $\mu = 1$. The frozen values are calculated using a single set of orbitals — the low-spin orbitals — to describe both magnetizations (see Appendix B). The relaxed values are calculated using the optimum orbitals for each state.

Table 7. Details of the GVB results for H_N rings. [a)]

system	a (Å)	$\mathcal{D}/N$ (eV/atom)	$\mathcal{S}_{12}$ $\mu = 0$	$\mathcal{S}_{12}$ $\mu = 1$	$\mathcal{S}_{12}$ average [b)]	$\delta\phi_1$
H_6	1.483	2.020	0.650	0.710	0.680	0.00514
H_8	1.483	1.975	0.584	0.634	0.609	0.00373
H_{10}	1.483	2.067	0.548	0.603	0.575	0.00401
H_{10}	1.260	3.497	0.734	0.759	0.747	0.00366
H_{10}	1.186	4.139	0.786	0.796	0.791	0.00323
H_{10}	1.112	4.883	0.828	0.825	0.827	0.00316

a) $\mathcal{D}$ is the magnon dispersion, $\mathcal{S}_{12}$ is the nearest-neighbor overlap integral, and $\delta\phi_1$ measures the difference between orbitals $\phi_1^{\mu=0}$ and $\phi_1^{\mu=1}$ (see Section III.A).
b) $(\mathcal{S}_{12}^{\mu=0} + \mathcal{S}_{12}^{\mu=1})/2$

Table 8. Fit of the Heisenberg model to $E^{GVB}_{N,A}$ for H_N rings.[a)]

system	a (Å)	$\mathcal{D}/N$ [b)] (eV)	$-\mathcal{J}$ (eV)	error (%)
H_6	1.483	2.020	1.409	4.33
H_8	1.483	1.975	1.398	2.59
H_{10}	1.483	2.067	1.473	0.71
H_{10}	1.260	3.497	2.492	1.57
H_{10}	1.186	4.139	2.950	1.91
H_{10}	1.112	4.883	3.480	2.23

a) $\mathcal{D}$ is the GVB magnon dispersion, and $\mathcal{J}$ is the effective nearest-neighbor exchange (see Section III.B). The error is $\Delta E^{RMS}/\mathcal{D}$ (see Section III.B).

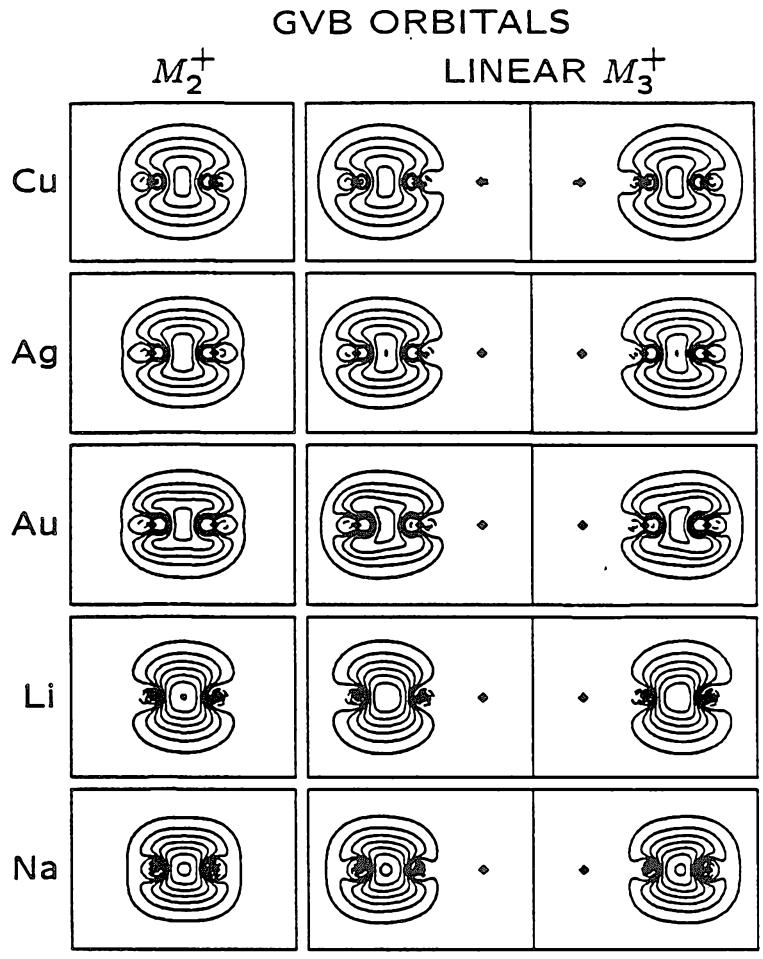

Figure 1. The optimum GVB valence orbitals for M_2^+ and linear M_3^+ (low spin), M = Cu, Ag, Au, Li, and Na. Each orbital contains one electron (one orbital for M_2^+ and two orbitals for M_3^+; overlaps for M_3^+ are given in Table 6). For Figures 1-2, the nearest-neighbor distance (a) is equal to that of the bulk metal (a = 2.556, 2.889, 2.884, 3.014, and 3.659 Å for Cu, Ag, Au, Li, and Na, respectively), and the boxes are scaled to a (box width = 3.6 a). Squares mark the atomic positions. Contours mark even amplitude increments of $0.2a^{-3/2}$. Solid and dashed contours denote positive and negative amplitudes, respectively. For M_2^+, the GVB and UHF orbitals are identical, since there is only one valence electron. For each of the linear M_3^+ clusters, the GVB orbitals are very similar to the UHF orbitals. However, for low-spin M_3^+, UHF leads to net spin densities whereas GVB does not.

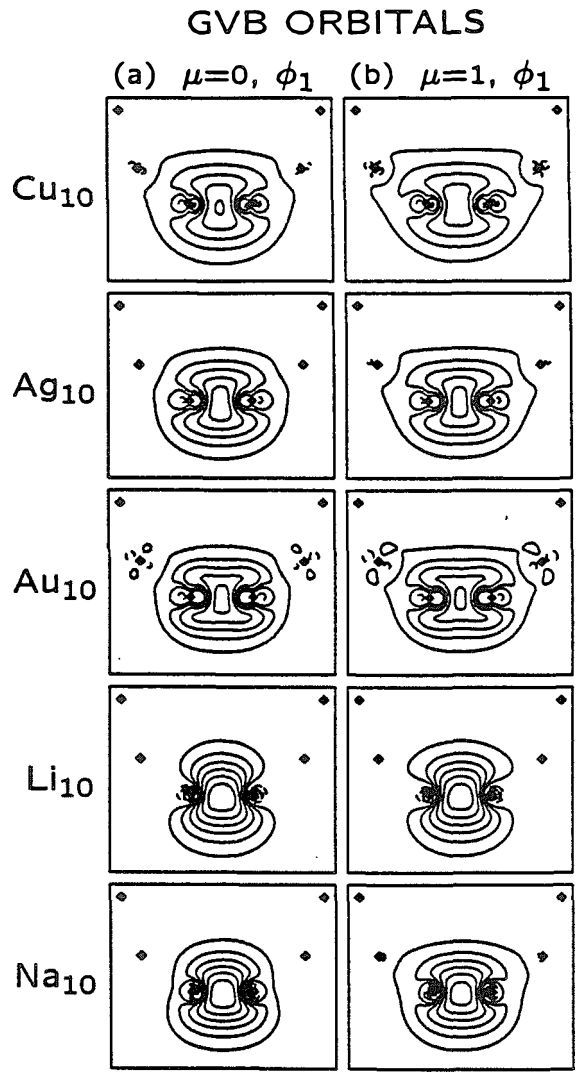

Figure 2. GVB valence orbitals for each of the Cu_{10}, Ag_{10}, Au_{10}, Li_{10}, and Na_{10} ring clusters (obtained by Hartree localization; adjacent orbital overlaps are given in Table 2). (a) Shows the low-spin ($\mu = 0$) orbital. (b) Shows the high-spin ($\mu = 1$) orbital.

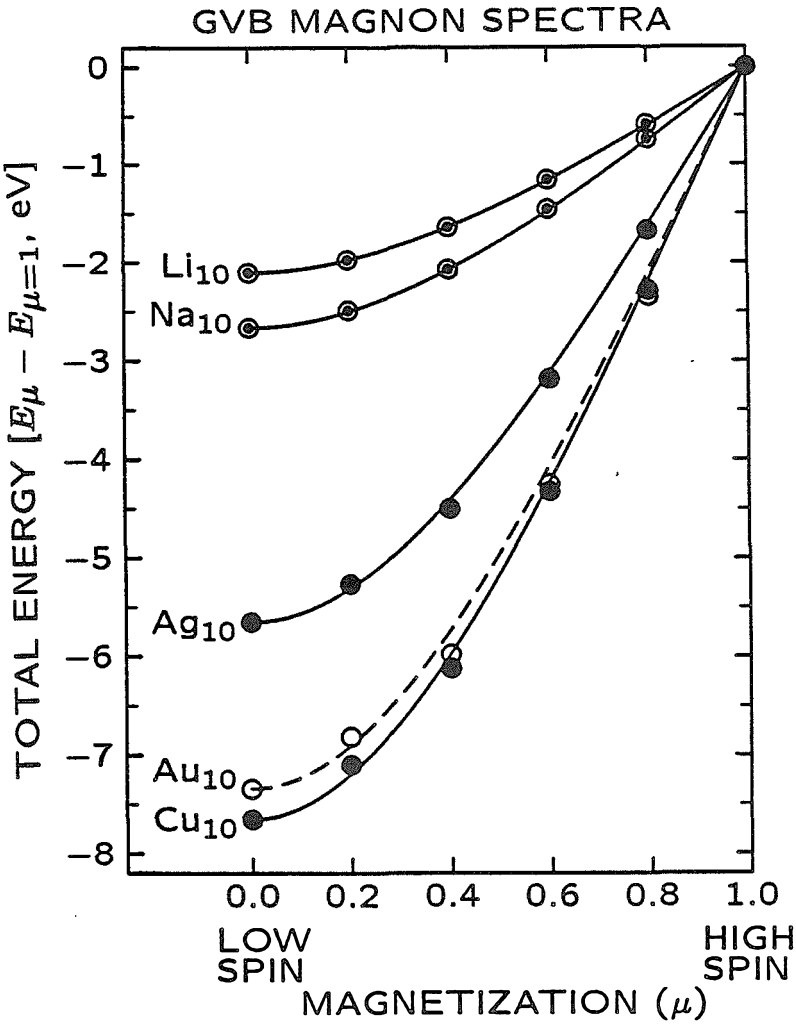

Figure 3. The GVB magnon spectra for the Cu_{10}, Ag_{10}, Au_{10}, Li_{10}, and Na_{10} ring clusters. In each case, (*i*) data points show the GVB total energy as a function of the magnetization (see Table 1), (*ii*) a curve shows the fit of the Heisenberg model to the GVB total energies (see Table 3), and (*iii*) the GVB total energy for $\mu = 1$ is chosen as zero energy. Analogous figures all follow this convention for GVB (Figures 4-10, and Figure 15).

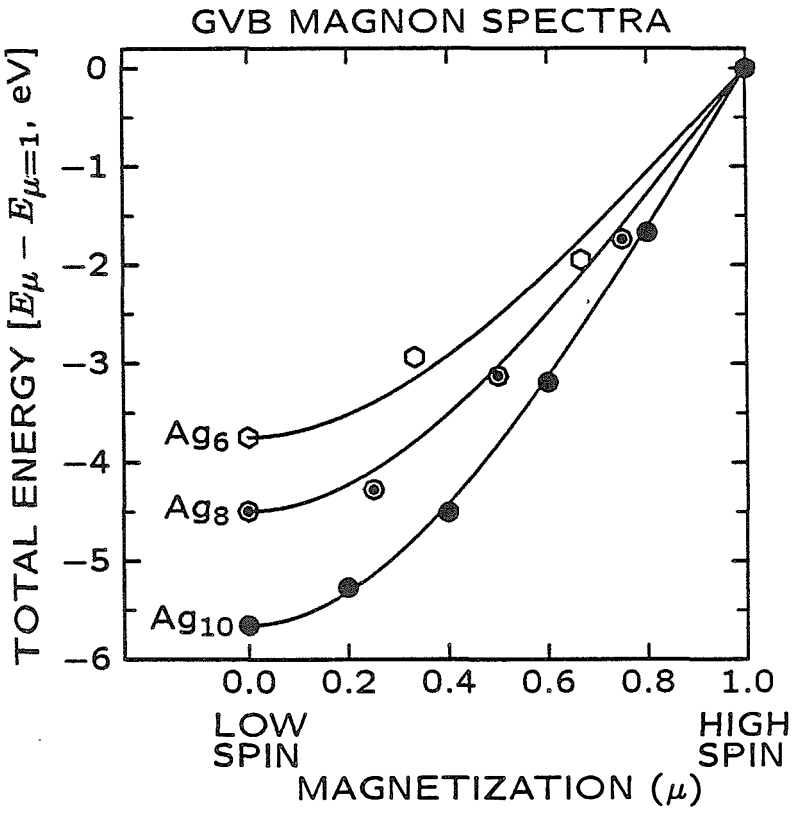

Figure 4. The GVB magnon spectra for Ag_6, Ag_8, and Ag_{10}. Data points show the GVB total energies, and the curves show the fits of HM to the GVB total energies (see Table 3).

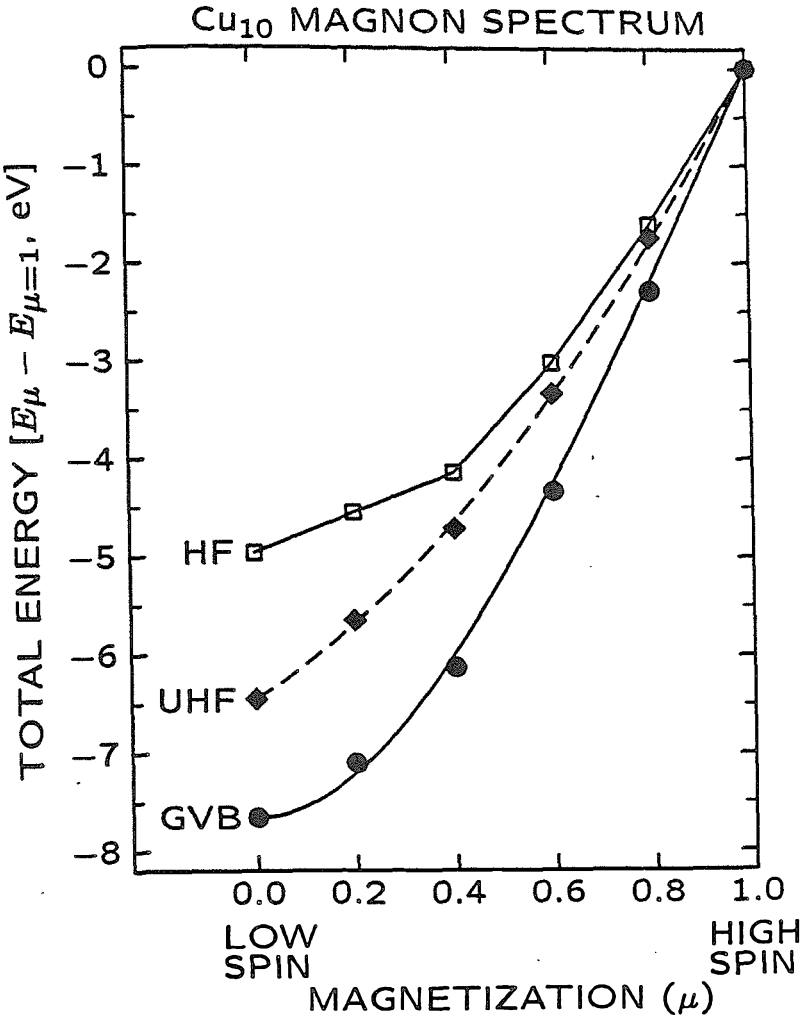

Figure 5. The Cu_{10} magnon spectrum. Data points show the total energy as a function of the magnetization for GVB, UHF, and HF, as indicated (see Table 1). The GVB results are interpolated by the Heisenberg model (see Table 3). The UHF results are interpolated by the generalized Ising model. The HF results are joined by straight line segments. Each of these three wavefunctions gives the same total energy for $\mu = 1$ (see Section II); hence, the total energy for $\mu = 1$ is chosen as zero energy. Analogous figures all follow this convention (Figures 6-10 and Figure 15).

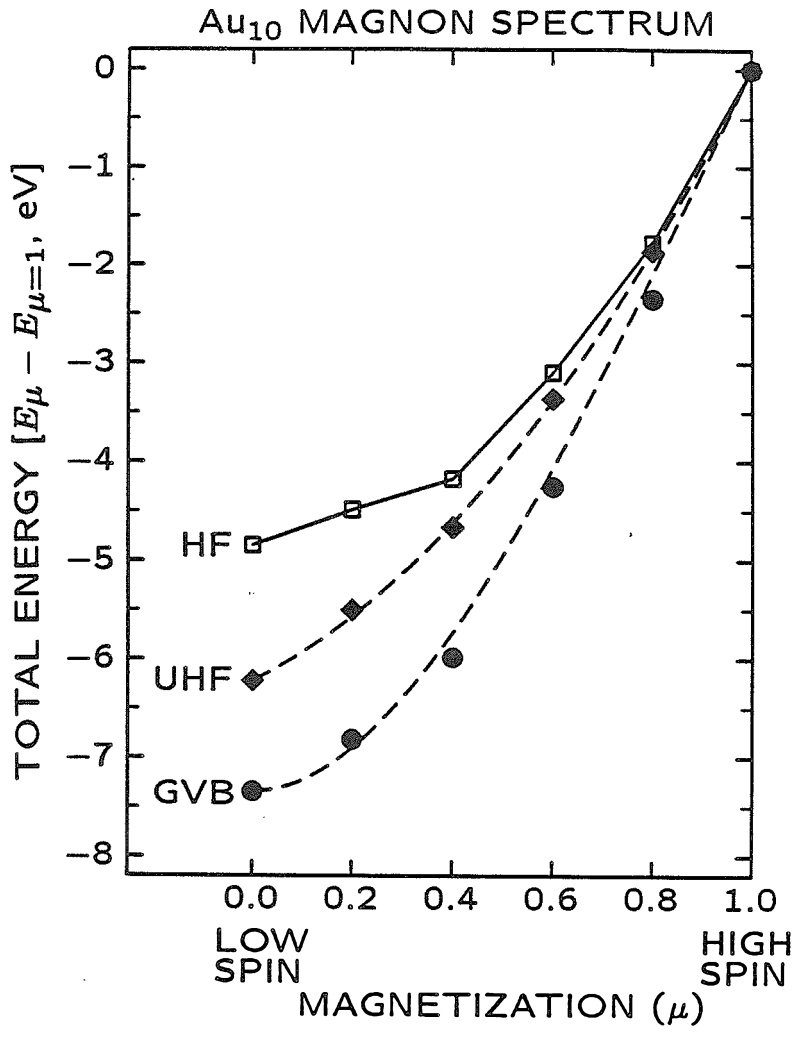

Figure 6. The Au_{10} magnon spectrum, as calculated with GVB, UHF, and HF, as indicated (see Table 1).

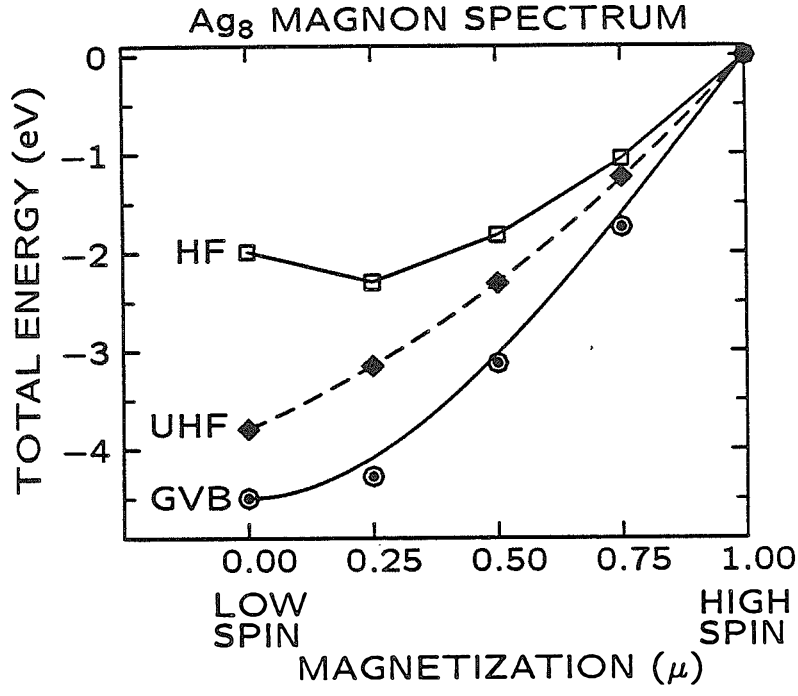

Figure 7. The Ag_8 magnon spectrum, as calculated with GVB, UHF, and HF, as indicated. The GVB results are interpolated by the Heisenberg model (see Table 3).

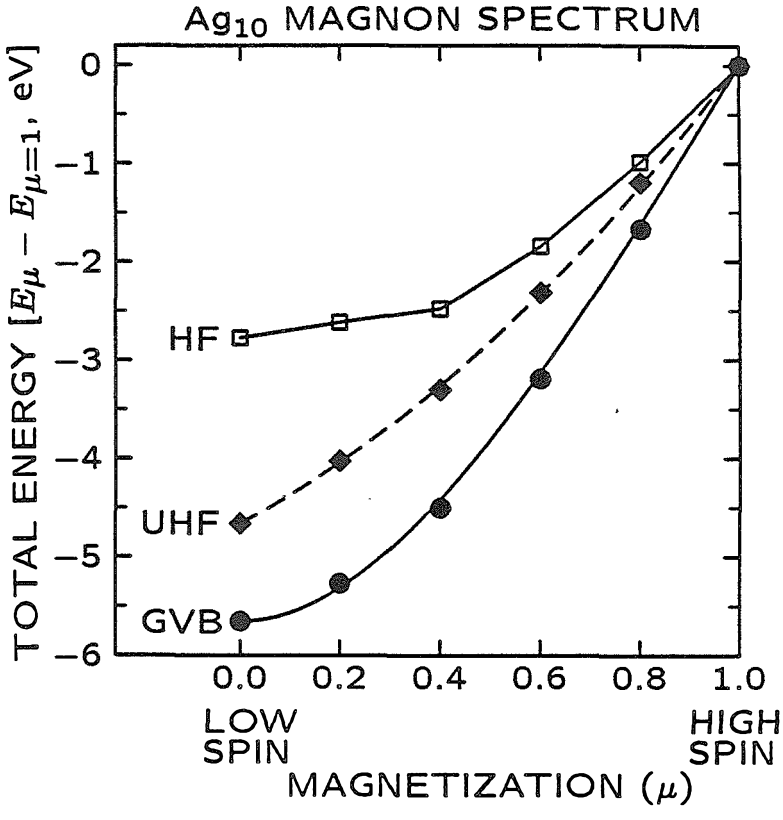

Figure 8. The Ag_{10} magnon spectrum, as calculated with GVB, UHF, and HF, as indicated (see Table 1).

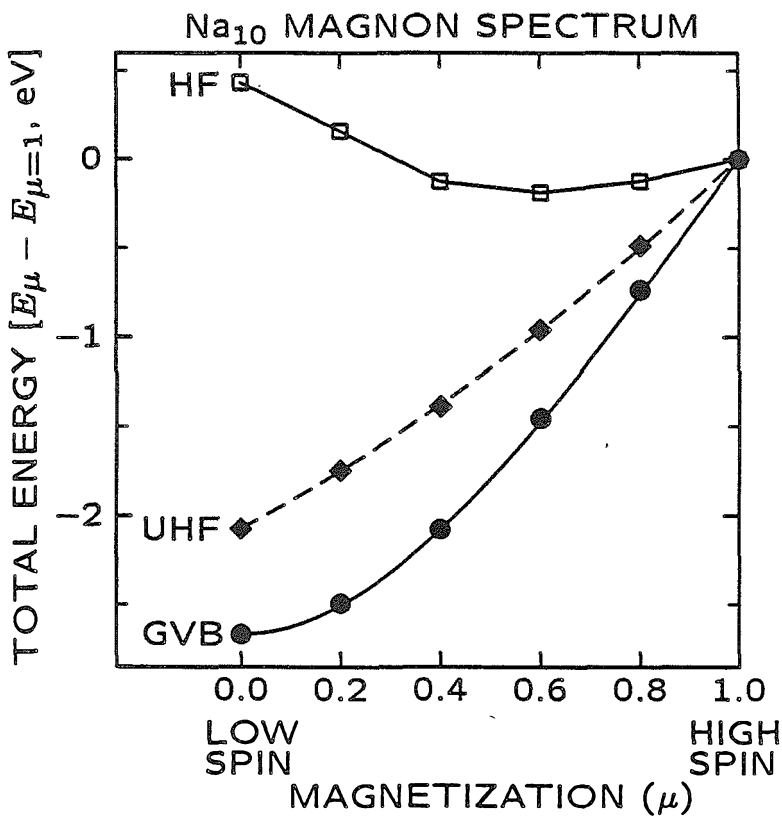

Figure 9. The Na_{10} magnon spectrum, as calculated with GVB, UHF, and HF, as indicated. The GVB results are interpolated by the Heisenberg model (see Table 3).

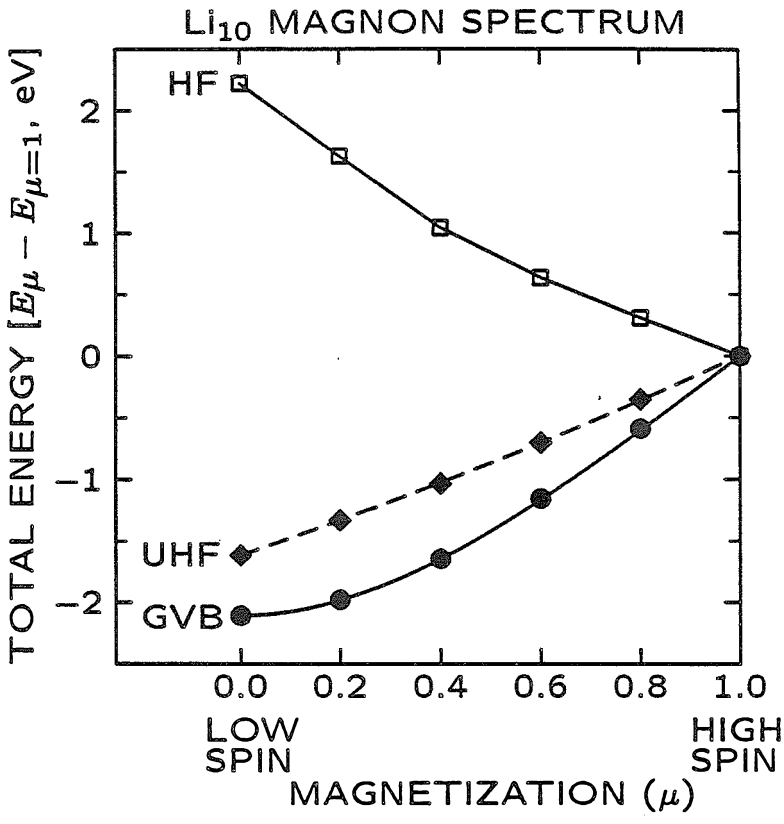

Figure 10. The Li_{10} magnon spectrum, as calculated with GVB, UHF, and HF, as indicated (see Table 1).

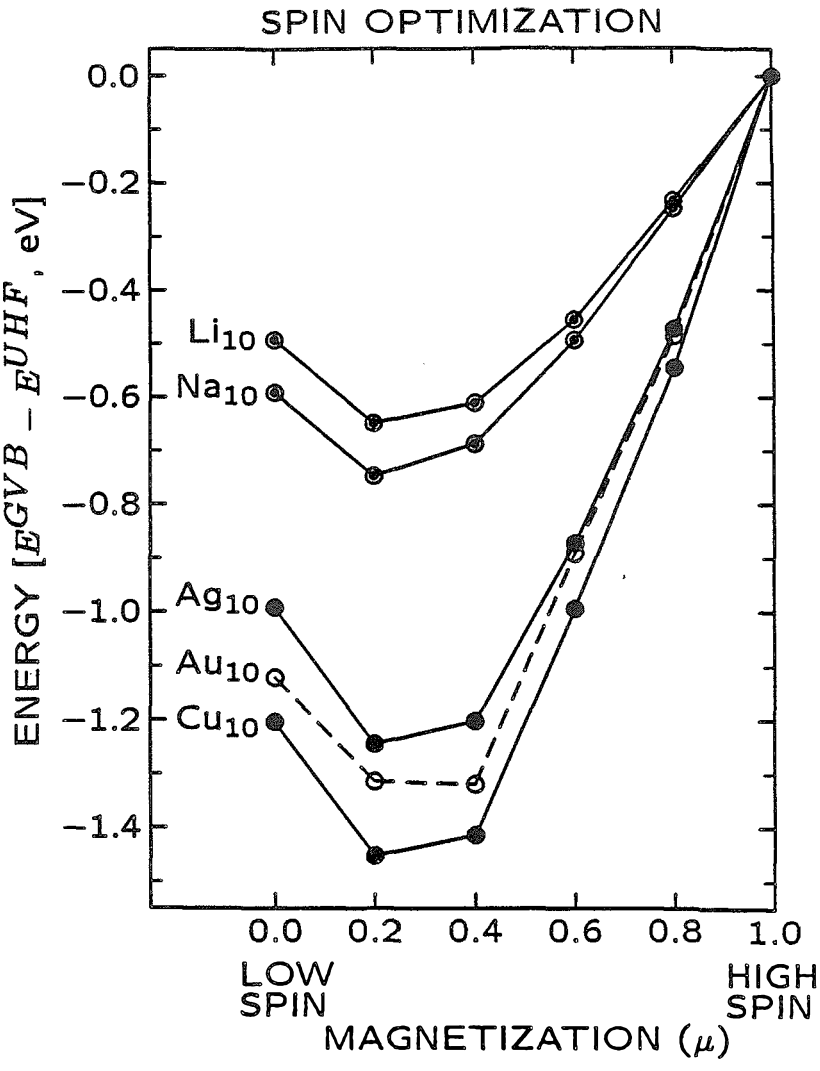

Figure 11. The energy stabilization due to spin optimization ($E^{GVB} - E^{UHF}$) as a function of magnetization for the various M_{10} ring clusters (see Table 5).

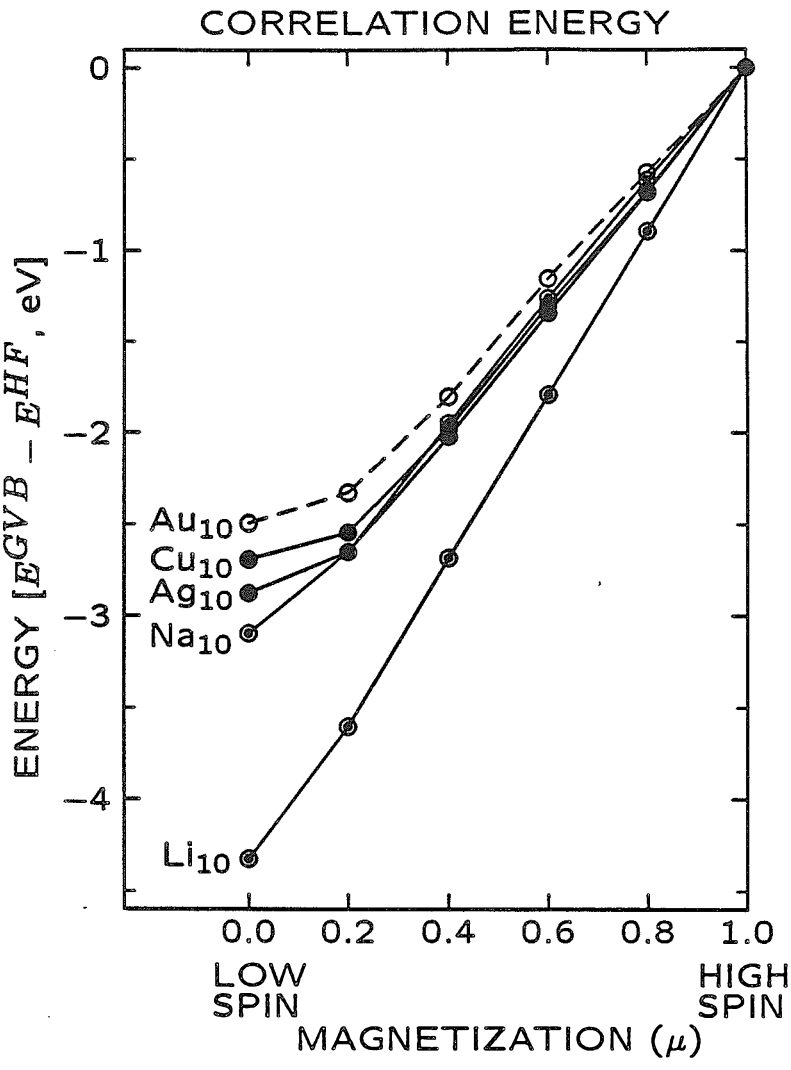

Figure 12. The energy stabilization due to static electron correlation ($E^{GVB} - E^{HF}$) as a function of magnetization for the various M_{10} ring clusters (see Table 5).

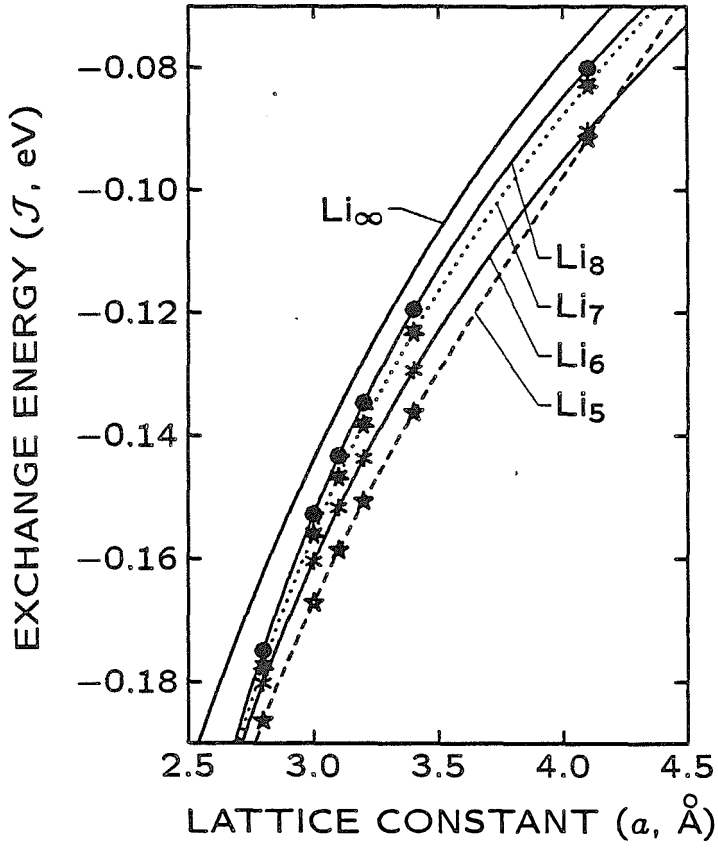

Figure 13. The effective nearest neighbor exchange energy ($\mathcal{J}$) as a function of a for Li_5, Li_6, Li_7, Li_8, and Li_∞, as indicated.

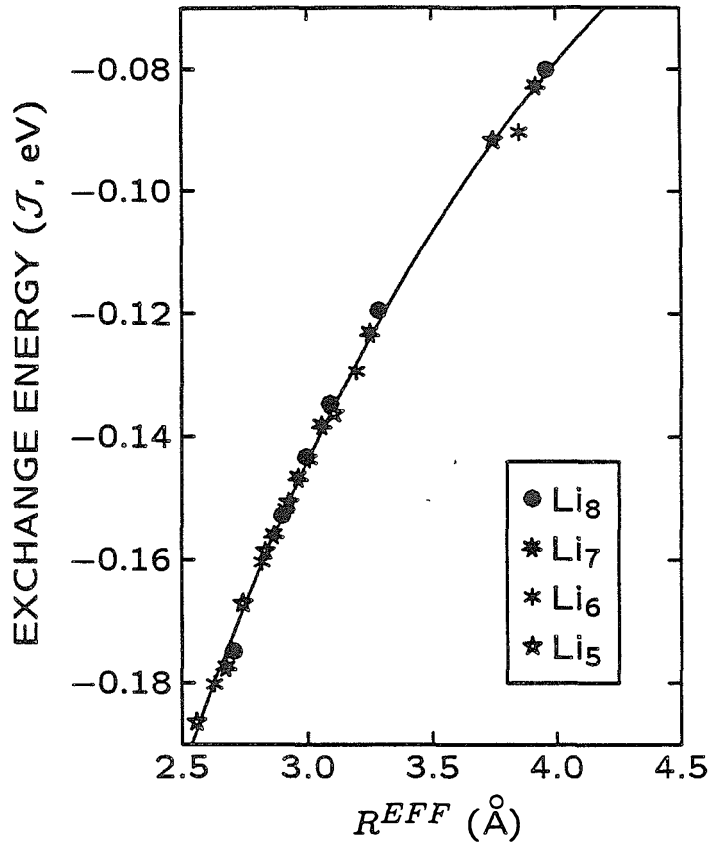

Figure 14. The effective nearest neighbor exchange energy ($\mathcal{J}$) as a function of the effective distance between adjacent orbitals (R^{EFF}) for Li_5, Li_6, Li_7, and Li_8, as indicated.

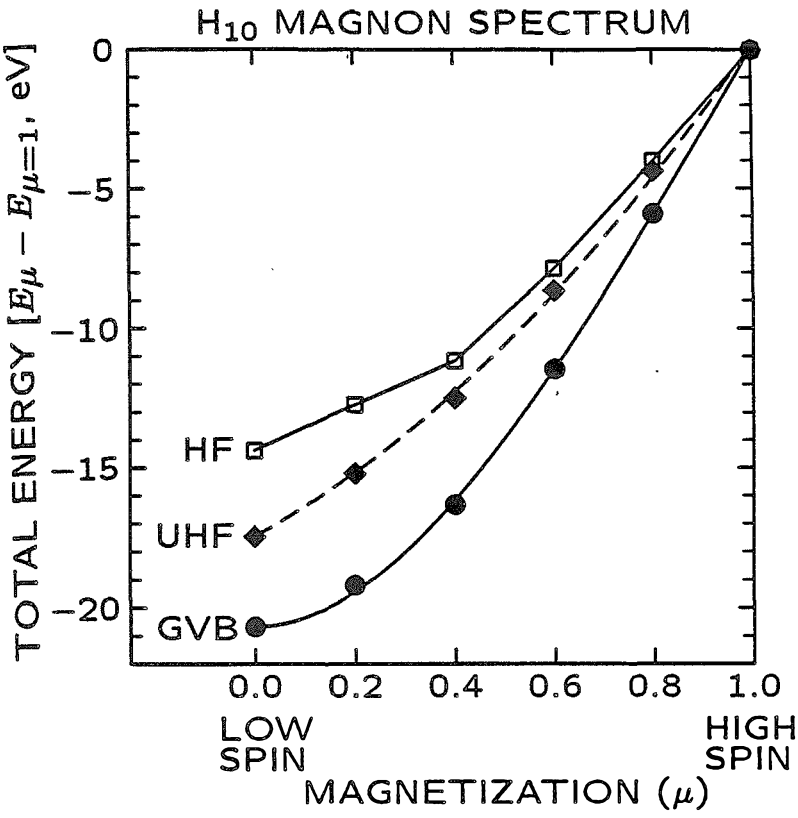

Figure 15. The H_{10} magnon spectrum. Data points show the total energy as a function of the magnetization for GVB, UHF, and HF, as indicated. The GVB results are interpolated by the Heisenberg model (see Table 8). The UHF results are interpolated by the generalized Ising model. The HF results are joined by straight line segments. Each of these three wavefunctions gives the same total energy for $\mu = 1$ (see Section II); hence, the total energy for $\mu = 1$ is chosen as zero energy.

Chapter 5

New Concepts of Metallic Bonding Based on Generalized Valence Bond Wavefunctions

Chapter 5 consists of three published articles coauthored with William A. Goddard III. Reprints of these articles follow.

VOLUME 55, NUMBER 23 PHYSICAL REVIEW LETTERS 2 DECEMBER 1985

New Concepts of Metallic Bonding Based on Valence-Bond Ideas

Mark H. McAdon and William A. Goddard, III

Arthur Amos Noyes Laboratory of Chemical Physics, California Institute of Technology, Pasadena, California 91125

(Received 23 May 1985)

From generalized-valence-bond calculations on numerous Li-atom clusters (Li_n and Li_n^+, $n \leq 13$), we conclude that the optimum bonding involves *singly occupied* orbitals localized interstitially (in tetrahedra). Rules based on the calculations are used to predict low-energy isomers (leading for Li_{13}^+ to low-symmetry structures that are significantly more stable than the icosahedron but retain local fivefold-symmetry axes) and are applied to infinite metallic systems.

PACS numbers: 36.40.+d, 31.10.+z, 31.20.Tz, 71.10.+x

The valence-bond principles of structural chemistry,[1] so useful in rationalizing the geometries and bonding for nonmetallic molecules and solids,[2-5] have *not* been similarly useful for understanding metallic systems. In order to lay the foundation for the development of analogous simple principles for *metallic systems*, we have applied *ab initio* generalized-valence-bond (GVB) approaches to examining the bonding in various one-, two-, and three-dimensional clusters of Li atoms. The qualitative principles arising from these studies are presented here (further details will appear elsewhere).[6] These principles should be useful in rationalizing and predicting the local geometric and electronic structures for clusters and amorphous metals,[6] and for defects and interfaces of crystalline metallic systems.

For one-dimensional systems we find one *singly occupied* orbital *localized* at each bond midpoint, forming one-electron bonds. This is shown for the Li_{10} ring cluster in Fig. 1. These bond-localized orbitals are very similar for other lithium rings and for Li_2^+, linear Li_3^+, Cu_2^+, and linear Cu_3^+.[6] The GVB wave function of the Li_{10} ring involves full optimization of the spin coupling (42 possible resonance structures) but is dominated by two primary resonance structures having adjacent (singly occupied) bond orbitals spin paired. This model for the bonding predicts correctly the distortions that occur when the ring structure is allowed to relax. The optimum geometric distortion is the one that increases the overlap of adjacent spin-paired orbitals while decreasing the overlap of adjacent orbitals that are not spin paired. In square H_4, the orbitals are atom centered, leading to an unstable rectangular distortion (no chemical bonding between the two H_2 fragments). For square Li_4, the orbitals are bond centered, leading to a rhombic distortion [Fig. 2(a)] that *is* unstable as a result of one-electron bonding. Such distortions lower the energy of one resonance structure but raise the energy of the other resonance structure, reducing the resonance energy substantially. Nevertheless, square Li_4 ($\theta = 90°$) distorts to a rhombus[6,7] ($\theta_{opt} = 57.3°$). Similarly, hexagonal Li_6 ($\theta = 120°$) distorts to a trigonal hexagon[6,8] ($\theta_{opt} = 69.3°$), as indicated in Fig. 2(b). Thus, optimum planar structures for Li_4 and Li_6 both resemble planar close-packed clusters.

Similar studies of larger two-dimensional close-packed arrays of Li atoms lead to the general result that *interior regions* have singly occupied orbitals localized at the *centers of equilateral triangles* while *surface (edge) regions* have singly occupied orbitals localized at

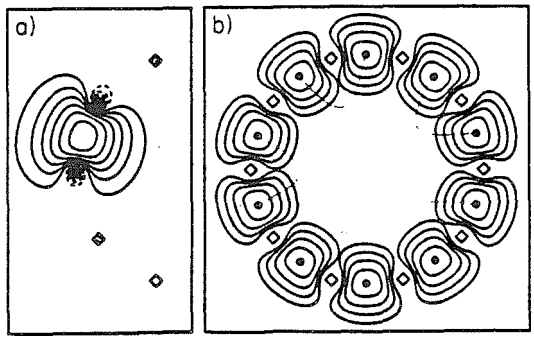

FIG. 1. The GVB orbitals for one of the two primary resonance structures for the Li_{10} ring cluster. Squares mark the atomic positions and dots joined by thin lines represent the electrons and spin coupling. Solid and dashed contours show positive and negative orbital amplitudes, respectively. Contour spacings are at 0.015 a.u. (a) One singly occupied GVB orbital. (b) Contours ≥ 0.045 a.u. for all ten GVB orbitals.

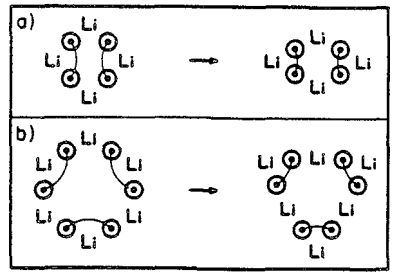

FIG. 2. Geometric distortions for the (a) Li_4 and (b) Li_6 ring clusters. Circles with dots represent the singly occupied bond orbitals. Lines connecting the dots show the dominant spin pairing.

bond midpoints. This is illustrated for planar Li_{10} in Fig. 3.

Use of simple pair-additive potentials would suggest that tetrahedral Li_4 is favored over the rhombus since it has one extra "bond." However, the rhombus is the stable geometry as predicted by the following GVB argument. The above results suggest that the four orbitals of tetrahedral Li_4 would be localized on the four faces and spin paired. The problem with this is that the orbitals in *different* pairs would be quite close ($0.41R$, where R is the side length), leading to large repulsive interactions. Instead, the optimum orbitals are localized on four of the six edges and spin paired so that nonpaired orbitals are at least $0.5R$ apart. However, the distortion to a planar (rhombic) structure increases the distance between nonpaired orbitals to $0.89R$, while retaining the favorable spin pairing. Thus the bonding principles predict and the calculations confirm that the stable geometry of Li_4 is the rhombus.

We next discuss the lowest-energy spin singlet for Li_{13}^+ clusters having a central (bulk) atom and twelve surface atoms: (i) I_h, the icosahedron; (ii) fcc, the truncated octahedron corresponding to the nearest neighbors of a face-centered-cubic lattice; and (iii) hcp, the hexagonal array corresponding to the nearest neighbors of a hexagonal close-packed lattice.

For I_h, the ground state involves orbitals localized at the centers of twelve of the twenty triangular faces and spin paired in rhombi (0.63 overlap) just as for the bulk atoms in Fig. 3. The four triangular faces adjacent to a spin-paired rhombus are empty (to avoid repulsive interactions between unpaired orbitals), as indicated in Fig. 4.

The fcc and hcp clusters have total energies 0.26 eV and 0.56 eV (per cluster) higher than I_h (i.e., 20 meV/atom and 44 meV/atom), respectively. Both have only eight tetrahedra, and some of the tetrahedra have two spin-paired orbitals (on opposite faces). For fcc, each tetrahedron shares edges (and no faces) with three others and the electrons are distributed so that each edge-sharing pair of tetrahedra contains three electrons. For hcp, there are three pairs of face-shared tetrahedra. This accommodates three pairs of spin-paired orbitals. The top and bottom tetrahedra are isolated and each contains one electron pair. This leaves two electrons that end up along two of the three equatorial edges that do *not* border a tetrahedron.

From these various results emerge the following rules for three-dimensional metallic structures: (α) Orbitals (each with one electron) are localized in different tetrahedral hollows where possible. (β) If necessary, two orbitals may be placed in one tetrahedron (localized on opposite faces or edges) but they must be spin paired. (γ) No more than three electrons may be distributed between a pair of *edge-shared* tetrahedra. (δ) No more than two electrons may be distributed between a pair of *face-shared* tetrahedra, and these must be spin paired (singlet). (ϵ) Additional electrons must be in surface orbitals at edge or face sites that do not share edges with occupied tetrahedra. (ζ) It is unfavorable to occupy more than four tetrahedra (or pairs of tetrahedra) sharing one central atom.

We expect that these rules may apply to the valence *sp* electrons of a variety of structures for elemental metals and alloys, including fcc, hcp, γ-brass,[9,10] the Laves phases,[10] and Frank-Kasper alloys.[10,11] The

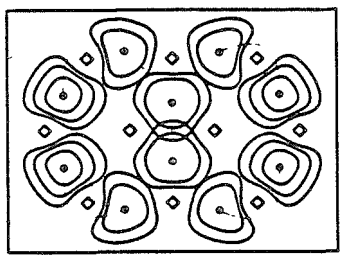

FIG. 3. All ten GVB orbitals for the principal resonance structure of planar close-packed Li_{10}. Squares mark the atoms, and dots joined by thin lines represent the paired electrons. The contours represent 0.015-a.u. increments of orbital amplitude, starting at 0.060 a.u. Each orbital is occupied by only one electron.

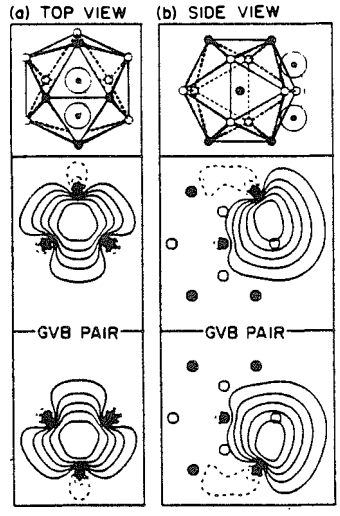

FIG. 4. GVB orbitals for one of the five primary resonance structures of icosahedral Li_{13}^+. The atoms are marked by circles; dots jointed by thin lines represent bond-paired electrons. Only one of the six equivalent bond pairs is shown (0.015-a.u. contour increments). Shaded triangular faces do not contain orbitals.

present rules may require modification for metallic structures possessing severely distorted tetrahedra (e.g., body-centered cubic) and for structures containing insufficient tetrahedra to accommodate all valence *sp* electrons (e.g., rule ϵ).

The above principles are consistent with the relative energies and suggest that the *optimum structures* of small clusters should *maximize the number of tetrahedra*. However, for the icosahedron, the twenty tetrahedra all share the *same* central bulk atom, violating rule ζ. This led us to predict several new Li_{13}^+ optimum-tetrahedral (OPTET) clusters that maximize the number of tetrahedra while satisfying rule ζ. Each new structure[6] has fifteen tetrahedra and is lower in energy than I_h. The best (Fig. 5) has a total energy 0.58 eV lower than the icosahedron (45 meV/atom)! These OPTET clusters generally lead to local fivefold-symmetry axes, and since exact fivefold symmetry is inconsistent with three-dimensional crystal structure, OPTET bonding could play an important role in the stabilization of amorphous structures.[6]

Larger OPTET clusters are constructed by the addition of atoms to concave surface sites of the smaller OPTET clusters, forming at least two new tetrahedra for each atom added. The Li_{26} OPTET cluster is isostructural with the $Cu_{10}Zn_{16}$ cluster of Cu_5Zn_8 (γ-brass)[9] (both contain 57 tetrahedra). The γ-brass structure is composed of these 26-atom clusters centered at body-centered-cubic (bcc) lattice positions. The γ-brass alloys usually have a valence-electron/atom ratio of 21/13, although an alloy of approximate composition Ag_3Li_{10} also forms the γ-brass structure.[10] Maximizing the number of tetrahedra also seems to be important for the stability of many other alloy structures.[11]

With such small clusters, surface effects are quite large so that planar clusters (which lead to an increased number of internal sites) are quite competitive. We have found a planar Li_{13}^+ cluster that has a total energy 0.18 eV lower than I_h (but 0.40 eV higher than the OPTET cluster).

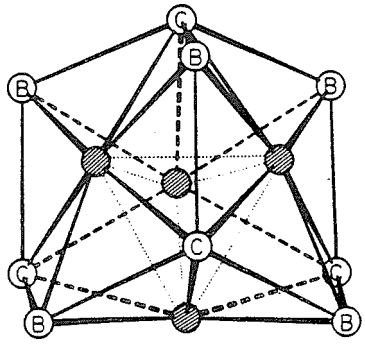

FIG. 5. The lowest-energy Li_{13}^+ OPTET isomer. This cluster consists of a central tetrahedron (shaded circles, dotted lines), four capping atoms (C), and five bridging atoms (B). This leads to a C_2-symmetry axis, two reflection planes, and five local C_5-symmetry axes.

These considerations suggest that there may be several regimes of structure for metal clusters. The smallest clusters either form planar structures (as in Li_4 and Li_6) or have very-low-energy planar configurations. For intermediate size, the OPTET structures are stable (e.g., Li_8, Li_{13}^+, and perhaps extending well into the 20's), while very large clusters may yield structures approaching bulk character (hcp, fcc, bcc). The surface reactivities[12] of these clusters can be expected to show dramatic dependences on the cluster regime (e.g., whether planar, OPTET, or high symmetry is favored).

Next, we apply these GVB ideas to close-packed (hcp and fcc) bulk metals and show how to rationalize certain solid solubilities and alloys in terms of electron/atom ratios.

Close-packed (cp) systems have twice as many tetrahedra as atoms. For the Be and Zn columns, the GVB model suggests that the optimum electronic structure be visualized in terms of one valence electron per tetrahedron. For a cp alkali or noble metal, only half the tetrahedra need be occupied by electrons, making the cp metals *far* more stable than the small cp clusters (where all tetrahedra are occupied, some with two electrons). Our rules do not state which cp structure is favored for these systems. Indeed, the alkali metals[13,14] and the alkaline-earth metals[13] seem to have nearly identical energies for hcp, fcc, and bcc. The noble metals (Cu,Ag, and Au) are all fcc while Zn and Cd are hcp.

For cp systems with three valence electrons per atom, half the tetrahedra must be doubly occupied, while the other half are singly occupied. In fcc, each tetrahedron shares edges with six other tetrahedra, whereas pairs of tetrahedra are face shared in hcp. On the basis of rule δ, we conclude that fcc should be strongly favored over hcp, and indeed, neither B, Al, Ga, nor In leads to hcp, while Al leads to fcc and In to a slightly distorted fcc.

With four valence electrons per atom, all tetrahedra would be doubly occupied, strongly disfavoring either cp structure (rules γ and δ). Indeed, except for Pb, the group-IV elements are either nonmetals (with strong two-electron covalent bonds) or metals with low coordination numbers. It is well known that Hg, Tl, Pb, and Bi exhibit properties suggesting that the (6*s*) pairs are particularly stable and not easily hybridized with the *p* orbitals to form normal sp^3 hybrids, perhaps rationalizing the fcc form for Pb.

Rules γ and δ place upper limits of $2e^-$/atom for hcp and $3e^-$/atom for fcc. These limits are consistent

with known alloy formations and solid solubilities,[10,15] e.g., comparing atoms with similar sizes [Ag ($1e^-$), Zn ($2e^-$), Al ($3e^-$), and Sn ($4e^-$); metallic radii[13] 1.44, 1.39, 1.43, and 1.54 Å, respectively], Ag and Zn are both highly soluble in fcc Al (23.8 and 66.5 at.%, respectively), while the solubility of Sn in Al is only 0.02 at.%. Similarly, the solubilities of Al and Sn in hcp Zn are small (2.4 and 0.14 at.%, respectively), while Ag is 5 at.% soluble in Zn and forms hcp-like alloys with up to 63.8% Ag (Ag_5Zn_8 forms γ-brass). The $3e^-$/atom limit does not restrict solubilities in fcc Ag ($1e^-$/atom); hence, the solubilities are all high (Zn, 40.2 at.%; Al, 20.34 at.%; Sn, 11.5 at.%).

We believe that these ideas of interstitially localized singly occupied orbitals will form a useful starting point in developing valence-bond ideas for predicting geometries, electronic structure, and properties of metallic clusters, and for describing localized states in metals and alloys such as defects or interfaces. These ideas may also provide useful concepts for predicting transport properties and the chemistry and catalytic properties of such systems.

This work was partially supported by the National Science Foundation through Grant No. DMR82-15650.

[1]L. Pauling, *The Nature of the Chemical Bond and the Structure of Molecules and Crystals* (Cornell Univ. Press, Ithaca, N.Y., 1960), 3rd ed.

[2]W. A. Goddard, III, T. H. Dunning, Jr., W. J. Hunt, and P. J. Hay, Accts. Chem. Res. 6, 368 (1973).

[3]W. A. Goddard, III, and L. B. Harding, Ann. Rev. Phys. Chem. 29, 363 (1978).

[4]G. T. Surratt and W. A. Goddard, III, Solid State Commun. 22, 413 (1977), and Phys. Rev. B 18, 2831 (1978).

[5]J. J. Barton, W. A. Goddard, III, and T. C. McGill, J. Vac. Sci. Technol. 16, 1178 (1979); C. A. Swarts, T. C. McTill, and W. A. Goddard, III, Surf. Sci. 110, 400 (1981); A. Redondo and W. A. Goddard, III, J. Vac. Sci. Technol. 21, 344 (1982); A. Redondo, W. A. Goddard, III, and T. C. McGill, Surf. Sci. 132, 49 (1983).

[6]M. H. McAdon and W. A. Goddard, III, to be published, and to be published.

[7]H.-O. Beckmann, J. Koutecký, and V. Bonačić-Koutecký, J. Chem. Phys. 73, 5182 (1980).

[8]Our results for Li_4 are consistent with a pseudo–Jahn-Teller description (Ref. 7). However, the pseudo–Jahn-Teller description does not predict the analogous distortion for the Li_6 ring.

[9]A. Taylor, *X-Ray Metallography* (Wiley, New York, 1961).

[10]W. Hume-Rothery and G. V. Raynor, *The Structure of Metals and Alloys* (Institute of Metals, London, 1962), 4th ed.

[11]F. C. Frank and J. S. Kasper, Acta Crystallogr. 12, 483 (1959), and 11, 184 (1958).

[12]M. D. Morse, M. E. Geusic, J. R. Heath, and R. E. Smalley, J. Chem. Phys. 83, 2293 (1985); R. L. Whetten, D. M. Cox, D. J. Trevor, and A. Kaldor, Phys. Rev. Lett. 54, 1494 (1985); S. C. Richtsmeier, E. K. Parks, K. Liu, L. G. Pobo, and S. J. Riley, J. Chem. Phys. 82, 3659 (1985).

[13]J. Donohue, *The Structure of the Elements* (Wiley, New York, 1974).

[14]R. W. Overhauser, Phys. Rev. Lett. 53, 64 (1984); K. Takemura and K. Syassen, Phys. Rev. B 28, 1193 (1983); M. S. Anderson and C. A. Swenson, Phys. Rev. B 31, 668 (1985).

[15]M. Hansen, *Constitution of Binary Alloys* (McGraw-Hill, New York, 1958); R. P. Elliot, *Constitution of Binary Alloys, 1st Supplement* (McGraw-Hill, New York, 1965); F. A. Shunk, *Constitution of Binary Alloys, 2nd Supplement* (McGraw-Hill, New York, 1969); W. G. Moffatt, *Constitution of Binary Alloys, 3rd Supplement* (McGraw-Hill, New York, 1983).

Journal of Non-Crystalline Solids 75 (1985) 149-160
North-Holland, Amsterdam

NEW CONCEPTS OF BONDING IN NONPERIODIC METALLIC SYSTEMS*

Mark H. McAdon and William A. Goddard III

Arthur Amos Noyes Laboratory of Chemical Physics,+
California Institute of Technology, Pasadena, California 91125

Using the generalized valence bond method, we have examined numerous Li atom clusters (up to 13 atoms). Our conclusion is that the optimum metallic bonding involves *singly-occupied* orbitals localized interstitially, e.g., in bond midpoints, triangular hollows, and tetrahedra. For Li_{13}^{+}, the low energy isomers have local five-fold symmetry axes (as in an icosahedron) but lead to low overall symmetry. The guiding principle is that the optimum structures (denoted OPTET) optimize the number of tetrahedral hollows while keeping the sharing of vertices below a threshold. These OPTET structures are significantly more stable than the high-symmetry icosahedral, hcp-like and fcc-like clusters. Speculations are given on the relevance of these results for amorphous metallic systems.

1. INTRODUCTION

The valence bond principles of structural chemistry[1], based on spin pairing of hybridized atomic orbitals localized on various atoms, lead to excellent rationalization of the geometries and bonding for nonmetallic molecules and solids; e.g., Si and Ge are tetrahedral in both crystalline and amorphous phases, Se and Te lead to helical chains for both crystalline and amorphous solids, As_4 is tetrahedral, etc. These simple valence bond ideas of nonmetallic systems have been confirmed by *ab initio* generalized valence bond (GVB) calculations[2,3] that lead directly to localized spin-paired atomic orbitals corresponding to various bond pairs. Valence bond principles have also proven valuable in understanding defects and surface reconstruction in nonmetallic solids such as the Si vacancy[4] and the GaAs surface[5].

This paper presents the qualitative principles of our new model of metallic bonding. These principles have led to the prediction of several low-energy (OPTET) isomers that (coincidentally?) have local five-fold symmetry axes and cannot lead to bulk solids with long range (periodic) order. GVB calculations confirm that these OPTET clusters are lower in energy than high symmetry icosahedral, fcc-like and hcp-like clusters. These principles may lead to new rationalizations and predictions concerning the geometric and electronic structures of defects and interfaces for metallic systems. In particular, these

*This work was partially supported by a grant from the National Science Foundation (No. DMR82-15650).
+Contribution No. 7221

principles may lead to new insights regarding how local structure and alloying may control formation of amorphous metallic systems.

2. RESULTS

In order to lay the foundation for developing these chemical concepts, we have used GVB approaches to examine the bonding in various one-dimensional (1D), two-dimensional (2D) and three-dimensional (3D) clusters of Li atoms[6]. In all cases, we discuss the many-electron states in which the electrons are all spin-paired (singlet). The electronic structures of the various clusters are given in terms of the singly-occupied GVB orbitals.

2.1 One-Dimensional Systems

The optimum GVB wavefunction of $Li_{(1D)}$ has a *singly-occupied orbital localized at each bond midpoint*. Typical bond orbitals are shown in Figure 1 for the Li_8 chain at an internuclear separation of R=3.1 Å [near the

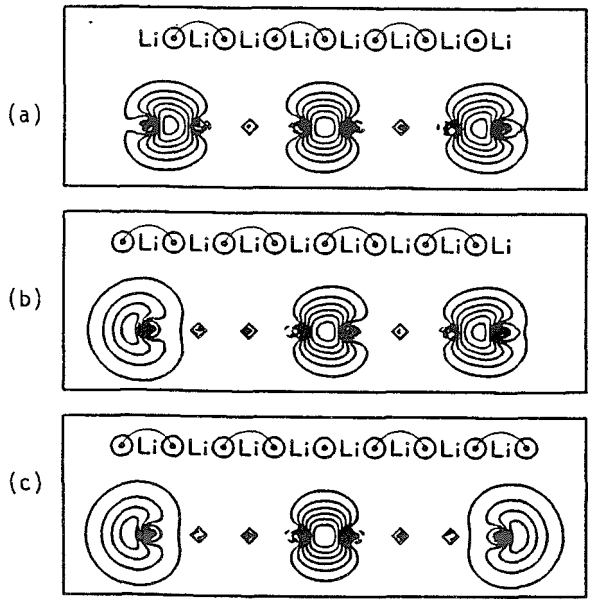

FIGURE 1
The GVB description of the (a) Li_8^+, (b) Li_8 and (c) Li_8^- chain clusters. The schematic diagrams show all of the singly-occupied GVB orbitals with the spin coupling for the principal resonance structure represented by connected dots. In each case orbitals at the middle and both ends are shown in contour plots. Contour spacings are at 0.015 a.u.

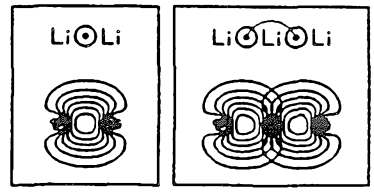

FIGURE 2
Contour orbital plots for the GVB orbitals of (a) Li_2^+ and (b) linear Li_3^+. Contour spacings are at 0.015 a.u. R = 3.1 Å.

equilibrium bond distance of $Li_{(1D)}$, R_e=3.14 Å [6]. For Li_8^+, Li_8 and Li_8^-, there are seven bond-localized orbitals (each very similar to the bond orbitals of Li_2^+ and linear Li_3^+ as shown in Figure 2) and zero, one or two "surface" orbitals. In the ground state, adjacent (singly-occupied) bond orbitals are spin-paired [leading to two equivalent resonance structures]; however, the overlap between paired bond orbitals is small (≈0.34; normal two-electron bonds have large overlaps, 0.7 to 0.8), so that even the higher spin states involve similar orbitals and strong bonding. Even the maximum spin state (e.g., triplet (S=1) for Li_3^+ or S=3.5 for Li_8^+) is bound strongly with respect to the separated atoms limit! Indeed the calculations lead to a vanishing singlet-triplet gap for $Li_{(1D)}$ [6].

2.2 Two-Dimensional Systems

Starting with the H_4 and Li_4 symmetric ring clusters (and considering just one of the two equivalent resonance structures), the optimum geometric distortion is expected to increase overlap of adjacent spin-paired orbitals while decreasing overlap of adjacent *nonpaired* orbitals. In square H_4, the orbitals are atom-centered, leading to an unstable rectangular distortion

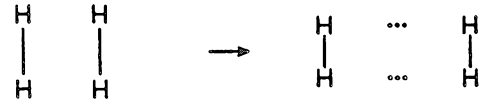

with no chemical bonding between the two H_2 fragments. For square Li_4, the orbitals are bond-centered, leading to a rhombic distortion

which is stable due to the one-electron bonding. Such distortions lower the energy of one resonance structure (and raise the energy of the other resonance structure) reducing the resonance energy substantially. Nevertheless, square Li_4 (θ = 90°) distorts to a rhombus (θ_{opt} = 57.3°)[7]. Similarly, hexagonal Li_6 (θ = 120°) distorts to a trigonal hexagon (θ_{opt} = 69.3°)[7]. Potential energy curves for these distortions are shown in Figure 3. Allowing similar distortions for $Li_{(1D)}$ results in a zig-zag chain (alternating 70° and 180° angles). The optimum planar structures for Li_4 and Li_6 both resemble planar close-packed clusters. As shown in Figure 4, the optimum orbitals for Li_6 are quite similar to those in $Li_{(1D)}$.

Examining larger two-dimensional close-packed arrays of Li atoms, we find the general result that interior regions tend to have orbitals localized at

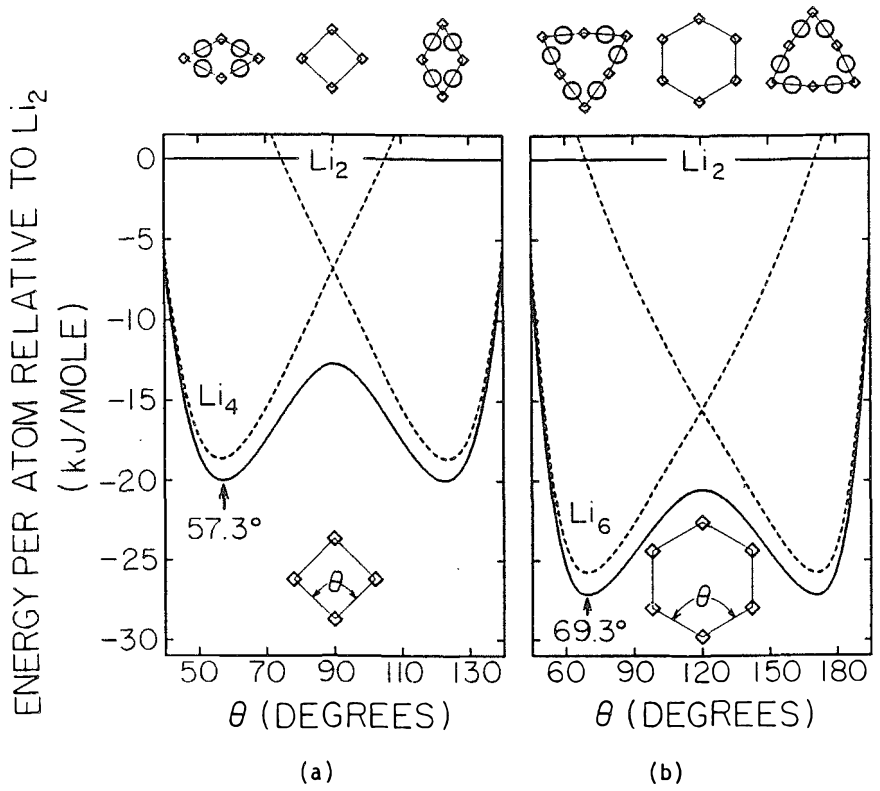

FIGURE 3.
Potential Energy curves for geometric distortions of the (a) Li_4 and (b) Li_6 clusters. Dashed curves represent the separate resonance structures, while solid lines show the energy including all possible resonance structures. The energy per atom is given relative to Li_2 (at equilibrium). Diagrams above the plots show the cluster geometries at various angles (θ) where squares mark the atomic positions and circles mark the positions of the orbitals.

the *centers of equilateral triangles* while *surface (edge) regions* have orbitals localized at *bond midpoints*. Extrapolating to the infinite two-dimensional (close-packed) system [$Li_{(2D)}$] leads to the description in Figure 5a, where alternate pairs of triangular hollows have spin-paired singly-occupied orbitals and adjacent such pairs are empty[9].

This GVB wavefunction for $Li_{(2D)}$ would lead to metallic character. Half of the triangular hollows are empty, providing means for conduction. The structure shown in Figure 5a is only one of an infinite number of low-lying resonance structures, another of which is illustrated in Figure 5b.

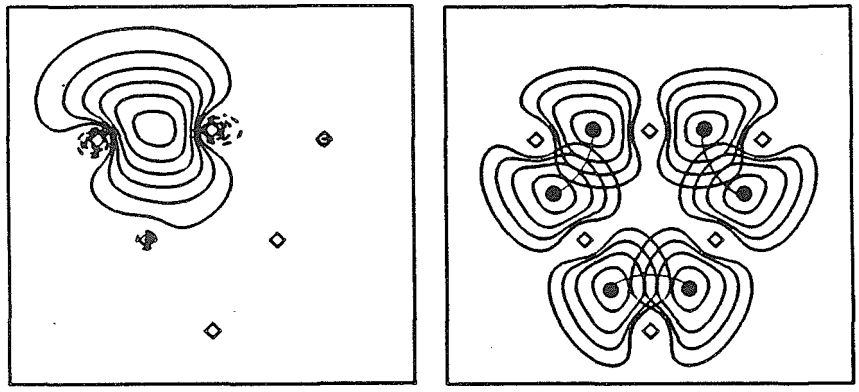

FIGURE 4
GVB orbitals for the planar Li_6 cluster. Solid and dashed lines show positive and negative orbital amplitudes, respectively. (a) Shows one of the six equivalent singly-occupied orbitals (0.015 contour spacings). (b) Shows contours $\geq$ 0.045 a.u. for all six orbitals. The atomic positions are marked by squares. The connected dots represent the dominant spin pairing.

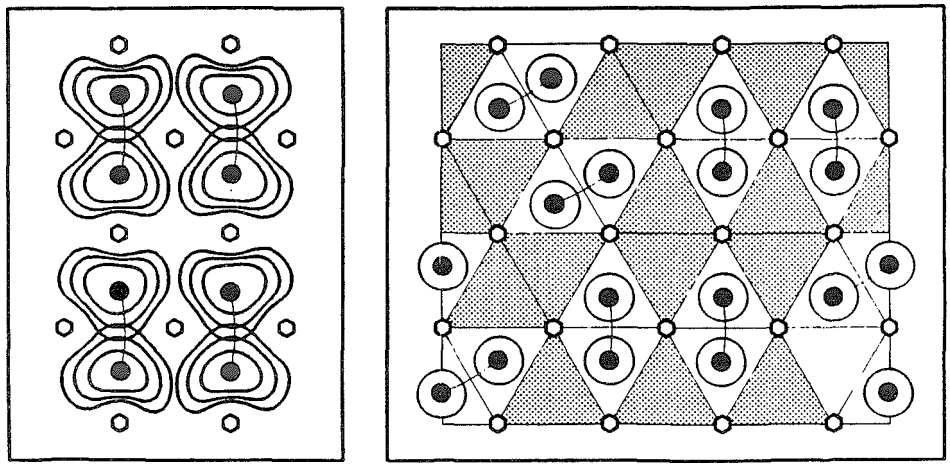

FIGURE 5
The GVB description of $Li_{(2D)}$. (a) Shows contours $\geq$ 0.060 a.u. for the planar Li_{12}^{4+} cluster. (b) shows an alternate resonance structure for $Li_{(2D)}$ where connected circles represent the singly-occupied orbitals and shaded rhombi represent empty hollows.

2.3 Three-Dimensional Systems

First we consider several high symmetry clusters consisting of one central (bulk) atom and 12 surface atoms: the icosahedral (I_h), face-centered cubic (fcc) and hexagonal close-packed (hcp) Li_{13}^+ clusters. In each case we find that the orbitals prefer to be singly-occupied and centered at tetrahedral interstices.

Of these three clusters, I_h is lowest in energy. The I_h ground state involves orbitals localized at the centers of 12 of the 20 triangular faces and spin-paired in rhombi (0.63 overlap) just as for the bulk atoms of $Li_{(2D)}$.

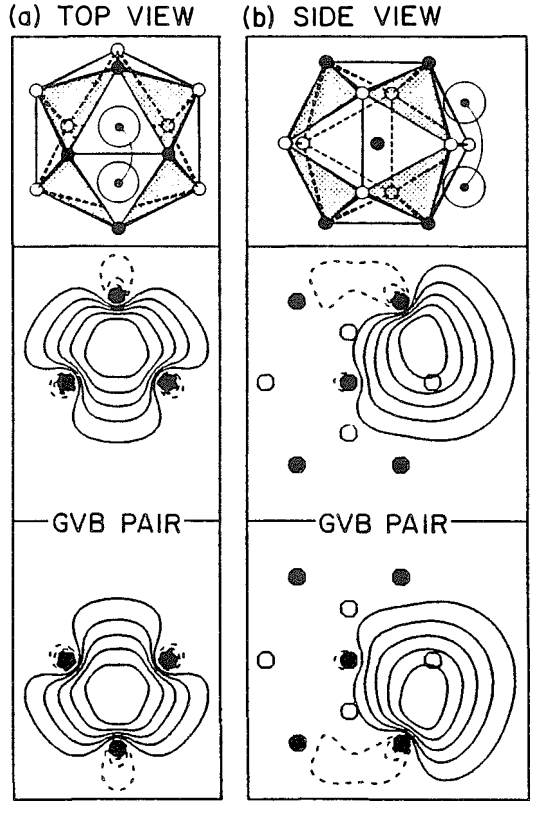

FIGURE 6
GVB orbitals for one of the five equivalent primary resonance structures of icosahedral Li_{13}^+. The atoms in the plane are marked by solid circles while atoms above and below the plane are marked by open circles. Connected dots represent the spin-paired electrons. Only one of the six equivalent bond pairs is shown (0.015 a.u. contour increments). Solid and dashed lines show positive and negative orbital amplitudes, respectively. Shaded triangular faces do not contain orbitals.

The four triangular faces adjacent to a spin-paired rhombus are empty (to avoid repulsive interactions between unpaired orbitals), as indicated in Figure 6.

The fcc and hcp clusters lie 0.26 and 0.57 eV higher than I_h, respectively. Both fcc and hcp have only eight tetrahedra, thus, some of the tetrahedra have two spin-paired orbitals (on opposite faces). For fcc, the tetrahedra are edge-sharing, and all twelve electrons are accomodated by the tetrahedra. For hcp, six of the tetrahedra share one face with an adjacent tetrahedron, and ten of the twelve electrons are accomodated by tetrahedra, leaving two remaining electrons that end up along surface sites (bond midpoints) that do *not* border a tetrahedron.

In order to compare the energies of planar and 3D clusters, we solved for the ground state electronic structures of several close-packed planar Li_{13}^+ clusters. The lowest energy planar structure (Figure 7) is 0.18 eV *lower* than I_h! Apparantly, with such small clusters, surface effects are quite large so that planar clusters (which lead to an increased number of internal sites) are quite competitive.

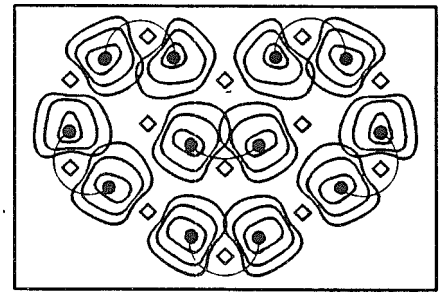

FIGURE 7
GVB orbitals for planar close-packed Li_{13}^+. Only contours $\geq$ 0.060 a.u. are shown (0.015 a.u. spacings). Squares mark the atomic positions. The dominant spin pairing is shown by the connected dots.

The above results suggest that the *optimum structures* of small clusters should *maximize* the number of *tetrahedra* and the number of *internal sites*. The icosahedron has the maximum number of tetrahedra (20), however, these 20 tetrahedra all share the *same* central bulk atom. Guided by a set of rules (See Section 3) based on the I_h, fcc and hcp results, we considered alternative arrangements of 13 atoms that maximize the number of tetrahedra while minimizing the number of tetrahedra shared by any given atom. This led us to predict

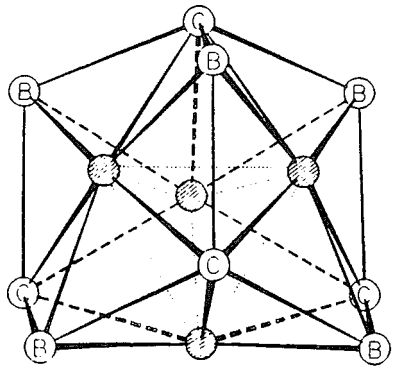

(I)

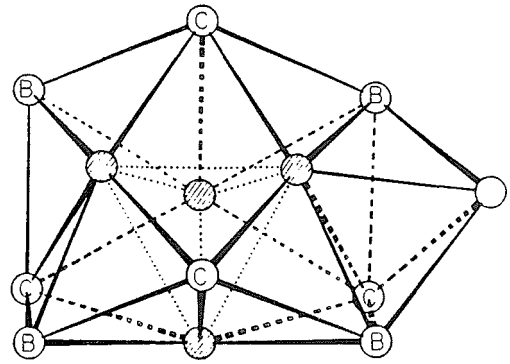

(II)

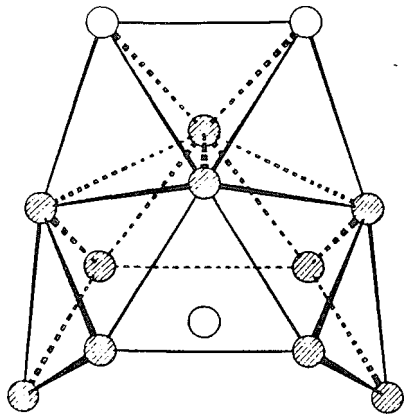

(III)

FIGURE 8
Three low-lying OPTET Li_{13}^+ isomers. Cluster (I) consists of a central tetrahedron (shaded atoms, dotted lines), four capping atoms (C) and five bridging atoms (B). Cluster (II) differs from (I) in the position of only one atom. The shaded atoms of cluster (III) form a portion of the icosahedral surface. All three clusters have multiple local five-fold symmetry axes. Clusters (I), (II), and (III) have point group symmetries C_{2v}, C_s and C_{2v} respectively.

several new Li_{13}^+ clusters [(I), (II) and (III) as shown in Figure 8], each lower in energy than I_h. The best, the tetra-capped penta-bridged tetrahedron (I), has an energy 0.58 lower than the icosahedron! The Li_{13}^+ isomers in Figure 8 all contain 15 tetrahedra. Structures (I) and (II) differ in the location of the thirteenth atom. In (I), the thirteenth atom bridges the central tetrahedron and in (II) the thirteenth atom occupies an exterior position. Cluster (III) was obtained by removing two adjacent atoms from the surface of the icosahedron and capping surface sites on the opposite side of the cluster (allowing all of the atoms to relax). Clusters (II) and (III) are only 0.08 and 0.19 eV higher than (I) respectively.

In summary, the relative energies of the various Li_{13}^+ clusters are: (I), 0.00 eV; (II), 0.08 eV; (III), 0.19 eV; planar, 0.40 eV; I_h, 0.58 eV; fcc, 0.84 eV; hcp, 1.15 eV.

3. DISCUSSION

Based on these results for the high symmetry Li_{13}^{+} clusters we derived the following rules for 3D structures[6].

α) Orbitals (each with one electron) are localized in different tetrahedral hollows where possible.

β) If necessary, two orbitals may be placed in one tetrahedron (localized on opposite faces or edges) but they must be spin-paired.

γ) However, no more than three electrons may be distributed between a pair of *edge-shared* tetrahedra.

δ) No more than two electrons may be distributed between a pair of *face-shared* tetrahedra, and these must be spin-paired (singlet).

ε) Additional electrons must be in surface orbitals at edge or face sites that do not share edges with occupied tetrahedra.

ζ) It is unfavorable to occupy more than four tetrahedra (or pairs of tetrahedra) sharing one central atom.

Rule ζ is related to the fact that the low-lying valence orbitals of Li are *2s* and *2p*, so that hybridization can lead to only four (linearly independent) orbitals associated with one atom. This also reduces the (Pauli principle) repulsion between orbitals that are *not* spin-paired (this becomes increasingly repulsive when the orbitals are close). The above principles are consistent with the relative calculated energies since I_h is lowest, with fcc and hcp 0.26 and 0.57 eV higher, respectively.

We have used these rules to predict the OPTET (optimum tetrahedral) clusters presented in Figure 8. It is interesting to note that the OPTET clusters generally posess local fivefold symmetry axes (as does I_h). Exact five-fold axes are not consistent with three-dimensional space groups and hence these OPTET arrangements which optimize the bonding in clusters are inconsistent with crystalline symmetry (long range order). It is interesting to speculate whether this OPTET type of local bonding with its penchant for local five-fold symmetry axes may be the driving force for forming amorphous structures in metallic systems[10].

These considerations suggest that there may be several regimes of structure for metal clusters. The smallest clusters either form planar structures (as in Li_4 and Li_6) or have very low energy planar configurations. For intermediate size, the OPTET structures are stable [e.g., Li_8[6], Li_{13}^{+}, and probably extending well into the 20's], while for very large clusters, structures approaching bulk character (hcp, fcc, bcc) may be stable.

The larger OPTET clusters are derived from adding atoms to the surface of the smaller OPTET clusters. This involves adding atoms to concave sites,

forming at least two new tetrahedra for each atom added. For larger clusters, the number of tetrahedra shared by a given atom will tend to increase as the ratio of empty to occupied tetrahedra increases. We expect there may be many $Li_{(n)}$ OPTET isomers lying within 0.1 eV of the optimum structure for larger values of n (where n is the number of atoms), and hence a greatly increasing number of different clusters will be in thermal equilibrium for larger n. Some of these clusters may be suitable nuclei for forming crystalline systems while others may prefer growth into amorphous solids. The relative energies and numbers of the different types of clusters may thus play an important role in controlling the kinetics for forming crystalline vs. amorphous systems.

3.1 Force Fields

Ab initio quantum chemical calculations of the quality descirbed above are limited to a relatively small number of atoms (less than 100). In order to simulate the properties of a small portion of a metal we need to examine structures and kinetics for far larger systems (at least 1000 atoms). Thus we believe that it is essential to develop force fields that accurately reflect the local bonding effects of metallic systems. The above studies suggest that these force fields cannot be described merely in terms of nuclear positions but must also involve the positions of the localized (correlated) electrons. Consequently we have been using our cluster results to develop force fields involving both nuclear and electronic coordinates[6]. These force fields involve such terms as atom - electon - atom bend and atom - electron - atom assymetric stretch, etc. Such force fields (involving multibody terms) may well provide a means for simulating amorphous metallic systems.

4. CONCLUSIONS

We believe that these ideas involving interstitially localized singly-occupied orbitals will form a useful starting point in developing valence bond ideas for predicting geometries, electronic structures, and properties of metallic clusters, and for describing localized phenomena in solids, such as defects or interfaces. They may provide useful conceptual ideas for predicting the chemistry and catalytic properties of such systems and for predicting the factors controlling stabilization of amorphous systems.

REFERENCES

1) L. Pauling, The Nature of the Chemical Bond, 3rd edition (Cornell University Press, Ithaca, New York, 1960).

2) W. A. Goddard III, T. H. Dunning, Jr., W. J. Hunt, and P. J. Hay, Accts. Chem. Res. 6 (1973) 368.

3) W. A. Goddard III and L. B. Harding, Ann. Rev. Phys. Chem. 29 (1978) 363.

4) G. T. Surratt and W. A. Goddard III, Solid State Commun. 22 (1977) 413 and Phys. Rev. B18 (1978) 2831.

5) J. J. Barton, W. A. Goddard III and T. C. McGill, J. Vac. Sci. Techonol. 16 (1979) 1178; C. A. Swarts, T. C. McGill and W. A. Goddard III, Surf. Sci. 110 (1981) 400; A. Redondo and W. A. Goddard III, J. Vac. Sci. Technol. 21 (1982) 344; A. Redondo, W. A. Goddard III and T. C. McGill, Surf. Sci. 132 (1983) 49.

6) M. H. McAdon and W. A. Goddard III, unpublished.

7) Our results for Li_4 are consistent with those of Beckmann *et al.* (See Ref. 8) who describe Li_4 *in terms of a pseudo-Jahn-Teller description. However, the pseudo-Jahn-Teller description does not predict the analogous distortion for the* Li_6 *ring.*

8) H.-O. Beckmann, J. Koutecký and V. Bonačic-Koutecký, J. Chem. Phys. 73 (1980) 5182; H.-O. Beckmann, J. Koutecký, P. Botschwina and W. Meyer, Chem. Phys. Lett. 67 (1979) 119.

9) These orbitals are based on GVB calculations using a model Li_{12}^{4+} cluster, composed of four unit cells with at total of eight valence electrons (the eight edge atoms each contribute half an electron to the unit cell).

10) C. L. Henley, Crystals and Quasi-Crystals in the Aluminum - Transition Metal System, this volume; N. D. Mermin and S. M. Troian, Phys. Rev. Lett. 54 (1985) 1524.

Reprinted from The Journal of Physical Chemistry, 1987, 91, 2607.

Generalized Valence Bond Studies of Metallic Bonding: Naked Clusters and Applications to Bulk Metals

Mark H. McAdon[†] and William A. Goddard III*

Arthur Amos Noyes Laboratory of Chemical Physics,[‡] California Institute of Technology, Pasadena, California 91125 *(Received: June 17, 1986)*

Using the generalized valence bond (GVB) method, we have examined the bonding in numerous small clusters of Li atoms (Li_n and Li_n^+, $n \leq 13$). Our conclusion is that the optimum bonding involves interstitially localized *singly occupied* orbitals, e.g., (1) bond-centered orbitals for one-dimensional clusters (e.g., rings such as Li_4, Li_6, Li_8, and Li_{10} and linear chains such as Li_3^+, Cu_3^+, Li_8^+, Li_8, Li_8^-, and Li_{13}^+), (2) equilateral-triangle-centered orbitals for planar close-packed clusters (e.g., Li_{10}, Li_{12}^{4+}, and Li_{13}^+), and (3) tetrahedron-centered orbitals for three-dimensional clusters (examples here include three high-symmetry [icosahedral (I_h), face-centered cubic (fcc), and hexagonal close-packed (hcp)] Li_{13}^+ structures and three low symmetry [γ-brass-like] Li_{13}^+ structures. Of the three high symmetry Li_{13}^+ clusters, I_h has the lowest energy while total energies for fcc and hcp are 0.26 and 0.56 eV higher, respectively. GVB wave functions for these three clusters suggest a set of rules predicting structures even more stable than the icosahedron. These lower energy structures [denoted as OPTET (optimum tetrahedral)] maximize the number of tetrahedra under the restrictions of the rules (e.g. minimizing the number of occupied tetrahedra sharing corners) and lead to relatively low symmetry, e.g. C_{2v}, C_s. These OPTET clusters coincide with truncations of the γ-brass structure. The lowest energy Li_{13}^+ OPTET cluster [γ-(4,4,5), C_{2v}] has a total energy 0.58 eV lower than that of the icosahedron. Suggestions are given on the relevance of these results for stability and reactivity of small clusters and on the extension of these ideas to infinite systems.

I. Introduction

The valence bond (VB) principles of structural chemistry,[1] based on spin pairing of hybridized atomic orbitals on various atoms, lead to excellent rationalization of the geometries and bonding for nonmetallic molecules and solids; e.g., bulk Si and Ge are tetrahedrally coordinated, Se and Te have helical chains in their solid forms, the As_4 molecule has a tetrahedron structure with a single bond along each edge, etc. These simple VB ideas of nonmetallic systems have been confirmed by ab initio generalized valence bond (GVB) calculations[2] that lead directly to localized spin-paired atomic orbitals corresponding to various bond pairs. Valence bond principles have also proven valuable in understanding defects and surface reconstruction in nonmetallic solids, e.g. the Si vacancy[3] and the GaAs(110) surface.[4]

For metallic systems, there has not been an analogous set of simple principles to predict a priori the optimum geometries and structures of clusters, defects, or interfaces. In order to lay the foundation for developing chemical concepts for *metallic* systems, we have employed GVB approaches to examine the bonding in various one-dimensional (1D),[5] two-dimensional (2D), and three-dimensional (3D) clusters of Li atoms. The results of this study have led directly to a new *generalized valence bond model of metallic bonding*[6,7] based on electrons localized in interstitial regions such as bond midpoints (1D clusters), triangular faces (2D clusters), and tetrahedral hollows (3D clusters). This model is

[†] A.R.C.S. Foundation Predoctoral Fellow, 1985–1986.
[‡] Contribution No. 7413.

(1) Pauling, L. *The Nature of the Chemical Bond*, 3rd ed.; Cornell University Press: Ithaca, New York, 1960.
(2) Goddard III, W. A.; Dunning, Jr., T. H.; Hunt, W. J.; Hay, P. J. *Acc. Chem. Res.* **1973**, *6*, 368. Goddard III, W. A.; Harding, L. B. *Annu. Rev. Phys. Chem.* **1978**, *29*, 363.
(3) Surratt, G. T.; Goddard III, W. A. *Solid State Commun.* **1977**, *22*, 413. *Phys. Rev. B* **1978**, *18*, 2831.
(4) Barton, J. J.; Goddard III, W. A.; McGill, T. C. *J. Vac. Sci. Technol.* **1979**, *16*, 1178. Swarts, C. A.; McGill, T. C.; Goddard III, W. A. *Surf. Sci.* **1981**, *110*, 400.
(5) McAdon, M. H.; Goddard III, W. A., unpublished results.
(6) McAdon, M. H.; Goddard III, W. A. *Phys. Rev. Lett.* **1985**, *55*, 2563.
(7) McAdon, M. H.; Goddard III, W. A. *J. Non-Cryst. Solids* **1985**, *75*, 149.

0022-3654/87/2091-2607$01.50/0

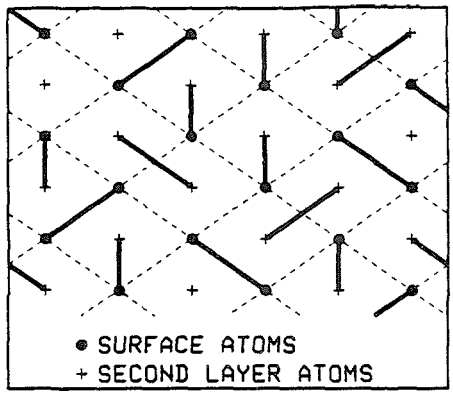

Figure 1. The simple VB description of metals [for the body-centered cubic Li(110) surface]. Thin lines connect nearest-neighbor atoms at the surface. Thick lines represent two-center, two-electron covalent bonds for one of numerous simple VB resonance structures.

summarized by a simple set of rules (see section IV) based on singly occupied valence electron orbitals centered in tetrahedral hollows.

We have used these rules to predict the low-energy Li_{13}^+ isomers [denoted as OPTET (optimum tetrahedral)]. GVB calculations confirm that these OPTET structures are significantly more stable than the traditional high-symmetry 13-atom structures. The high-symmetry icosahedron, fcc-like and hcp-like structures have total energies higher than the best OPTET cluster [OPTET(I)] by 0.58, 0.84, and 1.14 eV, respectively. These OPTET isomers all have local fivefold symmetry axes which result from the efficient packing of tetrahedra. Two of the three OPTET clusters (I and II) also clearly coincide with truncations of the γ-brass structure. Thus, we also refer to these two OPTET isomers as γ-brass clusters. The correspondence of the third structure to a truncation of γ-brass is rather subtle; however, OPTET(III) is more clearly based on a modification of the icosahedron.

We believe that these principles should prove useful in rationalizing and predicting the geometric and electronic structures of such localized phenomena as defects, interfaces, and chemisorbed species for metallic systems. We have applied the principles to bulk close-packed metals and find that they are consistent with known solid solubilities and alloy structures. The OPTET clusters could also form a basis for certain classes of amorphous metals,[7] since the exact fivefold symmetry axes favored by OPTET cannot lead to solids with long-range (periodic) order. Thus the principles presented here may lead to new insights regarding how local structure and alloying may control formation of amorphous metallic systems.

Section II presents further background material. Results for the various clusters are given in section III and details of the calculations are given in the Appendix. Extension of the rules to bulk metals is given in section IV.

II. The GVB Model

The *simple* VB description of metals[1,8] involves two-center, two-electron covalent bonds between adjacent atoms (Figure 1). Since metallic systems have too few electrons and are too highly coordinated to simultaneously allow one bond between each pair of adjacent atoms, the simple VB description involves numerous equivalent such bonding or resonance structures superimposed to describe the many-electron (total) wave function.[1,8,9] This simple extension of the VB concepts so useful for nonmetallic systems has not led to a very useful description of metallic systems.

A hint of the problem is seen from a simple estimate of the cohesive energy of lithium. The total cohesive energy or atomization energy of lithium would be estimated by adding all of the Li–Li bond energies to obtain the total bond energy for one bonding structure (resonance configuration) and then adding the additional stabilization (resonance energy) due to the interaction of all the resonance structures.[9] The effective bond energy for each Li–Li bond can be estimated from the dissociation energy[10] of the Li_2 molecule into free atoms [$Li_{(g)}$]

$$^1/_2Li_2 \rightarrow Li_g \qquad \Delta E = 0.53 \text{ eV/atom} \qquad (1)$$

This can be compared with the experimental bulk atomization energy[11] of the solid [Li_s]

$$Li_s \rightarrow Li_g \qquad \Delta E = 1.63 \text{ eV/atom} \qquad (2)$$

Thus, in order to explain the cohesive energy of the solid, the resonance energy would have to be 1.10 eV/atom, or over twice the intrinsic bond energy! Such a large resonance energy is clearly implausible.

An alternative to such VB descriptions is suggested by the following observations.

(1) The bond strength for the one-electron bond (Figure 2a) of the Li_2^+ molecule (1.30 eV[12,13] or 1.30 *eV per valence electron*) is 80% of the cohesive energy (per bonding electron) for Li metal [and a factor of 2.45 greater than the bond strength (per bonding electron) of Li_2].

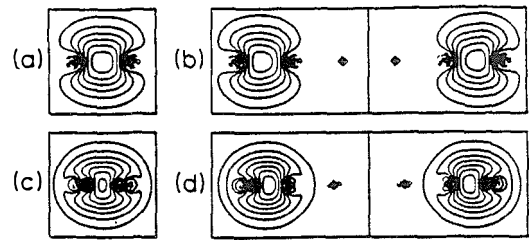

Figure 2. The optimum GVB valence orbitals for (a) Li_2^+, (b) linear Li_3^+, (c) Cu_2^+, and (d) linear Cu_3^+. Each orbital contains one electron. Two separate orbitals are shown for Li_3^+ (b, 0.21 overlap) and two separate orbitals are shown for Cu_3^+ (d, 0.40 overlap). The orbitals for Li_2^+ and linear Li_3^+ are shown for $R = 3.1$ Å. The orbitals for Cu_2^+ and linear Cu_3^+ are shown for $R = 2.556$ Å. All cases are drawn to equal scale (each box shows 6.2 Å width). In Figures 2 and 3 and in similar figures that follow, solid contours denote positive orbital amplitudes and dashed contours represent negative orbital amplitudes (for normalized singly occupied orbitals). Unless otherwise noted, the contours represent orbital amplitude increments of 0.015 au and squares mark the atomic positions.

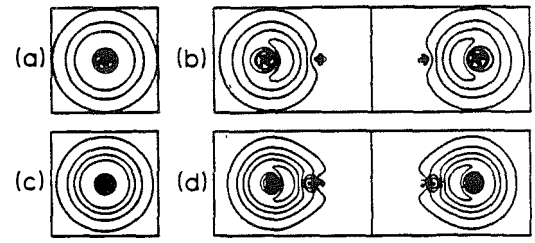

Figure 3. The optimum GVB valence orbitals for (a) Li atom, (b) Li_2, (c) Cu atom, and (d) Cu_2. Each orbital contains one electron. Two separate orbitals are shown for Li_2 (b, 0.58 overlap) and two separate orbitals are shown for Cu_2 (d, 0.62 overlap). The scales (and bond lengths for the dimers) are consistent with Figure 2.

(8) Pauling, L. *Proc. R. Soc. London, Ser. A* **1949**, *196*, 343.
(9) Feynman, R. P.; Leighton, R. B.; Sands, M. *The Feyman Lectures on Physics*; Addison-Wesley: Reading, MA, 1965.
(10) Verma, K. K.; Koch, M. E.; Stwalley, W. C. *J. Chem. Phys.* **1983**, *78*, 3614. In order to compare bond energies for the bulk metal and for Li_2, the total bond energy of Li_2, 1.06 eV/molecule ($Li_2 \rightarrow 2Li$) is divided by 2, obtaining the per atom bond energy, 0.53 eV/atom.
(11) Huitgren, R.; Desai, P. D.; Hawkins, D. T.; Gleiser, M.; Kelley, K. K.; Wagman, D. D. *Selected Values of the Thermodynamic Properties of the Elements*; American Society for Metals: Metals Park, OH, 1973.
(12) Konowalow, D. D.; Rosenkrantz, M. E. *Chem. Phys. Lett.* **1979**, *61*, 489.
(13) Bernheim, R. A.; Gold, L. P.; Tipton, T. *J. Chem. Phys.* **1983**, *78*, 3635.

(2) The bonding in linear Li_3^+ involves two singly occupied orbitals,[14] one localized at each Li–Li bond midpoint (Figure 2b) with an overlap (0.214) much smaller than that of normal two-electron bonds. These singly occupied bond orbitals are very similar to the optimum orbital of Li_2^+ (Figure 2a), but quite different from the 2s orbital of Li atom (Figure 3a) and the optimum orbitals of Li_2 (Figure 3b) on which the simple VB model is based.

Based on these observations,[15] we suspected that the best simple description of extended Li systems is in terms of *singly occupied orbitals localized interstitially*. This led to the *generalized* valence bond studies reported herein on one-, two-, and three-dimensional lithium clusters that do indeed indicate that the bonding involves singly occupied orbitals localized in bond midpoints, triangular faces, and tetrahedral hollows. In addition, the valence orbitals for Cu atom, Cu_2 (Figure 3c–d), Cu_2^+, and linear Cu_3^+ (Figure 2c–d) are very similar to those for Li atom, Li_2 (Figure 3a–b), Li_2^+, and linear Li_3^+ (Figure 2a–b). [For these lithium systems, the optimum GVB orbitals are plotted for a bond length (R) of 3.10 Å, which is in the range of the experimental bond lengths (or nearest-neighbor distances) for Li_2^+ (3.113 ± 0.013 Å),[13] the close-packed form of Li_s (3.105 Å at 78 K)[16] and the body-centered-cubic form of Li_s (3.016 Å at 78 K).[16] For the Cu systems, R = 2.556 Å was chosen which corresponds to the value for face-centered-cubic Cu_s at 298 K. For Cu, we used an effective potential[17] while the Li calculations are all-electron ab initio (see the Appendix).] The similarity of the valence orbitals for the Cu and Li systems suggests that the results presented in this paper for lithium should also apply to the noble metals and the valence sp electrons of transition metals.

III. Results

In the generalized valence bond (GVB) description, each valence electron is allowed to be in a different orbital, where the orbitals are allowed full freedom with respect to localization, delocalization, hybridization, and overlap. The form of the GVB wave function[2,18] ensures that the Pauli principle and proper spin symmetry are obtained independent of the orbitals. Thus, GVB differs from Hartree–Fock type wave functions, where the proper spin symmetry is obtained only when down-spin orbitals and up-spin orbitals coincide. Details of the GVB wave functions are given in Appendix A. In this section, it is sufficient to understand that the GVB wave function provides the optimal one-electron picture.[2,18]

The orbitals are calculated self-consistently and the total wave function is thought of in terms of N electrons, each electron in its own optimum orbital (moving in the field due to the remaining $N-1$ electrons in their optimum orbitals). Thus, we use the terms electron and orbital interchangeably. In general, we find that the GVB orbitals tend to be well localized, leading to a natural classification in terms of "bulk" orbitals or "surface" orbitals. We find that the bulk orbitals tend to be centered in bond midpoints, triangular faces, and tetrahedral hollows for 1D, 2D, and 3D structures, respectively. Surface orbitals tend to be centered in surface triangular faces or bond midpoints for 3D structures, and in edge bond midpoints for 2D structures. For the linear chain clusters (1D), the surface orbitals tend to be at the ends of the chain, polarized away from the chain toward the vacuum.

In this paper we focus upon clusters of Li atoms. However, similar calculations on other alkali metals (Na, K, Rb, Cs, Fr) and on noble metals (Cu, Ag, Au) are expected to yield very similar results.

(14) Kahn, L. R.; Goddard III, W. A. *J. Chem. Phys.* **1972**, *56*, 2685.
(15) An early (unpublished) test of these ideas by T. H. Upton and W. A. Goddard III showed that the ground state of hexagonal Li_6 involves one valence electron localized at each bond midpoint.
(16) Donohue, J. *The Structure of the Elements*; Wiley: New York, 1974.
(17) Hay, P. J.; Wadt, W. R. *J. Chem. Phys.* **1985**, *82*, 270. The effective potential for Cu included the effects of the [Ar] shell, leaving eleven electrons to be treated explicitly ($3d^{10}4s^1$). It is fairly obvious that the second coefficient for the d–f potential should be −0.4621680 rather than the listed value of +0.4621680, and with this change we were able to reproduce the results listed by Hay and Wadt in Tables XIII–XIV of their paper.
(18) Goddard III, W. A. *Int. J. Quantum Chem.* **1970**, *IIIS*, 593. Goddard III, W. A.; Ladner, R. C. *J. Chem. Phys.* **1969**, *51*, 1073.

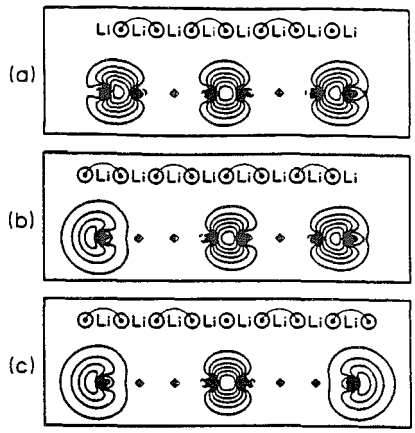

Figure 4. The GVB description of the (a) Li_8^+, (b) Li_8, and (c) Li_8^- chain clusters (R = 3.1 Å). The schematic diagrams show all of the singly occupied GVB orbitals with the spin coupling for the principal resonance structure represented by connected dots. In each case orbitals at the middle and both ends are shown in contour plots. Overlaps for adjacent spin-paired bond-centered orbitals are ≈0.34. Overlaps for diffuse surface orbitals spin paired to adjacent bond orbitals are ≈0.52.

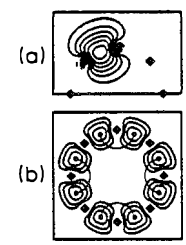

Figure 5. The GVB orbitals for one of the two primary resonance structures of the Li_8 ring cluster (R = 3.1 Å). Squares mark the atomic positions and dots joined by thin lines represent the electrons and spin coupling. (a) One singly occupied GVB orbital. (b) Contours ≥0.045 au for all eight GVB orbitals. Spin-paired orbitals have overlaps of 0.36.

A. One-Dimensional Clusters. The valence electronic structure of the infinitely long 1D Li chain [$Li_{(1D)}$] involves one electron localized at each bond midpoint, each electron forming a one-electron bond as in Li_2^+. This is shown for the Li_8 chain (Figure 4) and for the Li_8 ring (Figure 5), where the adjacent atom internuclear separation is R = 3.1 Å [near the equilibrium bond distance of R_e = 3.14 Å[5] for $Li_{(1D)}$]. The Li_8^+, Li_8, and Li_8^- chains have seven singly occupied bond orbitals in common, one centered at each of the seven bond midpoints, and zero, one, or two singly occupied "surface" orbitals. Each of the seven bond orbitals contains one electron and is very similar to the bond orbitals of Li_2^+ or linear Li_3^+. For the Li_8 ring, all eight valence electrons occupy bond midpoints.

In the lowest energy (primary) configurations, adjacent singly occupied orbitals are spin-paired [leading to two equivalent resonance structures for $Li_{(1D)}$]. The overlap between paired orbitals is small (≈0.34 for adjacent bond orbitals and ≈0.52 for a surface orbital paired to a bond orbital), whereas normal two-electron bonds have large overlaps of 0.7 to 0.8; thus, the bonding is dominated by the one-electron bonds, with two-electron spin-coupling effects somewhat less important.[5] The lowest energy many-electron states are all low spin. Nevertheless, higher spin states (including states with adjacent orbitals high-spin coupled) involve similar orbitals and also lead to strong bonding. [Indeed, even the maximum spin state (e.g., spin S = 4 for the Li_8 ring) is bound strongly with respect to the separated atoms limit![5]]

The orbitals in Figures 4 and 5 were optimized for the lowest energy resonance configuration (in some cases the orbitals are optimized for one of two equivalent lowest energy configurations). The Li_8^+ chain has one unpaired electron, leading to four primary

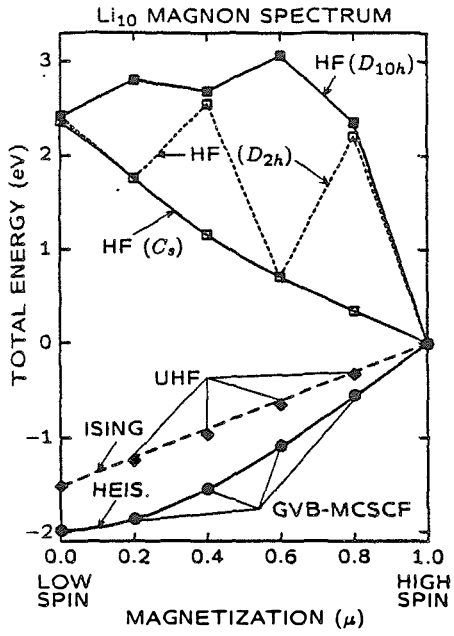

Figure 6. The total energy of Li_{10} (R = 3.1 Å) as a function of magnetization for HF, UHF, and GVB wave functions. The symmetry restrictions imposed on the HF orbitals are indicated in parentheses. Lines connecting the HF energies serve as a guide to the eye. The low-spin and high-spin states are fit to an Ising model for UHF (dashed line) and to a Heisenberg model for GVB (solid line). The root mean square errors for the fits of the Ising and Heisenberg models to the calculated energies of the four intermediate spin states are 0.044 and 0.010 eV for UHF and GVB, respectively.

resonance structures (one for each alternate bond midpoint), of which the two configurations lowest in energy have the unpaired electron at the bond midpoint adjacent to one of the surface atoms (see Figure 4a). The Li_8 chain has all electrons spin paired, but it leads to one surface orbital that can localize on either end of the chain, leading to two equivalent primary resonance structures (see Figure 4b). The unpaired electron of Li_8^- leads to five primary resonance configurations (see Figure 4c). Of these five configurations, the two configurations with one unpaired surface electron are substantially higher in total energy (≈0.25 eV) than the three configurations with one unpaired bond electron. This is because the overlap for a surface orbital paired to an adjacent bond orbital is ≈53% larger than the overlap between two adjacent spin-paired bond orbitals. The Li_8 ring (Figure 5) has two equivalent primary resonance configurations [as does $Li_{(1D)}$]. The full GVB wave function for each of these four systems is dominated by the primary spin couplings, but this wave function allows a full optimization of the spin coupling and thus includes resonance configurations where nonadjacent orbitals are spin paired (for the low-spin Li_8 ring, there are a total of 14 resonance configurations). This is analogous to the VB description of benzene, involving the two Kekulé (primary) and three Dewar (secondary) resonance structures.[1] In the full GVB wave function, the orbitals and spin coupling are optimized simultaneously, leading to orbitals that are similar to (but not identical with) those shown in Figures 4 and 5; e.g., the single-particle full GVB orbitals for the Li_8 ring are localized exactly in the center of the bond midpoints and have equal overlaps with each of the two adjacent orbitals, leading to a fully symmetrical (D_{8h}) description.

B. Electron Correlation Effects. At this point it is important to discuss the effects of electron correlation in describing the bonding in naked metal clusters. We shall illustrate these electron correlation effects with results for the magnon spectrum (spectrum of excited spin states) of the symmetrical Li_{10} ring calculated with the restricted Hartree–Fock (HF), unrestricted Hartree–Fock

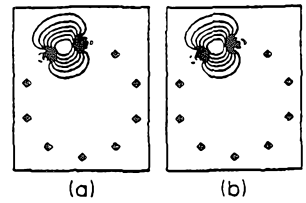

Figure 7. The Wannier orbital (ω_1) for the (a) high-spin state and (b) low-spin state of the Li_{10} ring. The scale and bond length (R = 3.1 Å) are consistent with Figures 4 and 5. In each case, the Wannier orbital is obtained from a Fourier transformation of ten D_{10h} symmetry orbitals and orbitals $\omega_2, \omega_3, \ldots, \omega_{10}$ are obtained by rotating ω_1.

(UHF), and generalized valence bond (GVB) wave functions. The energy of Li_{10} as a function of *magnetization*

$$\mu = \frac{2S}{n} \tag{3}$$

(n = 10) is shown in Figure 6 for various wave functions (Ψ), where S is the eigenvalue (or spin quantum number) of the total spin operator ($\hat{S}^2$)

$$\hat{S}^2\Psi_{n,S} = S(S+1)\hbar^2\Psi_{n,S} \tag{4}$$

e.g., S = 0, singlet; S = 1, triplet, etc. A thorough discussion of the results of these calculations will be presented elsewhere;[5] here, we shall simply touch upon the highlights. The general forms of these wave functions are discussed in greater detail in the Appendix.

The HF, UHF, and GVB wave functions are all identical for valence electron total high-spin (μ = 1) states. Here, the optimum canonical valence orbitals are consistent with D_{10h} symmetry; i.e., they are what is commonly referred to as molecular orbitals (MO). The valence electron configuration of the lowest energy high-spin state of Li_{10} is $a_{1g}(\uparrow)e_{1u}(\uparrow\uparrow)e_{2g}(\uparrow\uparrow)e_{3u}(\uparrow\uparrow)e_{4g}(\uparrow\uparrow)b_{2u}(\uparrow)$ where all valence orbitals are σ and each electron is up-spin ($\uparrow$ or α). This leads to an overall (many-electron) $^{11}B_{2u}$ state. The a_{1g} orbital has zero radial nodes (m = 0), the doubly degenerate $e_{\pi(g,u)}$ orbitals have m radial nodes, and the b_{2u} orbital has five radial nodes (m = 5). As expected, the MO one-electron energies increase roughly as m^2, where m is the number of radial nodes. The $^{11}B_{2u}$ state of Li_{10} is strongly bound, with a total bond energy of 2.63 eV with respect to separated atoms. Extrapolating the results for various Li_n rings and chains to infinite n leads to $Li_{(1D)}$ where the lowest energy high-spin state is bound with respect to separated Li atoms by 0.29 eV/atom.[5]

The bonding in high-spin Li_{10} is due to high-spin coupled one-electron bond orbitals. Each MO in this wave function is composed of linear combinations of the ten localized bond-centered functions, one of which is shown in Figure 7a. Clearly, the orbital obtained from the high-spin state shown in Figure 7a is quite similar to the orbitals obtained from low-spin states shown in Figures 4 and 5. The Li 2p atomic functions (f_{2p}) are of vital importance in forming these one-electron bonds. The Li 2p functions can be split into three groups: $p\pi_\perp$ having their nodes in the plane of the ring, $p\pi_\parallel$ pointing radially outward from the ring (and becoming π orbitals in the limit as $n \to \infty$), and $p\sigma$, tangent to the ring and pointing at adjacent atoms. Each localized bond orbital (ω_i) as shown in Figure 7a would be referred to in the solid-state literature as a *Wannier orbital*[19] and for Li_{10} the ω_i are composed of roughly half 2s character and roughly half 2pσ character, e.g.

$$\omega_i \approx f_{2s,a} + f_{2s,b} + f_{2p\sigma,a} - f_{2p\sigma,b} \tag{5}$$

where a and b signify two adjacent centers (recall that the bonding combination of 2pσ orbitals is out-of-phase). The ω_i also contain contributions due to 2s and 2p orbitals on nonadjacent atoms, but these contributions are quite small. The 2pσ orbitals are necessary to maintain the orthogonality of the adjacent high-spin orbitals,

(19) Wannier, G. *Phys. Rev.* **1937**, *52*, 191.

e.g., the combinations $f_{2s,a} + f_{2p,a}$ and $f_{2s,a} - f_{2p,a}$ are orthogonal. Hence the a_{1g} orbital is simply the plus or bonding combination of all ten localized bond-centered orbitals and has no 2p character since the 2p coefficients of the ω_i are out-of-phase. Likewise, the b_{2u} orbital is derived from the antibonding combination of the ten localized bond-centered orbitals and has no 2s character since the 2s coefficients of the ω_i are in-phase.

The b_{2u} orbital is crucial to the bonding of the high-spin Li_{10} ring. The $^{11}B_{1u}$ excited high-spin state of the Li_{10} ring obtained by the elementary excitation $b_{1u} \leftarrow b_{2u}$ is totally repulsive at the HF level for all internuclear separations. Both the b_{1u} and b_{2u} orbitals are σ with respect to the plane of the ring and have five radial nodes ($m = 5$). However, the b_{1u} orbital is composed of the antibonding combination of 2s functions while the b_{2u} orbital is composed of the bonding combination of $2p\sigma$ functions. It is important to note here that theories such as the jellium model[20] and the Hückel model[21] would fail in distinguishing between the b_{1u} and b_{2u} orbitals (and hence the $^{11}B_{1u}$ and $^{11}B_{2u}$ states).

Often single-determinant wave functions are used to describe the electronic states of extended systems. As discussed below, there are two general approaches: (1) UHF in which no restrictions are made upon the orbitals, often leading to total (many-electron) wave functions that are *not* eigenfunctions of $\hat{S}^2$ (and often do not have the proper spatial symmetry), and (2) HF in which spin and/or spatial restrictions are made in order to ensure that the total wave function has the correct spin and/or spatial symmetry. Although all methods (GVB, HF, UHF) are equivalent for the high-spin case, we find that neither UHF nor HF gives a correct description for other spin states.

The first point to emphasize for HF (and UHF) is that the optimum canonical orbitals are *not* always consistent with the symmetry of the molecule.

For all spins of Li_{10} other than $S = 5$, HF energies calculated with symmetry-adapted orbitals [orbitals optimized under the *restriction* that they transform according to the irreducible representations of D_{10h}] are significantly higher than those with the optimum orbitals (of C_s symmetry), as shown in Figure 6. Upon reducing the symmetry restriction to D_{2h} (or C_i), half of the spin states are still higher in energy than the results using C_s symmetry. This phenomenon of symmetry breaking is often described for bulk systems in terms of *charge density waves*[22,23] (HF) or *spin density waves* (UHF) and for Li_{10} derives from a fundamental inconsistency in the use of single Slater determinant wave functions. A single determinant wave function containing doubly occupied orbitals forces ionic character into the wave function, which is in turn deleterious to the energy. For Li_{10}, the fraction of ionic character in the HF wave function decreases (and hence the total energy decreases) if the orbitals are allowed to localize even though this lowers the symmetry.[5] Allowing for localization, the amount of ionic character (and thus the total energy) of the HF wave function increases monotonically with decreasing magnetization.

The UHF wave function avoids doubly occupied orbitals (and thus avoids ionic character), but, in the process, the orbitals tend to localize (i.e., break symmetry) resulting in spin density waves for all states of Li_{10} other than the $\mu = 1$ state. The UHF wave function is an eigenfunction of the spin projection operator ($\hat{S}_Z$)

$$\hat{S}_Z \Psi_n^{UHF}(M_S) = M_S \hbar \Psi_n^{UHF}(M_S) \qquad (6)$$

where M_S is simply the half difference between the number of up-spin (α) and the number of down-spin (β) electrons. The UHF wave function with spin projection M_S contains a mixture of spins from $S = |M_S|$ to $S = n/2$ and thus is not an eigenfunction of the $\hat{S}^2$ operator (4) [we follow the standard convention for UHF of associating $|M_S|$ with S in defining μ in eq 3 and in Figure 6]. The dependence of the UHF total energies on μ is in good agreement with a one-dimensional nearest-neighbor Ising model (IM)[5] which leads to a linear dependence of the total energy on μ with a slope of nJ where J is the effective nearest-neighbor exchange energy. The slope of the line through the low-spin and high-spin UHF energies leads to the value $J^{IM} = -0.1514$ eV.

Both the UHF and GVB many-electron wave functions for Li_{10} are based on ten valence orbitals; however, the GVB wave function is an eigenfunction of the $\hat{S}^2$ operator (4) while the UHF wave function is not. The GVB calculations presented here include all possible covalent and ionic configurations and thus are the most complete for each magnetization, corresponding to the best possible wave function for Li_{10} involving ten orbitals. For all spin states, these ten GVB orbitals can be taken as D_{10h} symmetry-restricted orbitals, unlike the situation for HF or UHF. These ten GVB orbitals can be transformed to give ten Wannier orbitals; indeed the GVB low-spin Wannier orbital (Figure 7b) is virtually indistinguishable from the high-spin Wannier orbital (Figure 7a). Hence, all of the spin states calculated with the GVB wave function are consistent with the D_{10h} symmetry, leading to many-electron states with symmetries $^{11}B_{2u}$, $^{9}A_{1g}$, $^{7}B_{2u}$, $^{5}A_{1g}$, $^{3}B_{2u}$, and $^{1}A_{1g}$. As a result, the GVB wave functions do not contain charge density or spin density waves for any of these states of Li_{10}. The GVB results lead to a monotonic increase in the energy with increasing magnetization, with zero slope at $\mu = 0$, suggesting that the singlet–triplet splitting approaches zero as n approaches infinity.[24] We find that for Li_{10} the GVB spin spectrum is accurately described in terms of a nearest-neighbor Heisenberg model (HM),[5,24] where J is chosen to match the energy difference between the $\mu = 0$ and $\mu = 1$ states, leading to a root mean square error of 0.012 eV for the four remaining spin states. For Li_{10}, this leads to $J^{HM} = -0.1415$ eV (in reasonable agreement with the Ising value $J^{IM} = -0.1514$ eV). This excellent agreement of the GVB calculations with the Heisenberg model is shown in Figure 6.

The HF wave function (C_s orbitals) contains charge density waves for the low-spin state of the Li_{10} ring cluster. The low-spin Li_{10} UHF wave function is characterized by spin density waves although it is completely free of charge density waves. The low-spin Li_{10} GVB wave function is completely free of both charge density and spin density waves.

The Li_{10} ring is stable with respect to dissociation into Li_2 molecules

$$^1/_{10}Li_{10} \rightarrow {}^1/_2Li_2 \qquad (7)$$

by 0.243 eV/atom for the GVB wave function, 22% of the difference in stability between bulk Li and Li_2 [eq 1 and 2]. The low-spin HF wave function contains so much unfavorable ionic character that it predicts the Li_{10} ring to be *unstable* with respect to dissociation into dimers (7) by 0.054 eV/atom. The UHF results overestimate the stability of Li_{10} with respect to Li_2 dimers, giving 0.312 eV/atom. This is because the UHF wave function leads to much larger spin contamination errors for Li_2 than for Li_{10}, a result that is expected since the high-spin state is bound for Li_{10} but highly repulsive for Li_2. The stability of Li_{10} with respect to atoms is 0.47 eV greater for GVB than for UHF (see Figure 6).

In summary, with no restrictions on symmetry (denoted as C_s in Figure 6), HF, UHF, and GVB all lead to monotonic variations in energy vs. spin. UHF agrees with GVB in favoring low spin, while HF favors high spin. Thus, the HF description of the magnon spectrum is in serious error, e.g., HF leads to a ferromagnetic (high-spin) ground state and charge density waves for all other spin states. This must not be taken lightly, since the HF, jellium,[20] and Hückel[21] models are all based on molecular orbital theory.

The UHF wave function gives the correct antiferromagnetic ground state but with spin density waves for the low and intermediate spin states. The UHF spectrum of spin states is well described in terms of an Ising Hamiltonian, but leads to results

(20) Cleland, A. N.; Cohen, M. L. *Solid State Commun.* **1985**, *55*, 35. Clemenger, K. *Phys. Rev. B* **1985**, *32*, 1359.

(21) Wang, Y.; George, T. F.; Lindsay, D. M.; Beri, A. C.; unpublished results. Lindsay, D. M.; Wang, Y.; George, T. F.; unpublished results.

(22) Overhauser, A. W. In *Highlights in Condensed Matter Theory; International School of Physics "Enrico Fermi"*, Course 89, Bassani, F.; Fumi, F.; Tosi, M. P.; Eds.; North Holland: Amsterdam, 1985; p 194. Overhauser, A. W. *Adv. Phys.* **1978**, *27*, 343.

(23) Giebultowicz, T. M.; Overhauser, A. W.; Werner, S. A. *Phys. Rev. Lett.* **1986**, *56*, 1485.

(24) Orbach, R. *Phys. Rev.* **1958**, *115*, 1181.

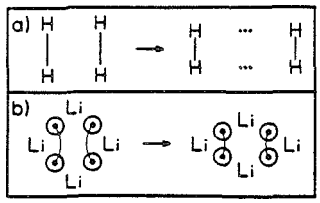

Figure 8. Geometric distortions for (a) H_4 and (b) Li_4. The bonds for H_4 are indicated by vertical lines (the electrons are atomic centered). For Li_4 circles with dots represent the singly occupied bond-centered orbitals, while lines connecting the dots show the dominant spin pairing.

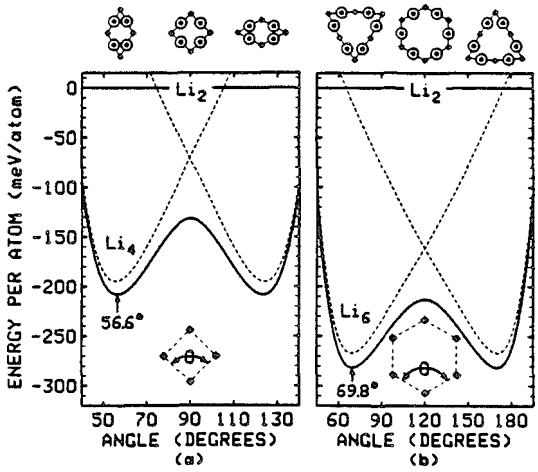

Figure 9. Potential energy curves for geometric distortions of the (a) Li_4 and (b) Li_6 clusters as a function of the bond angle, θ. In each case, the perimeters have been optimized for each value of θ. Dashed curves represent the separate resonance structures, while solid lines show the energy including all possible resonance structures. The energy per atom is given relative to Li_2 (at equilibrium). Diagrams above the plots show the cluster geometries at various angles (θ) where squares mark the atomic positions and circles mark the positions of the orbitals.

that are in disagreement with the more exact (GVB–Heisenberg) description [e.g., nonzero singlet–triplet gap for $Li_{(1D)}$].

The GVB wave functions for the various magnetizations retain full spatial and spin symmetries within a localized orbital description. Because the optimum GVB singly occupied orbitals have small overlaps, the magnon spectrum of Li_{10} (and also that of $Li_{(1D)}$) is described with excellent accuracy in terms of a simple Heisenberg Hamiltonian, where the coupling terms (J_{ij}) are extracted from the ab initio calculations.

Taken together, the GVB, UHF, and HF results in Figure 6 all indicate that it is *absolutely essential for* $Li_{(1D)}$ *that each orbital is occupied with only one electron.* Thus, in $Li_{(1D)}$, *the bonding is dominated by the singly occupied orbitals* with perturbations due to spin-pairing effects.

C. Tiny Clusters ($n \lesssim 8$). The GVB model for the 1D lithium rings and chains leads to correct predictions of the distortions that occur when the ring (or chain) structures are allowed to relax. The working principles in making these predictions for the optimum geometric distortions are (1) start with the symmetric ring geometry for neutral clusters and with the linear chain geometry for the cation or anion clusters, (2) pair up adjacent orbitals so as to maximize the number of bond pairs, (3) distort the geometry so as to increase overlaps in bond pairs by decreasing the distance between adjacent spin-paired orbitals, and (4) decrease the nonbonded repulsions (arising from orthogonalization due to the Pauli principle) by increasing the distance between adjacent orbitals that are *not* spin paired.

To illustrate how the bonding in Li_n affects geometrical structure we compare H_4 with Li_4. In square H_4, the optimum orbitals are

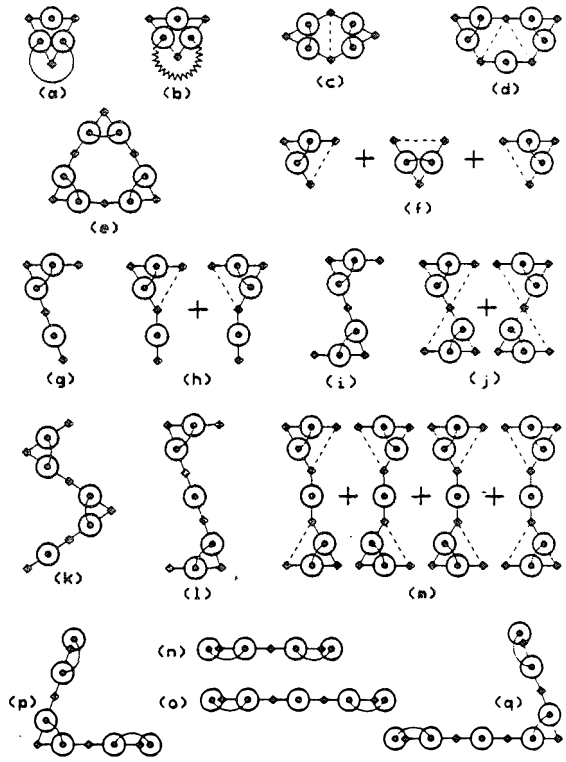

Figure 10. Low-energy isomers predicted by the 1D GVB model for (a) Li_3 saddlepoint; C_{2v}, $^2A_1$, (b) Li_3 minimum; C_{2v}, $^2B_2$, (c) Li_4; D_{2h}, ^1A_g, (d) Li_5; C_{2v}, $^2A_1$, (e) Li_6; D_{3h}, $^1A_1'$, (f) Li_3^+ (with resonance); D_{3h}, $^1A_1'$, (g) Li_4^+; C_s, $^2A'$, (h) Li_4^+ (with resonance); C_{2v}, $^2A_1$, (i) Li_5^+; C_{2h}, ^1A_g, (j) Li_5^+ (with resonance); D_{2h}, ^1A_g, (k) Li_6^+; C_s, $^2A'$, (l) Li_6^+; C_{2h}, ^2A_g, (m) Li_6^+ (with resonance); D_{2h}, ^2A_g, (n) Li_3^-; $D_{\infty h}$, $^1\Sigma_g^+$, (o) Li_4^-; $D_{\infty h}$, $^2\Sigma_g^+$, (p) Li_5^-; C_{2v}, $^1A_1$, and (q) Li_6^-; C_s, $^2A'$. Squares denote the atomic positions, circles with dots represent the singly occupied valence orbitals, and lines connecting the dots show the dominant spin pairing. In all cases the orbitals are centered on bond midpoints, and for the negative ions additional surface orbitals are present (see Figures 4 and 5). The acute bond angles range from 55° to 70°.

atom-centered. Thus the above principle leads to a rectangular distortion (see Figure 8a). Indeed, in this case the stable configuration has two separate H_2 molecules (no chemical bonding between the two H_2 fragments). On the other hand, for square Li_4, the optimum valence orbitals are *bond-centered* so that the above principles suggest a rhombic distortion (see Figures 8b and 9a). Because of the dominance of one-electron bonding, the Li_4 cluster is stable with respect to two Li_2 molecules for both the square and rhombic geometries. Indeed, as a result of the one-electron bonds along the four edges, the optimum edge lengths (R_e) for square Li_4 ($\theta = 90°$, $R_e = 3.026$ Å) and rhombic Li_4 ($\theta_{opt} = 56.6°$, $R_e = 3.083$ Å) are quite similar. For both H_4 and Li_4, the distortions away from the symmetrical geometry lower the energy of one resonance structure but raise the energy of the other resonance structure, reducing the resonance energy drastically. However, the gain in bonding for the favored structure more than compensates for the loss in resonance, and square Li_4 ($\theta = 90°$) distorts to a rhombus ($\theta_{opt} = 56.6°$), as indicated in Figure 9a.[25-28]

(25) Similar optimum geometries have been reported on Li_4, Na_4, and Na_6 using ab initio configuration interaction (CI) or local density functional (LDF) methods. Thus bond angles of $\theta_{opt} = 52.8°$ (CI, Li_4, ref 27), $\theta_{opt} = 53.1°$ (CI, Li_4, ref 26), $\theta_{opt} = 53.8°$ (CI, Na_4, ref 26), $\theta_{opt} = 53°$ (LDF, Na_4, ref 28), and $\theta_{opt} = 61°$ (LDF, Na_6, ref 28) were calculated.

(26) Beckmann, H.-O.; Koutecký, J.; Bonačič-Koutecký, V. *J. Chem. Phys.* **1980**, *73*, 5182 and ref 39.

(27) Rao, B. K.; Jena, P. *Phys. Rev. B* **1985**, *32*, 2058.

(28) Martins, J. L.; Buttet, J.; Car, R. *Phys. Rev. B* **1985**, *31*, 1804.

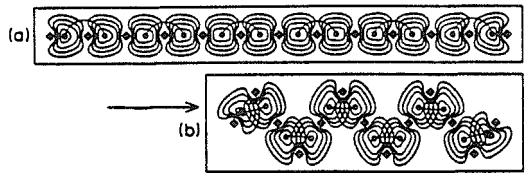

Figure 11. The GVB description of the geometric distortion of the (a) Li_{13}^+ linear chain cluster (R = 3.12 Å) into the (b) Li_{13}^+ zig-zag chain cluster (R = 3.12 Å, θ = 70°). In each case all 12 orbitals are shown. Contour spacings are at 0.015 au of orbital amplitude starting at 0.045 au. The atomic positions are marked by squares. Circles with dots represent the singly occupied bond-centered orbitals. Thin lines connecting the dots show the dominant spin pairing. Overlaps of adjacent spin-paired orbitals increase from ≈0.33 to ≈0.60 upon bending (a → b).

These same bonding principles govern the structures of other tiny naked clusters as well, and predictions of the low energy planar isomers for neutral, cation, and anion clusters of three to six atoms predicted by these principles are shown in Figure 10.

Starting with hexagonal Li_6 (θ = 120°, R_e = 3.079 Å), these bonding principles predict a distortion to a trigonal hexagon[29] (θ_{opt} = 69.8°, R_e = 3.064 Å, Figure 10e).[25] Potential energy curves for this distortion are shown in Figure 9b as a function of θ [where the edge length (R) is optimized for each value of θ[30]]. Indeed, the optimum orbitals for planar Li_6 are centered at the surface bond midpoints.[7] Topologically, the electronic structures of the Li_4 and Li_6 rings are equivalent to the π-electronic structures of cyclobutadiene (C_4H_4) and benzene (C_6H_6), respectively, except that the valence electrons of the lithium rings are localized on the bond *midpoints* while the π electrons of the CH rings are *atom-centered*. This suggests that both cyclobutadiene and benzene would also distort in the absence of the strong σ bonds.

For infinite 1D Li [$Li_{(1D)}$], allowing a distortion into two dimensions results in an infinite *zig-zag* chain (alternating 70° and 180° bond angles) as shown in Figure 11 for Li_{13}^+. This distortion is due to the same spin-pairing and overlap effects that govern H_4, Li_4, and Li_6.

The optimum structure for planar Li_5 is predicted and explained in a similar fashion. Starting with the Li_5 ring (θ = 108°), the GVB bonding principles suggest that the bond angle at each vertex atom shared by two adjacent orbitals of a bond pair decreases to 55–70° (increasing the bond pair overlaps), as shown in Figure 10d. Indeed ab initio configuration interaction (CI) calculations on Li_5[27] lead to a distorted ring geometry (two small angles of 61.2° and three large angles 120.5°, 120.5°, and 176.5°) that is consistent with this GVB description. In addition, local density functional (LDF) calculations[28] on Na_5 give a similar geometry (bond angles of 58.4°, 58.4°, 119.4°, 119.4°, and 184.5°). This suggests that the bonding of both Li_5 and Na_5 is dominated by electrons localized in bond midpoints.

Next we illustrate these principles for Li_3^+ and Li_3^-. Starting with linear Li_3^-, our model predicts that bending the bond angle would be unfavorable since it increases the overlap of adjacent orbitals that are not spin paired (Figure 10n). Thus, Li_3^- is linear. This is in agreement with ab initio calculations[31] for Li_3^-. Starting with linear Li_3^+ and bending the cluster increases the bond pair overlap and hence increases the bonding. At 60°, there are three equivalent bond midpoints, and, hence, three equivalent resonance structures (Figure 10f). Consequently, the equilateral triangle is the equilibrium structure.

To analyze neutral Li_3, we start with the equilateral triangle (θ = 60°). Neutral Li_3 is a special case, unlike those considered above, because of this very small bond angle and also because the equilateral triangle is the only regular polygon which cannot be distorted without changing the lengths of its sides. Thus, any variation of the bond angle to optimize the *two-electron* bonding according to the aforementioned principles is at expense of stretching or compressing *one-electron* bonds. Nevertheless, we find that the full GVB wave functions for low-lying geometries of Li_3 do indeed contain orbitals localized in bond midpoints and thus, the stationary point geometries of Li_3 can be described in terms of principles based upon orbitals localized in bond midpoints.

TABLE I: Summary of Results Calculated for M_3

	obtuse state		acute state		
wave function	bond angle, deg	perimeter, Å	bond angle, deg	perimeter, Å	ΔE,[a] meV
Li_3					
Hartree–Fock	75.4	9.361	50.5	9.065	−31.8
GVB	68.1	8.951	53.8	8.935	11.5
valence CI	71.5	9.090	52.2	9.038	8.3
valence CI[b]	71.1	8.956	53.8	8.940	6.9
Na_3, valence CI[c]	73.4	10.57	51.5	10.63	25.9
Cu_3, CI[d]	68.5	7.40	54.9	7.35	7.3
Ag_3, CI[d]	69.2	8.49	55.2	8.44	13.4

[a] Calculated difference in the total energy between the obtuse and acute states [the obtuse state is lower except for the uncorrelated (Hartree–Fock) wave function]. [b] Reference 32. [c] Reference 35. [d] Reference 37.

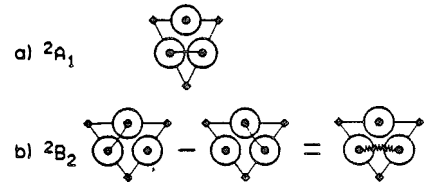

Figure 12. The GVB description of the two low-lying electronic states of Li_3. (a) The $^2A_1$ saddlepoint geometry (θ = 52.2°) which is described by a single valence-bond resonance structure. (b) The $^2B_2$ equilibrium geometry (θ = 71.5°) which is described equally well by either the resonance of two valence-bond structures or a single structure where two electrons are high-spin coupled and the third electron is coupled to the other two electrons to form an overall spin-doublet state.

Results for Li_3 are presented in Table I and Figure 12. Pairing two orbitals to form a bond pair favors distortion (at the shared atom) to a smaller angle (θ_{opt} = 52.2°) in order to increase the overlap of the bond pair of electrons and to decrease the interaction of the radical orbital with the bond pair (θ_{opt} = 63.9°). This leads to the $^2A_1$ state (acute bond angle) as shown in Figure 12a. A second low-lying state results from a resonance superposition of two primary resonance structures (see Figure 12b). This resonance superposition of two primary resonance structures is very similar to the spin coupling in the π-electron system of the allyl radical.[33] This resonance description is equivalent to an independent particle description composed of the triplet pairing of two electrons (indicated by jagged lines) and coupling with the remaining electron to obtain a spin doublet state (the "GF"[18,33] spin coupling). In this case, the bond angle at the atom shared by the triplet-coupled electrons must increase, leading to an "obtuse" isosceles trianglular structure ($^2B_2$) with apex angle of 71.5°.

Both the acute and obtuse structures are low-lying for Li_3. The global minimum of Li_3 is the GF spin-coupled "obtuse" triangle geometry (Figure 12b), while the valence-bond spin-coupled "acute" triangle geometry (Figure 12a) is 8.3 meV higher, representing the barrier to pseudorotation. The Hartree–Fock results (which neglect electron correlation effects) also indicate that both the acute and obtuse states are low-lying; however, Hartree–Fock

(29) Our results for Li_4 are consistent with a pseudo-Jahn–Teller description (ref 26). However, the pseudo-Jahn–Teiler description does not predict the analogous distortion for the Li_6 ring.

(30) Previous values of θ_{opt} = 57.3° and θ_{opt} = 69.3° for Li_4 and Li_6, respectively, reported in ref 7 were calculated by assuming a fixed perimeter as a function of θ.

(31) Eades, E. A.; Hendewerk, M. L.; Frey, R.; Dixon, D. A.; Gole, J. L. *J. Chem. Phys.* **1982**, *76*, 3075.

(32) Bagus, P. S.; del Conde, G.; Davies, D. W. *J. Chem. Soc., Faraday Discuss.* **1977**, *62*, 321.

(33) Levin, G.; Goddard III, W. A. *J. Am. Chem. Soc.* **1975**, *97*, 1649. Theor. *Chim. Acta* **1974**, *37*, 253.

yields the wrong ground state. The results of GVB calculations on Li_3 are in very good quantitative agreement with full valence CI results within the same valence double-ζ basis set and with other full valence CI calculations[32] with regard to the stationary point geometries and barrier to pseudorotation. Similar results have been found for other alkali trimers[35,36] as well as for Cu_3[37,38] and Ag_3,[37] indicating that the bonding mechanism is at least qualitatively similar for all of these systems. Results for Na_3,[35] Cu_3,[37] and Ag_3[37] are included in Table I for comparison. The importance of the one-electron bonding in these systems is illustrated by the similarity of the perimeters (obtained by adding the three bond lengths) for the acute and obtuse states.

Low-lying isomers for the larger charged clusters ($Li_{4,5,6}^{+,-}$) are predicted in a similar fashion by starting with the principle resonance structures of the linear chain clusters and varying the angles as described above. The predicted low-energy isomers for all of these clusters are also shown in Figure 10. The electronic structures for these isomers are indicated with circles with dots representing the singly occupied orbitals and lines connecting the dots indicating the dominant spin pairing. The isomers (l) and (m) of Li_6^+ are expected to have very little barrier to rotation about the central bond midpoint into a three-dimensional structure where the two planar Li_3 subunits are staggered. Similarly, the isomers for Li_5^+ are expected to exhibit free rotation about the central atom.

Because of the multitude of "reasonable" structures for metallic clusters, it is very important to have a correct set of guidelines such as those given in this section if one is to correctly determine the low-energy isomers. Previous theoretical approaches to determining the low-energy isomers have been to guess structures, and then calculate their energies. Thus, in the first high-quality (electron correlation inclusive) ab initio studies on Li clusters,[39] the correct structure of Li_4 was obtained and a D_{4h} oblate octahedron structure for Li_6 was proposed based on the Li_4 structure. In a subsequent multiple-reference singles and doubles CI ab initio investigation,[40] it was determined for Li_6 that the lowest energy structure was a C_{5v} pyramid, with the planar structure (similar to that of Figure 10e but $\theta = 60°$ was assumed) and the D_{4h} structures higher in total energy by 0.045 and 0.194 eV, respectively. In an improved multiple-reference singles and doubles CI ab initio investigation using modified virtual orbitals,[41] it was determined for Li_6 that the 60° planar structure is indeed the lowest energy structure, with the C_{5v} and D_{4h} structures higher in total energy by 0.039 and 0.240 eV, respectively. These studies were performed with complete geometry optimizations with the exception that planar isomer was optimized with the $\theta = 60°$ angle restriction. Thus, relaxing geometric restrictions for *all* isomers will result in an increase of θ and thus an increase of the stability of the planar isomer over the other isomers for Li_6.

More recently, gradient approaches have been utilized to determine the forces on guess structures to obtain stationary isomers.[27,28] However, these approaches have been limited to eight or less atoms and may be somewhat sensitive to the initial starting structures, especially if there are energy barriers separating the various low-energy isomers.

The general picture that is consistent with a number of theoretical studies[27,28,41] and our own preliminary calculations[34] is that these "1D zig-zag" clusters are competitive up to $n \approx 8$. The zig-zag Li_8 cluster puckers out of the plane in a fashion similar to cyclohexane. As the clusters increase in size, there is a tendency toward forming more compact structures (e.g., planar close-packed structures for the very small clusters), due to the resonance and/or delocalization stability obtained by increasing the number and/or quality of sites to place the electrons.

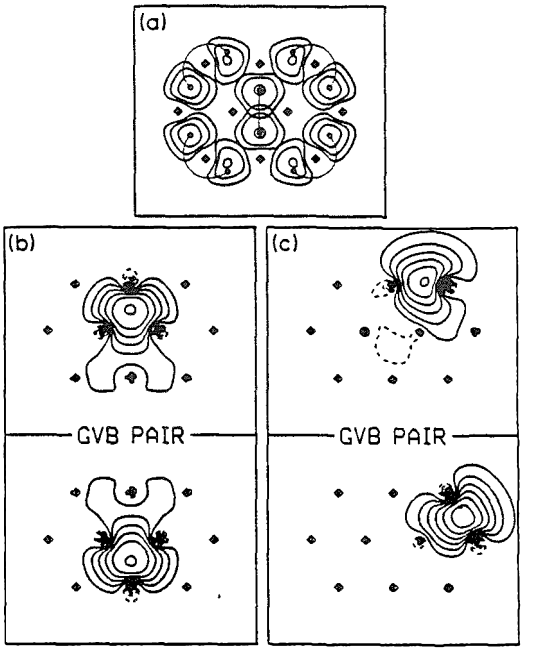

Figure 13. (a) All ten singly occupied GVB orbitals for the principal resonance structure of planar close-packed Li_{10} (R = 3.1 Å; contour increments starting at 0.060 au). Squares mark the atoms, and dots joined by thin lines represent the paired electrons. (b) Bulk bond pair, 0.71 overlap. All contours are included. (c) Surface bond pair, 0.50 overlap. All contours are included.

D. Two-Dimensional Clusters. The optimum planar structures for Li_4, Li_5, and Li_6 resemble planar close-packed clusters. Examining larger 2D close-packed arrays of Li atoms, we find the general result that *interior regions* have singly occupied orbitals localized at the *centers of equilateral triangles* while *surface* (*edge*) *regions* have singly occupied orbitals localized at *bond midpoints*. This is illustrated for planar Li_{10} in Figure 13. Extrapolating to the infinite 2D (close-packed) system [$Li_{(2D)}$] leads to the description in Figure 14a where alternate pairs of triangular hollows have bond pairs and triangular hollows adjacent to the bond pairs are empty.

This GVB description for $Li_{(2D)}$ could lead to charge density waves (CDW). However, there are an infinite number of ordered and disordered resonance structures (such as those shown in Figure 14b–c) that may enter into the many-electron wave function. Charge density waves have been proposed to account for certain experimental electronic anomalies for bulk (3D) alkali metals[22] and have recently been observed by neutron diffraction for bcc potassium.[23] It is interesting to speculate whether the present GVB model involving the spin-pairing localized interstitial orbitals would lead to CDW in bcc, hcp, or fcc bulk metals.

This GVB description for $Li_{(2D)}$ may lead to metallic character. Half of the triangular hollows are empty, providing low-lying charge-transfer states required for conduction. The existence of essentially an infinite number of disordered resonance structures such as that shown in Figure 14c suggests a high density of low-lying many-electron states.

E. Three-Dimensional Clusters. We next discuss the GVB wave functions for Li_{13}^+ clusters having one central (bulk) atom and twelve surface atoms. The three high-symmetry structures examined, listed in order of increasing energy, are (1) I_h, the

(34) McAdon, M. H.; Goddard III, W. A., unpublished results.
(35) Martin, R. L.; Davidson, E. R. *Mol. Phys.* **1978**, *35*, 1713.
(36) Thompson, G. A.; Lindsay, D. M. *J. Chem. Phys.* **1981**, *74*, 959.
(37) Walch, S. P.; Bauschlicher, C. W.; Langhoff, S. R. *J. Chem. Phys.* **1986**, *85*, 5900.
(38) Moskovits, M. *Chem. Phys. Lett.* **1985**, *118*, 111. Also see Lindsay, D. M.; Thompson, G. A.; Wang, Y. Presented at the 191st National Meeting of the American Chemical Society, New York, NY, April 13–18, 1986, appearing elsewhere in this issue.
(39) Beckmann, H.-O.; Koutecký, J.; Botschwina, P.; Meyer, W. *Chem. Phys. Lett.* **1979**, *67*, 119.
(40) Plavsic, D.; Koutecký, J.; Pacchioni, G.; Bonačič-Koutecký, V. *J. Phys. Chem.* **1983**, *87*, 1096.
(41) Fantucci, P.; Bonačič-Koutecký, V.; Koutecký, J. *J. Comput. Chem.* **1985**, *6*, 462.

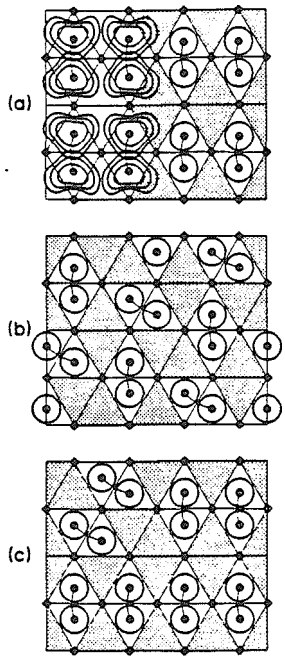

Figure 14. (a) The GVB description of $Li_{(2D)}$. The upper left corner shows contours ≥0.060 au for eight GVB orbitals optimized without restriction for the planar Li_{12}^{4+} cluster. The edge atoms of a planar unit cell count half, since each contributes half an electron to the cell and half an electron to the adjacent cell. Hence, the model Li_{12}^{4+} cluster is composed of four unit cells (two atoms per cell) with a total of eight valence electrons. The orbitals for the planar Li_{12}^{4+} cluster were obtained for 12 "real" atoms (four GVB pairs, 0.52 overlap each pair). The description of $Li_{(2D)}$ is obtained by translation of the planar Li_{12}^{4+} cluster where connected circles represent the singly occupied orbitals and shaded triangles represent empty hollows. (b) An alternative ordered resonance structure for $Li_{(2D)}$. (c) A disordered resonance structure for $Li_{(2D)}$.

TABLE II: Relative Energies of Li_{13}^{+} Clusters[a]

cluster	structure	relative energy: total, eV	relative energy: per atom, meV/atom
OPTET(I)	γ-(4,4,5), C_{2v}	0.000	0.0
OPTET(II)	γ-(4,4,4,1), C_s	0.057	4.4
OPTET(III)	I_h-(1,11,2), C_{2v}	0.197	15.1
planar	C_{2v}	0.400	30.8
icosahedron	I_h-(1,12), I_h	0.581	44.7
fcc	(1,12), O_h	0.837	64.4
zig-zag chain	C_{2h}	0.947	72.9
hcp	(1,12), D_{3h}	1.144	88.0
linear chain	$D_{\infty h}$	1.678	129.1

[a] The structures are shown in Figures 11, 15–17, 19, and 20. Results are calculated at the GVB-CI level with basis set D. See the Appendix and Table VI for further details.

icosahedron; (2) fcc, the truncated octahedron corresponding to the nearest neighbors of a face-centered cubic lattice; and (3) hcp, the hexagonal array corresponding to the nearest neighbors of a hexagonal close-packed lattice. We will concentrate our studies here on the positive ion, Li_{13}^{+}, since all the electrons can be spin paired, providing a useful model for the bonding in large clusters. Also, positively charged metal clusters have been examined experimentally and hence techniques to test the predictions may soon become practical. The results are given in Table II (see the Appendix for details).

The I_h cluster (Figure 15) ground state involves electrons localized at the centers of twelve of the twenty triangular faces. Each electron is spin-paired to an electron in an adjacent (edge-shared) surface triangle to form a rhombus (0.63 overlap)

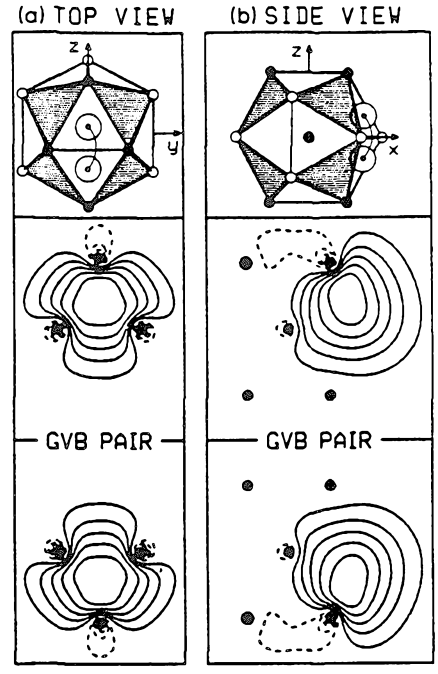

Figure 15. GVB orbitals for one of the six equivalent bond pairs of icosahedral Li_{13}^{+} (six pairs occur along the $\pm x$, $\pm y$, and $\pm z$ directions; the $+x$ pair is shown). (a) The top view where the orbital contours in the surface planes are shown. (b) A side view where the orbital contours in a symmetry plane bisecting the cluster are shown. In each case, the atoms in the plotting plane are marked by filled circles while atoms above and below that plane are marked by open circles. Connected dots represent the spin-paired electrons. Shaded triangular faces do not contain orbitals. Overlaps of spin-paired orbitals are 0.63.

just as for the bulk electrons of $Li_{(2D)}$ (Figures 13 and 14). The four triangular faces adjacent to a spin-paired rhombus are empty (to avoid repulsive interactions between unpaired electrons), as indicated in Figure 15. Each of the twelve I_h Li_{13}^{+} valence orbitals is equivalent. Figure 15 shows the GVB electron pair on the $+x$ axis. The many-electron wave function is composed of six equivalent such GVB pairs (one GVB pair along each of the $\pm x$, $\pm y$, and $\pm z$ axes).

The fcc cluster (Figure 16) has only eight tetrahedra (rather than the twenty of I_h). These eight tetrahedra are all geometrically equivalent and have three interior edges and three surface edges. Each interior tetrahedral edge is shared by two tetrahedra; thus, each tetrahedron shares an edge with three other tetrahedra. We find that all twelve singly occupied valence orbitals localize among the eight tetrahedra of the fcc cluster, leading to a total energy for the fcc cluster 0.26 eV higher than that for I_h (20 meV/atom). Four tetrahedra each have two orbitals (centered on opposite faces, spin-paired with 0.75 overlap), accounting for eight of the twelve valence electrons. These doubly occupied tetrahedra are staggered so that no doubly occupied tetrahedron shares an edge with any other doubly occupied tetrahedron. The other four tetrahedra each have only one orbital (centered on an exterior face), accounting for the four remaining valence electrons. The four electrons in the singly occupied tetrahedra are well separated from one another, leading to a ground-state singlet having two weakly coupled bond pairs (−0.28 overlap for each pair). The optimum singly occupied orbitals for fcc Li_{13}^{+} are shown in Figure 16 for each type of bond pair. Focusing on a tetrahedron containing two electrons, one finds that the three adjacent edge-sharing tetrahedra each contain only one electron (in order to avoid the repulsive interactions endemic to two sets of paired electrons).

The hcp cluster (Figure 17) also has eight tetrahedra; however, six of the tetrahedra for hcp occur in pairs sharing one *face*, while

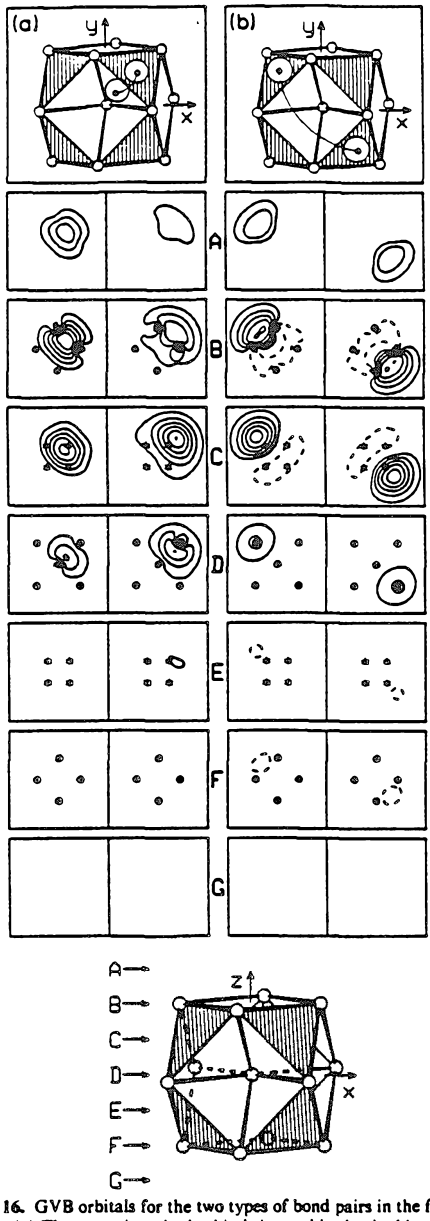

Figure 16. GVB orbitals for the two types of bond pairs in the fcc Li_{13}^+ cluster. (a) The two spin-paired orbitals located in the doubly occupied 111 tetrahedron and (b) the orbital localized in the singly occupied $1\bar{1}1$ tetrahedron (and spin-paired with the orbital of the $\bar{1}11$ tetrahedron). Here cross sectional amplitudes of each of the orbitals are given at different evenly spaced (001) planes. Planes B, D, and F pass through atoms, marked by filled circles. Planes C and E pass through the centers of tetrahedral hollows, marked by asterisks. Planes A and G pass through virtual tetrahedral centers.

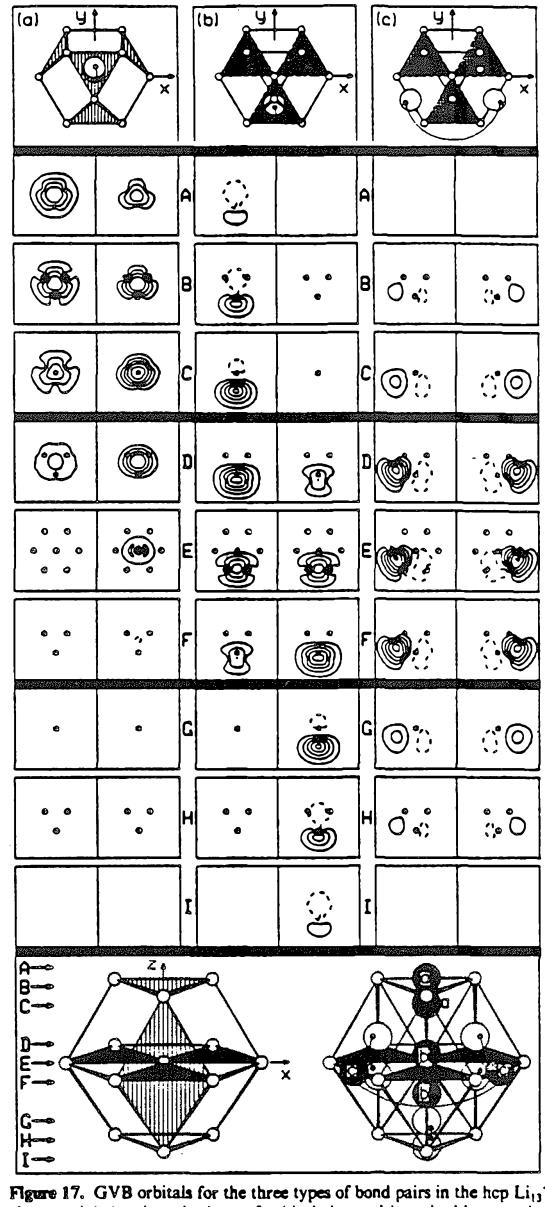

Figure 17. GVB orbitals for the three types of bond pairs in the hcp Li_{13}^+ cluster. (a) A spin-paired set of orbitals located in a doubly occupied tetrahedron. (b) A spin-paired set of orbitals distributed over a face-shared pair of tetrahedra. (c) A spin-paired set of orbitals distributed over two bond midpoints. Here, cross-sectional amplitudes of the orbitals are given at nine (0001) planes intersecting the z axis at $z = 1.25$, 1.0, 0.75, 0.25, 0.0, −0.25, −0.75, −1.0, and −1.25 (in units of $c/2$, where c is the length of the hcp unit cell in the z direction). Planes B, E, and H intersect atomic positions, marked by filled circles. Planes C, D, F, and G pass through the centers of tetrahedra, marked by asterisks. Planes A and I pass through virtual tetrahedral centers in the vacuum, e.g., tetrahedra that would be present if the cluster were allowed to grow in the $\pm z$ directions.

the other two are isolated, sharing edges with the above paired tetrahedra. The result is a total energy 0.56 eV higher than I_h (43 meV/atom). The three face-shared tetrahedral pairs each have one set of spin-paired orbitals, with one electron localized in the tetrahedron above the shared face and one electron localized below the shared face. This accounts for six valence electrons (three GVB pairs with overlaps of 0.58, 0.58, and 0.62). The two remaining tetrahedra each contain one spin-paired set of orbitals (four electrons, two GVB pairs, 0.78 overlap). The remaining two electrons cannot go into tetrahedra without a severe energetic penalty; placing a third electron in a face-sharing pair of tetrahedra leads to very strong antibonding interactions. Consequently, the last two electrons end up along two of the three equatorial edges that do *not* border a tetrahedron (one GVB pair, −0.36 overlap). Summarizing, ten of the twelve valence electrons occupy tetrahedra, while the remaining two valence electrons occupy surface bond midpoints (that do not border tetrahedra). These optimum

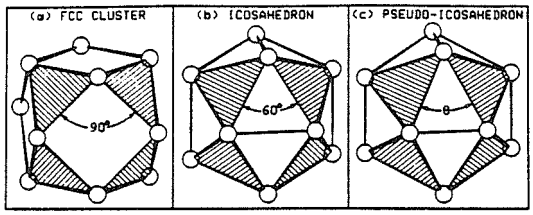

Figure 18. The Jahn–Teller-like distortion of the Li_{13}^+ icosahedron cluster leading to a pseudo-icosahedron. (a) The fcc cluster (cubo-octahedron, O_h symmetry). (b) The icosahedron (I_h symmetry), formed by compressing the square faces of the fcc cluster ($\theta = 90°$) into rhombi ($\theta = 60°$). (c) The pseudo-icosahedron (T_h symmetry) formed by further compressing the same faces ($\theta < 60°$). The T_h point group symmetry is preserved for all θ.

singly occupied orbitals for hcp Li_{13}^+ are indicated in Figure 17 for the three types of bond pairs.

The GVB descriptions for these three highly symmetrical clusters all involve breaking the high symmetry. Thus, there will be a separate resonance structure for each symmetry operation that takes the localized bonding structure into a new equivalent (but not identical) structure. Including all of these resonance structures in the many-electron wave functions leads to degenerate states and thus the resonance energy is small and Jahn–Teller-like distortions shall occur. For example, the GVB description of I_h Li_{13}^+ leads to five equivalent resonance structures which split into a quadruply degenerate ground state ^1G_g and a nondegenerate excited state ^1A_g. The energy lowering of the ^1G_g state relative to the energy of one resonance structure is expected to be approximately one fourth that of the energy raising of the ^1A_g state relative to the same reference energy.[9] The ^1G_g state is thus subject to a Jahn–Teller-like distortion. If we assume that the optimum distortion can be determined by analyzing the dominant spin pairing of just one of the resonance structures (as is true for H_4, Li_4, Li_6, and linear Li_{13}^+, see Figures 8, 9, and 11) then the optimum structure of the icosahedral-like Li_{13}^+ isomer is expected to be a ^1A_g state of T_h symmetry (T_h is a subgroup of both I_h and O_h, and D_{2h} is a subgroup of T_h). This T_h structure can be described by starting with the fcc cubo-octahedral structure, squashing the square faces to form the icosahedron, and then further squashing to form the optimum pseudo-icosahedral isomer, as shown in Figure 18. Such a distortion is expected to result in improved overlaps in the six equivalent bond pairs, since the dihedral angle between adjacent paired faces is reduced. Similar distortions are predicted for the fcc and hcp clusters; however, since all of these clusters are highly coordinated, such distortions may be rather small (unlike the cases for the Li_4 square or the Li_6 hexagon), leading to relatively small lowerings of the total energy.

From the results on the three high-symmetry Li_{13}^+ clusters, it is clear that the valence electrons prefer to localize in interstitial regions (tetrahedra). Using a set of concepts derived from these results (as embodied in the set of rules of section IV), we considered arrangements of 13 atoms that maximize the number of tetrahedra under the restriction that the number of tetrahedra shared by any given atom should be relatively small (much less than 20). This restriction stems from the observation that twelve valence electrons cannot all simultaneously bond in an effective manner to one central atom. Thus, the valence electrons for the I_h cluster are centered at surface triangular hollows whereas the exact tetrahedral centers are the preferred sites (in the absence of the large orthogonality and electron–electron repulsion effects associated with too many electrons trying to bond to the same central atom). This led to the prediction of several new Li_{13}^+ clusters (Figure 18) each with 15 tetrahedra.

GVB calculations show that each of these three clusters, denoted as OPTET (optimum tetrahedral), is lower in energy than I_h. These OPTET isomers all lead to local fivefold symmetry axes as a consequence of the efficient packing of tetrahedra. Two of the three OPTET clusters (I and II) also clearly coincide with

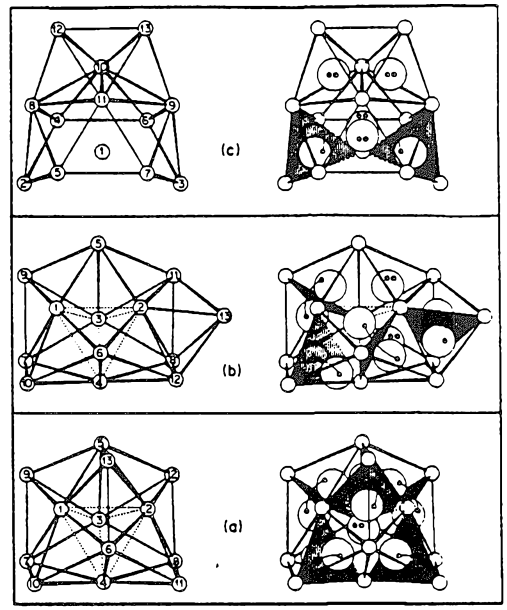

Figure 19. Three low-lying OPTET Li_{13}^+ isomers. (a) OPTET(I) which consists of a central tetrahedron (atoms 1–4, joined by dotted lines), four capping atoms (atoms 5–8), and five bridging atoms (atoms 9–13). (b) OPTET(II) which differs from OPTET(I) in the position of only one atom (atom 13). (c) OPTET(III) which consists of a central atom (atom 1) surrounded by ten atoms in the first shell (atoms 2–11 forming an incomplete icosahedral shell) and two atoms in the second shell (atoms 12 and 13). In each case, the nuclear framework is shown on the left-hand side and the electronic structure is shown schematically on the right-hand side. The positions of doubly occupied tetrahedral hollows are shown with a large circle (representing the pair of orbitals) filled by two dots (representing the electrons). The positions of singly occupied orbitals and the principle spin pairing are represented by large circles filled with one dot each, joined by thin arcs. Faces shared by singly occupied tetrahedra are shaded. OPTET clusters (I), (II), and (III) have symmetries C_{2v}, C_s, and C_{2v}, respectively. All three clusters have multiple local fivefold symmetry axes.

truncations of the γ-brass structure. The correspondence of the third structure to a truncation of γ-brass is rather subtle; OPTET(III) is more clearly based on a modification of the icosahedron. It is convenient to label these OPTET clusters in terms of their overall point group symmetries and the number of atoms in successive shells for the respective structure type. With this convention, the OPTET(I) structure is referred to as γ-(4,4,5), C_{2v}. The OPTET(II) [γ-(4,4,4,1), C_s] and OPTET(III) [I_h-(1,10,2), C_{2v}] have total energies higher than OPTET(I) by 0.05 and 0.20 eV, respectively. The high-symmetry I_h, fcc, and hcp clusters have total energies higher than OPTET(I) by 0.58, 0.84, and 1.14 eV, respectively (see Table II).

Of all Li_{13}^+ structures examined, the OPTET(I) cluster (Figure 19a) has the lowest total energy. The geometric and electronic structures of the OPTET(I) cluster are described as follows. The central tetrahedron formed by atoms 1, 2, 3, and 4 is doubly occupied (two electrons, two orbitals, 0.72 overlap). Four capping atoms (atoms 5–8 in Figure 19a) form four tetrahedra sharing faces with the central tetrahedron. Each of these four capping tetrahedra are empty (i.e., orbitals are not centered on these four capping tetrahedra; however, orbitals centered on adjacent tetrahedra have amplitudes that diminish as they approach the centers of these four tetrahedra). The five remaining atoms (labeled 9–13 in Figure 19a) form bridges to the four central atoms and to the capping atoms, leading to a total of ten new tetrahedra, each sharing one edge with the central tetrahedron and one face with the four empty tetrahedra. Each of these ten tetrahedra is singly occupied, and these ten electrons partition into five face-sharing bond pairs. We shall denote such face-sharing bond pairs

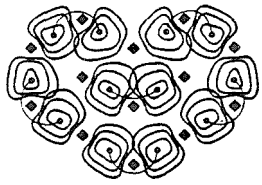

Figure 20. GVB orbitals for planar close-packed Li_{13}^+. Only contours ≥0.060 au are shown (0.015-au spacings). The overlap of the bulk bond pair is 0.60. The average overlap for surface bond pairs is 0.52. Squares mark the atomic positions. The dominant spin pairing is shown by the connected dots.

as a–(b,c,d)–e where a–b–c–d and b–c–d–e indicate the two tetrahedra and (bcd) denotes the shared face. Hence, the bond pairs 5–(1,3,9)–7, 5–(2,3,11)–8, 6–(1,4,10)–7, and 6–(2,4,12)–8 each have an overlap of 0.57 and the remaining 5–(1,2,13)–6 bond pair has an overlap of 0.66. As discussed above, this sequence starts with a tetrahedron, capping the faces and bridging the edges, leading to the characteristic cluster of the γ-brass structure. Consequently, we denote OPTET(I) as γ-(4,4,5), C_{2v}.

The OPTET(II) cluster is just 0.057 eV higher in total energy than OPTET(I). The OPTET(II) structure differs from the OPTET(I) structure by moving one atom from the third γ-brass shell to the fourth γ-brass shell so it is denoted as γ-(4,4,4,1), C_s. The electronic structure of the OPTET(II) ground state is diagrammed in Figure 19b. The 2–3–4–8 tetrahedron is located near the center of the cluster (on the symmetry plane) and is doubly occupied (0.72 overlap). Three tetrahedra sharing faces with the 2–3–4–8 tetrahedron are empty (1–2–3–4, 2–3–8–11, and 2–4–8–12). The 2–3–5–11 tetrahedron is also doubly occupied (0.71 overlap) and shares the 2–3 edge with the doubly occupied 2–3–4–8 tetrahedron. The remaining eight electrons occupy separate tetrahedra and are divided into four face-sharing bond pairs. These four remaining bond pairs are 11–(2,8,13)–12, 0.63 overlap; 5–(1,3,9)–7, 0.62 overlap; 6–(1,4,10)–7, 0.64 overlap; and 1–(2,4,6)–12, 0.63 overlap. With just one exception, tetrahedra sharing faces with these six bond pairs are empty. The exception to this rule is exhibited by two singly occupied tetrahedra (1–2–4–6 and 1–4–6–10). These tetrahedra share the 1–4–6 face but their electrons are not spin-paired with one another. A careful examination of these two orbitals shows that they are staggered in order to reduce the nonbonded repulsions. The 1–2–4–6 orbital is strongly polarized toward the 1–2–6 face while the 1–4–6–10 orbital is strongly polarized toward the 4–6–10 face; thus, these two orbitals have only one atom in common (atom 6).

The OPTET(III) structure (Figure 19c) is derived by plucking two adjacent atoms away from the surface of the high symmetry I_h cluster and adding them to adjacent capping positions on the opposite surface. This cluster is denoted as I_h-(1,10,2), C_{2v} and leads to a total energy 0.20 eV higher than OPTET(I) but 0.38 eV *lower* than I_h. The electronic structure of the OPTET(III) ground state (Figure 19c) consists of four doubly occupied tetrahedra, four singly occupied tetrahedra (divided into two face-sharing pairs), and seven empty tetrahedra. Two edge-sharing tetrahedra (8–10–11–12 and 9–10–11–13) are each doubly occupied (0.67 overlap each pair). Two additional atom sharing tetrahedra (1–5–7–11 and 1–4–6–10) are also both doubly occupied (0.74 overlap each pair). All seven tetrahedra sharing faces with these doubly occupied tetrahedra are empty. The remaining four electrons are divided into two face sharing tetrahedral pairs; 4–(1,2,8)–5 and 6–(1,3,9)–7, 0.56 overlap each pair. Each of these four singly occupied tetrahedra shares one edge with a doubly occupied tetrahedron.

Summarizing, we find typical orbital overlaps are 0.74–0.78 for doubly occupied tetrahedra. Face-sharing singly occupied tetrahedral orbitals typically have overlaps in the range of 0.57 to 0.63. Overlaps outside these ranges result occasionally from atypical surroundings [e.g., adjacent tetrahedra that are empty or doubly occupied].

With such small clusters, surface effects are quite large so that planar clusters (which lead to an increased number of internal sites) are quite competitive. Thus the planar cluster of Figure 20 has an energy 0.18-eV lower than I_h [0.40-eV higher than OPTET(I)]. Although the linear chain cluster is not a competitive structure [1.68 eV higher in total energy than OPTET(I)], the zig-zag chain cluster formed by bending the chain at alternate atomic sites (increasing bond pair overlaps as shown in Figure 11) is 0.20 eV lower in total energy than the hcp cluster [the zig-zag chain is 0.95 eV higher in total energy than OPTET(I)].

IV. Discussion

The results discussed in section III have led to a new generalized valence bond model of metallic bonding based on electrons localized in interstitial regions such as bond midpoints (1D clusters), triangular faces (2D clusters), and tetrahedral hollows (3D clusters). In section IVA we illustrate the use of these basic concepts by applying them to predictions concerning the Li_4 tetrahedron. This GVB model for metallic bonding is summarized in section IVB by a set of rules that applies to three-dimensional clusters. These rules lead to the prediction that OPTET clusters are the most stable (lowest energy) structures for naked lithium clusters from eight atoms up to about forty atoms. These OPTET clusters are discussed in section IVC. The use of these rules to rationalize properties of condensed systems (bulk solids) is illustrated in sections IVD and IVE where we examine the structures, conductivities, and solid solubility limits of bulk close-packed metals. This GVB model of metallic bonding also suggests a new type of metallic force field which should lead to improved modeling of metallic systems containing thousands of atoms (section IVF).

A. Analysis of the Li_4 Tetrahedron. To illustrate the concepts of this GVB model of metallic bonding, consider the Li_4 system. A simple model of bonding in terms of pairwise additive potentials would lead to the result that the tetrahedron is favored over the rhombus and other structures for Li_4 (it has one extra "bond"). Indeed, the results of the previous section might suggest that the four orbitals of tetrahedral Li_4 are localized on the four faces and spin-paired. The problem with this is that the distance between orbitals in *different* pairs would be quite small ($0.41R$), leading to large repulsive interactions. (As in the previous section, R denotes the *nearest-neighbor distance*, e.g., for tetrahedral Li_4, R is the edge length.) Indeed, we find from GVB calculations that the optimum orbitals of the Li_4 tetrahedron are instead localized on four of the six edges and spin-paired so that orbitals in different pairs are at least $0.5R$ apart. However, starting with this description, one would expect (and we find) that the distortion to a planar (rhombic) structure is favored (leading to a distance of $0.89R$ between nonpaired orbitals). Thus, the GVB bonding principles predict (and the calculations confirm) that the stable geometry of Li_4 is the rhombus (planar).

B. The Rules. From the results on three high-symmetry clusters, it is clear that the optimum bonding involves valence electrons that prefer to localize in separate tetrahedral hollows. This suggests that the *optimum structures* of small clusters are those that *maximize the number of tetrahedra*, as is the case for I_h, with 20 tetrahedra. However, for the icosahedron, the 20 tetrahedral hollows all share the *same* central bulk atom (the eight tetrahedra for the fcc and hcp clusters also all share the central atom; see Figures 15–17). This is unfavorable for the following reasons.

(1) To describe an orbital localized in a tetrahedral interstitial requires a hybrid combination of the valence orbitals from each of the four atoms of the tetrahedron, with an equal contribution from each atom. For lithium, the low-lying orbitals are 2s and 2p and hence, each atom can contribute effectively to only four orthogonal interstitial orbitals (with the overlapping orbitals of a bond pair, one might be able to describe up to two electrons per orthogonal orbital and hence a total of eight electrons near one atom).

(2) The orthogonality induced (Pauli principle) repulsion between orbitals that are *not* spin-paired becomes large when these orbitals are close (as they must be when sharing a common vertex).

Thus, the three OPTET clusters (Figure 19) and the planar cluster (Figure 20) are all lower in energy than the I_h cluster (Figure 15).

From the results on the various clusters, we have abstracted the following rules for three-dimensional metallic structures.

(α) Orbitals (each with one electron) are localized in different tetrahedral hollows where possible.

(β) If necessary, two electrons may be placed in one tetrahedron (localizing on opposite faces or edges) but they must be spin-paired.

(γ) No more than two electrons may be distributed between a pair of *face-shared* tetrahedra, and these must be spin-paired (singlet).

(δ) No more than three electrons may be distributed between a pair of *edge-shared* tetrahedra.

(ϵ) No more than four bond pairs of electrons may share one central bulk atom, and no more than three bond pairs of electrons may share one central surface atom.

(ζ) Additional electrons must be in surface orbitals at edge or face sites that do not share edges with occupied tetrahedra.

The above principles are consistent with the calculated wave functions and total energies where the OPTET(I) cluster is lowest, with I_h, fcc, and hcp higher by 0.58, 0.84, and 1.14 eV, respectively.

C. OPTET Clusters. At this point, it is appropriate to note that infractions of the above rules for *small* clusters are unavoidable and thus are tolerated to a certain degree by such small clusters; e.g., orbitals that may prefer to be localized in tetrahedra may polarize strongly toward faces or even edges under certain circumstances in order to minimize nonbonded (orthogonality induced) repulsions. For example, although the three OPTET clusters are all composed solely of surface atoms, OPTET(I) contains two atoms each involved in four bond pairs (in violation of rule ϵ; furthermore, these two atoms are *adjacent*). OPTETS (II) and (III) each contain one such atom. In addition, OPTETs (II) and (III) each have a single infraction against rule δ (edge-sharing), while OPTET (II) also has a single violation against rule γ (two orbitals in face-shared tetrahedra that are not spin-paired). Overall, this accounts for two infractions for OPTETS (I) and (III) and three infractions for OPTET(II). Thus, the explanation of the relatively high energy of OPTET(III) in comparison with OPTETS (I) and (II) lies in the relatively large number of doubly occupied tetrahedra [four for OPTET(III) vs. one for OPTET(I) and two for OPTET(II)].

We have shown in section IIIB that the electronic structures of very small clusters (less than eight atoms) are characterized by electrons localized in bond midpoints, leading to very small bond angles (57–70°). Our various calculations indicate that the OPTET or γ-brass structures should be the most stable for clusters as small as Li_8 [γ-(4,4), T_d] up to clusters as large as 40 atoms or so. The Li_8 OPTET cluster involves a complete filling of the first two γ-brass shells and consists of a central tetrahedron with four capping atoms, making a total of five tetrahedra. Incidentally, this Li_8 cluster is a serious violator of rule δ (edge-sharing); its electronic structure consists of four doubly-occupied tetrahedra (the central tetrahedron is empty), each sharing three edges with adjacent doubly-occupied tetrahedra (six infractions against rule δ). As a consequence, each of these four bond pairs consists of one orbital localized on a bond midpoint and one orbital localized on a face, for a net overlap of $\approx$0.67, significantly smaller than the 0.74–0.78 overlap for typical (rule-abiding) doubly occupied tetrahedra. The first three γ-brass shells are complete at 14 atoms, leading to the γ-(4,4,6), T_d Li_{14} structure with 17 tetrahedra. By applying the rules to this Li_{14} cluster, we predict an electronic structure consisting of a doubly occupied central tetrahedron and six pairs of face-sharing singly occupied tetrahedra along the six edges of the central tetrahedron. Thus, this Li_{14} cluster may be quite stable, although it does result in four infractions against rule ϵ. The lowest energy Li_{13}^+ cluster is derived from this Li_{14} cluster by removing one atom from the outer shell and the two electrons occupying the face-shared tetrahedral pair formed by that atom.

Larger OPTET clusters are constructed by adding atoms to concave surface sites of the smaller OPTET clusters, forming at least two new tetrahedra for each atom added. For larger OPTET clusters, the number of tetrahedra shared by a given atom tends to increase as the ratio of empty to occupied tetrahedra increases. Eventually, the clusters reach sufficient size such that none of the rules are broken. Several low-lying OPTET isomers may be competetive for any given size of cluster. The fourth and fifth γ-brass shells contain 12 atoms each, leading to a M_{26} cluster with 57 tetrahedra [γ-(4,4,6,12), T_d] and a M_{38} cluster with 97 tetrahedra. [γ-(4,4,6,12,12), T_d]. Each of the four first-shell atoms of the M_{26} cluster has full icosahedral coordination. In the M_{38} cluster, all eight atoms in the first two γ-brass shells have full icosahedral coordination.

The OPTET clusters generally lead to local fivefold symmetry axes, a result that arises from the efficient packing of tetrahedral hollows. Thus, a strict adherence to forming near perfect tetrahedra is inconsistent with 3D space groups but could play an important role in stabilization of amorphous structures.[7] However, allowing major distortions to a small fraction of the tetrahedra can lead to periodic structures. For example, the γ-(4,4,6,12), T_d cluster of Li_{26} is isostructural with the 26-atom $Zn_4Cu_4Cu_6Zn_{12}$ cluster forming the basic motif of γ-brass (Cu_5Zn_8).[42] These 26-atom clusters are centered at bcc lattice positions to form the γ-brass bulk structure. Thus, bulk γ-brass (Cu_5Zn_8) contains numerous fairly regular tetrahedra and relatively few severely distorted tetrahedra. In addition, many other alloy structures involve rather complicated networks of tetrahedra, e.g., the Frank–Kasper alloys[43,44] and the Laves phases.[43] Thus, the rules of section IVB should provide a basis for a better understanding of the electronic structures of many alloys.

The limiting values (as $n \to \infty$) for the number of bulk sites per atom are one bond midpoint per atom for 1D, two triangular hollows per atom for planar close-packed, no more than five tetrahedral hollows per atom for OPTET, two tetrahedra per atom (and one octahedron per atom) for hcp or fcc, and six quasi-tetrahedra per atom for bcc. The quasi-tetrahedra for bcc each have four edges of normal length and two edges that are 15% longer in length. Perfect tetrahedra (with six edges of equal length) alone cannot be packed into a bulk structure without involving significant distortions (strain). Thus, for very large clusters, structures consistent with periodicity (hcp, fcc, bcc) eventually dominate.

D. GVB Descriptions of Bulk Metals. The previous discussions show that the optimum intermediate-sized clusters are *not* the most symmetric ones but that the stable structures can be predicted by using basic principles. These principles are summarized by a set of rules given in section IVB. Here, we apply these rules to close-packed (hcp and fcc) bulk elemental metals. In section IVE we present a simple rationalization of some dramatic trends in solid solubilities of alloys.

Close-packed (cp) systems have twice as many tetrahedra as atoms. In fcc, each tetrahedron shares edges with six other tetrahedra, whereas in hcp, each tetrahedron shares one face with another tetrahedron and edges with three other tetrahedra.

For a cp alkali or noble metal, only half the tetrahedra need be occupied by electrons, making the cp metals far more stable than the small cp clusters (where all tetrahedra are occupied, some with two electrons). With half the tetrahedral sites empty, these extended systems are excellent conductors.

The Be and Zn columns, with *two valence sp electrons* per atom, have one electron per tetrahedron. Thus, the GVB model suggests that the optimum electronic structure be visualized in terms of one valence electron per tetrahedron. This is consistent with an *experimental wave function* for hcp beryllium metal derived from coherent X-ray diffraction data, where it is concluded that "charge flows into the tetrahedral hole regions and out of the nuclear regions and octahedral channels."[45] For the perfect crystal all sites are filled, leading to a semimetal. The conductivity is expected to be very sensitive to vacancies and the number of electrons on impurity atoms (hole conductor for group I (group 1),[55] normal

(42) Taylor, A. *X-Ray Metallography*; Wiley: New York, 1961.

(43) Hume-Rothery, W.; Raynor, G. V. *The Structure of Metals and Alloys*, 4th ed.; Institute of Metals: London, 1962.

(44) Frank, F. C.; Kasper, J. S. *Acta Crystallogr.* **1959**, *12*, 483. **1958**, *11*, 184.

(45) Massa, L.; Goldberg, M.; Frishberg, C.; Boehme, R. F.; La Placa, S. J. *Phys. Rev. Lett.* **1985**, *55*, 622.

conductor for group III (group 13)). Our rules do *not* predict which cp structure is favored for systems with two or less valence sp electrons per atom. The differences in energy between the hcp and fcc forms for these systems could involve more subtle longer range interactions. Indeed, the alkali metals[16,46] and the alkaline-earth metals[16] seem to have nearly identical energies for hcp, fcc, and bcc. The low temperature structure of Li is currently unknown, but believed to be ≈75% close-packed rhombohedral 9*R* (abcbcacab stacking of the planar close-packed layers; hcp has aba stacking and fcc has abc stacking) and ≈25% bcc.[46] The noble metals (Cu, Ag, and Au) are all fcc while Zn and Cd are hcp.[16]

For cp systems with *three valence sp electrons* per atom, half the tetrahedra must be doubly occupied, while the other half are singly occupied. For both hcp and fcc it is possible to arrange the occupations so that adjacent tetrahedra are not *both* doubly occupied (satisfying rule δ). In this arrangement, each pair of adjacent tetrahedra contains three electrons. However, the hcp structure contains adjacent face-sharing tetrahedral pairs, while the fcc structure contains only edge-sharing tetrahedral pairs; thus, based on rule γ, we conclude that fcc should be *strongly favored* over hcp for group III (group 13). Indeed, neither B, Al, Ga, nor In leads to stable hcp structures, while Al leads to fcc and In to a slightly distorted fcc. With a hole in every other tetrahedron, these systems are good conductors.

With four valence electrons per atom, all tetrahedra would be doubly occupied, strongly disfavoring either cp structure (rules γ and δ). Indeed, except for Pb, the group IV (group 14) elements are either nonmetals (with strong two-electron covalent bonds) or metals with low coordination numbers. It is well-known that Hg, Tl, Pb, and Bi exhibit properties suggesting that the 6s pairs are particularly stable and do not easily form the normal sp hybrids with the 6p orbitals, perhaps rationalizing the fcc form for Pb and the hcp form for Tl.

E. Solid Solubilities. Rules δ and γ place upper limits of $2e^-$/atom for hcp structures and $3e^-$/atom for fcc. These limits are consistent with known alloy formations and maximum solid solubility limits.[43,47] Thus, comparing atoms with similar sizes [Ag ($1e^-$), Zn ($2e^-$), Al ($3e^-$), and Sn ($4e^-$) with metallic radii[16] of 1.44, 1.39, 1.43, and 1.54 Å, respectively], Ag and Zn are both highly soluble in fcc Al [23.8 and 66.5 at. % (atomic percent), respectively] while the solubility of Sn in Al is only 0.02 at. %. Similarly, the solubilities of Al and Sn in hcp Zn are small (2.4 and ≈0.10 ± 0.04 at. %, respectively) while Ag–Zn alloys form hcp phases with up to 33 at. % Ag (Ag_1Zn_2). The $3e^-$/atom limit does not restrict solubilities in fcc Ag ($1e^-$/atom); hence, the solubilities are all high (Zn, 40.2 at. %; Al, 20.34 at. %; Sn, 11.5 at. %).

The fact that the maximum solubility limits of Sn in Al and of Sn or Al in Zn are very small (and not zero) is not necessarily a result of a slight violation of the rules. These solubilities may depend crucially on imperfections of the substrate (e.g., stacking faults, vacancies, dislocations, impurities, etc.). The solute atoms may tend to migrate to dislocations, surfaces, or polycrystalline grain boundaries and may actually lead to the creation of a higher density of such defects than present in the pure metal at the same temperature. For Al in Zn, the maximum solubility (2.4 at. % at 655 K or $0.94T_m$ where T_m is the melting temperature) decreases to 1.2 at. % at $0.76T_m$ and 0.15 at. % at $0.43T_m$. Thus, at lower temperatures (fewer vacancies), the limits of such solubility decrease. There are substantial disagreements among the various experiments regarding the exact values of the solubilities for Sn in Zn. Three different experiments regarding the solubility of Sn in Zn range from too small to measure (0.0 at. %) to slightly greater than 0.06 at. % (at $0.97T_m$; somewhat greater than 0.03 at. % at $0.43T_m$) to less than 0.14 at. % (presumably near T_m). The solubility of Sn in Al reaches its maximum of 0.02 at. % at $0.96T_m$, diminishes to 0.009 at. % at $0.86T_m$, and is negligibly small at $0.47T_m$. Indeed, the solubilities seem to vanish as the temperature is lowered for each of these three cases. Presumably, the density of defects similarly decreases with decreasing temperature. In contrast, for cases where the solid solubilities are high, the solubilities tend to decrease somewhat with increasing temperature but often reach sizable limits as the temperature approaches absolute zero (these systems are presumably metastable).

Here we have focused on global electron/atom trends. Of course, certain binary combinations might lead to local electronic structures that would further restrict solubility. For example, $Ag_{1-x}Sn_x$ is hcp for $0.118 \leq x \leq 0.246$ and a slightly distorted hcp for $0.237 \leq x \leq 0.25$. The $2e^-$/atom limit applied to hcp $Ag_{1-x}Sn_x$ leads to the restriction $x \leq 0.33\bar{3}$, which is somewhat less restrictive than the experimental limit of $x \leq 0.25$ (1.75 e^-/atom). Similarly, the $2e^-$/atom limit applied to hcp $Ag_{1-x}Al_x$ leads to the restriction $x \leq 0.50$. This is in agreement with the experimental limits of $0.23 \leq x \leq 0.42$ for hcp $Ag_{1-x}Al_x$.

F. Force Fields. Fully correlated ab initio GVB calculations of the quality described herein are currently limited to a relatively small number of atoms (less than 100). This is a severe limitation since many phenomena in metallic systems would require thousands of atoms for a proper description. In order to extend our studies to such large systems, we have been using our cluster results to develop force fields that could be used in both static and dynamical simulations.[34] We find that, because of the special interstitial nature of the bonding, these force fields should not be described merely in terms of nuclear positions but must also involve the positions of the localized (correlated) electrons. Thus, the force field must involve both nuclear *and* electronic coordinates. These force fields involve such three-body terms as atom–electron–atom bend and atom–electron–atom asymmetric stretch, etc. Although still under investigation, we believe that such force fields will allow an accurate description of metallic systems that will permit reliable simulations for large systems.

V. Summary

Results of generalized valence bond studies for a variety Li_{13}^+ geometries lead to a set of rules based on the paradigm of electrons localized in tetrahedral hollows. These rules lead to predictions of structure [e.g., the "zig-zag" clusters for M_n, $n \lesssim 8$ and the "OPTET" clusters for M_n, $8 \leq n \lesssim 40$] and to new rationalizations of solid solubility limits involving close-packed bulk metals. We expect that these rules apply to the valence sp electrons of a variety of structures for pure metals and for alloys, including fcc, hcp, γ-brass,[42,43] the Laves phases,[43] and Frank–Kasper alloys.[43,44] The present rules may require modification for metallic structures that possess severely distorted tetrahedra (e.g., body-centered cubic) and for structures that contain too few tetrahedra to accommodate all of the valence sp electrons (e.g., rule ζ).

The interstitial localization of the valence electrons suggests a new approach to force fields for describing metallic systems where terms involving both electronic and nuclear positions are included. Such force fields should allow simulation of the GVB wave functions for systems containing thousands of metal atoms.

The rules in combination with the force field should form a useful starting point in developing valence bond ideas for predicting geometries, electronic structure, and properties of metallic clusters, and for describing localized phenomena in solids, such as defects interfaces, or chemisorbed species. This should provide useful conceptual ideas for predicting the chemistry and catalytic properties of such systems.

Acknowledgment. This work was partially supported by grants from the National Science Foundation (Nos. DMR82-15650 and DMR84-21119).

Appendix A. Calculational Details

In this Appendix we describe various details concerning the calculations. The results presented in the previous sections of this

(46) Overhauser, R. W. *Phys. Rev. Lett.* **1984**, *53*, 64. Takemura, K.; Syassen, K. *Phys. Rev. B* **1983**, *28*, 1193. Anderson, M. S.; Swenson, C. A. *Phys. Rev. B* **1985**, *31*, 668.

(47) Hansen, M. *Constitution of Binary Alloys*; McGraw-Hill: New York, 1958, and supplements by Elliot, R. P. (1965), Shunk, F. A. (1969), and Moffatt, W. G. (1983). Also see reviews in *Bull. Alloy Phase Diagrams*, 1980–1986.

communication stem from the usual generalized valence bond (GVB) self-consistent field[2,48-51] and configuration interaction (CI)[52] methods as described in the various sections of this Appendix. For comparison, this Appendix also includes results obtained from unrestricted (spin-polarized) Hartree–Fock (UHF) and restricted (nonspin-polarized) Hartree–Fock (HF). Section A.1 describes a series of studies with various basis sets. The results described in the previous sections are derived from all-electron ab initio wave functions using basis set D and are discussed in more detail in section A.3. A series of studies for the three high-symmetry clusters is presented in section A.2. Further details of the various wave functions are discussed in sections A.4 and A.5.

A.1. Basis Sets. As an initial test for the basis sets, we calculated equilibrium bond lengths (R_e), force constants (k_e), bond energies (D_e), and total energies (E_e) for both Li_2^+ and linear Li_3^+. These cases (Li_2^+ and linear Li_3^+) were chosen because the bonding is similar to that of Li_{13}^+. Thus, in all cases the lowest energy many-electron states are described by valence orbitals localized in interstitial regions. The results are given in Table III.

Basis sets A–G all share the same 3s Dunning[53] *valence double-ζ* (VDZ) contraction of the 9s Huzinaga[54] *Gaussian-type orbital* (GTO) s basis. These bases differ only in the choice of p basis and d basis (see Table IV).

Bases B, E, F, and G all entail variations of the Dunning (4p) GTO p basis (derived from the ^2P Li $1s^22p^1$ atomic state). These four sets of p GTO are contracted into a single set of functions (*minimum basis set*, MBS) in basis set B, and they are contracted double-ζ (DZ) in bases E, F, and G. In addition, the p basis is scaled by a factor of 1.1 for basis sets F and G. The scale factor ($\zeta = 1.10$) is near optimal (with respect to the total energy) for Li_2^+ ($\zeta_{opt} = 1.114$) and for Li_3^+ ($\zeta_{opt} = 1.111$) calculated at bond length $R = 3.14$ Å. Basis set G also includes a single set of d GTO's optimized for Li_2^+ at $R = 3.14$ Å ($\alpha_{opt} = 0.13$).

Basis set C contains a single set of p GTO's with an exponent $\alpha = 0.10$. This p exponent ($\alpha = 0.10$) is near optimum for Li_2^+ ($\alpha_{opt} = 0.110$ at $R = 3.1$ Å, $\alpha_{opt} = 0.106$ at $R = 3.24$ Å), for rhombic Li_4 ($\alpha_{opt} = 0.102$ at $R = 3.064$ Å, $\theta = 60°$), and for Li_8 ($\alpha_{opt} = 0.113$ at $R = 3.1$ Å, tetracapped tetrahedron). These GTO p exponents are considerably tighter than that optimized for the ^2P Li ($1s^22p^1$) excited state atom ($\alpha_{2p} = 0.0466$). The exponent $\alpha = 0.10$ corresponds to scaling α_{2p} by a factor $\zeta = 1.46$.

Basis set D contains two sets of p GTO contracted MBS (2p/1p) into a single set of Slater-like functions. This is accomplished by starting with the optimum two-Gaussian basis[54] for the 2p state of H and scaling the orbital exponents while holding the contraction ratio fixed ($d_2/d_1 = 2.411792$). Note that the Li 2p atomic state is very similar to the H 2p state since the Li nucleas (3+) is effectively shielded by the Li $1s^2$ core electrons for this state. The scale factor ($\zeta = 1.5$) was optimized for Li_2^+ at $R = 3.19$ Å.

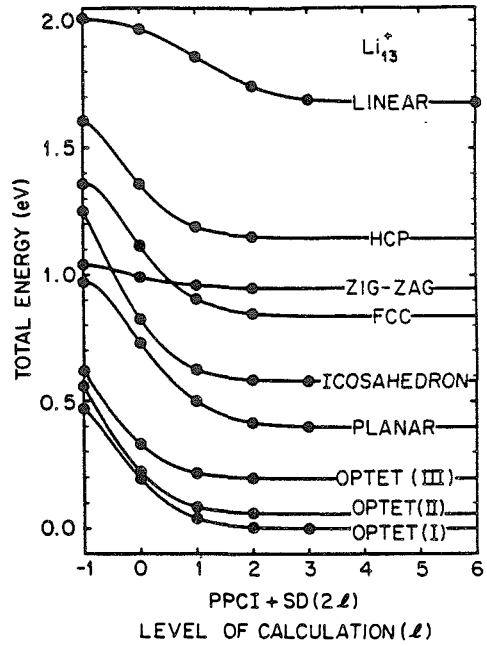

Figure 21. Total energies for nine Li_{13}^+ clusters for the PPCI+SD(2*l*) wave functions as a function of *l*. Total energies are shown relative to the PPCI+SD(12) total energy of OPTET(I).

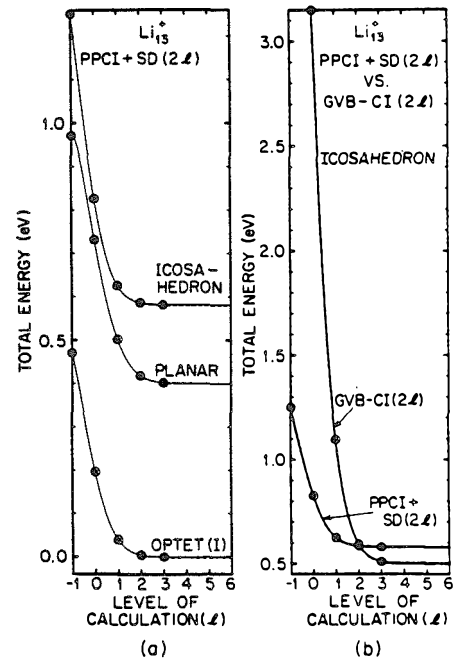

Figure 22. (a) Total energies for the OPTET(I), I_h, and planar Li_{13}^+ clusters for the PPCI+SD(2*l*) wave functions as a function of *l* [relative to the PPCI+SD(12) total energy of OPTET(I)]. The solid lines show the extrapolations to $l = 6$ using $l = -1, 0, 1, 2$, and 3. The dashed lines show the extrapolations to $l = 6$ using $l = -1, 0, 1$, and 2. The difference in total energy for the two extrapolations is 1.6 meV for OPTET(I), 0.9 meV for I_h, and 2.0 meV for the planar cluster. (b) Total energies of the I_h Li_{13}^+ cluster for the PPCI+SD(2*l*) and the GVBCI(2*l*) tunctions of the full GVB-CI as a function of *l* [relative to the PPCI+SD(12) total energy of OPTET(I)]. The difference in the extrapolated energies for PPCI+SD(12) and GVBCI(12) is 0.080 eV.

(48) Hunt, W. J.; Hay, P. J.; Goddard III, W. A. *J. Chem. Phys.* **1972**, *57*, 738.

(49) Bobrowicz, F. W.; Goddard III, W. A In *Modern Theoretical Chemistry: Methods of Electronic Structure Theory*, Schaefer III, H. F., Ed.; Plenum: New York, 1977; Vol. III, Chapter 4.

(50) Bair, R. A.; Goddard III, W. A.; Voter, A. F.; Rappé, A. K.; Yaffe, L. G.; Bobrowicz, F. W.; Wadt, W. R.; Hay, P. J.; Hunt, W. J. GVB2P5 program, unpublished. See Bair, R. A. Ph.D. Thesis, California Institute of Technology, 1980, and ref 48.

(51) Yaffe, L. G.; Goddard III, W. A. *Phys. Rev. A* **1976**, *13*, 1682. Goodgame, M. M. Ph.D. Thesis, California Institue of Technology, 1984.

(52) Hay, P. J.; Dunning, Jr., T. H.; Goddard III, W. A. *J. Chem. Phys.* **1975**, *62*, 3912.

(53) Dunning, Jr., T. H.; Hay, P. J. In *Modern Theoretical Chemistry: Methods of Electronic Structure Theory*, Schaefer III, H. F., Ed.; Plenum: New York, 1977; Vol. III, Chapter 1.

(54) Huzinaga, S. *J. Chem. Phys.* **1965**, *42*, 1293.

(55) In this paper the periodic group notation (in parentheses) is in accord with recent actions by IUPAC and ACS nomenclature committees. A and B notation is eliminated because of wide confusion. Groups IA and IIA become groups 1 and 2. The d-transition elements comprise groups 3 through 12, and the p-block elements comprise groups 13 through 18. (Note that the former Roman number designation is preserved in the last digit of the new numbering: e.g., III → 3 and 13.)

TABLE III: Basis Set Comparison for $Li_2^+(^2\Sigma_g^+)$ and for Linear $Li_3^+(^1\Sigma_g^+)$;[a] Basis Sets C and D Were Selected for Studies of the Li_{13}^+ Systems

basis set[a]	scale factor (p basis)	R_e, Å	k_e, eV Å^{-2}	D_e,[b] eV	E_e, hartree
Li_2^+					
A (9s,0p,0d)/(3s,0p,0d)		3.377	0.458	0.543	-14.687 68
B (9s,4p,0d)/(3s,1p,0d)	1.0	3.286	0.718	1.070	-14.707 05
C (9s,1p,0d)/(3s,1p,0d)	1.46	3.195	0.918	1.182	-14.711 16
D (9s,2p,0d)/(3s,1p,0d)	1.5	3.152	0.951	1.206	-14.712 05
E (9s,4p,0d)/(3s,2p,0d)	1.0	3.181	0.901	1.225	-14.712 75
F (9s,4p,0d)/(3s,2p,0d)	1.1	3.141	0.945	1.236	-14.713 15
G (9s,4p,1d)/(3s,2p,1d)	1.1	3.146	0.890	1.274	-14.714 53
STO 5s,5p,3d[d]		3.127	0.883	1.280	-14.716 18
experiment[e]		3.133 (13)	0.888 (10)	1.2980 (7)	
Li_3^+					
A (9s,0p,0d)/(3s,0p,0d)		3.126	1.225	0.493	-22.137 53
C (9s,1p,0d)/(3s,1p,0d)	1.46	3.149	1.760	0.804	-22.172 45
D (9s,2p,0d)/(3s,1p,0d)	1.5	3.113	1.782	0.808	-22.173 46
E (9s,4p,0d)/(3s,2p,0d)	1.0	3.140	1.705	0.830	-22.174 99
F (9s,4p,0d)/(3s,2p,0d)	1.1	3.115	1.754	0.830	-22.175 40
G (9s,4p,1d)/(3s,2p,1d)	1.1	3.123	1.670	0.856	-22.177 71

[a] All wave functions are full GVB. Li_2^+ is a one-valence electron system, so that GVB and HF are equivalent. Since Li_3^+ is a two-valence electron system, GVB-PP and GVB-CI are equivalent. [b] The dissociation limits are $Li_2^+ \rightarrow Li + Li^+$ and $Li_3^+ \rightarrow Li + Li_2^+$. [c] 1 hartree = 27.21161 eV. [d] Results using a large Slater-type orbital (STO) basis set, ref 12. The Li + Li^+ assymptote for this basis set is lower than that for Bases A-G by 0.00142 hartree. This is due to a better description of the $1s^2$ core electrons with the STO basis set. [e] Results obtained by extrapolating several Rydberg series of Li_2, ref 13. Numbers in parentheses indicate the experimental uncertainty in the last digit. [f] R_e is the bond distance, k_e the force constant, D_e the bond energy, and E_e the total energy.

TABLE IV: p Bases Contractions Used in Various Calculations[a]

basis set	exponent α_i	contraction coefficient d_i
A	(no p functions)	
B	1.488	0.038 770
	0.266 7	*0.236 257*
	0.072 01	0.830 448
	0.023 70	0.817 656
C	0.10	
D	0.313 371	0.325 652
	0.072 882	0.785 405
E	1.488	0.038 770
	0.266 7	*0.236 257*
	0.072 01	0.830 448
	0.023 70	
F, G[b]	1.800 48	0.038 770
	0.322 707	0.236 257
	0.087 1321	0.830 448
	0.028 6770	

[a] The results of test calculations on Li_2^+ and linear Li_3^+ using these basis sets are given in Table III. In this study, basis set F was used in all Li_n calculations for $n \leq 10$ unless otherwise stated. Basis sets C or D were used in all calculations for $n > 10$. [b] Basis set G also includes a set of d GTO's with exponent $\alpha = 0.13$.

The overall trends of differences in the calculated results (Table III) among the various bases are very similar for both Li_2^+ and linear Li_3^+. The various bases are listed in order of increasing overall quality, as determined by the variational principle (decreasing total energy). The Li_2^+ results calculated with basis set G are in reasonable agreement with results calculated with a large Slater-type orbital (STO) basis[12] and with experiment.[13]

The importance of p and d polarization functions is indicated from a comparison of the results for bases A, F, and G. For Li_2^+, the p_σ functions and d_{z^2} functions contribute 54.4% and 3.0%, respectively, of the total bond energy (of basis set G).

Comparing MBS p-basis results (bases B, C, and D) indicates that the optimum p function for bonding is much more compact ($\zeta \approx 1.5$) than the Li 2p atomic function ($\zeta = 1.0$). [The optimum scale factor for the DZ p basis ($\zeta = 1.1$; F,G) is smaller because of the added flexibility of the DZ basis.] Scaling the p basis ($\zeta > 1.0$) results in a decrease in the calculated R_e and an increase in the calculated k_e.

These results indicate that bases C and D should be reasonably accurate for cluster calculations. Calculations with bases E, F, and G generally result in increases in the computation time by factors of at least 5, 5, and 40, respectively. We have employed basis set E in the calculations presented here for all clusters of ten atoms or less. For these cases, the GVB results refer to untruncated GVB-CI wave functions (full CI within the valence

TABLE V: Optimum Geometries for the High-Symmetry Li_{13}^+ Clusters[a]

	basis set C				basis set D[a]	
structure	R_e^{RMS},[b] Å	k_e, eV Å^{-2}	E_e, hartree	ΔE_e, eV	E_e, hartree	ΔE, eV
GVB-PP[c]						
icosahedron	3.241	15.0	-96.673 71	0.00	-96.687 83	0.00
fcc	3.239	12.9	-96.667 10	0.18	-96.683 88	0.11
hcp	3.244	13.3	-96.659 26	0.39	-96.674 77	0.36
PPCI+SD(0)[d]						
icosahedron	3.234	15.1	-96.688 25	0.00	-96.703 44	0.00
fcc	3.245	12.7	-96.676 66	0.32	-96.692 81	0.29
hcp	3.228	13.4	-96.667 70	0.56	-96.683 89	0.53
PPCI+SD(2)[d]						
icosahedron	3.230	15.2	-96.695 69	0.00	-96.710 84	0.00
fcc	3.243	12.6	-96.684 33	0.31	-96.700 64	0.28
hcp	3.222	13.5	-96.673 78	0.60	-96.690 14	0.56

[a] Calculated at $R^{RMS} = 3.19$ Å (see section A.1). [b] $R_e^{RMS} = R_e^{BS} = R_e^{SS}$ for the fcc and hcp clusters. For the icosahedron, $R_e^{BS} = 0.964 R_e^{RMS}$; $R_e^{SS} = 1.014 R_e^{RMS}$. [c] GVB-PP is a 64-configuration MCSCF wave function that allows an independent particle description. [d] The full 73 789-configuration GVBCI was truncated to PPCI+SD(0), 535 configurations, and PPCI+SD(2), 2875 configurations (see section A.4). [e] R_e^{RMS} is the average bond distance, k_e the force constant, E_e the total energy, ΔE the relative energy.

TABLE VI: Relative Total Energies (eV) for Li_{13}^+ Clusters (Basis Set D)

structure[a]	HF[b]	UHF[c]	GVB-PP[d]	PPCI+SD(2l)[e,f] l = 0	l = 1	l = 2	l = 3	l = 6
OPTET(I)[g]	0.00	0.00	0.00	0.00	0.00	0.00	0.00	0.00
OPTET(II)[g]	−0.29	0.10	0.09	0.03	0.04	0.06	0.06	0.06
OPTET(III)[g]	−0.03	0.10	0.15	0.14	0.18	0.19	0.20	0.20
planar	1.13	0.03	0.50	0.54	0.46	0.41	0.40	0.40
icosahedron	0.75	0.18	0.78	0.63	0.59	0.58	0.58	0.58
fcc	0.98	0.32	0.89	0.92	0.86	0.84	0.84	0.84
zig-zag chain	0.88	1.27	0.57	0.80	0.92	0.94	0.95	0.95
hcp	1.02	0.53	1.14	1.16	1.15	1.15	1.14	1.14
linear chain	4.70	0.84	1.54	1.77	1.82	1.74	1.69	1.68
correlation[h]	0.00	0.93	1.77	2.04	2.20	2.23	2.24	2.24

[a] The structures are shown in Figures 11, 15–17, 19, and 20. R^{RMS} = 3.19 Å except for the linear chain (R^{RMS} = 3.12 Å) and for the zig-zag chain (R^{RMS} = 3.12 Å, θ = 70°). [b] The HF wave function (closed shell) contains only one configuration (one determinant). The orbitals were optimized with spin restrictions but without spacial (symmetry) restrictions. [c] The UHF wave function (M_S = 0) contains only one configuration (one determinant). The orbitals were optimized without any restrictions (spin or spacial). [d] The GVB-PP wave function contains 64 configurations in the natural orbital representation, but leads only one configuration (64 spin determinants) in the GVB single particle representation. The orbitals were optimized with the usual strong-orthogonality and PP restrictions. The GVB-PP and PPCI (l = −1) total energies are almost identical. The largest difference in total energy for these two wave functions is for the OPTET(I) cluster (0.00035 eV). [e] The PPCI+SD(0), PPCI+SD(2), PPCI+SD(4), PPCI+SD(6), and PPCI+SD(12) wave functions [535, 2875, 7615, 12595 and 16336 configurations, respectively] are truncations of the full GVB-CI wave function [73789 configurations]. The GVB-CI wave function overcomes the strong orthogonality and PP restrictions of GVB-PP. [f] The l = 3 and l = 6 total energies were obtained by extrapolating the PPCI+SD(2l) total energies as a function of l as shown in Figures 21 and 22, except for the following cases where the total energies were calculated exactly. l = 3: OPTET(I), planar icosahedron and linear chain; l = 6: linear chain. [g] The low symmetry clusters generated from rules α through ζ; see Figure 19. [h] The electron correlation energy of the OPTET(I) cluster is listed for each wave function. The correlation energy for each wave function is defined as the difference between the total energy calculated with that wave function and the HF total energy (−96.65158 hartree).

TABLE VII: Cartesian Coordinates for the Li_{13}^+ OPTET Clusters [a]

atom(s)	x, Å	y, Å	z, Å
OPTET(I), ρ = 0.071 Å			
1, 2	0.000 00	±1.593 47	1.127 55
3, 4	±1.563 94	0.000 00	−1.179 28
5, 6	±2.619 08	0.000 00	1.838 00
7, 8	0.000 00	±2.735 47	−1.767 69
9, 10, 11, 12	±2.728 11	±2.679 28	0.000 00
13	0.000 00	0.000 00	3.816 22
OPTET(II), ρ = 0.059 Å			
1	0.000 00	−1.600 50	1.080 96
2	0.000 00	1.482 29	1.125 96
3, 4	±1.569 28	0.000 00	−1.253 32
5, 6	±2.750 71	−0.026 11	1.650 63
7	0.000 00	−2.720 96	−1.859 73
8	0.000 00	2.688 11	−1.856 32
9, 10	±2.709 53	−2.724 83	−0.112 60
11, 12	±2.607 53	2.765 03	0.000 00
13	0.000 00	4.591 90	0.654 58
OPTET(III), ρ = 0.070 Å			
1	0.000 00	0.000 00	−0.207 16
2, 3	0.000 00	±2.879 94	−1.474 51
4, 5, 6, 7	±2.613 25	±1.640 63	0.000 00
8, 9	0.000 00	±2.579 08	1.667 27
10, 11	±1.616 48	0.000 00	2.538 28
12, 13	0.000 00	±1.610 04	4.738 12

[a] R^{RMS} = 3.19 Å; ρ is the root mean square deviation of R^{RMS}. The OPTET clusters are shown in Figure 19.

orbitals) where the orbitals have been optimized at the GVB-CI level. The calculations on the Li_{10} ring cluster are described in greater detail elsewhere.[5] The calculations on Li_{13}^+ employ bases C or D and are described in further detail in the subsequent sections of this Appendix.

A.2. High-Symmetry Li_{13}^+ Clusters. The I_h, fcc, and hcp clusters (Figures 15–17) each consist of a central "bulk" atom surrounded by 12 surface atoms equidistant from the bulk atom. We performed calculations for several internuclear separations (R^{BS}) between the bulk and surface atoms and interpolated the results to obtain equilibrium values (R_e^{BS}). Results at the perfect-pairing GVB (GVB-PP)[48] and configuration interaction GVB (GVB-CI) levels are shown in Table V. Details of the GVB-PP and various truncated GVB-CI wave functions [PPCI+SD(0), PPCI+SD(2), etc.] are given in sections A.4 and A.5. The GVB-CI wave function allows a less-restricted treatment of the electron correlation than the GVB-PP wave function. Consequently, the GVB-CI leads to slightly lower total energies (≈0.44 eV) and slightly smaller bond lengths (≈0.009 Å) in comparison to GVB-PP.

For the icosahedron, R^{BS} is 4.9% smaller than the surface–surface bond distance (R^{SS}). In order to compare bond lengths of different structures, we use the root mean square distance (R^{RMS}). For the fcc and hcp structures $R^{RMS} = R^{BS} = R^{SS}$, whereas for the I_h structure, $R^{RMS} = 0.986R^{SS} = 1.037R^{BS}$. The validity of R^{RMS} as a measure of size is indicated by the close correspondences: $R_e^{RMS}(I_h)$ = 3.230 Å, R_e^{RMS}(fcc) = 3.243 Å, and R_e^{RMS}(hcp) = 3.222 Å.

For the hcp cluster we fixed the c/a ratio[43] at 1.633 so that all the nearest-neighbor distances are equal. Thus, the fcc and hcp clusters both have the same number of bulk–surface and surface–surface nearest neighbors. Even so, hcp leads to a bond distance 0.02 Å smaller than fcc.

Optimum bond lengths (R_e^{RMS}), force constants, total energies, and relative energies (ΔE_e) were calculated for the I_h, fcc, and hcp clusters by using basis set C. Since the energy differences among these three high-symmetry Li_{13}^+ are rather small (≈21 meV/atom), we also carried out calculations using a slightly better p basis (basis set D). We did *not* optimize R^{RMS} with basis set D; rather we chose R^{RMS} = 3.19 Å based on the average of the I_h, fcc, and hcp values for basis set C (R_e^{RMS} = 3.23 Å) corrected by the difference in R_e values calculated with the two basis sets for linear Li_3^+ (0.04 Å, see Table III). The results calculated by using basis C (Table V) justify choosing a fixed R^{RMS} rather than optimizing separate values for the various clusters. Actually, the relative energies are rather insensitive to the value of R. Thus, changing R^{RMS} by as much as 0.05 Å from R_e^{RMS} would lead to errors in the total energy of less than 0.02 eV (assuming $k_e < 16.0$ eV Å^{-2}). The relative energies (ΔE) of basis set D compare quite favorably with those of basis set C. Thus, at the GVB-CI level [PPCI+SD(2)], the maximum difference in ΔE between the two basis sets is 0.04 eV. We have chosen basis set D and R^{RMS} = 3.19 Å for the lower symmetry clusters (to avoid the expense of further geometry optimizations). Since the total energies for basis set D are slightly lower [≈0.015 hartree] than those for basis set C, the ΔE values from basis set D are expected to be somewhat more reliable than those from basis set C.

A.3. Results for Li_{13}^+ Clusters Using Basis Set D. Total energies (E) of nine Li_{13}^+ structures are given in Table VI for

TABLE VIII: Truncated GVB-CI Results for the Li_{13}^+ Icosahedron

wave function[a]	E, hartree	truncation[b] error, mhartree	size of CI wave function SC	SEF	DET	CPU time,[c] h
PPCI	-96.687834	24.639	64	64	64	0.00
PPCI+SD(0)	-96.703443	9.029	535	760	1876	0.06
PPCI+SD(2)	-96.710836	1.636	2875	4300	11236	0.38
PPCI+SD(4)	-96.712295	0.177	7615	11680	31096	1.60
PPCI+SD(6)	-96.712457	0.015	12595	19720	53176	3.63
PPCI+SD(12)	-96.712472[b]	0.000	16336	26176	71488	6[d]
GVBCI(0)	-96.618059	97.344	1	1	1	0.00
GVBCI(2)	-96.693517	21.886	478	703	1819	0.00
GVBCI(4)	-96.711957	3.446	11078	28278	98694	0.23
GVBCI(6)	-96.715067	0.336	46835	147042	558810	3.50
GVBCI(12)	-96.715403[b]	0.000	73789	226512	853776	9[d]

[a] Basis set D, R^{RMS} = 3.19 Å. [b] The PPCI+SD(12) and GVBCI(12) energies were obtained by extrapolating the results for $2l$ = -2, 0, 2, 4, and 6 to $2l$ = 12 (see Figure 2). [c] Machine time required on a DEC VAX 11/780 computer. The GVBCI($2l$) calculations utilize symmetry in solving for the wave functions (D_{2h} for the Li_{13}^+ icosahedron); cases with lower symmetries would involve much more CPU time, e.g., by factors of more than 4, 16, and 64 for C_{2v}, C_s, and C_1 symmetries, respectively. [d] Estimated CPU time.

HF, unrestricted HF (UHF), GVB-PP, and various truncated GVB-CI wave functions. Details of these wave functions are given in sections A.4 and A.5.

For seven of the nine clusters we have chosen R^{RMS} = 3.19 Å based on results given in section A.2. For the linear chain Li_{13}^+ cluster (Figure 11a) we chose R = 3.12 Å based on R_e = 3.143 Å for the infinite Li chain [$Li_{(1D)}$] calculated with basis set E[5] and the 0.027-Å correction between basis set E and basis set D (see Table III). For the zig-zag chain (Figure 11b), we chose R = 3.12 Å and a bond angle (θ) of 70°. This bond angle (θ = 70°) is close to that optimized for Ψ^{GVB-PP} for the Li_{13}^+ zig-zag chain (θ_{opt} = 70.7° at R = 3.12 Å) and to the optimum bond angle of the planar Li_6 cluster (θ_{opt} = 69.8°, Figure 9b) calculated at the full GVB level.

The OPTET clusters (Figure 19) are similar to the icosahedron in that the nearest-neighbor bond lengths (or tetrahedral edge lengths) cannot all be chosen equal. For the icosahedron, the ratio R^{BS}/R^{SS} is fixed by symmetry. The OPTET clusters have relatively low symmetries, thus there is considerable freedom in choosing the various bond lengths. Geometries for the OPTET clusters were obtained by minimizing the root mean square deviation (ρ) of all (N) nearest-neighbor bond lengths (R_i). Thus

$$\rho^2 = \frac{1}{N}\sum_{i=1}^{N}(R_i - R^{RMS})^2 \qquad (8)$$

was minimized for N = 38 different bond lengths for each of the three OPTET clusters (each of the OPTET clusters contains 38 nearest-neighbor contacts). Obtaining the geometries in this fashion is equivalent to minimizing the strain energy, assuming equivalent harmonic bonds between each pair of nearest-neighbor atoms. Cartesian coordinates for the three OPTET clusters (R^{RMS} = 3.19 Å) are given in Table VII. Nearest-neighbor bond lengths for these clusters all lie in the range R = 3.19 ± 0.11 Å, while next-nearest neighbors are at $R \approx$ 5.2 Å.

It is important to include the valence electron correlation effects implicit in the GVB wave function. For the I_h cluster, we estimate that the total energy of the full (untruncated) GVB-CI wave function is -96.71540 hartree (see section A.5). In comparison, the PPCI+SD(4), GVB-PP, UHF, and HF wave functions lead to total energies that are higher than the estimated full GVB-CI total energy by 0.08, 0.75, 0.98, and 2.49 eV, respectively [1 eV = 36.74902 mhartrees].

We find that the PPCI+SD($2l$) wave functions lead to very efficient truncations of the full GVB-CI wave function and include a large fraction of the energy difference between GVB-PP and full GVB-CI (see section A.5). PPCI+SD($2l$) energies for the various Li_{13}^+ clusters are plotted as a function of l in Figure 21 [PPCI+SD(-2) ≡ PPCI ≈ GVB-PP] and extrapolated to $2l$ = n_e (n_e is the total number of valence electrons; n_e = 12 for Li_{13}^+). Since the various curves in Figure 21 do not all have exactly the same form, we have used "cubic" splines[34] with segments having the functional form

$$E(l) = \sum_{i=0}^{3} c_i (n_e - 2l)^{4i} \qquad (9)$$

to perform the various extrapolations (the power of four was found to be required in order to give accurate extrapolations). In order to test the extrapolations, we compare the extrapolated limits (l = 6) obtained with four points (l = -1, 0, 1, and 2) with those obtained with five points (l = -1, 0, 1, 2, and 3). Figure 22a shows the 4-point (dashed line) and 5-point (solid line) extrapolations for the OPTET(I), planar (Figure 20), and I_h clusters. The 4-point total energy limits are lower than the 5-point limits by 1.6, 0.9, and 2.0 meV for the OPTET(I), planar, and I_h clusters, respectively. The linear cluster differs from the other clusters in that the convergence of the PPCI+SD($2l$) energies with increasing l is rather slow, thus we calculated the PPCI+SD(12) energy exactly. For the linear cluster, the 4-point and 5-point l = 6 extrapolated limits are higher than the l = 6 calculated value by 37 and 3.6 meV, respectively. These results indicate that the extrapolated total energies in Table VI differ from calculated values by only negligible amounts (≈2 meV).

Figure 21 shows that the relative energies (ΔE_e) of the various clusters are fairly consistent for the GVB-PP and truncated GVB-CI wave functions [PPCI+SD($2l$), l = 1, 2, 3, ..., 6], except for the zig-zag chain cluster. (Eliminating the zig-zag chain cluster, the GVB-PP and various PPCI+SD($2l$) wave functions all give the same ordering of the eight remaining Li_{13}^+ structures.) In comparison to the PPCI+SD(12) results, the root mean square errors in ΔE_e values for the various PPCI+SD($2l$) wave functions are 0.165, 0.089, 0.057, 0.023, and 0.004 eV for l = -1 (PPCI or GVB-PP), 0, 1, 2, and 3, respectively. Since the difference in *total energy* between the PPCI+SD(12) and full GVB wave functions is only ≈0.08 eV (see section A.5), the PPCI+SD(12) ΔE values represent a very good approximation to the full (untruncated) GVB-CI. The error in the PPCI+SD(12) ΔE values as compared with the full GVB-CI is expected to be much better than ≈0.08 eV due to cancellation effects.

For several cases the relative energies for HF and UHF differ substantially from those of GVB. In comparison with the PPCI+SD(12) results, the root mean square errors in ΔE for HF and UHF are 1.11 and 0.47 eV, respectively. The closed-shell HF wave function correctly predicts that, of the nine structures, the OPTET clusters are the lowest in energy and the linear chain is the highest in energy. However, HF does not predict the correct ordering of the three OPTET clusters and gives relative energies for the planar cluster and linear chain that are 0.73 and 3.02 eV too high, respectively. Although the UHF results are somewhat more reliable than the HF results, the planar and linear chain clusters are still poorly described (0.37- and 0.83-eV errors in ΔE, respectively).

A.4. Self-Consistent Field Wave Functions. Here we describe the HF, UHF, and GVB wave functions which have been solved for self-consistently; e.g., the orbitals have been optimized in such

a manner as to give the lowest possible energy (within the particular basis set) for the particular form of wave function. In general, we have allowed the orbitals to break symmetry, almost always leading to substantially lower energies than similar wave functions where symmetry restrictions are imposed on the orbitals.

For the Li_{13}^+ clusters, the Li $1s^2$ core orbitals are optimized at the Hartree–Fock level for a suitable valence state of Li_{13}^+ and left frozen at this level and uncorrelated in subsequent calculations. The difference in total energy (E) between generalized valence bond (GVB) calculations performed in this manner and GVB calculations allowing the $1s^2$ core orbitals to relax (but remain uncorrelated) is negligible, e.g., 0.10 mhartree for I_h Li_{13}^+.

The closed-shell restricted Hartree–Fock many electron wave function (Ψ^{HF}) of Li_{13}^+ is written

$$\Psi^{HF} = \hat{A}[\Phi^{CORE}\psi_1(1)\psi_1(2)\psi_2(3)\psi_2(4)\psi_3(5)\psi_3(6) \ldots\psi_6(11)\psi_6(12)\chi^{HF}] \quad (10)$$

where $\hat{A}$ is the antisymmetrizer (determinantal operator), Φ^{CORE} contains the 13 doubly occupied Li 1s core orbitals, $\{\psi_i\}$ are doubly occupied orthogonal valence orbitals, and

$$\chi^{HF} = \alpha(1)\beta(2)\alpha(3)\beta(4)\alpha(5)\beta(6)\ldots\alpha(11)\beta(12)] \quad (11)$$

is the HF spin function where α and β are the electronic spin functions describing the up-spin ($m_s = {}^1/_2$) and down-spin ($m_s = -{}^1/_2$) projections, respectively. Although it is often customary to apply symmetry restrictions to the HF orbitals when solving for their optimum shapes, this often results in higher energies than similar calculations without such spatial symmetry restrictions.[5] Thus, we solved for the optimum (self-consistent) orbitals $\{\psi_i\}$ for Ψ^{HF} without imposing spatial symmetry restrictions.

The low-spin unrestricted Hartree–Fock many electron wave function (Ψ^{UHF}) is written

$$\Psi^{UHF} = \hat{A}[\Phi^{CORE}\varphi_{1A}\varphi_{1B}\varphi_{2A}\varphi_{2B}\varphi_{3A}\varphi_{3B}\cdots\varphi_{6A}\varphi_{6B}\chi^{HF}] \quad (12)$$

where it is understood that the electronic coordinates are labeled sequentially. Again, we solved Ψ^{UHF} self-consistently without imposing spatial symmetry restrictions on the orbitals $\{\varphi_{iA}, \varphi_{iB}\}$. Making the restriction $\varphi_{iA} = \varphi_{iB}$ results in Ψ^{HF}, thus the UHF total energy is never higher than the HF total energy (Ψ^{UHF} eschews the HF restriction of doubly occupied valence orbitals). Here, singly occupied orbitals are partitioned into two sets $\{\varphi_{iA}\}$ and $\{\varphi_{iB}\}$. Because of the Pauli principle ($\hat{A}$), orbitals within one set are mutually orthogonal but are allowed to overlap orbitals of the other set. Although the spin *projection* of each electron is quantized in χ^{HF}, Ψ^{UHF} is not an exact eigenfunction of the *total* spin operator ($\hat{S}^2$) and hence does not give the correct spin spectrum of the many-electron states.[5]

The perfect-pairing GVB wave function ($\Psi^{GVB\text{-}PP}$) has the form

$$\Psi^{GVB\text{-}PP} = \hat{A}[\Phi^{CORE}(\phi_{1A}\phi_{1B})(\phi_{2A}\phi_{2B})(\phi_{3A}\phi_{3B})\ldots(\phi_{6A}\phi_{6B})\chi^{PP}] \quad (13)$$

where

$$\chi^{PP} = (\alpha\beta - \beta\alpha)(\alpha\beta - \beta\alpha)(\alpha\beta - \beta\alpha)\ldots(\alpha\beta - \beta\alpha) \quad (14)$$

describes a singlet spin eigenstate (of $\hat{S}^2$) in which singly occupied, nonorthogonal pairs of orbitals (ϕ_{iA}, ϕ_{iB}) are described as two-electron singlet spin eigenstates and solved for self-consistently (energy-optimized). For Li_{13}^+, the optimum canonical UHF orbitals are somewhat delocalized over the cluster, while the optimum GVB-PP orbitals tend to be fairly localized. Although the GVB-PP wave function is a proper exact eigenfunction of $\hat{S}^2$, the spin function χ^{PP} is not in general optimum. In $\Psi^{GVB\text{-}PP}$, the strong orthogonality[48] restriction is imposed; i.e., for Li_{13}^+ the 12 valence orbitals are partitioned into six bond pairs, and each orbital is allowed to overlap only the orbital that it is paired with (e.g., ϕ_{1A} is allowed to overlap ϕ_{1B}) but is restricted to be orthogonal to all of the other orbitals). The qualitative aspects of the electronic structure are discussed in terms of $\Psi^{GVB\text{-}PP}$ since the localized GVB-PP one-electron orbitals provide a useful conceptual description of the bonding.

The GVB-PP description is excellent for systems such as hydrocarbons or crystalline silicon in which there is only one favorable way to spin pair the orbitals on various atoms to form strong (high overlap) two-center, two-electron bonds. However, for metallic systems such as Li_{13}^+, each localized valence orbital may have several near neighbor orbitals with which it could overlap and be spin-paired. Thus, there may be several nearly equivalent ways (resonance structures) of forming bond pairs. For such systems, it is important to allow each localized orbital to overlap *all* adjacent orbitals and to optimize the spin function χ (including thereby the optimum combination of bonding structures) in order to maximize the total exchange energy stabilization resulting from all of these adjacent overlaps.[5] In order to allow for the optimum description of such resonance effects, a *full* GVB description is needed.

The full GVB wave function has the form

$$\Psi^{GVB} = \hat{A}[\Phi^{CORE}\phi_1\phi_2\phi_3\ldots\phi_{12}\chi^{GVB}] \quad (15)$$

with one orbital per valence electron (as in Ψ^{UHF} and $\Psi^{GVB\text{-}PP}$), but now the spin function (χ^{GVB}) and the orbitals $\{\phi_i\}$ are optimized simultaneously without restrictions.[18] Thus, the valence orbitals are no longer partitioned artificially into two sets (as in UHF) or six bond pairs (as in GVB-PP). Rather, each orbital is allowed to overlap all the other orbitals. Unfortunately, Ψ^{GVB} is not practicable for N larger than eight or ten (because of the large number of overlapping terms); thus, it is customary to approximate Ψ^{GVB} by using orbitals derived from $\Psi^{GVB\text{-}PP}$ in a CI expansion (GVB-CI).[52] A full CI over GVB orbitals also requires a large amount of computational effort for 12 electrons (especialy for low symmetry cases), and consequently we have employed truncations of $\Psi^{GVB\text{-}CI}$, as described in the following section.

A.5. Truncated GVB-CI Wave Functions. The GVB-PP wave function of Li_{13}^+ involves 13 doubly occupied 1s core orbitals and 12 singly occupied valence orbitals partitioned into six bond pairs $\{(\phi_{iA}, \phi_{iB}), i = 1, 2, \ldots, 6\}$. The 12 valence orbitals are optimized self-consistently for each geometry, while allowing the orbitals to localize (no symmetry restrictions are imposed) and overlap in pairs. For describing the GVB-CI, it is useful to expand the GVB (overlapping) orbitals $\{\phi_{iA}, \phi_{iB}\}$ in terms of GVB orthogonal *natural orbitals*[50,52] $\{\psi_{iA}, \psi_{iB}\}$ as

$$\phi_{iA} = (\sigma_{iA}^{1/2}\psi_{iA} + \sigma_{iB}^{1/2}\psi_{iB})/(\sigma_{iA} + \sigma_{iB})^{1/2} \quad (16)$$

$$\phi_{iB} = (\sigma_{iA}^{1/2}\psi_{iA} - \sigma_{iB}^{1/2}\psi_{iB})/(\sigma_{iA} + \sigma_{iB})^{1/2} \quad (17)$$

where the expansion coefficients $\sigma_{iA} > 0$, $\sigma_{iB} > 0$ are related to the overlap of ϕ_{iA} and ϕ_{iB}

$$(\sigma_{iA} - \sigma_{iB})/(\sigma_{iA} + \sigma_{iB}) = (\phi_{iA}|\phi_{iB}) \quad (18)$$

$$\sigma_{iA}^2 + \sigma_{iB}^2 = 1.0 \quad (19)$$

In this way, $\Psi^{GVB\text{-}PP}$ can be rewritten in terms of doubly occupied (natural) orbitals $(\psi_{1A}, \psi_{1B}\ldots\psi_{6A}, \psi_{6B})$ as

$$\Psi^{GVB\text{-}PP} = \hat{A}[\Phi^{CORE}(\sigma_{1A}\psi_{1A}\psi_{1A} - \sigma_{1B}\psi_{1B}\psi_{1B}) \ldots(\sigma_{6A}\psi_{6A}\psi_{6A} - \sigma_{6B}\psi_{6B}\psi_{6B})\chi^{HF}] \quad (20)$$

Since each of the six bond pairs involves two configurations in the natural orbital representation, this CI form of $\Psi^{GVB\text{-}PP}$ involves $2^6 = 64$ spatial configurations (SC) and one spin term (χ^{HF}). In comparison, the independent particle form of $\Psi^{GVB\text{-}PP}$ involves just one SC but 64 spin terms (in χ^{PP}). Thus, both forms of $\Psi^{GVB\text{-}PP}$ lead to 64 determinants for Li_{13}^+.

A full (untruncated) GVB-CI (allowing all possible combinations of 12 electrons among 12 orbitals) involves 73 789 SC [226 512 spin eigenfunctions (SEF), 853 776 determinants (DET)]. Consequently, we have employed truncations of $\Psi^{GVB\text{-}CI}$.

We find that a particular set of truncations of $\Psi^{GVB\text{-}CI}$ [based on the CI form of $\Psi^{GVB\text{-}PP}$] is quite useful for Li_{13}^+. First we partition the 64 SC of $\Psi^{GVB\text{-}PP}$ into seven sets. The "zeroth order" set consists of the single (dominant) SC with two electrons in the first natural orbital for each of the six bond pairs

$$\text{PPCI(0):} \quad |\psi_{1A}^2\psi_{2A}^2\psi_{3A}^2\psi_{4A}^2\psi_{5A}^2\psi_{6A}^2| \quad (21)$$

The second-order set consists of the six SC involving a double excitation in just one of the six pairs, e.g.

$$\text{PPCI(2):} \quad |\phi_{1B}^2\phi_{2A}^2\phi_{3A}^2\phi_{4A}^2\phi_{5A}^2\phi_{6A}^2| \tag{22}$$

In general, the $2l$-th order set [PPCI($2l$)] consists of the $\binom{6}{l}$ SC involving double excitations in l of the six bond pairs, thus the 64 SC partition as 1 + 6 + 15 + 20 + 15 + 6 + 1 for the sets of order 0, 2, 4, 6, 8, 10, and 12, respectively.

The PPCI wave function is simply the CI wave function involving these 64 SC. Thus Ψ^{PPCI} is nearly equivalent to $\Psi^{GVB\text{-}PP}$, the only difference being the coefficient restrictions of $\Psi^{GVB\text{-}PP}$, which leads to Ψ^{PPCI} having total energies generally lower than $\Psi^{GVB\text{-}PP}$ by about 0.01 millihartree. PPCI+SD(0) is defined as the wave function consisting of PPCI plus all single and double excitations (within the GVB natural orbitals) from PPCI(0). The PPCI+SD(2) truncation is PPCI plus all single and double excitations from the seven configurations included in PPCI(0) and PPCI(2). In general, PPCI+SD($2l$) is defined as the wave function consisting of PPCI+SD($2l - 2$) plus all additional single and double excitations from PPCI($2l$).

The limit of the PPCI+SD($2l$) series is PPCI+SD(n_e), where n_e is the total number of valence electrons (n_e = 12 for Li_{13}^+). The PPCI+SD(n_e) wave function is equivalent to PPCI times singles and doubles (PPCI×SD) and includes all excitations up to second order from all 64 SC in PPCI). For Li_{13}^+, the PPCI wave function differs from the full GVB-CI wave function by excitations up to sixth order, since PPCI already includes selected *closed-shell* excitations up to twelfth order from the dominant SC.

We find for Li_{13}^+ that the PPCI+SD($2l$) truncations of $\Psi^{GVB\text{-}CI}$ lead to an efficient method of including nearly all of the important electronic correlation effects of the full GVB-CI; e.g., PPCI+SD(12) includes ≈90% of the total energy difference between GVB-PP and full GVBCI. We tested the PPCI+SD($2l$) truncations for the I_h cluster by comparing the total energies with those calculated with the GVB-CI($2l$) truncations as described below (see Table VIII and Figure 22b).

The GVB-CI(0) wave function consists of the dominant SC of the zeroth order set. GVB-CI(2) is defined as GVB-CI(0) plus all single and double excitations from the dominant SC. In general, GVB-CI($2l$) consists of GVB-CI($2l - 2$) plus $l - 1$ and l order excitations from the dominant SC, thus GVB-CI(12) is the full (untruncated) GVB-CI wave function.

Results for the PPCI+SD($2l$) and GVB-CI($2l$) truncated CI wave functions are given in Table VIII and Figure 22b for l = −1, 0, 1, 2, and 3 and are extrapolated to l = 6 for the I_h cluster. Both series of truncations are fairly well converged at l = 3. The error in the PPCI+SD(12) *total* energy (compared to the estimated full GVB-CI result) is only 0.08 eV. Errors in the PPCI+SD(12) *relative* energies (due to truncation of the GVB-CI) are certainly much smaller (due to cancellation effects).

Registry No. Li, 7439-93-2.

Thesis Conclusions

In Volume 1 of the serial *Solid State Physics*, Wigner and Seitz[1] state, "If one had a great calculating machine, one might apply it to the problem of solving the Schrödinger equation for each metal and obtain thereby the interesting physical quantities. ... It is not clear, however, that a great deal would be gained by this. It would be preferable instead to have ... a simple description of the essence of the factors which determine cohesion and an understanding of the origins of variation in properties from metal to metal."

This thesis presents results leading to new concepts of metallic bonding, derived from generalized valence bond theory — real-space concepts that do not require "thinking in reciprical (k) space." In the process of deriving these concepts, we refute a number of myths concerning one-dimensional metals. Hence, one-dimensional metals need not exhibit Peierls distortions,[2] spin density waves or charge density waves. For one-dimensional metal clusters composed of monovalent atoms (Cu, Ag, Au, Li, and Na), generalized valence bond theory leads to fully symmetrical charge densities, fully symmetrical spin densities, and magnon spectra that fit the Heisenberg Hamiltonian.[3]

Generalized valence bond theory leads to the conclusion that, for metallic systems, the valence electrons occupy interstitial regions — bond midpoints for one-dimensional systems, triangular hollows for two-dimensional systems, and tetrahedral

hollows for three-dimensional systems. Hence, for the n-dimensional metallic system, the "characteristic" localized valence orbital is composed of sp hybrid orbitals from $n+1$ adjacent atoms.

The new concepts of metallic bonding are summarized by the following set of rules for the valence sp electrons of metallic systems.

(α) Orbitals (each with one electron) are localized in different tetrahedral hollows where possible.

(β) If necessary, two electrons may be placed in one tetrahedron (localizing on opposite faces or edges) but they must be spin-paired.

(γ) No more than two electrons may be distributed between a pair of *face-shared* tetrahedra, and these must be spin-paired (singlet).

(δ) No more than three electrons may be distributed between a pair of *edge-shared* tetrahedra.

(ϵ) No more than four bond pairs of electrons may share one central bulk atom, and no more than three bond pairs of electrons may share one central surface atom.

(ζ) Additional electrons must be in surface orbitals at edge or face sites that do not share edges with occupied tetrahedra.

These rules are used to derive the low-lying isomers of small metal clusters, and are expected to prove useful in predicting the chemistry and catalytic properties of such systems.[4]

Applying these rules to bulk metals leads to a new explanation of the solubility limits governing the alloys of monovalent, divalent, trivalent, and tetravalent atoms

— the Hume-Rothery rules.[5] These rules are expected to be most valuable in describing localized states in metals and alloys such as defects or interfaces. These new concepts of metallic bonding are expected to apply to a variety of metals and alloys — including *fcc* and *hcp*, γ-brass, the Laves phases,[6] and Frank-Kasper alloys.[7]

References

[1] E. P. Wigner and F. Seitz, *Solid State Physics* **1**, 97 (1955).

[2] R. Peierls, *Quantum Theory of Solids* (Clarendon Press, Oxford, 1955).

[3] W. Heisenberg, *Z. Phys.* **49**, 619 (1928).

[4] E. A. Carter, Ph. D. Thesis, California Institute of Technology, 1987.

[5] W. Hume-Rothery and G. V. Raynor, *The Structure of Metals and Alloys, 4th Ed.* (Institute of Metals, London, 1962).

[6] A. Taylor, *X-Ray Metallography* (Wiley, New York, 1961).

[7] F. C. Frank and J. S. Kasper, *Acta Cryst.* **12**, 483 (1959) and *ibid*, **11**, 184 (1958).